

University of Wollongong - Research Online

Thesis Collection

Title: Development of advanced electrode materials for use in rechargeable lithium batteries

Author: Scott A Needham

Year: 2007

Repository DOI:

Copyright Warning

You may print or download ONE copy of this document for the purpose of your own research or study. The University does not authorise you to copy, communicate or otherwise make available electronically to any other person any copyright material contained on this site.

You are reminded of the following: This work is copyright. Apart from any use permitted under the Copyright Act 1968, no part of this work may be reproduced by any process, nor may any other exclusive right be exercised, without the permission of the author. Copyright owners are entitled to take legal action against persons who infringe their copyright. A reproduction of material that is protected by copyright may be a copyright infringement. A court may impose penalties and award damages in relation to offences and infringements relating to copyright material.

Higher penalties may apply, and higher damages may be awarded, for offences and infringements involving the conversion of material into digital or electronic form.

Unless otherwise indicated, the views expressed in this thesis are those of the author and do not necessarily represent the views of the University of Wollongong.

Research Online is the open access repository for the University of Wollongong. For further information contact the UOW Library: research-pubs@uow.edu.au

University of Wollongong Thesis Collections

University of Wollongong Thesis Collection

University of Wollongong

Year 2007

Development of advanced electrode
materials for use in rechargeable lithium
batteries

Scott Andrew Needham
University of Wollongong

Needham, Scott A, Development of advanced electrode materials for use in rechargeable lithium batteries, PhD thesis, Institute for Superconducting and Electronic Materials, University of Wollongong, 2007. <http://ro.uow.edu.au/theses/696>

This paper is posted at Research Online.
<http://ro.uow.edu.au/theses/696>

NOTE

This online version of the thesis may have different page formatting and pagination from the paper copy held in the University of Wollongong Library.

UNIVERSITY OF WOLLONGONG

COPYRIGHT WARNING

You may print or download ONE copy of this document for the purpose of your own research or study. The University does not authorise you to copy, communicate or otherwise make available electronically to any other person any copyright material contained on this site. You are reminded of the following:

Copyright owners are entitled to take legal action against persons who infringe their copyright. A reproduction of material that is protected by copyright may be a copyright infringement. A court may impose penalties and award damages in relation to offences and infringements relating to copyright material. Higher penalties may apply, and higher damages may be awarded, for offences and infringements involving the conversion of material into digital or electronic form.

Development of Advanced Electrode Materials for use in Rechargeable Lithium Batteries

A thesis submitted in fulfillment of the requirements
for the award of

DOCTOR OF PHILOSOPHY

by

SCOTT ANDREW NEEDHAM, BEng (Hons 1), MMgmt

University of Wollongong



Institute for Superconducting and Electronic Materials
and the
Faculty of Engineering

2007

© 2007

Scott Andrew Needham

All Rights Reserved

Declaration

I, Scott Andrew Needham, declare that this thesis, submitted in fulfillment of the requirements for the award of Doctor of Philosophy, in the Institute for Superconducting and Electronic Materials, in the Faculty of Engineering, University of Wollongong, is wholly original work unless otherwise referenced or acknowledged. This thesis has not been submitted for qualifications at any other academic institution.

A handwritten signature in cursive script, reading "Needham".

Wollongong, Australia

December 2006

For Anita, Benjamin and Oliver

Acknowledgements

I thank the Director of ISEM, Professor Shixue Dou, for providing the support and financial assistance for my PhD project, but especially for introducing me to the intriguing field of rechargeable lithium batteries. I am particularly grateful to my academic supervisors, Dr. Guoxiu Wang and Prof. Huakun Liu, for their guidance, availability, and open-mindedness throughout my research. They were ever vigilant to provide me with additional learning opportunities by supporting my attendance at specialized training courses and international conferences. I also express my gratitude to my unofficial academic supervisor, Dr. Andrzej Calka, for his insightful discussions on the finer points of mechanical milling and electric discharge assisted milling. I am also indebted to the Australian Research Council (ARC) for their financial support in the form of an Australian postgraduate award, ARC Linkage project LP0453766, and the Centre of Excellence program.

I thank all the hard working technical and administrative staff of the Faculty of Engineering and ISEM that “greases the wheels of the research machine”. A staff member’s most cherished reward is often the satisfaction in ensuring that a device can be built, a machine runs efficiently, or that a system operates smoothly. I have made many new friends at ISEM, both accomplished academics and talented students. This has made my tenure at ISEM an absolute pleasure, and I wish everyone the best of luck in their chosen pursuits. In particular, I thank my friend Germanas Peleckis – it has been a real life journey – and we must continue to believe that every cloud has a silver lining.

Finally, words cannot express my gratitude for the unwavering support of my family. I thank my mother and father, John and Gail Needham, and my parents-in-law, Done and Rajna Stefoski, for their constant support and interest in my studies. But most of all, I thank my beautiful wife Anita and my two baby boys, Benjamin and Oliver. They have shared the highs and lows of research and provided me with the strength, understanding and love to enable the completion of this thesis. My PhD studies have also been marked by the passing of my Nanna, Enid Muir, and Grandfather, Bill Needham – You both will exist forever in my heart.

Abstract

Batteries are a necessary companion to most portable electronic devices, and the rechargeable lithium battery is the most energy dense and lightest of all the competing battery types. These features make it the most likely battery to be used in future electronic devices, which will be smaller and have increased functionality. Therefore, the performance of the rechargeable lithium battery must continue to be improved in terms of capacity, rate capability, and cycle life. This thesis contributes to this goal by developing new materials and novel synthesis techniques for application in advanced rechargeable lithium batteries.

A significant contribution to the ever-growing collection of works on the doping of LiCoO_2 and LiFePO_4 structures in an attempt to raise their practical storage capacities is presented. The practical capacity of these materials can sometimes be increased by aliovalent doping due to the formation of charge-carrying holes, which impart a higher electrical conductivity. In the case of LiCoO_2 doped with Mg, V and Mo prepared by traditional solid-state methods, the lithium storage capacity was not improved compared to the un-doped LiCoO_2 . This was attributed to the formation of lithium-containing secondary phases, which resulted in a lithium deficient primary phase and a higher concentration of Jahn-Teller Co^{4+} ions. These effects disrupted the intercalation framework and produced a poor electrochemical performance. In contrast, work on the doping of titanium into LiFePO_4 confirmed that a complete solid solution could be formed using a sol-gel method, despite several previous works suggesting that the aliovalent doping of this structure was impossible. Doping 1 mol% titanium into the LiFePO_4 structure improved the capacity to only 5 % less than the theoretical maximum attainable capacity. The mechanism for this improvement was related to increased *p*-type semiconductivity in the material.

A novel materials synthesis technique, electric discharge assisted mechanical milling (EDAMM), was applied for the first time to the preparation of functional oxides. LiCoO_2 and LiFePO_4 cathode materials and $\text{SrTi}_x\text{Co}_{1-x}\text{O}_3$ ($x = 0, 0.1, 0.2, 0.5$), which has possible magnetic applications, were synthesized in a matter of minutes with either micro-sized or nano-sized powder morphologies. The electrochemical performance of the cathode materials

was shown to be comparable to those delivered by powders synthesized by traditional solid-state techniques. $\text{SrTi}_x\text{Co}_{1-x}\text{O}_3$ powders could be formed as complete solid solutions with interesting magnetic properties. The EDAMM method shows commercial potential, as it can synthesize a wide range of functional oxide powders in high quantities. Concerning the synthesis of novel materials, this work also reports on the first ever formation of uniform and aligned NiO nanotubes. The nanotubes were up to 60 μm long, had an outer diameter of 200 nm and a wall thickness of 20-30 nm. Compared to nanocrystalline NiO, the nanotubes delivered a 30 % increase in the discharge capacity after repeated cycling. Electrochemical impedance spectroscopy suggests that this improvement was due to kinetic advantages.

Finally, unique carbon-based SnSb and transition metal oxide nanocomposite materials formed by various chemical techniques are shown to offer promise as anode materials due to their high capacity and excellent cycle life. The use of SnSb alloys has previously been hindered by their poor cyclability, which is caused by volume changes during cycling that result in a loss of electrical contact. Physically mixing carbon in a 1:1 weight ratio with the active material does not improve the cyclability of the electrode, but improves the realized capacity by increasing the electrical conductivity. A superior method of utilizing carbon in a composite form is to synthesize a SnSb-CNT powder, in which the SnSb is chemically bonded onto the carbon nanotube (CNT) nano-network. These powders demonstrated a high reversible capacity and stable cyclability. This method is an effective and promising option to address the problem of volume changes in all high capacity alloys. The $\text{Co}_3\text{O}_4\text{-C}$ composite powders were produced by spray pyrolysis of a sugar-metal ion solution. The capacity in cells was $> 800 \text{ mAh g}^{-1}$ for over 50 cycles, which solved the capacity fade problems. The improved electrochemical properties were related to the presence of a carbon sheath formed during processing, which acted to prevent excessive electrolyte reduction and retard the development of a thick solid electrolyte interphase (SEI). A disordered C matrix was also formed throughout the bulk powder during processing, which assisted in cushioning the volume changes associated with the electrochemical reaction.

Table of Contents

1. Introduction	1
2. Literature review	6
2.1 Rechargeable Lithium Batteries	6
2.1.1 A Brief History	6
2.2 Fundamental Considerations	10
2.2.1 Principles of Operation	10
2.2.2 The Cell Voltage	11
2.3 Cathode Materials	13
2.3.1 Lithium Cobalt Oxide	14
2.3.1.1 Structural and Electrochemical Properties	14
2.3.1.2 Doping of LiCoO_2 Compounds <i>via</i> Solid-State Methods	18
2.3.1.3 Alternative Synthesis Methods	20
2.3.2 Lithium Iron Phosphate	22
2.3.2.1 A Shifting Ideology	22
2.3.2.2 Structural and Electrochemical Properties	23
2.3.2.3 Effect of Dopants	26
2.3.2.4 Alternative Synthesis Methods	27
2.4 Anode Materials	28
2.4.1 Carbon	28
2.4.1.1 Forms of Carbon	29
2.4.1.2 Lithium Intercalation and Failure Mechanisms	32
2.4.1.2.1 Dependence on Carbon Type	32
2.4.1.2.2 Electrolyte Considerations	34
2.4.1.3 Composites using Carbon from Agricultural Sources	36
2.4.2 SnSb Metal Pnictide	37
2.4.2.1 Crystal Structure	39
2.4.2.2 Reactions with Lithium and Synthesis Techniques	41

2.4.3	Transition Metal Oxides	45
2.4.3.1	Reactions of Co_3O_4 with Lithium	47
2.5	Nanostructures	49
2.5.1	Synthesis of Nanotube Materials <i>via</i> the Template Method	52
2.6	Battery Electrolytes	54
2.6.1	Organic Solvents	54
2.6.2	Lithium Salts and Other Active Components	55
3.	Experimental	56
3.1	Overview	56
3.2	Methods of Synthesis	57
3.2.1	Solid-State	57
3.2.2	Sol-Gel	57
3.2.3	Electric Discharge Assisted Mechanical Milling	58
3.2.4	Nanoscale Templating	60
3.2.5	Reductive Precipitation	61
3.2.6	Spray Pyrolysis	62
3.3	Methods of Characterization	63
3.3.1	Structure and Morphology	63
3.3.2	Particle Surface Area Measurements	64
3.3.3	Electrical Conductivity	65
3.3.4	Magnetic Measurements	66
3.3.5	XAFS and XANES	66
3.4	Electrochemical Assessment	69
3.4.1	Electrode Fabrication and Test Cell Assembly	69
3.4.2	Galvanostatic Charge/Discharge Cycling	70
3.4.3	Cyclic Voltammetry	71
3.4.4	Electrochemical Impedance Spectroscopy	71
4.	$\text{LiM}_x\text{Co}_{1-x}\text{O}_2$ Compounds Prepared <i>via</i> a Solid-State Method	73
4.1	Introduction	73

4.2	Experimental	73
4.3	Results and Discussion	74
4.3.1	Structural and Morphological Characterization	74
4.3.2	Electrochemical Properties	83
4.4	Summary	85
5.	The Effect of Titanium Doping on LiFePO₄ Prepared <i>via</i> a Sol-Gel Method	86
5.1	Introduction	86
5.2	Experimental	87
5.3	Results and Discussion	88
5.3.1	Structural and Morphological Characterization	88
5.3.2	Electrochemical Properties	95
5.4	Summary	97
6.	Functional oxides Prepared <i>via</i> a Novel Electric Discharge Assisted Mechanical Milling Method (EDAMM)	98
6.1	Introduction	98
6.2	Experimental	99
6.3	Results and Discussion	100
6.3.1	Synthesis and Characterization of LiCoO ₂	100
6.3.2	Electrochemical Properties of LiCoO ₂	103
6.3.3	Synthesis and Characterization of LiFePO ₄	104
6.3.4	Electrochemical Properties of LiFePO ₄	106
6.3.5	Synthesis and Characterization of SrTi _{1-x} Co _x O ₃	108
6.3.6	Magnetic Properties of SrTi _{0.5} Co _{0.5} O ₃	110
6.4	Scalability and Commercialization of EDAMM	112
6.5	Summary	113
7.	NiO Nanotubes Prepared <i>via</i> a Nanoscale Templating Method	114
7.1	Introduction	114

7.2	Experimental	114
7.3	Results and Discussion	115
7.3.1	Structural and Morphological Characterization	115
7.3.2	Electrochemical Properties	117
7.3.3	Electrochemical Impedance Spectroscopy	121
7.4	Summary	122
8.	SnSb-Carbon Composites Prepared <i>via</i> a Reductive Precipitation Method	123
8.1	Introduction	123
8.2	Experimental	124
8.3	Results and Discussion	125
8.3.1	Structural and Morphological Characterization of SnSb Alloys	125
8.3.2	Electrochemical Properties of SnSb-C	126
8.3.3	Summary on SnSb-C	130
8.3.4	Structural and Morphological Characterization of SnSb-CNT	130
8.3.5	Electrochemical Properties of SnSb-CNT	134
8.3.6	Summary on SnSb-CNT	137
9.	Transition Metal Oxide-Carbon Composites Prepared <i>via</i> the Spray Pyrolysis Method	138
9.1	Introduction	138
9.2	Experimental	138
9.3	Results and Discussion	139
9.3.1	Structural and Morphological Characterization	139
9.3.2	Electrochemical Properties	142
9.3.3	Electrochemical Impedance Spectroscopy	144
9.4	Summary	147

10. Conclusions and Recommendations	148
11. References	150
List of Symbols and Abbreviations	168
List of Materials and Chemicals	172
List of Figures	174
List of Tables	182
List of Author Publications	183

1. Introduction

Energy generation and energy storage are two of the biggest challenges currently facing society, and as such, are issues that attract tremendous interest from research groups, governments, and industry alike. According to the Boston Consulting Group, the international battery industry generates around US\$ 50 billion per year in revenue, and the requirement for portable power is set to increase by 26 % per year well into the foreseeable future. Consumers are demanding more portability and functionality in electronic devices, which compels manufacturers to integrate multiple devices into a single miniaturized product. A good example of this trend is the inclusion of digital cameras, radios, and music (mp3) players into mobile phones. These devices consequently require more power and flexibility in the rate at which the power is delivered to support their added functionality.

From all of the competing battery technologies, the rechargeable lithium battery is fundamentally the best at delivering the highest power capacity at variable rates. Since the “birth” of the first mass-produced commercial rechargeable lithium cell only 15 years ago, a substantial body of theoretical and practical knowledge has been compiled. Despite these positive aspects, it could be argued that these efforts have translated into only modest improvements in the practical capability of the battery. Indeed, by any measure of performance, rechargeable lithium batteries have not kept pace with the exponential improvements made in the processors that control electronic devices, as described by *Moore's law*^a.

In rechargeable lithium batteries, there are several main areas of research; anode materials, cathode materials, separators, electrolytes (*i.e.*, solvent-salt combination and solid vs. liquid technologies), and the overall construction or design of the cell.

^a In 1965, Gordon Moore, Director of Fairchild Semiconductor's Research and Development Laboratories, wrote an article on the future development of the semiconductor industry for the 35th anniversary issue of *Electronics Magazine*. In the article, Moore noted an exponential increase in the number of components on a chip, which became later known as Moore's Law. In the 1980s, Moore's Law started to be described as the doubling of the number of transistors on a chip every 18 months. At the beginning of the 1990s, Moore's Law became commonly interpreted as the doubling of microprocessor power every 18 months. In the late 1990s, Moore's Law was associated with the claim that computing power at fixed cost is doubling every 18 months.

By far the greatest efforts, judged by publication volume alone, are within the areas of anode and cathode material research. Research in these areas is basically approached in one of three directions:

1. an attempt to discover new materials and/or new classes of materials;
2. the development of new methods to synthesize the known electrode materials;
3. the fine-tuning of existing structure(s) by way of compositional changes, surface modification, formation of composites, or morphological changes, for example.

Regardless of the direction of the approach, the overall goal is to develop materials that have better properties for use in rechargeable lithium batteries; that is, materials that possess a higher lithium storage capacity, a longer cycle life, and improved rate capabilities. By far, the riskiest approaches involve the development of new methods or new materials. However, just as is true in the financial markets, the riskier the investment, in general, the greater the potential return.

The pervading trends in research into electrode materials are the fabrication of nanoscale materials and the development of complex composite materials into which the benefits of each constituent material can be built. Sometimes the properties of composite materials can be synergistically enhanced beyond the benefits provided by each individual part. Battery systems must also be capable of being miniaturized in line with the consumer desire for increased portability of electronic devices.

Chapter 2 presents a succinct review of the extensive body of literature related to rechargeable lithium batteries. The chapter includes a brief history of the development of various lithium-based battery systems, some fundamental theoretical considerations, and the current state of research and development of the electrode materials investigated in this thesis.

Chapter 3 presents the overall experimental methodology used for this work in both written and visual formats. The chapter includes the following brief descriptions: the techniques used to prepare the electrode materials; the methods of structural and physical characterization; the stages in fabricating a coin cell; and the various

methods used to assess the electrochemical performance of the materials. Additional specific details are given in the beginning of each chapter as required.

Chapter 4 discusses results on the cation doping of the most popular commercial cathode material (LiCoO_2) as a method to reduce the structural change experienced when a battery is cycled to a high upper voltage cut-off. Powders with the composition $\text{LiM}_{0.02}\text{Co}_{0.98}\text{O}_2$ ($\text{M} = \text{Mg}, \text{V}, \text{Mo}$) were prepared using a simple solid-state method. There is currently no literature on the synthesis and electrochemical performance of LiCoO_2 doped with vanadium and molybdenum. Synchrotron x-ray diffraction (XRD) and the Rietveld refinement technique were used to determine structural parameters and whether a complete solid solution could be formed. X-ray absorption spectroscopy (XAS) and electrical conductivity measurements were used to elucidate the electronic properties of the prepared compounds. Coin cells were constructed using the as-synthesized powders as the active material, and the electrochemical performance of these cells was assessed by using cyclic voltammetry (CV) and galvanostatic charge/discharge cycling.

Chapter 5 continues with cation doping as an approach to fine-tune the electronic structure of cathode materials in order to improve their electrochemical performance. In this chapter, the promising LiFePO_4 material and a titanium doped variety ($\text{LiTi}_{0.01}\text{Fe}_{0.99}\text{PO}_4$) are prepared *via* a sol-gel process. Synchrotron XRD and the Rietveld refinement technique were used to determine structural parameters and whether titanium atoms could be properly substituted into the LiFePO_4 lattice. High resolution imaging of the prepared powders was conducted using field emission transmission electron microscopy (FE-TEM). The electronic structure of the powders was analyzed using x-ray absorption spectroscopy (XAS) and x-ray absorption near edge spectroscopy (XANES) techniques. Coin cells were constructed using the as-synthesized powders as the active material, and the electrochemical performance of these cells was assessed by using CV and galvanostatic charge/discharge cycling.

Chapter 6 explores the fabrication of LiCoO_2 and LiFePO_4 cathode materials and $\text{SrTi}_{1-x}\text{Co}_x\text{O}_3$ ($x = 0, 0.1, 0.2, \text{ and } 0.5$) compounds by a novel electric discharge assisted mechanical milling (EDAMM) materials synthesis technique. EDAMM is a rapid, high-energy technique that utilizes mechanical milling and plasma processing

simultaneously. The as-synthesized powders were characterized using XRD, TEM, scanning electron microscopy (SEM), and inductively coupled plasma (ICP) techniques. Their functionalities are assessed by electrochemical and magnetic measurements, with the results compared to those from the same powders synthesized by traditional methods.

Chapter 7 is based on the first-ever report(s) on the synthesis and performance of uniform and aligned NiO nanotubes as anode materials. The synthesis technique involved first forming Ni(OH)₂ nanotubes within the walls of an alumina template and then converting these nanotubes to NiO nanotubes by a simple heating step. The nanotubes were characterized using XRD, SEM, and TEM. Coin cells were constructed using the nanotube powders as the active material, and the electrochemical performance of these cells was assessed by using CV, galvanostatic charge/discharge cycling, and ac electrochemical impedance spectroscopy (EIS). The results of the electrochemical testing are compared to those from a nanocrystalline NiO reference powder.

In Chapter 8, promising SnSb-carbon nanocomposites are investigated as next generation anode materials. Composite materials that use various carbons as a stable framework structure have recently shown particular promise in extending the cycle life of these materials. The beginning of this chapter reports on the synthesis and electrochemical performance of nanosized SnSb and SnSb-Sn powders physically mixed with various quantities of carbon black. The latter section of this chapter presents work on a physically bonded nanocomposite made by coating SnSb onto the surface of carbon nanotubes (CNTs). The structure and morphology of the materials were characterized by XRD, TEM, FE-TEM, SEM, and Raman spectroscopy. Gas sorption experiments were conducted to determine the Brunauer-Emmett-Teller (BET) specific surface area of the powders. Coin cells were constructed using the as-synthesized powders as the active material, and the electrochemical performance of these cells was assessed by using CV and galvanostatic charge/discharge cycling.

Chapter 9 presents work on another extremely promising carbon based composite anode material ($\text{Co}_3\text{O}_4\text{-C}$) synthesized by spray pyrolysis of a cobalt nitrate-sugar solution at elevated temperature. Microstructural characterization was conducted by XRD, SEM, TEM, and energy dispersive x-ray spectroscopy (EDXS). Coin cells were constructed using the nanotube powders as the active material, and the electrochemical performance of these cells was assessed by using CV, galvanostatic charge/discharge cycling, and ac EIS.

General conclusions and suggestions for continuing these works are given in Chapter 10.

2. Literature Review

2.1 Rechargeable Lithium Batteries

2.1.1 A Brief History

The concept of using an electrochemical reaction to do useful work was first demonstrated in drawings by the Egyptians over 4000 years ago.^[1] Actual battery artifacts discovered in Iraq in 1936 (known as the *Baghdad Batteries*) suggest that the battery may have been commonly used in society sometime between 250 BC and 640 AD.^[2] However, the development of modern batteries as a form of energy storage can be traced to Galvani in the 1790s.^[3] Interest rapidly grew in this new technology and by 1800, Volta had dispatched a communication to the Royal Society of London that outlined his design of a device that could produce a constant current from the proper assembly of dissimilar metals.^[4] The device consisted of alternating slabs of silver and zinc separated by cloth soaked in brine which became known as the “voltaic pile”. In 1802, Cruickshank replaced silver with copper and inserted the cell into a brine filled box, which enabled cells to be mass produced.^[5] Over the next 150 years, various battery systems were developed by a number of different scholars. A concise, but non-exhaustive list of the most important contributors to this research includes the likes of Davy^[2], Daniell^[6], Planté^[6], Laclanché^[7], Junger^[2], and Edison^[8].

Initial interest in developing a lithium-based battery was aroused after consideration of the fundamental properties of the element: lithium is the most electropositive (-3.04 V versus the standard hydrogen electrode (SHE) and lightest ($MW = 6.94$ g mol⁻¹, $\rho = 0.53$ g cm⁻³) metal, thus facilitating the design of storage systems with high energy density. Fig. 2.1 shows the amount of electrical energy per unit of weight (Wh kg⁻¹) and per unit of volume (Wh l⁻¹) that modern competing battery technologies are able to deliver.

Figure 2.1: *Gravimetric and volumetric energy density comparison of different battery technologies.*^[9]

Among these, it is clear that lithium-based batteries offer the highest energy density and cell design flexibility. A market research organization, Frost and Sullivan, reported in 2003 that 66 % of sales revenue from all rechargeable batteries used in portable electronic devices was from rechargeable lithium types, and forecast this figure to rise to 92 % by 2009.^[10] The rechargeable lithium battery has up to 3 times the gravimetric energy density of Ni–Cd batteries and a 50 % longer life cycle. Compared to Ni-MH batteries, rechargeable lithium batteries have roughly 2 times the gravimetric energy density and can be manufactured at a similar cost.

The first lithium-based battery was demonstrated in the early 1970s and was a primary or non-rechargeable type, consisting of a SOCl_2 positive electrode and a lithium metal negative electrode.^[11] About this time, it was discovered that several inorganic compounds could react with lithium and sodium in a reversible way. This led to the development of alternative battery systems that utilized layered transition metal dichalcogenides (TiS_2)^[12], chain chalcogenides (NbSe_3)^[13], or amorphous solids (MoS_3)^[14] as positive electrode materials versus a lithium metal negative electrode. These early efforts marked the discovery of what are now classified as

intercalation^b compounds, and initiated intensive research into the development of high-energy rechargeable lithium systems.^[15]

Despite the exceptional operation of some of these positive electrode materials, the overall cell suffered serious shortcomings related to the lithium metal-electrolyte combination. It was observed that dendritic growth on the surface of the lithium occurred due to the metal being re-plated during each charge/discharge cycle. The most rapid dendrite growth occurred at areas with high electrolyte exposure. After several cycles, the dendrite growth rate was further intensified due to shorter lithium ion diffusion distances. Eventually, these dendrites would perforate the separator and reach the cathode, which would cause an internal short circuit. Thermal runaway would ensue and the battery would typically “vent with flame” or explode.^[16]

Concomitant with the struggles to solve the safety concerns associated with the early rechargeable lithium systems, significant advances occurred with several intercalation compounds. It was established that oxides could provide higher capacities and voltages than the heavier chalcogenides.^[17, 18] This dispelled the belief that only low-dimensional materials could give adequate ion diffusion and catalyzed the efforts of researchers to investigate a broader range of structures. In 1980 Muzushima *et al.*^[19, 20] proposed the now renowned open framework Li_xMO_2 (M = Co, Ni or Mn) family of compounds as more suitable positive electrode materials.

Concerning the negative electrode, efforts were being focused on circumventing the serious safety issues surrounding the use of lithium metal. Several alternative approaches were proposed that involved either modification of the electrolyte or replacement of the electrode material. The most effective approach proved to be the replacement of metallic lithium with a second insertion material such as $\text{Li}_x\text{Fe}_2\text{O}_3$ or Li_xWO_2 . This meant that lithium would be intercalated into the lattice of the insertion material rather than being deposited over the surface, which solved the problem of dendritic growth. The idea to use an intercalation compound as both the negative and positive electrode was first demonstrated in 1978 by Murphy *et al.*^[21] and soon after by Scrosati *et al.*^[22, 23] who coined the term *rocking chair* battery to describe the back

^b Intercalation derives from the term used to describe the process of inserting an extra day (29th of February) into the calendar to maintain the synchrony between the calendar year and the solar year. In chemistry, intercalation is thus strictly the term used to describe the insertion of a guest atom or ion into a planar crystalline host without losing the structural integrity of the host.

and forth motion of lithium ions during cell charge and discharge processes. More recently, terms such as *Li-ion* and *shuttlecock* have been used to describe the mode of operation of the battery.

To compensate for the increase in potential of the negative electrode, the high-potential insertion compounds that had been proposed by Muzushima *et al.* (Li_xMO_2)^[19, 20] were now considered essential for use as the positive electrode. These materials displayed a higher insertion voltage than the traditionally used disulphides due to a more pronounced ionic character of M–O bonds compared with M–S bonds.^[9] A decade later, the Sony Corporation paired a LiCoO_2 positive electrode with a carbonaceous negative electrode^[24, 25] to create and commercialize the first mass produced rechargeable lithium battery.^[26]

Since this milestone, many different types of carbon have been trialed or are currently employed as the anode in rechargeable lithium batteries. For instance, the Sony Corporation routinely employs coke and polyfurfuryl alcohol (PFA) – based hard carbon materials in its batteries.^[27] Matsushita, Sanyo, and Toshiba have used mesocarbon microbeads (MCMB), graphite-coke hybrids, and pitch-based carbon fibres as the anode materials, respectively.^[28-30] Many commercial batteries commonly employ stabilized graphite materials as anodes.^[31]

Despite this positive progress, modern day rechargeable lithium batteries still have serious drawbacks. Some electrode materials suffer irreversible deleterious physical, chemical, or structural changes in the first discharge. For other materials, these changes can be caused by prolonged charge/discharge cycling or long term storage. As a result, these batteries will often exhibit poor cyclability, power-fade, self-discharge and a practical capacity that is significantly lower than theoretical predictions.^[32-34] Some of these problems can be related to surface phenomena occurring at the solid-liquid interface, but all relate to the fundamental design of the materials in use. Problems with potentially promising electrode materials can sometimes be overcome by seeking out new methods for their synthesis, using composites, stabilizing structures through doping, and surface modification techniques.

2.2 Fundamental Considerations

2.2.1 Thermodynamics

The process of energy storage in rechargeable lithium batteries follows thermodynamic laws and formulae derived from electrochemical reactions. These formulae can be used to predict whether certain processes are possible and to quantify the energy available in a system. The equilibrium potential or voltage (ΔE) of a cell can be empirically calculated by relating the thermodynamic driving force of a chemical reaction to other thermodynamic variables. To begin, the Gibbs-Helmholtz relation states that the free energy of an electrochemical reaction (ΔG) is the difference between the reaction enthalpy ($\Delta H = \Delta U + P\Delta V$) and the entropic term ($T\Delta S$):

$$\Delta G = \Delta H - T\Delta S \quad (2.1)^c$$

The terms ΔG , ΔH , and ΔS are state functions and depend only on the identity of the materials and the initial and final states of the reaction. Literally, Eqn. 2.1 states that the energy available for useful work in an electrochemical cell is equal to the difference between the energy released/absorbed and the energy associated with order/disorder. Under constant temperature and pressure, we have the following direct relationship between the free energy and the electrical work (w_e) done by a cell:

$$\Delta G = \Delta U + P\Delta V - T\Delta S = -w_e \quad (2.2)$$

Therefore, the work can be related to the cell voltage and the net available electrical energy by:

$$\Delta G = -w_e = -nFE \quad (2.3)^d$$

^c For materials in a standard state at unit activity and 298 K, $\Delta G^\circ = \Delta H^\circ - T\Delta S^\circ$

^d For materials in a standard state at unit activity and 298 K, $\Delta G^\circ = -nFE^\circ$

where n is the number of electrons transferred per mole of reactants (*i.e.*, $n = 1$ in lithium cells) and F is the Faraday constant. A reaction is considered spontaneous with a negative ΔG and as seen in Eqn. 2.3, such reactions will have a positive E . The combined term (nF) represents the amount of electrical energy produced and is determined by the amount of material available for a reaction. The cell voltage is uniquely defined for each reaction couple and reflects the intensity of the reaction. Standard electrode voltages are denoted with a degree sign superscript and are determined at 1 M solute concentration, 1 atm pressure, and 298 K. In general electrochemistry, it is orthodox that voltages are measured with respect to a SHE and expressed for the reduction reaction. From the periodic table, fluorine is reduced according to $F_{2(g)} + 2e^- \rightarrow 2F_{(aq)}^-$ ($E^\circ = 2.87$) and represents the strongest oxidizing agent. At the other extreme, lithium is reduced according to $Li_{(aq)}^+ + e^- \rightarrow Li_{(s)}$ ($E^\circ = -3.04$) and represents the strongest reducing agent. The standard voltage of a complete cell can easily be calculated from the standard voltages of participating species. In accordance with the convention used in the lithium batteries field, all voltages quoted hereafter are defined with respect to lithium (Li^+/Li), unless otherwise indicated.

In a practical situation under non-standard conditions, the free energy and voltages are different. Determination of the voltage of a full cell must take into account the activity of the different reacting species. The thermodynamic relation between the free energy, the standard free energy, and the activity of species in the reaction $aA + bB \rightarrow cC + dD$ is given by:

$$\Delta G = \Delta G^\circ + RT \ln Q \quad (2.4)$$

with

$$Q = \frac{[C]^c [D]^d}{[A]^a [B]^b} \quad (2.5)$$

where Q is the reaction quotient, $[C]$ is the molar concentration of product C, and $[D]$ is the molar concentration of product D, *etc.* Substitution of Eqn. 2.3 into Eqn. 2.4 yields the Nernst equation, which relates the electrical voltage to differences in the chemical voltage and ionic concentration:

$$\Delta E = \Delta E^{\circ} - \frac{RT}{nF} \ln Q \quad (2.6)$$

Faraday's laws provide a direct relationship between the extent of a reaction and the current flow in a cell:

$$w = \frac{It(MW)}{nF} \quad (2.7)$$

where w is the weight (g) of material transformed, I is the current flow (A), t is the time (h) of current flow, and MW is the molecular or atomic weight of the material being transformed.

2.2.2 Kinetics

The equilibrium voltage of a cell will be reduced when a current is drawn due to kinetic limitations. This process is known as overvoltage or polarization (η) and can exist in several different forms. Activation polarization (η_a) is related to the kinetics of the electrochemical redox reactions that occur at the electrode-electrolyte interfaces within the battery. These reactions are considered to follow a route where the rate limiting step is the dissociation of an activated complex. The relationship between reaction rate and overvoltage for activation polarization is given by the Tafel equation:

$$\eta_a = \pm \beta \log \frac{i}{i_0} \quad (2.8)$$

where i is the rate of oxidation or reduction in terms of current density, and β^* is a constant. Ohmic polarization (η_o) arises from the combined resistance of the electrolyte, the conductive and binding additives, the materials used in construction of the cell, and any non-conductive film that may be formed on the surface of an electrode. Ohmic polarization appears and disappears instantly when current flows

^c β represents the equation $2.3RT / \alpha nF$, where n , F , R , T are as previously defined and is generally in the 0.05-0.15 V range. The α term is a symmetry coefficient which describes the shape of the rate controlling energy barrier.

and ceases. This effect is commonly referred to as the internal resistance of the cell, and under ohmic resistance, there exists a linear Ohm's Law relationship:

$$\eta_o = IR \quad (2.9)$$

Concentration polarization (η_c) arises from limited mass transport capabilities within a system. This can be manifest as inadequate diffusion to and from an electrode surface of active species that are required to sustain a reaction. The concentration polarization can be expressed by:

$$\eta_c = \frac{RT}{n} \ln \frac{C}{C_0} \quad (2.10)$$

where C is the concentration at the electrode surface and C_0 is the concentration in the bulk solution. The transport of reactants/products to/from the electrode surface is a common feature of electrode reactions. Modern rechargeable lithium battery electrodes are designed to increase the available electrode surface area and lower the current density for a more efficient operation.

2.2.3 Gibbs Phase Rule

Crystallographic changes that occur during the charge/discharge cycling of rechargeable lithium battery electrodes can also be manifest as changes in the cell voltage. To understand how phase and voltage are related, Fig. 2.2 shows a temperature and a voltage binary phase diagram for hypothetical alloys of composition Li_xM .

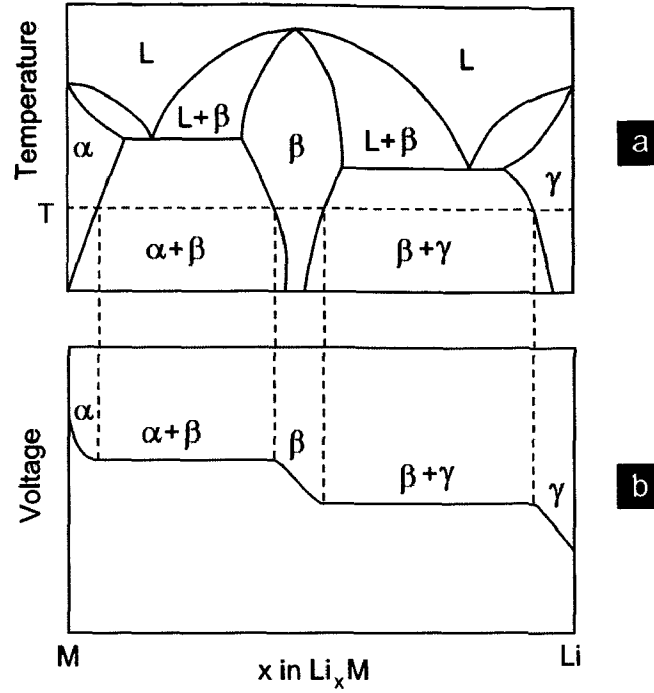


Figure 2.2: (a) Temperature and (b) voltage binary phase diagrams of hypothetical alloy Li_xM . A voltage plateau corresponds to a phase coexistence region. (Adapted [35])

In the temperature phase diagram (Fig. 2.2a) at T , electrochemical cycling causes the lithium concentration to move horizontally, between $x = 0$ and $x = 1$. As x is varied, crystallographic phase changes occur. In the voltage phase diagram (Fig 2.2b), these phase changes correspond to regions of invariance (*i.e.*, $\alpha + \beta$ and $\beta + \gamma$) and continuous change (*i.e.*, α , β , and γ) in cell voltage. This can be understood through Gibbs' phase rule, which states that the number of degrees of freedom (f) is given by:

$$f = c - p + 2 \quad (2.11)$$

where f represents the number of independent intensive variables that need to be specified in value to fully determine the state of the system (*i.e.*, temperature, pressure, voltage, molar concentrations, *etc.*), c is the number of components, and p is the number of phases present. When an electrochemical cell is cycled at a fixed temperature and pressure, two degrees of freedom are specified. This means that in a two component system with a single phase, there is only one degree of freedom ($f = 1$), and the voltage will vary continuously with lithium concentration. However, in a

Literature Review

Two phase region a degree of freedom is lost ($f = 0$) and the remaining intensive thermodynamic variables are fixed. Thus, the cell voltage will remain constant for all values of x within this coexistence region. Most electrodes, such as LiC_6 , exhibit a series of voltage plateaus during electrochemical cycling. IN this way, a charge/discharge profile can be used to identify various coexistence regions in the binary phase diagram in a constant temperature.

2.2 Fundamental Considerations

2.2.1 Principles of Operation

The rechargeable lithium battery consists of two intercalation electrodes that can both host lithium ions as they are transferred on charge and discharge. The lithium ions are supplied by a lithium-containing transition metal oxide such as LiCoO_2 , LiNiO_2 or LiMn_2O_4 , which serves as the positive electrode or cathode. At present, carbonaceous materials such as graphite serve as the negative electrode or anode. Electrode materials typically have a layered structure with large open channels for the diffusion and storage of the lithium ions. Suitable electrode materials therefore can accommodate guest ions without destruction of the lattice. A schematic representation of the discharge process in a typical rechargeable lithium battery is shown in Fig. 2.3. The electrochemical reactions that occur at the cathode and anode are shown in Eqn. 2.12 and Eqn. 2.13, respectively.

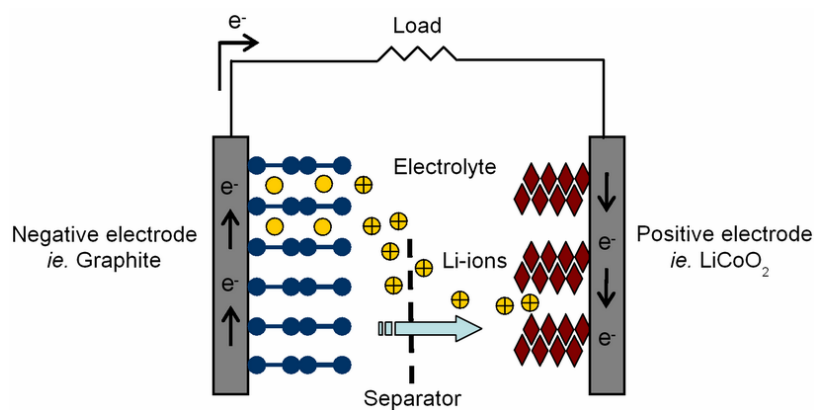
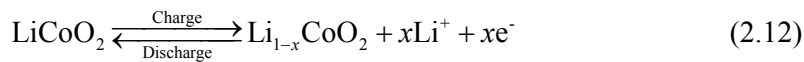


Figure 2.3: Schematic of the discharge process in a rechargeable lithium battery.



On discharge, lithium ions are extracted from the layered graphite anode and are transported spontaneously to the cathode lattice *via* an electrolyte solution. Concomitantly, the electrons generated from the reaction flow through an external circuit to do work (*e.g.*, to power an electronic device). On charge, the electrical load is replaced with an energy source that imposes a reverse voltage larger than the battery's equilibrium voltage, and the flow of electrons is reversed. At the same time, lithium ions are released from the LiCoO_2 lattice of the cathode and are inserted into the layered graphite structure from the electrolyte solution. It should be noted that a commercial cell is built in the discharged state, and must therefore be charged before use.

The electrode system must allow for the flow of both lithium ions and electrons. That is, it must be both a good ionic conductor and an electronic conductor. Conductive materials such as carbon black are routinely added to insulating electrochemically active materials. To physically hold the electrode together, a binder is also added. The electrochemical reaction can only occur at those junctions where the active material, the conductive diluent, and the electrolyte are in contact.

A porous, electrically insulating material, known as the separator membrane, is soaked in electrolyte and placed between the anode and cathode to prevent their direct contact. Electrolytes are usually liquid solvent based and can be subdivided into aqueous, non-aqueous, and solid types. Inorganic salts dissolved in non-aqueous liquids are the most common electrolyte solutions used in rechargeable lithium batteries. The electrolyte provides an ionic conduction path, which is needed for efficient cell operation. Each electrolyte is stable only within a certain voltage and temperature range.

2.2.2 The Cell Voltage

High energy is a consequence of the choice of electrode materials. Fig. 2.4 shows the voltage and capacity values for various positive and negative electrode candidates. In the ideal case where there are no energy losses, the cell voltage can be defined as follows:

$$\Delta E^{\circ} = E^{\circ}(\text{pos}) - E^{\circ}(\text{neg}) \quad (2.14)$$

Figure 2.4: *Voltage vs. capacity for cathode and anode electrode materials presently used or under serious consideration for the next generation of rechargeable lithium cells.^[9]*

The overall theoretical cell voltage (ΔE°) is obtained by simply subtracting the negative electrode potential ($E^{\circ}(\text{neg})$) from the positive electrode potential ($E^{\circ}(\text{pos})$). To maximize the cell potential, lithium metal as the negative electrode ($E^{\circ}(\text{neg}) = 0$ vs. Li^{+}/Li) would be the best choice. However, lithium metal is not used due to the safety concerns previously discussed. Alternatively, small negative values $E^{\circ}(\text{neg})$ can be obtained using host materials where lithium exists at an activity close to that in the metallic state. A good example is graphite, which has an electrode voltage of approximately +0.25 V over the range $0.1 < x < 1$ for Li_xC_6 . For the positive electrode, the highest possible positive value of $E^{\circ}(\text{pos})$ is desirable. With a suitable choice of both anode and cathode materials, a minimum cell potential of about 3 V at the end of discharge is obtainable.

2.3 Cathode Materials

The number of different materials which are suitable as cathode hosts in rechargeable lithium batteries is limited. The bulk of the research and commercialization of cathode materials has centered on two arbitrary categories of insertion materials. The first contains layered compounds that feature anion sheets separating alternate layers of a redox-active transition metal and lithium. This group is exemplified by LiTiS_2 ,^[36] LiCoO_2 ,^[19, 20] $\text{LiNi}_{1-y}\text{Co}_y\text{O}_2$,^[37] and $\text{LiNi}_y\text{Mn}_y\text{Co}_{1-2y}\text{O}_2$ ^[38]. Materials in this group possess an inherent advantage in energy stored per unit of volume due to their compact lattice structures. The second group has open framework structures and include vanadium oxides,^[21] the tunnel compounds of manganese dioxide,^[39, 40] and the transition-metal phosphates such as LiFePO_4 .^[41] The predominant advantage of this latter group of materials is the generally lower cost and toxicity of the constituent elements. Since insertion materials were first proposed as positive electrodes, attention has shifted almost completely from the chalcogenides (TiS_2) to oxides.

The key criteria to screen potential cathode materials for use in a rechargeable lithium battery are as follows:

- The material must react with lithium in a reversible manner. This dictates an intercalation type reaction with minimal structural modification upon lithium insertion. Materials that display a high degree of reversibility generally demonstrate good cyclability on repeated charge/discharge cycling.
- The electrochemical reaction should occur with a high negative free energy ($-\Delta G$). This ensures that the reaction occurs at a high voltage. High theoretical energy capacity is attained by using a host structure with a low molecular weight and an ability to intercalate a large amount of lithium (at least one Li^+ / transition metal atom).
- The material should have a high lithium chemical diffusion coefficient to allow high power density, which is particularly important in high rate applications.

- High electronic conductivity is also desirable in an intercalation oxide, as Li^+ diffusion can occur only when accompanying electron motion is also possible. However, materials with low conductivity, but which are otherwise promising, may be rendered useful by preparing a composite.
- Overall, to satisfy commercial and environmental demands, the material should be chemically stable, non-toxic, and inexpensive to synthesize.

2.3.1 Lithium Cobalt Oxide

2.3.1.1 Structural and Electrochemical Properties

Lithium cobalt oxide (LiCoO_2) exhibits two allotropic crystal structures; cubic and hexagonal, which are often identified in the literature by means of the common processing temperatures. In general, the spinel-related cubic crystal structure is adopted at a low temperature (LT- LiCoO_2), while the layered hexagonal structure is formed at high temperatures (HT- LiCoO_2). In fact, the use of LT and HT abbreviations to identify the different crystal structures of lithium cobalt oxide is misleading, since hexagonal LiCoO_2 can also be synthesized at relatively low temperatures. The hexagonal and cubic structures are based on the same oxide sub-lattice, but can be distinguished by the spatial arrangement of cations.

The most salient difference between these two structures is the varied electrochemical performance that they deliver. The initial capacity and cycle life of cubic- LiCoO_2 is inferior to that of the layered hexagonal analog.^[42, 43] This is illustrated in Fig. 2.5, which shows the first galvanostatic charge curves of Li/cubic- Li_xCoO_2 and Li/hex- Li_xCoO_2 cells.

Figure 2.5: The first galvanostatic charge of Li/cubic-LiCoO₂ (dotted line)^[44] and Li/hex-LiCoO₂ (full line)^[45] electrochemical cells.

The cubic-Li_xCoO₂ electrode shows an initial rapid increase in voltage at $x = 0.95$, which is attributed to a single-phase reaction process and the generation of a defect rock salt phase Li_{0.95}CoO₂. After this, the electrochemical extraction of lithium ions occurs as a two phase reaction at a constant voltage plateau of 3.6 V from $x = 0.95$ to $x = 0.1$. The first cycle capacity of cubic-LiCoO₂ is in the range of 80 mAh g⁻¹.^[46] This material displays significant charge/discharge irreversibility in the initial cycles and poor cycle life due to instability of the quasi-spinel structure caused by oxidation of Co²⁺.^[47] Garcia *et al.*^[48] concluded that the formation of an unusually thick passive layer and resulting slow lithium ion transport also contribute to the observed poor cyclability. Conversely, the first cycle of hex-LiCoO₂ typically delivers a capacity of 140-150 mAh g⁻¹ with a lower irreversible capacity and an improved cycle life.^[49] In this case, the development of a coherent passivation film is the key to good electrochemical performance. Various detailed characterization studies of this film in hex-LiCoO₂ have been conducted *via* ac impedance and electron microscopy techniques.^[50, 51]

Hex-LiCoO₂ was first described by Mizushima *et al.*^[20] in 1980 and commercialized by the Sony Corporation in 1991.^[26] This layered structure is well suited as an intercalation cathode due to a good mobility of lithium ions and its tolerance of the internal strains of intercalation.^[52] The compound is easy to prepare and displays the desirable electrochemical properties of a high working voltage, structural stability, and long cycle life. It is therefore considered the industry standard cathode material

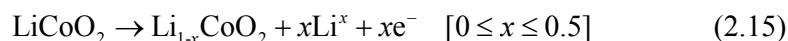
in rechargeable lithium cells. In this thesis, it should be assumed that a general reference to “LiCoO₂” refers to the layered hexagonal version, unless otherwise specified.

The crystal structure of LiCoO₂ is shown in Fig. 2.6 and is of the α -NaFeO₂ type with rhombohedral symmetry ($R\bar{3}m$). The Co³⁺ and Li⁺ ions occupy the octahedral voids on alternating (111) planes to form alternating cation layers.^[53, 54] The O²⁻ ions exist in a close packed face centered cubic (fcc) layer that forms a strong bond with neighboring cobalt atoms to produce O-Co-O slabs. This is due to the high electron affinity of the low spin Co⁴⁺/Co³⁺ couple, which makes the oxygen layers strongly polarizable toward the cobalt layers. Lithium ions are then able to move freely in the two-dimensional plane perpendicular to the *c*-axis, with the rate of lithium ion diffusion related to the spacing between oxygen layers.

Figure 2.6: (a) The LiCoO₂ unit cell. (b) The structure of LiCoO₂ consists of layers of transition metal^c (TM) separated from lithium layers by oxygen. (c) Lithium moves from one octahedral site to another by passing through an intermediate tetrahedral site where it encounters strong repulsion from a nearby TM cation. The table shows the activation barrier for lithium motion for cobalt and nickel near the activated state. (Adapted^[55, 56])

^c Transition metals are all elements from group 3 to group 12 on the periodic table. IUPAC defines a transition metal as "an element whose atom has an incomplete d sub-shell, or which can give rise to cations with an incomplete d sub-shell."

The theoretical capacity of LiCoO_2 is 274 mAh g^{-1} , however, the maximum practical capacity is significantly lower due to a large anisotropic structural change that occurs during the delithiation process.^[57] Specifically, when x exceeds 0.5 in the Li_xCoO_2 compound, a monoclinic phase is formed, which is accompanied by $\sim 2.6\%$ volume expansion along the c -axis. This structural instability involves cobalt dissolution, which then participates in side reactions with the electrolyte solution, and this contributes to capacity fade during cycling.^[58-60] To avoid this problem, commercial cells that utilize a LiCoO_2 cathode are usually cycled with an upper cutoff voltage of 4.2 V. This corresponds to repeatedly extracting and inserting about 0.5 lithium atoms per LiCoO_2 molecule and gives a specific capacity of approximately 140 mAh g^{-1} . The electrochemical charging process is described by the electrode reaction:



The diffusion of lithium in LiCoO_2 is relatively high ($5 \times 10^{-9} \text{ cm}^2 \text{ s}^{-1}$), which enables high cycle rate capabilities (10 mA cm^{-2}). However, the conductivity of Li_xCoO_2 remains a challenge, as it can change dramatically with composition. Imanishi *et al.*^[61] have reported that Li_xCoO_2 behaves like a metal at $x = 0.6$ and a typical semiconductor at $x = 1.1$.

The most common method of preparation of LiCoO_2 is by solid state reaction. This is a simple and inexpensive method since the precursor powders are ground, mixed, and calcined at $750\text{--}900^\circ\text{C}$. The process may begin with many different precursors; Li_2O_2 and CoO ,^[62] Li_2CO_3 and Co_3O_4 ,^[63] $\text{LiOH}\cdot\text{H}_2\text{O}$ and CoCO_3 ,^[64] Li_2CO_3 and CoCO_3 ,^[65, 66] or $\text{Li}(\text{CH}_3\text{COO})\cdot 2\text{H}_2\text{O}$ and $\text{Co}(\text{CH}_3\text{COO})_2\cdot 4\text{H}_2\text{O}$.^[67, 68] The formation of LiCoO_2 always occurs through the reaction of the lithium precursor and Co_3O_4 , regardless of the choice of cobalt precursor.^[68, 69] The use of acetates as precursor materials will produce intermediate compounds at a lower temperature and thus allow the formation of hex- LiCoO_2 below 500°C .^[67]

Prolonged calcination at elevated temperatures causes grain growth and particle coarsening, which significantly impairs the electrochemical properties of the material. For instance, work within the Institute for Superconducting and Electronic

Materials (ISEM) by Konstantinov *et al.*^[70] showed that calcination at 900 °C for 24 h produced a single phase hex-LiCoO₂, but with a large average particle size of several micrometers. Long-term, high temperature firing will also cause non-homogeneity, irregular morphology, and a broad particle size distribution – all being deleterious to good electrochemical performance. For these reasons, LiCoO₂ preparation by alternative methods has been widely investigated.

2.3.1.2 Doping of LiCoO₂ Compounds *via* Solid-State Methods

Many efforts have been made to improve the electrochemical performance and reduce the cost and toxicity of LiCoO₂. Initially, LiNi_xCo_yO₂ compounds were investigated, since nickel and cobalt can substitute for each other in any amount without disturbance to the lattice. Commercially available LiNi_xCo_yO₂ products include LiNi_{0.5}Co_{0.5}O₂, LiNi_{0.8}Co_{0.2}O₂, and LiNi_{0.75}Co_{0.25}O₂. Ozuku *et al.*^[71] reported that structural changes in LiCo_{0.5}Ni_{0.5}O₂ are identical to those that occur in LiCoO₂ upon insertion and extraction of lithium ions, while Li *et al.*^[72] demonstrated that LiNi_{1-x}Co_xO₂ (0.1 < *x* < 0.3) powders can produce a raft of outstanding electrochemical properties when the powder morphology and crystal size are carefully controlled.

Other elements that have been investigated as dopants of LiCoO₂ include Al, B, Bi, Cu, Cr, Fe, Ga, Mg, Si, Sn, Ti, Zn, and Zr. Theoretical studies by Ceder *et al.*^[58] and Venkatraman *et al.*^[73] predict that doping of LiCoO₂ with a transition metal (TM) will produce a higher capacity, whereas doping with a non-TM will increase voltage at the expense of capacity. The level of chemical solubility of any particular dopant within the LiCoO₂ lattice can vary significantly. Overall, doping must achieve a solid solution of LiM_xCo_{1-x}O₂ that is iso-structural with LiCoO₂. The selection of dopant and doping levels should also suppress anisotropic structural change by maintaining interlayer distance.

It is generally accepted that the doping of metal ions into other cathode materials such as LiMn₂O₄ and LiNiO₂ has proven successful. In contrast, of the numerous investigations into the doping of LiCoO₂, the most successful have yielded only modest improvements in the electrochemical performance. Table 2.1 shows a survey

of some of the reports on cation doping of LiCoO_2 found in the literature. The underlying trend is that little success has been achieved by doping LiCoO_2 with bi- or tri-valent metal ions, however, doping with aliovalent ions is more promising. Venkatraman *et al.*^[73] developed the following formula to assist in predicting the theoretical capacity of a doped material:

$$C_T = \frac{26.8 [1 - 5s + f(1-s)(Z-4)]}{MW} \quad (2.16)$$

where C_T is the theoretical capacity in mAh g^{-1} , s = vacancy content, f = dopant concentration when valency of the doped cation is constant, Z = valency of the doped metal ions, and MW = molecular weight of the layered compound. Hence, a composition that employs a higher valence cation combined with a synthesis method which yields a low vacancy concentration will give a higher theoretical capacity.

Table 2.1: *A selection of cation doped LiCoO_2 compounds prepared by solid-state methods. Test cells constructed using 1 M LiPF_6 dissolved in 1:1 ethylene carbonate:diethylcarbonate (EC:DEC) electrolyte solution and subjected to galvanostatic charge/discharge cycling between 3.0 V and 4.2 V.*

$\text{LiM}_x\text{Co}_{1-x}\text{O}_2$ (M, x)	Synthesis conditions	Impurity phases	Discharge capacity (mAh g^{-1}) /cycle no.	Optimal doping level	Ref
Al, 0-0.75	Nitrate coprecip., 300-800 °C air 2h	Nil; $x < 0.5$	80/5	0.25	[74]
B, 0-0.2	Solid state, 450 °C 24 h, 800 °C 24 h	Nil	102/30	0.2	[57]
Bi, 0.05	Solid state, 850 °C 10 h, 850 °C 10 h	Yes	70/50	N/A	[75]
Sn, 0.05	Solid state, 850 °C 10 h, 850 °C 10 h	Yes	140/50	N/A	[75]
Cr, 0.05	Solid state, 850 °C 10 h, 850 °C 10 h	Yes	100/50	N/A	[75]

Table 2.1: *continued.*

$\text{LiM}_x\text{Co}_{1-x}\text{O}_2$ (M, x)	Synthesis conditions	Impurity phases	Discharge capacity (mAh g ⁻¹) /cycle no.	Optimal doping level	Ref
Mg, 0.03-0.06	Solid state, 800 °C 10 h, 800 °C 10 h	Nil	124/10	0.06	[76]
Si, 0.01-0.35	Co-precip., 200 °C 10 h, 400 °C 5 h, 950 °C 25 h	Yes; $x = 0.35$	155/50	0.01	[77]
Ti, 0.05	Solid state, 850 °C 10 h, 850 °C 10 h	Yes	140/50	N/A	[78]
Ga, 0.005, 0.1	Citrate mixture, solid- state 900 °C 10 h	Nil	40/30	0.005	[79]
Zr, 0.05	Solid state, 850 °C 10 h, 850 °C 10 h	Nil	155/50	N/A	[75]

2.3.1.3 Alternative Synthesis Methods for LiCoO_2

It has been almost 30 years since LiCoO_2 was first proposed as a cathode material to be used in rechargeable lithium batteries. During this time, there have been various new preparation methods for LiCoO_2 . Anatoli^[49] presents a comprehensive review of this development history and also illustrates the dependence of the morphological characteristics (grain size, size distribution, and crystallinity) and electrochemical properties on the chosen method of synthesis. To be considered a viable alternative, the synthesis method should ideally offer improved morphological and electrochemical reactivity when compared to traditional solid-state processes. The development and application of these new methods also aim to deliver economic advantages, such as being able to produce larger quantities, more rapidly, and at a lower cost. For instance, the sol-gel method requires much lower calcination temperatures of 550–750 °C and shorter calcination times of 1–10 h than any solid-state reaction.^[80-83] By using the sol-gel method and highly reactive precursor materials such as CoOOH and Co(OH)_2 , LiCoO_2 can be formed with an average particle size of 0.016 μm at 600 °C.^[80] The hydrothermal method requires even lower

reaction temperatures of 150–250 °C for 0.5–24 h to synthesize well crystallized plates of LiCoO_2 in the 0.07–0.2 μm range.^[84] Fine-grained LiCoO_2 can also be rapidly synthesized at temperature < 700 °C by supercritical water synthesis^[85] in 1 min and by microwave synthesis^[86] in 10 min. Indeed, all of these low temperature preparation methods create ultra-fine LiCoO_2 powders with submicron average particle sizes.

Other techniques that typically involve higher processing temperatures (750–900 °C) include the water-in-oil emulsion (reverse micelle),^[87] hydrothermal precipitation,^[88] spray-dry,^[70, 89] freeze dry,^[90] and molten salt^[91] synthesis methods. These techniques logically lead to formation of LiCoO_2 with the largest particle size, generally in the 1–10 μm range.

It can be inferred from the above study that formation of LiCoO_2 occurs by different reaction mechanisms, depending on the preparation method. LiCoO_2 is formed by a crystallographic rearrangement from cubic to hexagonal when prepared by most synthesis methods, including high temperature solid-state reaction, combustion, mechanical activation, freeze-drying, and molten salt synthesis. Hex- LiCoO_2 can also be obtained directly when prepared by a low temperature solid-state reaction using cobalt hydroxide precursor, or *via* a cobalt oxidation reaction in solution when accompanied by the formation of intermediate lithium over-stoichiometric compounds (*i.e.*, $\text{Li}_{1+x}\text{Co}_{1-x}\text{O}_2$).

The capacity of the LiCoO_2 cathode may be increased by charging beyond 4.2 V to use more than 0.5 lithium per LiCoO_2 molecule, but it must be done in a way that also avoids the associated structural change that occurs at higher voltages. Recently, surface engineering approaches have been used as an effective technique to allow a higher upper voltage cut-off to be used without suffering structural problems. This has been achieved by encapsulating LiCoO_2 particles with stable compounds such as MgO , SnO_2 , SiO_2 , TiO_2 , Al_2O_3 , and ZrO_2 .^[92–100] Chen and Dahn^[92] have shown that coated LiCoO_2 may be cycled to cutoff voltages up to 4.7 V and can deliver a specific capacity of around 170 mAh g^{-1} . The advantage of this technique is related to a “barrier effect” that occurs by the formation of an outer shell. The shell acts to

simultaneously stabilize the layered structure in its highly delithiated state and limit detrimental side reactions by reducing the exposure of the LiCoO_2 core to the electrolyte solution. The mechanism of protection is related to minimizing the exposure of Co^{4+} to acidic HF^{d} within the electrolyte solution. Further incremental improvements in capacity can be made by replacing the LiPF_6 salt or by completely drying the LiCoO_2 by heating to over $550\text{ }^\circ\text{C}$. However, it is unlikely that the capacity of LiCoO_2 compounds could exceed 180 mAh g^{-1} over several hundred cycles.^[101, 102]

2.3.2 Lithium Iron Phosphate

2.3.2.1 A Shifting Ideology

The most popular cathode insertion compounds include the layered rock salt systems of LiCoO_2 and LiNiO_2 , and the spinel framework system of LiMn_2O_4 . Considerable efforts over the years have been undertaken to optimize the processing conditions of these materials and to understand their structure and electrochemical performance. However, some intrinsic characteristics of these materials have prompted a search for suitable substitutes. For instance, in LiMn_2O_4 , lithium exhibits a lower mobility within the Mn_2O_4 framework, which limits its power capability. Also in this system, structural changes associated with a Jahn-Teller deformation of the framework lead to a poor charge/discharge cyclability. As already discussed, the Li_xCoO_2 system also suffers structural modifications at $x > 0.5$ and therefore is only practically capable of about half of its theoretical capacity. A common disadvantage of these traditional materials is that they contain expensive and toxic transition metals.

Apart from electrochemical performance, the most generic consideration in identifying a new electrode material for commercial rechargeable lithium cells is the availability and cost of materials. This is particularly important for materials being considered for large scale applications such as in electric vehicles (EVs), hybrid electric vehicles (HEVs), and stationary storage batteries. At a fundamental level, an electrode based on iron would satisfy economic and environmental concerns, since it would be cheap, easy to extract or process, and non-toxic. Iron is the fourth most

^d HF is unwanted, but forms through the interaction of trace amounts of H_2O (in electrolyte solution or on the electrode surface) and LiPF_6 salts.

abundant element (5 % mass) found in the earth's crust and one of only eight elements that are found commonly in surface minerals.

One of the first iron-based compounds investigated was layered LiFeO_2 , which operates on the $\text{Fe}^{4+}/\text{Fe}^{3+}$ redox couple.^[103] Unfortunately, this compound produces unimpressive battery performance and is highly metastable. Other iron-based compounds investigated include FePS_3 ,^[104] FeOC1 ,^[36] and FeOOH ,^[105] but all of these have been rejected due to unsuitable electrochemical properties. The major problem for most of these proposed alternatives is that they operate on the $\text{Fe}^{3+}/\text{Fe}^{2+}$ redox couple, which occurs at ~ 1 V, and is impractically low for use as a cathode. However, in 1997, a breakthrough discovery by Pahdi *et al.*^[41, 106-108] reported that the olivine-type scaffolded structure, built from corner-sharing FeO_6 octahedra and tetrahedral polyanions $(\text{XO}_4)^{2- \text{ or } 3-}$ with $\text{X} = \text{S}, \text{P}, \text{As}, \text{Mo}, \text{ or } \text{W}$ could be designed to lower the $\text{Fe}^{3+}/\text{Fe}^{2+}$ redox energy to useful levels. In this system, the energy of the $\text{Fe}^{3+}/\text{Fe}^{2+}$ couple can be varied depending upon the choice of the counter cation (X) within the polyanion. The cation will induce strong covalent (X-O) bonding within the polyanion, reducing the strength of the Fe-O bond, and thus lowering the $\text{Fe}^{3+}/\text{Fe}^{2+}$ redox energy. The stronger the covalent bonding within the polyanion, the lower is the $\text{Fe}^{3+}/\text{Fe}^{2+}$ redox energy and the higher the voltage. Good examples of this effect can be seen in LiFePO_4 ,^[41] $\text{LiFe}_2(\text{SO}_4)_3$,^[109] and $\text{Li}_3\text{Fe}_2(\text{PO}_4)_3$,^[110] where the $\text{Fe}^{3+}/\text{Fe}^{2+}$ couple occurs at potentials close to 3.4 V, 3.6 V, and 2.8 V, respectively. In addition to possessing useful operating redox potentials, some of these materials have large theoretical capacities and have shown excellent cycling stability.

2.3.2.2 Structural and Electrochemical Properties

Lithium iron phosphate (LiFePO_4) has proved to be the most promising iron-based cathode material and is expected to soon be available in many commercial rechargeable lithium cells. The orthorhombic structure of LiFePO_4 is shown in Fig. 2.7, where lithium, iron, and phosphorous atoms occupy octahedral $4a$, octahedral $4c$, and tetrahedral $4c$ sites, respectively. The oxygen ions form a slightly distorted, hexagonal close packing arrangement. The iron ions form zigzag chains of octahedra in alternate basal planes bridged by the tetrahedral phosphate groups (PO_4), while

lithium ions occupy octahedral sites in the remaining basal planes. The strong covalent bonding between the oxygen and P^{5+} to form $(PO_4)^{3-}$ units allows for greater stabilization of the structure compared to layered oxides such as $LiCoO_2$, where the oxide layers are weakly bound by van der Waals forces.

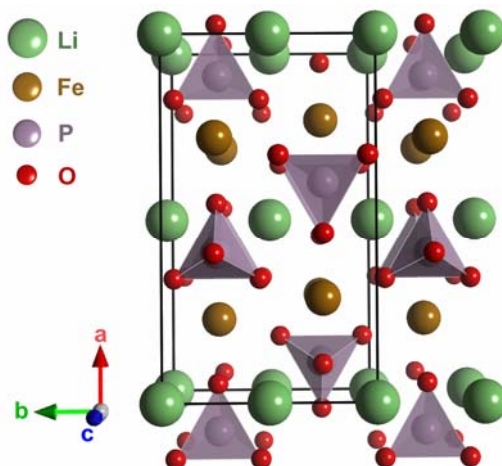
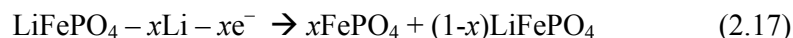


Figure 2.7: The orthorhombic crystal structure of $LiFePO_4$.

The $LiFePO_4$ structure has a theoretical capacity of 170 mAh g^{-1} and Fig. 2.8 shows how the practical insertion and extraction of lithium occurs between 2.0 V and 4.5 V. It is clear that the voltage remains static over a large composition range, which indicates that the extraction and insertion reactions proceed by the motion of a two-phase interface. Numerous chemical experiments have confirmed the co-existence of the orthorhombic $FePO_4$ and $LiFePO_4$ phases and that the growth of one phase occurs at the expense of the other. The extraction of lithium from $LiFePO_4$ (charge) occurs as follows:



The lithium extraction process also induces a 6.81 % volume decrease in the cathode, which conveniently compensates for the volume expansion of the carbon anode that occurs simultaneously. The opposite reaction for the insertion of lithium into the orthorhombic $FePO_4$ (discharge) occurs as follows:

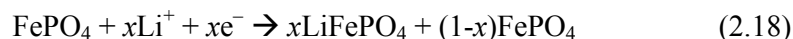


Figure 2.8: Charge/discharge cycling of LiFePO_4 conducted at 1 mA cm^{-2} . (Adapted [101])

Due to the coexistence of LiFePO_4 and FePO_4 during cell operation, it is therefore important to understand the reactivity and thermal stability of both compounds. Firstly, the LiFePO_4 structure is inherently unstable because of the edge sharing between octahedra and tetrahedra and under pressure can convert to the spinel phase.^[101] In addition, the transformation of LiFePO_4 to an electrochemically inactive version that has lithium in tetrahedral sites has also been reported.^[111] Concerning FePO_4 , at least two crystalline variations are possible; the orthorhombic form which is iso-structural with LiFePO_4 , where iron is found in FeO_6 octahedra, and a trigonal form in which iron is found in FeO_4 tetrahedra. The trigonal form is composed of FeO_4 and PO_4 tetrahedra and resembles a quartz-like structure. This form is electrochemically un-reactive and should be avoided as Fe^{2+} is not stable in this configuration.^[112]

The biggest drawback of LiFePO_4 is that it displays extremely low electrical conductivity, which leads to a low rate capacity and low room temperature lithium utilization within the structure. Pure LiFePO_4 samples are reported to have an electronic conductivity of $10^{-9} \text{ S cm}^{-1}$,^[113] whereas samples made from reagent grade carbon-containing materials have a conductivity of around 10^{-5} - $10^{-6} \text{ S cm}^{-1}$.^[114] By elevating the temperature from 21°C to 60°C , a LiFePO_4 cathode can almost double the reversible capacity.^[115] Other significant improvements in electrical conductivity

have been made, mostly through various materials processing approaches to obtain tailored particle morphologies. Armand *et al.*^[116] were the first to show that by coating an electronically conducting layer on LiFePO_4 , almost full theoretical capacity can be achieved at 80 °C, while Huang *et al.*^[117] have shown that LiFePO_4 -C composites can exhibit high conductivity and up to 95 % lithium capacity at room temperature. This result was achieved by a combination of intimate mixing with a graphitic precursor, and careful control of particle size to nanometer dimensions. The intimate mixing of other conductive particles such as copper or silver have also been shown to afford similar improvements.^[118] More recent studies propose that conductive coatings may even be avoidable altogether by using only nanoparticles with a narrow size distribution.^[119, 120] These results highlight the need for processing methods that allow careful control of phase purity and particle morphology.

2.3.2.3 Effect of Dopants

Another popular method for improving the electrochemical performance of LiFePO_4 cathodes is by doping with metals aliovalent to lithium. In particular, Chung *et al.*^[113] reported that low-level solid solution doping of LiFePO_4 by a range of ions (Mg^{2+} , Al^{3+} , Ti^{4+} , Zr^{4+} , and Nb^{5+}), when combined with controlled cation non-stoichiometry, can increase the electronic conductivity by over 8 orders of magnitude. They argued that doping of cation deficient phases is charge compensated by Fe^{3+} , thereby introducing *p*-type conductivity. This scenario is analogous to what occurs in other cation deficient transition metal oxides such as $\text{Li}_{1-x}\text{CoO}_2$.^[121] However, later reports suggest that these effects might be due to impurity phases at grain boundaries.^[119, 122] In particular, Herle *et al.*^[119] examined the compositions $\text{Li}_x\text{Zr}_{0.01}\text{FePO}_4$ ($0.87 \leq x \leq 0.99$) and found that a nano-network of metal rich phosphide (Fe_2P) located within the grain boundaries of LiFePO_4 crystals was responsible for the enhanced electronic conductivity. The Fe_2P was formed during high temperature processing, particularly in the presence of a reducing agent such as carbon.

Further evidence of the possible formation of impurity phases was presented by Islam *et al.*^[123] in a study on various dopants that had charges ranging from 2^+ to 5^+ . Purely on energetic grounds, LiFePO_4 was found to be intolerant of high valence doping (*i.e.*, Al, Ga, Zr, Ti, Nb, and Ta) at either the lithium or iron octahedral sites.

Conversely, favorable energies were found only for divalent dopants such as magnesium or manganese at the iron site. In support of these calculations, structural studies by Delacourt *et al.*^[124] on the niobium-doping of LiFePO₄ found that a complete solid solution could not be formed, and niobium existed as either an amorphous or crystalline (β -NbOPO₄) secondary phase. Several other authors have shown that only divalent cations at low concentrations can be successfully doped into the LiFePO₄ structure.^[125, 126] Electrochemical results of these studies indicate improved rate performance and cycling stability.

2.3.2.4 Alternative Synthesis Methods

In most previous studies, solid-state synthesis has been the chosen method of LiFePO₄ preparation,^[117, 127, 128] although more recent investigations commonly use hydrothermal synthesis,^[129-131] pulsed laser deposition (PLD),^[132] sol-gel,^[118, 133, 134] and mechanical milling.^[135] Hydrothermal synthesis is able to produce an ordered olivine phase in a single step, but often gives poor electrochemical properties.^[101] This is due to cation mixing, where about 7 % of the iron atoms are located in the lithium sites which impedes lithium ion diffusion through the tunnel. Proper ordering of the lithium and iron atoms can be achieved through an additional heat treatment of the hydrothermal material at 700-750 °C.^[136] Recent studies suggest that the hydrothermal approach can be fine-tuned to produce material with excellent electrochemical behavior, thus eliminating the need for a conductive coating.^[137]

Yang *et al.*^[138] have recently synthesized carbon coated LiFePO₄ powder by ultrasonic spray pyrolysis using an inexpensive trivalent iron precursor. The pure olivine phase can be prepared with a two-step process of spray pyrolysis at 450 °C and subsequent heat-treatment at 650 °C for 4 h. A 15 wt% amorphous carbon coating evenly distributed on the final LiFePO₄ powders was shown to produce a first cycle discharge capacity of 150 mAh g⁻¹ at a low galvanostatic rate and 50 °C, but progressively worsened with cycling. Phase pure, highly crystalline LiFePO₄ powder has also been formed with an inverse opal structure by calcining the precursors of Li⁺, Fe²⁺ and PO₄³⁻ in the presence of organic latex micro-spheres.^[139] Regardless of the route chosen to synthesize LiFePO₄, almost all require lengthy heat treatment schedules that usually exceed 10 h as well as multi-stage processing steps.

2.4 Anode Materials

A number of different materials have been investigated as possible anode materials for rechargeable lithium batteries. These include the various carbon materials as well as a range of transition metal oxides, nitrides, and intermetallics. Carbon-based composite materials are increasingly being examined in an effort to synergistically enhance the anode properties.

2.4.1 Carbon

The introduction of carbon as an anode material in rechargeable lithium batteries first began in 1976 when Bessenhard^[140] reported that a layered graphite structure could intercalate various alkali metal ions. Unfortunately, these electrodes suffered from exfoliation and disintegrated into powder during charge/discharge cycling. In the early 1980s, Basu^[24] registered a patent that proposed a battery using a pre-lithiated carbon anode coupled to a NbSe₃ cathode. The carbon anode was prepared by dipping it into a molten lithium bath prior to cell assembly. About the same time, numerous studies were being undertaken into new electrolyte systems. This work culminated in the discovery of a highly reversible system that used a graphite anode and an electrolyte solution composed of propylene carbonate (PC) solvent and LiClO₄ salts.^[141] Buoyed by the progress of intercalation materials as the cathode, research into new anode materials steered towards graphite. Then in 1987, the Sony Corporation announced that lithium insertion was also possible in non-graphitic carbon materials.^[142] This breakthrough instigated an avalanche of investigations into a range of carbon types, different carbon sources, and new electrolyte systems.

Carbon is the most versatile element of the periodic table. The variety of structures, textures and particle shapes is limitless. Carbon can exist in forms ranging from the highly ordered to the completely disordered. Some of the most popular commercially available carbon types include natural and synthetic graphites, carbon blacks, carbon fibres, and active carbons. More recently, various micro- and nano-architectures have been synthesized that include MCMB and carbon nanotubes (CNT). An extensive collection of literature now exists on the chemistry and electrochemistry of all types of carbon materials.^[143, 144] Analysis of published data suggests that the best electrochemical performances can be obtained at either ends of the structural

evolution, from both crystalline and highly disordered carbons. However, at present, graphites offer the best compromise: low cost, low irreversible capacity ($< 100 \text{ mAh g}^{-1}$), good reversible capacity ($\sim 400 \text{ mAh g}^{-1}$), and a constant low redox potential (0.1-0.25 V). The key point in the literature on various carbons is that for each morphology or structural modification, there is a corresponding variation in the electrochemical behaviour.^[145, 146] Even among the allotropic modifications of graphite (hexagonal, rhombohedral) there exists a substantial difference in the intercalation chemistry and cycling efficiency. The rhombohedral form is stable at lower temperatures, and therefore, exhibits better structural stability and cycle life.^[147] It should be noted that non-graphitic carbons do offer substantially higher capacities than graphite, so there are also potential benefits that can be realized through further development of these anode materials.

2.4.1.1 Forms of Carbon

Most of the different forms of carbon are able to be synthesized *via* a simple heat treatment. Dahn *et al.*^[148] and Tirado^[15] describe the three classes of carbons relevant to rechargeable lithium battery applications as graphitic, hydrogen containing (soft), and non-graphitic (hard) types. CNTs represent a new morphology of carbon that possesses physical and chemical properties distinct from those of these traditional structures, and they will be discussed in more detail later.

To understand how the different structures are derived, it is useful to consider that the preparation of a primary precursor occurs initially through heating inorganic compounds such as hydrocarbons, petroleum, biomass, and coal in an inert atmosphere. During the early stages of pyrolysis ($> 600 \text{ }^{\circ}\text{C}$), the organic compounds decompose and emit carbon-containing gases, such as CO, CO₂ and CH₄.^[149] Some of the resultant volatilized products during carbonization may be recovered and used as secondary precursors for different carbons. For example, petroleum pitch and coal tar pitch are secondary precursors that are produced during carbonization of petroleum and coal. The remaining carbon atoms condense into planar aromatic structures or graphene sheets that are terminated with hydrogen atoms. At 650-800 $^{\circ}\text{C}$, if the decomposing precursor forms a semi-fluid state, then planar sheets align in a roughly parallel fashion. These precursors yield soft or graphitizable carbons,

which can be easily converted to graphite upon further heating at high temperature. Conversely, if the organic precursor is sufficiently cross-linked, then a fluid state is not realized during decomposition and the graphene sheets will not align. These materials are difficult to graphitize at any heat treatment temperature and are appropriately termed hard or non-graphitizable carbons. Hard carbons are most commonly prepared by the poly-condensation of oil pitch.

Fig. 2.9 shows the different degrees of organization found in carbon materials. Hard and many soft carbons heated below 1000 °C form misaligned layers that feature dangling bonds and other high energy sites (Fig. 2.9a). These carbons are described visually by Dahn's *falling cards* model^[150] and demonstrate a high level of inherent nanoporosity.^[151] Hard carbons heated above 1000 °C will induce partial alignment and growth of graphene sheets. However, in this carbon, macro-scale alignment of graphene layers will not occur at any heat treatment temperature, and the carbon remains extremely disordered. On the other hand, the heat treatment of a soft carbon at 1000-1500 °C will induce a turbostratic character (Fig. 2.9b). These structures have graphene layers that show perfect intraplane order, but a completely random interplane arrangement. As temperature is increased, the lateral dimensions of the graphene sheets grow to 150 Å, and at ~2000 °C, the layers become parallel but turbostratic misalignment is retained due to layer pinning.

Figure 2.9: *Planar view of the level of organization in various carbons: (a) high energy defects present in hard carbons and some soft carbons heated below 1000 °C; (b) stacking faults and turbostratic arrangement particularly displayed in soft carbons heated in the 1000-1500 °C range; (c) hexagonal and rhombohedral graphite. (Adapted ^[15])*

Above 2000 °C there exists enough thermal energy for some layers to become unpinned and begin to rotate into a set graphite stacking arrangement. According to Dahn *et al.*,^[148] the probability of finding adjacent graphene sheets in turbostratic misalignment decreases from 1 at 2000 °C to almost 0 for soft carbons heated to 3000 °C. Perfectly graphitized carbons with high crystallinity (*i.e.*, interlayer distance < 0.336 nm) are generally prepared at around 2500 °C. The most common arrangement is the hexagonal Bernal^[152] structure, where the carbon layers are arranged in the ...ABAB... sequence with a shift of the B layers with respect to the A layers (Fig. 2.9c). The other crystalline form that can exist is rhombohedral, and has an ABCABC stacking sequence where the C layers are shifted with respect to the B layers. This variation is never pure and co-exists with the hexagonal form at levels up to 40 %.^[153] Prolonged heating at temperatures in excess of 2000 °C will gradually eliminate the rhombohedral structure, which indicates that the hexagonal

structure is more thermodynamically stable at higher temperatures. These two phases are virtually indistinguishable in terms of reversible capacity.^[154] However, graphites that contain a higher proportion of rhombohedral stacking produce lower irreversible capacity loss, and also avoid the problems associated with graphite exfoliation.^[155] Graphite exfoliation occurs due to the penetration of large species into the interlayer spaces. Layer opening is more difficult in graphites with high rhombohedral phase content than for pure hexagonal phase due to the presence of dislocations and phase boundaries.^[156]

2.4.1.2 Lithium Intercalation and Failure Mechanisms

2.4.1.2.1 Dependence on Carbon Type

The primary precursor source of carbon and the heat treatment history determine the microstructural characteristics (*i.e.*, crystallite size, interplanar spacing, surface area, and composition) of the final product. These characteristics then determine the possible electrochemical utility measured in terms of capacity and reversibility of reaction with lithium. The level of disorder directly affects the nature of reaction with lithium. To maximize the stored energy per unit mass in a battery, it is crucial to determine which types of carbon react reversibly with the largest amount of lithium per unit mass of carbon. The theoretical capacity of graphitic carbon is 372 mAh g⁻¹, based on the intercalation-deintercalation reaction:



Complete intercalation occurs only in a perfect graphite structure, but the intercalation mechanism dominates in graphitized soft carbons and natural graphite. Fig. 2.10a shows the first cycle capacity and corresponding irreversible capacity loss expected for various carbons as a function of processing temperature. Hard carbon electrodes produce high capacity, but also a high irreversible capacity, while graphite electrodes produce moderate reversible capacities close to theoretical predictions and a low irreversible capacity. The relative stability of a graphite electrode is due to side reactions that occur during the first charge, which result in the formation of a passivation layer on the electrode surface, called the solid electrolyte interphase

(SEI) layer. The SEI layer is ionically conducting, but electronically insulating, which enables the transfer of lithium ions and prevents further decomposition of the electrolyte. An additional function of the SEI is that it can allow for desired electrochemical reactions to occur even at voltages outside the window of stability of some common electrolytes.

Figure 2.10: *Electrochemical performance of various carbons: (a) first cycle capacity (thick line) and irreversible capacity (thin line) vs. heat treatment temperature for soft carbons. (Adapted ^[15]); (b) typical second charge/discharge cycle for graphite and hard carbon. (Adapted ^[146])*

Fig. 2.10b compares typical voltage capacity curves for a graphite and a hard carbon electrode, determined by monitoring voltage during the second charge/discharge cycle. The lithium insertion behaviour in a hard carbon electrode is different from that observed in a graphite electrode. The cycling profile of a hard carbon electrode shows a continuously sloping charge/discharge curve from 0.2 V to 1.2 V. These carbons react with lithium *via* mechanisms dominated by surface phenomena at high energy sites and the filling of micropores.^[150, 157, 158] In hard carbons, lithium can be absorbed on both surfaces of a single layer of carbon (see Fig. 2.9a), thus giving double the theoretical capacity (*i.e.*, 740 mAh g⁻¹).^[150] However, these electrodes

also suffer significant hysteresis or irreversible capacity loss. The amount of irreversible capacity depends on the gas exposure time during processing and storage, and involves reactions with species such as hydroxyl and carboxyl functional groups or adsorbed water. The disordered nature of these electrodes also makes them less sensitive to the nature of the electrolyte when compared to graphite.

2.4.1.2.2 Electrolyte Considerations

All types of carbon experience irreversible side reactions concentrated on the first electrochemical absorption of lithium ions that are largely due to electrolyte instability. This phenomenon leads to a definite loss in the capacity of the electrode. No electrolyte has been found to completely withstand the low electrochemical potential of highly lithiated carbons. In the best instances, the electrolytes are only reduced until the passivating layer can be formed. This process is clearly visible on galvanostatic curves as an irreversible plateau close to 0.8 V.

For lithiated graphite, the major failure mechanism is co-intercalation of solvent molecules that are pushed together with lithium ions between the graphene planes. In the absence of passivation, co-intercalation of solvent molecules and lithium ions, together with increased gas pressure built up from solvent reduction reactions^e, simply exfoliates the graphite and decomposes it to a powder.^[159] This situation is particularly likely to occur in ether-type solutions with lithium salts. Aurbach *et al.*^[160-170] have produced a comprehensive collection of studies on lithium intercalation in various graphite materials (*i.e.*, natural and synthetic graphite flakes, MCMC, and graphite fibers) in different electrolyte solutions. These works reveal that a key factor in determining the stability of graphite electrodes in lithium insertion processes is the extent to which a protective SEI film is formed before co-intercalation can occur.

There are three different behaviors in SEI film formation that are demonstrated in Fig. 2.11 by considering a graphite electrode in different electrolyte solutions.

^e For example, $\text{PC} + 2\text{e}^- + 2\text{Li}^+ \rightarrow \text{CH}_3\text{CH}(\text{OCO}_2\text{Li})\text{CH}_2(\text{OCO}_2\text{Li}) \downarrow + \text{CH}_3\text{CH}=\text{CH}_2 \uparrow$, or

$\text{EC} + 2\text{e}^- + 2\text{Li}^+ \rightarrow \text{CH}_2(\text{OCO}_2\text{Li})\text{CH}_2\text{OCO}_2\text{Li} \downarrow + \text{CH}_2=\text{CH}_2 \uparrow$

Excellent SEI stability is found in ethylene carbonate (EC) solutions, where a thin, coherent, and compact surface film is formed rapidly (Fig 2.11a). This is due to the formation of various, highly-passivating, lithium alkyl carbonates and lithium carbonates during the reduction of the electrolyte. Solvents such as fluoro ethylene carbonate (FEC)^[171] and ethylene sulphite (ES),^[172] which have a structural similarity with EC, have also proven to be effective. In electrolytes such as methyl formate (MF), the film porosity and thickness is slightly higher, and this results in larger irreversible capacity (Fig. 2.11b). The worst case scenario occurs in PC-containing electrolytes, where a highly porous and thick SEI is formed. This results in a very high irreversible capacity (Fig. 2.11c). The useful reversible capacity in this case is extremely low. In this way, the active mass retains its basic structure, but individual particles become electrically isolated from the current collector. In practice, solvent mixtures containing two solvents are usually employed, and some studies have recommended mixtures of up to four solvents for optimal efficiency.^[173]

Figure 2.11: *SEI film formation in a graphite electrode for electrolytes based on EC (a), MF (b), and PC (c) solvents. (Adapted ^[174])*

In any event, the formation of a passivating layer occurs in all carbons working at low potential and results in an unavoidable loss in capacity upon prolonged charge/discharge cycling. This is due to small changes in the graphite volume during lithium intercalation–deintercalation, which will produce cracks in the surface film and allow further reaction of the active surface with solution species. Breakdown and repair of the surface films can lead to a gradual thickening of the surface layer over time and cannot be completely prevented by any currently known electrolyte solution.

2.4.1.3 Composites using Carbon from Agricultural Sources

Carbon derived from sucrose (table sugar) has been widely studied in the lithium battery field. Pyrolysis of sugar solutions triggers a series of complex decomposition reactions that result in the synthesis of hard, disordered carbon powders. These reactions first begin when sucrose is hydrolyzed; it firstly decomposes into its two smaller monosaccharide iso-structural constituents, namely glucose and fructose (Eqn. 2.20).^[175] Slow heating then initiates a series of up to 25 sequential reactions whereby different classes of compounds are formed that include aldehydes, ketones, and carboxylic acids.^[176] There are two main exothermic reactions of decomposition that occur before 600 °C. The first produces large quantities of CO₂ and H₂O (Eqn. 2.21), while the second results in the formation of the disordered carbon product (Eqn. 2.22).



Xing *et al.*^[177, 178] and Buiel *et al.*^[179] have studied the influence of processing temperature and other operating parameters on the electrochemical performance of these powders. Irreversible capacity can be reduced by careful optimization of the heat treatment temperature and by the presence of ethylene gas.^[179] Higher heat treatment temperatures (> 600 °C) can close micropores and produce fullerene-like structures with lower irreversible capacity. Conversely, ball milling of the same sugar-derived carbon powders leads to highly oxidized particle surfaces and a higher

irreversible capacity.^[178] Carbon powders derived from other agricultural-based raw materials, such as rice husks^[180], coffee beans, green tea, sugar cane,^[181] and cotton,^[182] have also been evaluated for use in battery applications, although the results of these studies have generally been less promising than those using sugar-based carbons.

The appeal of sugar-based carbon powders is that they are able to be produced simultaneously with other compounds. In this way, a carbon-alloy or carbon-oxide composite can be synthesized with the carbon being formed *in-situ* and existing as either a carbon coating or a fine dispersion. Good examples of this approach have been developed within the ISEM laboratories by Yuan *et al.*^[183] using SnO₂ and Bewlay *et al.*^[184] using LiFePO₄. The purpose of the SnO₂ study was to synthesize a nanostructured material that would incorporate a suitable matrix to assist in relieving the stresses associated with volume expansion caused by repeated charge/discharge cycling. This was achieved through the spray pyrolysis of various sugar – SnCl₂·2H₂O solutions in air at 700 °C. It was found that electrodes composed of a 51 wt% C – SnO₂ composite powder could maintain a reversible capacity of around 480 mAh g⁻¹ compared to less than 300 mAh g⁻¹ for a pure SnO₂ electrode over 50 cycles.

Concerning the synthesis of the insulating LiFePO₄ compound, the primary aim was to enhance the electrical conductivity. The *in-situ* formation of a 31 wt% disordered carbon matrix *via* spray pyrolysis was found to increase the electrical conductivity by seven orders of magnitude compared to pure LiFePO₄ powders, while composite powders that were prepared with as little as 3 wt% disordered carbon gave up to three orders of magnitude improvement in the electrical conductivity.

2.4.2 SnSb Metal Pnictide

Many metals such as Bi, Cd, Pb, Sb, Si, and Sn can reversibly accommodate lithium. In fact, most demonstrate lithium storage capacities that are much higher than those of carbonaceous materials. These metals represent an interesting alternative to carbons and were among the first materials considered as replacements for the metallic lithium anode in rechargeable lithium batteries. However, their use has been hindered by significant volume changes during lithium uptake and removal that can

cause electrode cracking, loss of electrical contact between the particles and/or current collector, and a reduced battery life. Fig. 2.12 shows the theoretical capacity and volume expansion of some lithium alloys.

Figure 2.12: *The theoretical capacity and volume expansion of various lithium alloys. (Adapted^[185, 186])*

The first attempted solution to the problem of volume expansion in these alloys was proposed by Boukamp *et al.*^[187] in their *mixed-conductor matrix* concept. In this concept, particles of the lithium storage metal were finely dispersed within a mixed-conducting, metallic matrix in order to obtain a porous microstructure and a high reactant surface area. The critical function of the matrix was to maintain the microstructural integrity of the dispersed reactant, but it also served to collect current and facilitate rapid lithium transport. The idea was demonstrated using a Li_xSi reactant phase in a matrix of Li_7Sn_3 , with charge/discharge cycling being conducted in a potential range in which the Li_7Sn_3 matrix was un-reactive.

Over a decade later, the FUJI Photo Films company introduced their *tin-based amorphous composite oxide (TCO)^f* concept.^[188] In this approach, tin oxide was irreversibly reduced to form nanostructured or amorphous domains of metallic tin and Li_2O in the first charge. In subsequent cycles, the tin would react reversibly with lithium while the Li_2O matrix remained virtually inert. In this way, the inactive material was formed *in-situ* and provided a microstructural network that would

^f The composition of the material used in the original patent was $\text{Sn}_{1.0}\text{B}_{0.56}\text{P}_{0.40}\text{Al}_{0.42}\text{O}_{0.36}$. Only tin contributed to the electrochemical capacity of the cell, while the other oxides of boron, aluminium, and phosphorous added to the dimensionally stable glassy network.

enable improved cycling stability. Unfortunately, both the *mixed-conductor matrix* and *TCO* systems were a compromise that produced lower gravimetric and volumetric capacities due to the necessary inactive phases in the electrode.

A more ambitious approach to this problem was demonstrated by Bessenhard and co-workers in a series of reports on the Sn-Sb system.^[186, 189-194] This system undergoes complicated recrystallization reactions with lithium, in which both components react with lithium but at different stages in the charge and discharge cycles. This two-step process significantly improved capacity, since it resulted in a composite of two finely interdispersed lithiated phases. Furthermore, the cycling stability was also improved due to a “buffer effect” whereby the un-reacted phase would cushion the volume changes that occur within the reacting phase. This approach also reduced the capacity fade observed by using only metallic electrodes, but did not completely eliminate the problem. The theoretical lithium storage ability of these compounds is similar to those of their component elements, since both elements participate in the reaction at some time. The key barrier to the practical usage of such systems is maintaining good cycling stability without sacrificing the high capacity afforded by the use of these metals.

2.4.2.1 Crystal Structure

The exact structure and composition of ‘SnSb’ (β phase) has been debated for many years. The structure has been variously described as primitive cubic^[195], of NaCl-type,^[196] and as rhombohedral.^[197, 198] It is now apparent that the crystallographic cell is indeed rhombohedral ($R\bar{3}m$) with the structure defined by periodic stacking of tin and antimony atomic planes in the c direction (Fig. 2.13). The phase occurs in nature as the mineral *stistaite*^g, but was first discovered in 1970 as an inclusion in native tin.^[199]

^g The general composition of naturally occurring stistaite is $\text{Sn}_{0.561}\text{Sb}_{0.437}\text{Cu}_{0.002}$.

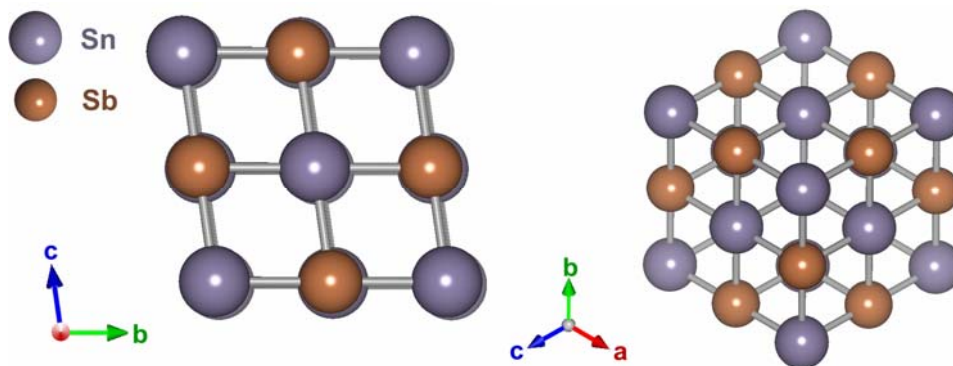
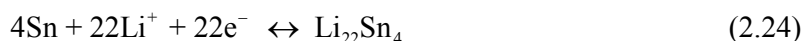


Figure 2.13: Different views of the rhombohedral crystal structure in β phase SnSb.

Considerable variability in the extent of the solid solution range has also been reported. The initial phase diagram of the Sn–Sb system detailed two intermediate solid solution phases: β phase (40–44 % Sb) and γ phase (50–56 % Sb).^[200] Other work by Morris-Jones *et al.*^[196] reported that only a single intermediate β phase existed that had an extended $\text{Sn}_{1-x}\text{Sb}_{1+x}$ homogeneity range (40–54 % Sb) and included the nominally ideal SnSb composition.^[196] The existence of only a single phase (β) over a large solid solution range was confirmed by Hägg *et al.*,^[201] but with a particular composition range (45–55 % Sb). However in a more recent study, Vassiliev *et al.*^[198] concluded that the β phase did not exist as a solid solution, but rather should be described as four distinct compounds of stoichiometry SnSb, $\text{Sn}_{12}\text{Sb}_{13}$, Sn_2Sb_3 , and SnSb_2 . Furthermore, they proposed that variations in stoichiometry would be governed by the hexagonal stacking sequence of tin and antimony layers along the c -axis as well as cation mixing of tin in the antimony layers. Oberndorff *et al.*^[202] concurred with this explanation and also identified the compounds Sn_4Sb_3 and Sn_3Sb_4 at 220 °C. However, they found no evidence for the presence of an equiatomic compound SnSb as an equilibrium phase at this temperature. It should be noted that it is nearly impossible to distinguish between the above-mentioned compounds using XRD due to their structural similarities and the almost identical scattering factors of tin and antimony. Therefore, any phase(s) of roughly equiatomic proportions are assigned as SnSb throughout this thesis.

2.4.2.2 Reactions with Lithium and Synthesis Techniques

Compared to graphite electrodes, the insertion of lithium into a metallic matrix causes more drastic three-dimensional rearrangements. The electrochemical reaction of SnSb with lithium has been described by Winter *et al.*^[203] as a two stage process, in which antimony reacts first, to form Li_3Sb and domains of metallic tin (Eqn. 2.23). At lower potentials, tin reacts with lithium in a step-wise fashion to eventually form the fully lithiated $\text{Li}_{22}\text{Sn}_4$ phase (Eqn. 2.24). As a consequence of this particular reaction mechanism, a further nanostructuring of the SnSb phase occurs *in-situ* during cycling. This mechanism has also been proposed to explain the reversible reaction of lithium with the InSb system.^[204]



It has been shown in several works that electrodes containing a slight excess of tin (*i.e.*, SnSb-Sn) can produce superior capacity compared to only SnSb.^[194, 205, 206] SnSb-Sn powders with an average particle size < 300 nm prepared by chemical precipitation can produce capacities in the 500-600 mAh g⁻¹ range and good cyclability for up to 50 cycles.^[191, 194] Common to both SnSb and SnSb-Sn is a low coulombic efficiency (50-65 %) in the first charge/discharge cycle. This low first cycle efficiency has been attributed to the following causes; SEI film formation, the reduction of oxide impurities to metals and Li_2O , a loss of electrical contact, and the trapping of lithium at defect sites or within reaction zones. Low first cycle efficiency is also common in many other alloy systems, but is reported to be particularly prevalent in those containing tin. To determine whether this problem was intrinsic to tin, or if it was related to the prevailing microstructure, morphology or construction of the electrode, Wachtler *et al.*^[194] conducted an electrochemical study on electroplated tin thin films at various current densities. In this work, it was found that a first cycle efficiency of 95 % could be achieved at a current density of 0.1 mA cm⁻². It was therefore concluded that the low first cycle efficiency in these materials was not due to the intrinsic properties of tin, but rather a reduction of oxide impurities and possible loss of contact with the current collector. This result indicated that

significant improvements could be made by careful attention to the purity and morphology of the active material, as well as proper electrode design.

SnSb and SnSb-Sn powders used for rechargeable lithium batteries are usually commonly synthesized by chemical precipitation from aqueous or organic solutions of the respective metal ions using a reductive agent such as zinc or NaBH_4 . As shown in Fig. 2.14, this approach can yield micro- or nano-sized particles with drastically different morphologies.

Figure 2.14: SEM of SnSb-Sn powders: (a) reduced by NaBH_4 ; (b) reduced by Zn in aqueous solution; (c) reduced by Zn in glycol.^[206]

Reduction with NaBH_4 will often lead to materials with small particle size, low crystallinity, high surface area, and a relatively high fraction of surface impurities. These powders commonly produce a low first cycle efficiency, but a good longer-term cycling stability. On the other hand, reduction with zinc yields materials with larger particle size, higher crystallinity, lower surface area, but a relatively small amount of impurities. These powders deliver a higher first cycle irreversible capacity (~13 %), but a inferior cycle life. It should be recognized that a larger particle size will exaggerate any normal expansion effects and increase the risk of electrical disengagement from the current collector. Furthermore, significant cracking of the SEI film will occur which will be repaired by reactions between the electrolyte and the fresh surface of the active material. In this case filming reactions will extend over a large number of cycles and be reflected as poor coulombic efficiency.

Fig. 2.15 shows the potential profiles in the first charge/discharge cycle of SnSb-Sn powders prepared by the various reductive precipitation reactions. For easy understanding, the first charge curve can be separated into three distinct regions. Between 1.3 V and 0.8 V, the electrolyte reduction and SEI formation process

occurs. Note also that the irreversible reduction of oxidic and hydroxylic surface impurities of the SnSb-Sn material takes place. At 0.8 V, a potential plateau due to formation of the Li-Sb phase is visible. The antimony becomes unbonded from the tin whereby the remaining tin segregates. Finally, between 0.7 V and 0.2 V, the multistep formation of the various Li-Sn phases takes place and is completed with the formation of $\text{Li}_{22}\text{Sn}_4$. The charge curves of the materials prepared by zinc reduction show distinct plateaus in this potential region, which can be related to the high crystallinity and the relatively large particle size.

Figure 2.15: *Potential profiles in the first charge/discharge cycle of SnSb-Sn powders prepared by reductive precipitation. (Adapted ^[206])*

A separate method of preparing SnSb and SnSb-Sn particles is carbothermal reduction from SnO_2 and Sb_2O_3 precursors.^[207] However, the particles are often extremely large (50-100 μm) and require further crushing or ball milling to reduce the particle size to a practical level. Other, less common preparatory methods involve melting a mixture of tin and antimony metal powders followed by mechanical filing^[189] or electrochemical deposition directly onto a copper foil.^[208] These methods generally produce inferior morphology and electrochemical properties to chemical methods, are more expensive, and lack reproducibility.

In general, methods that produce materials with smaller particles are favored for use in rechargeable lithium batteries. This is because the materials show less observable

volume variation, retain a stable microstructure during cycling, and possess a kinetic advantage. However, the particle size can be too small. A particle size of less than about 100 nm in SnSb, silicon, silver, and antimony based materials can accelerate particle aggregation during lithium insertion and extraction, which leads to large volume changes and reduced electrochemical performance.^[209, 210] In addition, the kinetic advantage of nanosized materials disappears.

To balance these effects, some groups have been focused on tailoring SnSb-C composites. For example, nanosized SnSb alloy has been deposited and dispersed uniformly on the surface of MCMB^[211] and hard carbon spherules^[212] by a co-precipitation method in glycerin solution. The MCMB-based composites show improved cycling performance due to the dispersion of < 30 wt% nanosized alloy particles on the carbon surface. This alleviates particle aggregation that usually occurs during lithium insertion and extraction. A reversible capacity in the range of 400-500 mAh g⁻¹ can be achieved, along with extremely stable charge/discharge cycling. When the weight ratio of SnSb alloy exceeds 30 %, the MCMB can no longer prevent the nano-SnSb alloy from aggregating, and the capacity quickly fades. In the case of hard carbon spherules, Fig. 2.16 shows a low resolution SEM image of the morphology of pre- and post-coated particles. A high first cycle coulombic efficiency of 82 % has been reported, but with rather low coulombic efficiency at following cycles. The cause of this was related to the formation of an unstable SEI film on the surface of the nano-alloy. Despite these drawbacks, the combination of the alloy and carbon in a designed structure shows great potential for improving the energy density and cycle life of rechargeable lithium batteries.

Figure 2.16: *Low resolution SEM images of a hard carbon spherule before (a) and after (b) coating with SnSb alloy. (Adapted ^[212])*

2.4.3 Transition Metal Oxides

Transition metal (TM) oxides were long regarded as only cathode materials, and their potential utility as anode materials was unknown. This was until it was demonstrated that a small amount of lithium ions could be removed from their crystal structure at low potential, making them also potentially suitable anode hosts. The first oxides investigated were WO_2 , MoO_2 , and Nb_2O_5 , but these showed little promise.^[213] It was not until the FUJI Photo Film company commercialized their *TCO* concept in 1982, that the scientific community intensified studies into numerous other oxides. None of the systems proposed were serious alternatives to the advanced carbons, until in 2000 Poizot *et al.*^[214] reported ground-breaking results on the properties of nanosized TM oxides. In this work, electrodes made from nanosized TM oxides, such as NiO , CoO , FeO , CuO , Cu_2O , and Co_3O_4 , were shown to exhibit reversible capacities up to three times higher than industry standard graphite electrodes. Fig. 2.17 shows the crystal structure of Co_3O_4 , while Fig. 2.18 shows the structure of NiO for comparison.

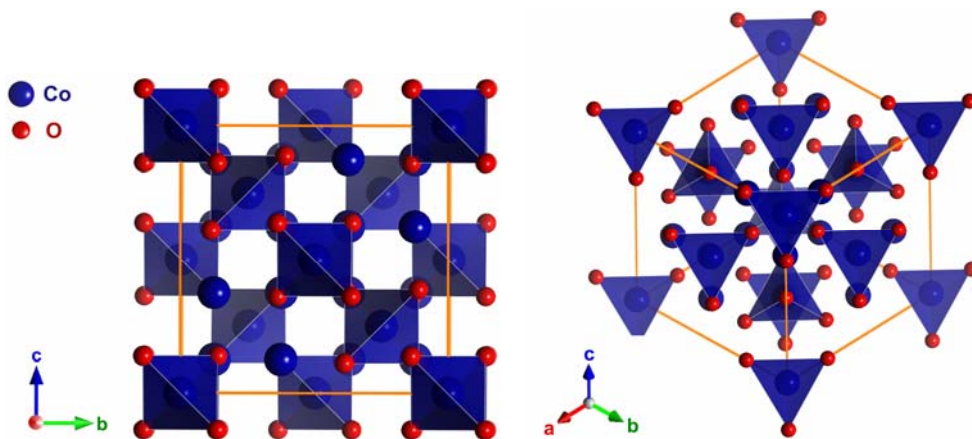


Figure 2.17: Different views of the cubic crystal structure of Co_3O_4 .

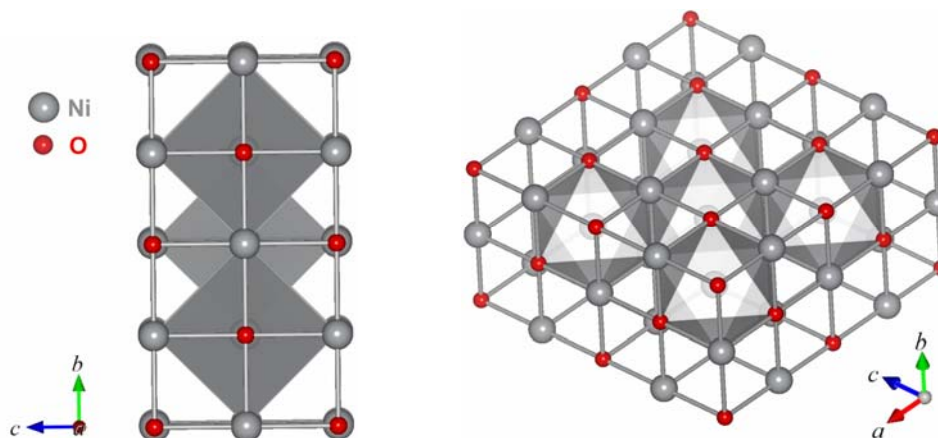
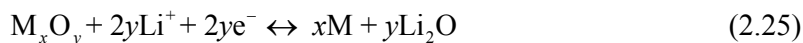


Figure 2.18: *Different views of the cubic crystal structure of NiO.*

Understandably, TM oxides had not seriously been considered as promising host structures due to the lack of available empty sites for lithium ions and their inability to form an alloy with lithium. Rather, the reaction of these materials with lithium was shown to entail a general displacement redox reaction, as follows:



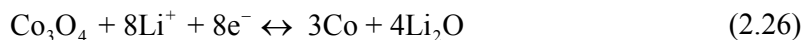
Many previous studies had observed that Li_2O was virtually electrochemically inactive once formed, which was supported by basic thermodynamic considerations predicting that the extraction of lithium from Li_2O was unlikely. However, Poizot *et al.*^[214] surmised that the binding energy of Li_2O is sufficiently reduced by the small particle size of Li_2O and the catalytic activity of the transition metal formed during cell discharge. This explanation seemed reasonable since it was well accepted that the physical and chemical behaviors of a nanomaterial can be vastly different from those of its bulk state. For example, the melting point of gold can vary from its referenced temperature of 1064 °C to less than 200 °C when the particles become smaller than 20 Å.^[215] Transition metal nanoparticles of elements such as cobalt are also commonly used as catalysts in the reduction of H_2 and O_2 on the surface of single wall nanotubes,^[216] as catalysts in various condensation or polymerization reactions,^[217] and also in the decomposition of $\text{Li}_2\text{S}^{\text{h}}$.^[218] Moreover, reversible

^h It is pertinent that Li_2S has a similar bond enthalpy to Li_2O ($\Delta\text{H}(\text{Li}_2\text{S}) = 312.5 \text{ kJ mol}^{-1}$, $\Delta\text{H}(\text{Li}_2\text{O}) = 333.5 \text{ kJ mol}^{-1}$).

electrochemical reactions involving the formation-decomposition of Li_2O in rechargeable lithium cells, while novel at room temperature, were already reported by Thackeray *et al.*^[219] to occur at 420 °C during the insertion of lithium into $\alpha\text{-Fe}_2\text{O}_3$.

2.4.3.1 Reactions of Co_3O_4 with Lithium

In light of this novel mechanism, intensive investigations into Co_3O_4 were launched as early data indicated that it could react with more than 8 lithium per formula unit down to 0 V with a reversible capacity of 1100 mAh g⁻¹.^[220] The basic decomposition reaction (Eqn. 2.26) of the Co_3O_4 -based electrode into cobalt nanograins and Li_2O during the first discharge and its reoxidation into nanometric Co_3O_4 upon the following charge were quickly confirmed.^[221] However, work originally conducted by Thackeray *et al.*^[222] in 1985 suggested that sometimes lithium could also be inserted into the framework to form a partially ordered rock salt compound $\text{Li}_x\text{Co}_3\text{O}_4$.



This work was further developed by Larcher *et al.*^[221] who concluded that, depending on the texture of the starting material, two competing mechanisms to achieve the full decomposition of the Co_3O_4 electrode could exist. These two-step reaction routes are represented diagrammatically in Fig 2.19. One involves the reduction of Co_3O_4 into CoO and Li_2O while the other one involves the formation of $\text{Li}_x\text{Co}_3\text{O}_4$, with both intermediates decomposing into cobalt nanograins and Li_2O on further reduction.

Using powders that contained larger Co_3O_4 domains or applying a low discharge current, would preferentially lead to CoO as an intermediate compound (reaction 2). Whereas, using powders with smaller Co_3O_4 domains or applying a high discharge current would favor the formation of the inserted $\text{Li}_x\text{Co}_3\text{O}_4$ intermediate compound (reaction 1). By carefully tuning the texture of the active material (specific surface area and crystallite size) and by altering the cycling procedure (rate and temperature), the reduction path for cobalt oxide can therefore be controlled. However, no

additional work has been done on the effect of the chosen reaction path and textural evolution upon cycling on the overall electrochemical performance of the cell.

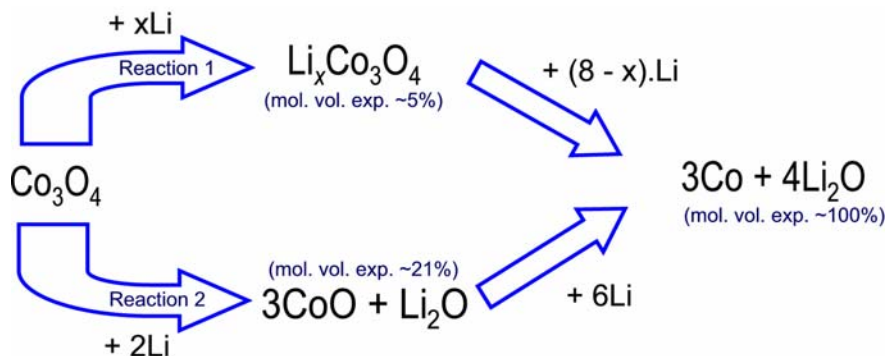


Figure 2.19: Schematic representation of two alternative routes for the electrochemical reaction of Co_3O_4 with lithium.

Unfortunately, TM oxide anodes in rechargeable lithium batteries have not been commercially successful due to capacity fade and a poor cycle life.^[223, 224] The cause of these problems can be attributed to the significant volume changes that occur during lithium uptake and removal and the nature and electrochemical behaviour of the SEI formed on the electrode's surface. The SEI begins forming in the first discharge (reduction of TM oxide) as a result of secondary reduction reactions in the electrolyte and has the appearance of a “polymer-like” gel.^[225] Subsequent charging of the cell will either cause a partial dissolution of the SEI and therefore reduce the layers thickness, or have negligible effect. If the layer is partially dissolved in the initial cycle, it can be repaired in the next discharge, and therefore, the SEI layer thickness remains essentially constant. In the alternative scenario, if no dissolution occurs, repeated charge/discharge cycling can cause the SEI layer to thicken.

It is well known that the nature of the SEI can be controlled by selection of an appropriate electrolyte. However, there is also clear evidence to suggest that the nature and therefore the electrochemical properties of the SEI can be equally influenced by the selection of TM oxide and its texture (*i.e.*, crystallite and particle size, and surface area and composition). Problems of poor ionic transfer due to SEI thickening have been particularly reported in TM oxide nanocrystalline powders that

had an extremely high surface area. For instance, work by Yuan *et al.*^[226] on Co_3O_4 powders has shown that by using an average crystallite size of 37 nm rather than 15 nm, the capacity retention of the electrode after 20 cycles could be improved from 30 % to over 90 % of the first cycle capacity. Careful control of the powder texture is essential to enable the SEI to be indirectly engineered in order to improve the cycle life of the TM oxide electrode.

2.5 Nanostructures

There are several significant advantages associated with the use of nanomaterials in electrodes for rechargeable lithium batteries. These include:

- A better accommodation of the strain caused by volume changes upon lithium intercalation/deintercalation. This will reduce the likelihood of electrode cracking and potentially extend the cycle life of the cell.
- The possibility of new reactions that do not occur in the bulk form of a material.
- Higher charge/discharge rates made possible by increased electrode-electrolyte contact area.
- Reduced path length for ionic and electronic transport. This can allow materials that have an inherently low electronic conductivity to perform better and also further aid the cell performance in high power applications.

Conversely, there are some potential disadvantages of using nanomaterials that include:

- An increase in undesirable electrode-electrolyte reactions due to high surface area, leading to self discharge and to poor cyclability.
- Lower volumetric energy due to inferior particle packing.
- Often more complex synthesis than traditional processes.

Controlling the shape and size of nanoparticles can offer significant advantages. This is illustrated by recent results of studies by Armstrong *et al.*^[227-231] on $\text{TiO}_2\text{-B}^{\text{i}}$. The $\text{TiO}_2\text{-B}$ polymorph is an excellent intercalation host for lithium, which has a near constant voltage plateau occurring at 1.5–1.6 V and a theoretical capacity of 335 mAh g^{-1} . Various morphologies were synthesized by a simple hydrothermal route in the form of bulk powders, nanoparticles, nanowires, and nanotubes. The diameter of the nanowires was in the range of 20–50 nm, and they were several micrometers in length. The tubes were multiwalled with external diameters of around 20 nm and internal diameters in the range of 5–8 nm, with the length extending up to 1 μm . As shown in Fig 2.20, these studies confirmed that the ability to intercalate lithium was the greatest in the nanotubes ($\text{Li}_{1.01}\text{TiO}_2$, capacity 338 mAh g^{-1}), followed by the nanowires ($\text{Li}_{0.91}\text{TiO}_2$, capacity 305 mAh g^{-1}) and the bulk powder ($\text{Li}_{0.71}\text{TiO}_2$, capacity 240 mAh g^{-1}). Since all materials adopted the same crystal structure, such differences were related to the particle dimensions and surface areas of the bulk (20 $\text{m}^2 \text{g}^{-1}$), nanowire (36 $\text{m}^2 \text{g}^{-1}$) and nanotube (190 $\text{m}^2 \text{g}^{-1}$) materials. Smaller particles have a larger surface area, and will therefore give larger electrode-electrolyte contact areas. This effect, coupled with the shorter diffusion paths within the smaller particles logically leads to easier intercalation in the order of tubes, wires, and bulk materials.

Figure 2.20: Variation of voltage with lithium content for $\text{TiO}_2(\text{B})$ materials cycled at a constant current of 10 mA g^{-1} between 1 V and 3 V. (Adapted^[230])

ⁱ The “B” refers to the phase of TiO_2 . In the more common rutile, anatase, and brookite phases, the structure consists of edge- and corner-sharing TiO_6 octahedra; however, in this case they are arranged to form perovskite-like pathways along which inserted lithium ions may undergo easy transport.

The only electrochemical measure for which the nanotube morphology was not superior was irreversible capacity loss. For TiO₂-B nanotubes, significantly more lithium was able to be inserted on discharge than was extracted on the subsequent charge. The best performance in this regard was by the use of nanowire morphology, with this electrode demonstrating excellent cyclability with less than 0.1 % capacity loss per cycle for 200 cycles.

The above example demonstrates perhaps the most troublesome disadvantage in the use of some nano-architectures; the possibility of significant side reactions with the electrolyte. Usually these will reduce the cyclability of the electrode, but in the worst case, can lead to safety concerns. Redox reactions in these materials must occur within the stability window of the electrolyte in order to prevent the uncontrollable formation of an SEI layer. In this way, the many advantages of using various nanostructures for electrodes in rechargeable lithium batteries may be exploited.

The discovery of carbon nanotubes (CNT)^j by Iijima^[232] in 1991 has fuelled worldwide interest in the synthesis of complex nano-architectures. The CNT possesses outstanding chemical and physical properties that can be utilized in many applications. Their methods of fabrication and the full scale of their practical applications can be found in a series of focused review articles.^[233, 234] At a fundamental level, nanotubes possess several different areas of contact that include phase boundaries, defect zones, and inner/outer surfaces. These features render the materials highly reactive with lithium, but also provide opportunities for further functionalization and design. Examples frequenting the literature include the combination of nanotubes and nanorods by the tube-in-tube or the rod-in-tube approach. This is an outstandingly elegant means of intrinsic functionalization that takes advantage of both the inner surface of nanotubes and the high aspect ratio of nanorods. In this regard, the oxidic nanotubes promise even more unique properties and advantages over traditional morphologies which may lead directly to new technological applications.

^j It is noteworthy that Sumeo Iijima modestly described these structures in his first paper as “microtubules of graphitic carbon”. The term nanotube was not introduced into the literature until the following year.

2.5.1 Synthesis of Nanotube Materials *via* the Template Method

One of the most interesting nano-materials synthesis methods involves the preparation of an ordered array of nanowires or nanotubes by a templating technique. This works by using membranes that contain cylindrical pores with monodisperse diameters, and a nanoscopic fibril or tubule of the desired material is synthesized within each pore. The concept was first demonstrated by the preparation of nanoscopic metal fibrils in 1970 by Possin.^[235] Substantial efforts later by Martin *et al.*^[236-240] have led to the template synthesis of nanotubes and nanowires composed of polymers, metals, semiconductors, carbon, and various lithium intercalation materials. The techniques used to synthesize such materials within the pores of the template membranes include electro-less metal deposition, electrochemical methods, and *in-situ* polymerization. The various oxides that have been synthesized for use in rechargeable lithium batteries include: SnO_2 ,^[241] Co_3O_4 ,^[242] Fe_2O_3 ,^[243] and TiO_2 anode materials, and LiCoO_2 ,^[244] LiMn_2O_4 ,^[244] $\text{LiNi}_{0.8}\text{Co}_{0.2}\text{O}_2$,^[244] and V_2O_5 ^[245, 246] cathode materials. Work on SnO_2 presents a typical example of nanostructures that can be synthesized by a templating process. Tubules of nanostructured SnO_2 were prepared by soaking a polycarbonate template in a SnO_2 sol, with the nanostructure being revealed by gentle abrasion of the template using oxygen plasma. Fig. 2.21 shows that an electrode made from SnO_2 nanotubules displays superior rate capabilities and capacity retention when compared to a SnO_2 thin film electrode.

Figure 2.21: Comparison of the electrochemical performance of SnO_2 thin films and nanostructured powders: (a) rate capability; (b) cyclability. (Adapted^[241])

Nanotube structures of Co_3O_4 have also been prepared more recently by Shi *et al.*^[247] by using cobalt complexes pre-coated onto colloidal particles. Impressive Co_3O_4 nanofibers and nanotubes, as shown in Fig. 2.22a-c, have also been prepared by Li *et al.*^[242] by thermal decomposition of cobalt nitrate within an ordered porous alumina matrix. This method produced highly nanoporous structures with high surface areas that ensured high reactivity with lithium. A corresponding improvement in cycling performance is demonstrated in Fig 2.22d which compares the cycle life of various Co_3O_4 nanostructures. Other recent trends have involved the fabrication of more complicated nanotube composites such as Si-CNT,^[248] Ag-Fe-Sn-CNT,^[249] and Sn/Sn-Ni-CNT.^[250]

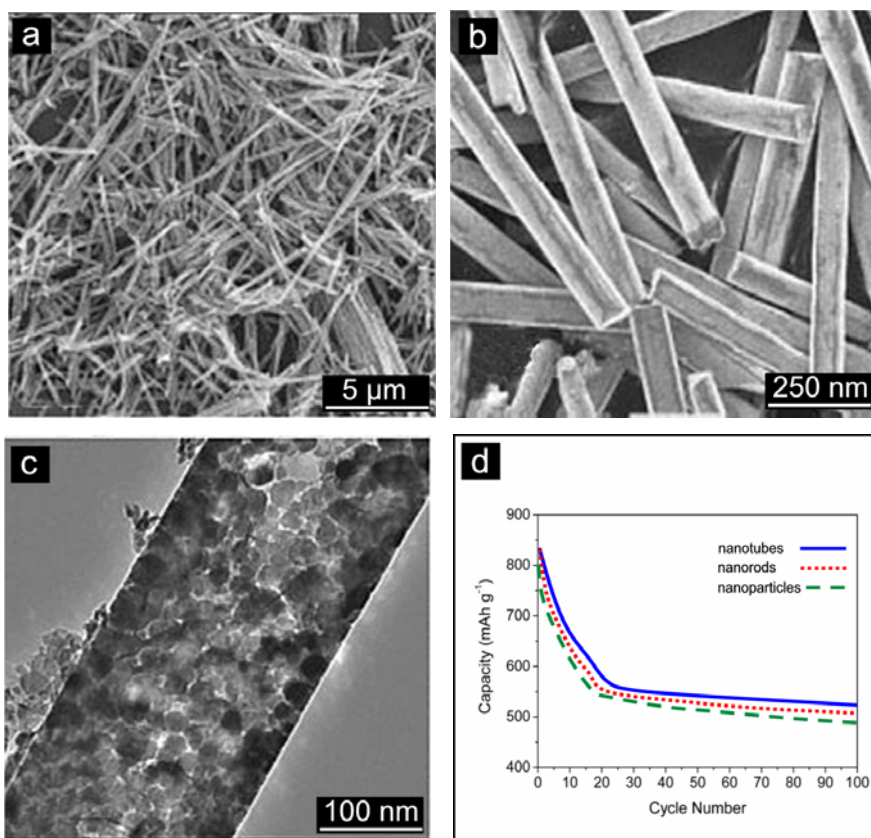


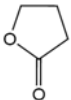
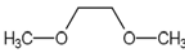
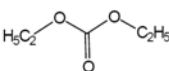
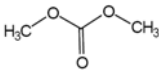
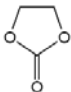
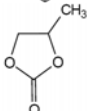
Figure 2.22: SEM images (a), (b), and a TEM image of the morphology of Co_3O_4 nanotubes (c). The discharge capacity of Co_3O_4 nanotubes, nanorods, and nanoparticles at a constant current of 50 mAh g^{-1} (d).

2.6 Battery Electrolytes

2.61 Organic Solvents

One of the primary requirements for an electrolyte is that it must have a wide electrochemical stability window. Aqueous electrolytes can not be used, and only a few non-aqueous alternatives are suitable. Various acids and alcohols are prohibited since the electrolyte must also be aprotic, as active protons react with lithium to give hydrogen gas. Inorganic salts dissolved in organic liquids are the most commonly used electrolyte solutions used at present due to superior ionic conductivity at ambient temperature. Since rechargeable lithium batteries operate between $-20\text{ }^{\circ}\text{C}$ and $60\text{ }^{\circ}\text{C}$ solvents with a low melting point, high boiling point, and low vapor pressure are desirable. The physical properties of some important organic solvents used in rechargeable lithium batteries are summarized in Table 2.2. In practice, suitable mixtures are made from two or more solvents which combine the favorable properties of the constituents and modifications are made to an electrolyte system to suit the particular operating requirements of the cells.^[251]

Table 2.2: *Physical properties of important organic solvents*

Solvent, abbreviation	Structural Formula	Melting Point ($^{\circ}\text{C}$)	Boiling Point ($^{\circ}\text{C}$)	Viscosity (cP)	Dielectric Constant, ϵ
γ -Butyrolactone, γ-BL		-43	204	1.751	39.10
1,2-Dimethoxyethane, DME		-58	85	0.455	7.20
Diethyl carbonate, DEC		-43	126	0.751	2.82
Dimethyl carbonate, DMC		5	91	N/A	3.12
Ethylene carbonate, EC		39	248	1.86 ($20\text{ }^{\circ}\text{C}$)	89.63 ($40\text{ }^{\circ}\text{C}$)
Propylene carbonate, PC		-49	242	2.530	64.64

Liquid solvents that fulfill the dual requirements of a high lithium ion conductivity ($>10^{-3} \text{ S cm}^{-1}$) and a broad electrochemical stability window are mainly carbonates, ethers, and esters of various kinds. Of these, the carbonates are the most common choice under ambient conditions, because of their superior cycling behaviour. Ethylene carbonate (EC) and propylene carbonate (PC) provide sufficiently high conductivity and a broad stability window. However, as previously discussed, PC causes severe exfoliation of graphitic carbon electrodes due to extensive co-intercalation during charging. EC is the preferred solvent in that context, but is a solid at room temperature. It is therefore common to mix these with other solvents with less conductivity to obtain a working electrolyte over a wider temperature interval.

2.62 Lithium Salts and Other Active Components

Soluble lithium salts are added to the solvents as charge carriers of the current passed in the cell during the electrochemical process. Good solubility and charge separation of anion and cation are needed to obtain this high conductivity. This is normally achieved by choosing bulky anions with low negative charge density.^[252] Examples of salts used are LiClO_4 , LiAsF_6 , LiPF_6 , LiBF_4 , LiCF_3SO_3 , and $\text{LiN}(\text{SO}_2\text{CF}_3)_2$. The LiClO_4 and LiAsF_6 salts are not used in commercial cells because of the explosion risk of the ClO_4^- anion, and the high toxicity and undesirable degradation products of the AsF_6^- anion. The other salts mentioned are currently used or being considered for use in practical cells.

3. Experimental Techniques and Procedures

3.1 Overview

A flowchart of the experimental methodology used in this work is shown in Fig. 3.1.

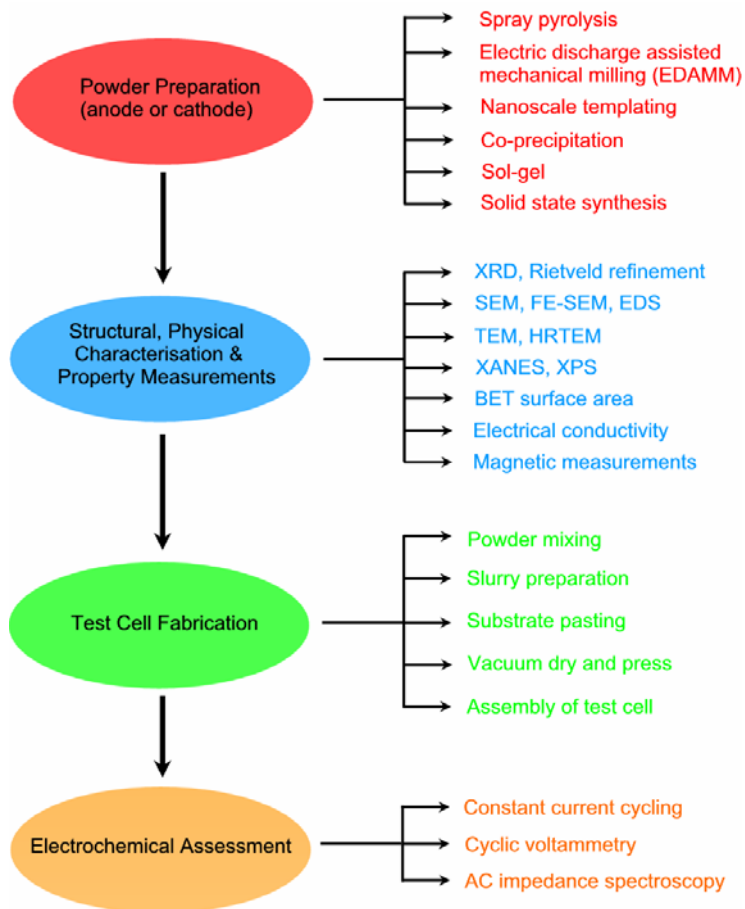


Figure 3.1: A flow chart detailing the experimental techniques and procedures.

Various cathode and anode powders were prepared using different synthesis techniques. Cathode powders were prepared by solid state synthesis ($\text{LiM}_{0.02}\text{Co}_{0.98}\text{O}_2$, where $\text{M} = \text{Zr}, \text{V}, \text{Mg}, \text{or Mo}$), sol-gel (LiFePO_4 and Ti-doped LiFePO_4), and electric discharge assisted mechanical milling (LiFePO_4 and LiCoO_2) methods. Anode powders were prepared by nanoscale templating (NiO), reductive precipitation (SnSb , SnSb-Sn , and SnSb-CNT composite), and spray pyrolysis (NiO , Co_3O_4 and $\text{Co}_3\text{O}_4\text{-C}$ composite) techniques. All powders were then subjected to

rigorous structural and physical characterization. Test cells were assembled using an electrode coated with the synthesized powders, and a lithium metal counter electrode. The electrochemical properties of the test cells were investigated using charge/discharge cycling, cyclic voltammetry, and ac impedance spectroscopy.

3.2 Methods of Synthesis

3.2.1 Solid-State

$\text{LiM}_{0.02}\text{Co}_{0.98}\text{O}_2$ ($\text{M} = \text{Mg}, \text{V}, \text{Mo}$) powders were prepared in separate experiments using Li_2CO_3 , Co_3O_4 , and either MgO , V_2O_3 , or Mo_2O_3 reagents. Stoichiometric quantities were wet mixed with ethanol in an agate mortar and dried in a vacuum oven at $150\text{ }^\circ\text{C}$ for 2 h. The dried mixtures were ground and transferred to alumina boats and annealed at $850\text{ }^\circ\text{C}$ for 12 h in an air filled tube furnace. The powders were slowly cooled to ambient temperature, reground, and annealed for a further 12 h to improve their crystallinity.

3.2.2 Sol-Gel

LiFePO_4 and $\text{LiTi}_{0.01}\text{Fe}_{0.99}\text{PO}_4$ powders were synthesized *via* a sol-gel preparation route that used $\text{LiOH}\cdot\text{H}_2\text{O}$, $\text{FeC}_2\text{O}_4\cdot 2\text{H}_2\text{O}$, $\text{NH}_4\text{H}_2\text{PO}_4$, and $\text{Ti}(\text{OCH}_3)_4$ as reactants. Stoichiometric quantities of reactants were dissolved in deionized water, to which polyacrylic acid and citric acid were added as complexing agents for the formation of the gel. The solutions were stirred vigorously and heated to $85\text{ }^\circ\text{C}$ until a viscous gel was formed. The as-formed gel was then heated to $500\text{ }^\circ\text{C}$ in an argon atmosphere to decompose any organic compounds. The decomposed precursors were further sintered at $750\text{ }^\circ\text{C}$ in a reducing atmosphere of 10 % hydrogen in argon to prevent the oxidation of Fe^{2+} cations. A 3.0–4.0 wt% carbon coating was formed by the decomposition of the organic precursors that was assessed by SEM and thermal gravimetric analysis (TGA).

3.2.3. Electric Discharge Assisted Mechanical Milling (EDAMM)

EDAMM is a new and exciting materials synthesis technique that was developed by Calka *et al.*^[253] at the University of Wollongong in 2002. In that report, EDAMM was shown to provide kinetic benefits beyond those achievable by using conventional mechanical milling techniques only. Until now, the EDAMM technique has mostly been applied to metal nitriding, elemental alloying, and rapid reduction processes in various oxides. The work detailed herein represents the first application of this technique to the processing of advanced functional oxide materials. EDAMM is used to synthesize LiCoO_2 and LiFePO_4 cathode powders, and a range of high temperature $\text{SrTi}_{1-x}\text{Co}_x\text{O}_3$ compounds where $x = 0, 0.1, 0.2$, and 0.5 , which are promising candidates for magnetic applications. Significant alterations to the original EDAMM apparatus set-up and redesign of the power source were required to successfully synthesize these functional powders.

The experimental apparatus consisted of a modified vibrational rod mill that served as both a mechanical milling device and a reaction chamber. Precursor powders were weighed in the correct stoichiometric proportions, hand mixed for 10-15 min, and fed into the mill in exact 0.25 cm^3 batches. The reaction chamber was supplied with a steady flow ($200 \text{ cm}^3 \text{ min}^{-1}$) of a selected gas (O_2 , or $\text{N}_2 + 3\% \text{ H}_2$) *via* inlet/outlet valves. If the device was used as a vibrational mill only, a hardened stainless steel plunger repeatedly impacted on the precursor powders at a selected frequency/amplitude, fracturing the powder particles to promote reactions.

For EDAMM, a custom built power supply was connected to the mill floor and plunger through an alternating current, high voltage transformer, which generated 3 kV and 10–800 mA impulses in the kHz range. Depending upon the powder species present in the mill, the vibration frequency/amplitude of the plunger, and the electrical parameters selected, we were able to promote the formation of low power (10–50 W) or high power (50-350 W) thermal arc discharge. In addition, an athermal glow discharge (cold plasma) was able to be formed under certain processing conditions. Work by Davis *et al.*^[254] supports the existence of glow discharges when operating at power levels $< 100 \text{ W}$ in the mA and kV realm of current and voltage response, even at atmospheric pressure.

A schematic of the principle of operation of the experimental apparatus is shown in Fig. 3.2, with a glow discharge (Fig. 3.2a) and arc discharge (Fig. 3.2b) occurring roughly between the plunger and reaction vessel. Fig. 3.2c shows that an arc discharge will create a main plasma channel and less intense plasma “tree branches”, which act to raise the localized temperature within the reacting powder particles. Joule heating is generated by the simultaneous actions of the arc discharge and the impact forces of the vibrating plunger.

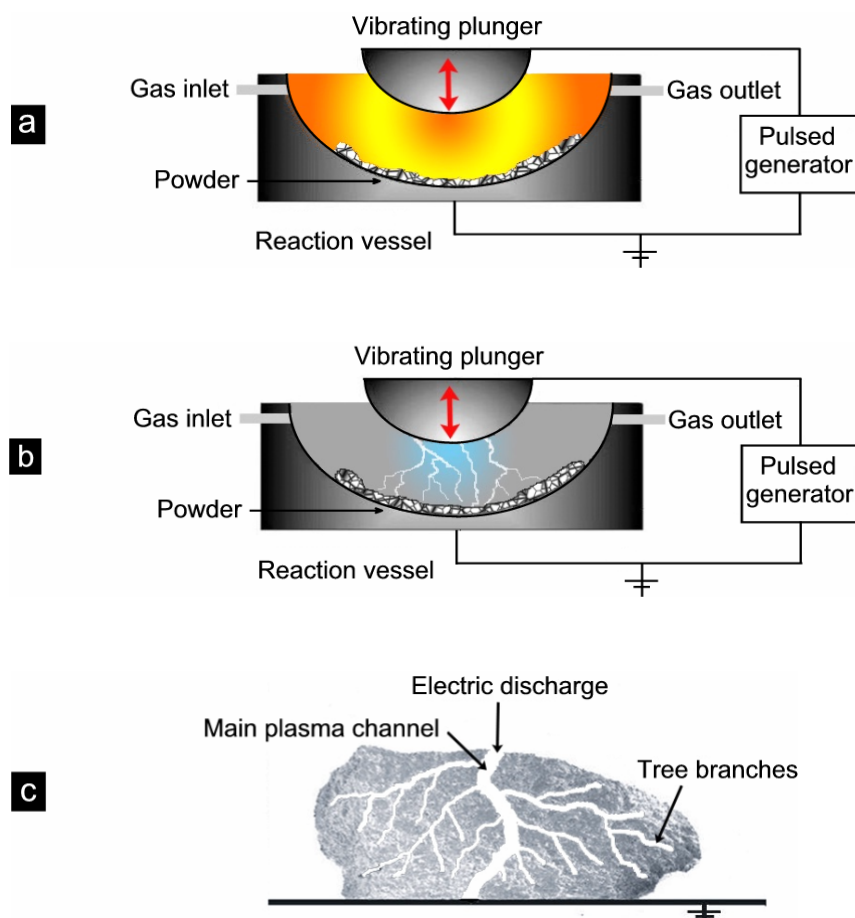


Figure 3.2: Schematic of the EDAMM powder synthesis technique. The vibration of a stainless steel plunger connected to an ac voltage can cause the formation of various electric discharges for variable times; (a) athermal glow, and (b) thermal arc. (c) The interaction of an arc discharge with a powder particle produces a main plasma channel (trunk) and minor plasma channels (branches) of lower intensity.

3.2.4 Nanoscale Templating

Uniform NiO nanotubes that measured up to 60 μm long with an outer wall diameter of 200 nm and wall thickness of 20-30 nm were synthesized by a templating procedure. Fig. 3.3 shows a schematic of the NiO nanotube synthesis process. The first step in this process was to synthesize $\text{Ni}(\text{OH})_2$ nanotubes by using a commercially available anodic aluminium oxide (AAO) template. The details of the procedure to form $\text{Ni}(\text{OH})_2$ nanotubes were first developed by Li *et al.*^[255]

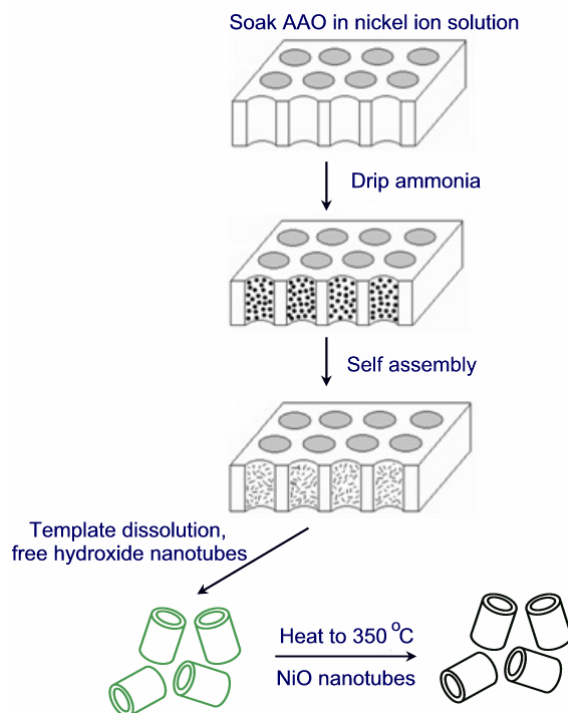
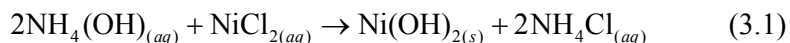


Figure 3.3: Schematic showing the preparation of NiO nanotubes.

The template was soaked in a 0.5 M NiCl_2 solution to impregnate the inner walls with nickel ions. A 2 M NH_4OH solution was then dripped slowly onto the template. Gravitational forces gradually coerced the ammonia solution through the pores, which reacted with nickel ions to precipitate a $\text{Ni}(\text{OH})_2$ film on the inner walls of the template. The overall chemistry of the procedure can be represented by the following double displacement reaction:



Care was taken to ensure the top and bottom surfaces of the template were free of hydroxide precipitate. Nanotube bundles were released by completely dissolving the template in a 2 M NaOH solution for 2 h, then centrifuging in deionized H₂O and then acetone for 5 min. Finally, the as-formed Ni(OH)₂ nanotubes were converted to bunsenite NiO nanotubes by heat treatment in air at 350 °C for 1 h.

3.2.5 Reductive Precipitation

Fig. 3.4 shows the various SnSb-based powders synthesized by reductive precipitation of metal chlorides from aqueous solution. To produce the SnSb alloy powder, metal chloride salts with a 1:1 ionic concentration of Sn²⁺ and Sb²⁺, and 110 g l⁻¹ of Na₃C₆H₅O₇·2H₂O (complexant) were added to 350 mL of deionized water. In separate glassware, a reductive solution was prepared that contained 4.5 g l⁻¹ NaOH and 5 g l⁻¹ NaBH₄ added to 140 mL of deionized water. The two solutions were cooled to 3 °C, and the metal ion solution was carefully added drop-wise to the reductive solution under vigorous magnetic stirring. The resultant suspension was separated by centrifuge and rinsed several times using deionized H₂O, 0.35 M HCl, and acetone. Finally, a black precipitate was recovered, vacuum dried overnight at 30 °C, and stored in an argon-filled glove box.

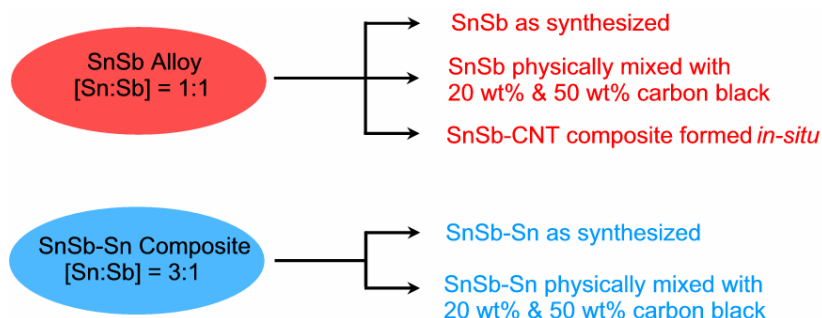


Figure 3.4: Various SnSb-based powders prepared by the reductive precipitation method.

The SnSb-Sn powder was produced using exactly the same experimental technique, but with a 3:1 respective ionic concentration of Sn²⁺ and Sb²⁺. Selected area energy dispersive x-ray spectroscopy (EDXS) indicated that the SnSb-Sn powder was composed of 55 wt% tin and 45 wt% antimony, giving an excess of ~10 wt% tin.

Composites of SnSb and SnSb-Sn alloys with carbon were also formed in order to assess the effectiveness of carbon additions. Both the SnSn and SnSb-Sn powders were physically mixed with 20 wt% and 50 wt% carbon black. Another separate experiment involved the addition of 0.25 mg of multiwalled carbon nanotubes to the 1:1 ionic solution during synthesis, to form a chemically bonded SnSb-CNT composite powder.

3.2.6 Spray Pyrolysis

This method was used to synthesize spherical NiO, Co₃O₄ and Co₃O₄-C composite anode powders *in-situ*. Fig. 3.5 schematically depicts the 1.5 × 0.3 m quartz tube vertical furnace that was purpose built by Ceramic Engineering furnace manufacturers, Australia. The furnace was comprised of three independent heating zones that were operated using Eurotherm 847 temperature controllers. Aqueous nitrate or chloride solutions were transported at 3-5 mL min⁻¹ *via* a peristaltic pump to the top of the furnace, where they were combined with either compressed air or a selected carrier gas. The mixture was atomized through an ultrasonic nozzle into the furnace. An extractor pump set at 32-36 Hz was used to collect the reacted powders and vent waste gases to the atmosphere. This method was simple, flexible, and able to produce high quantities of spherical powder particles with a narrow size distribution. The particle sizes could be controlled within limits by adjusting the solution flow rate and the ultrasonic spray nozzle features, which in turn would alter the size of the atomized droplets at the top of the furnace.

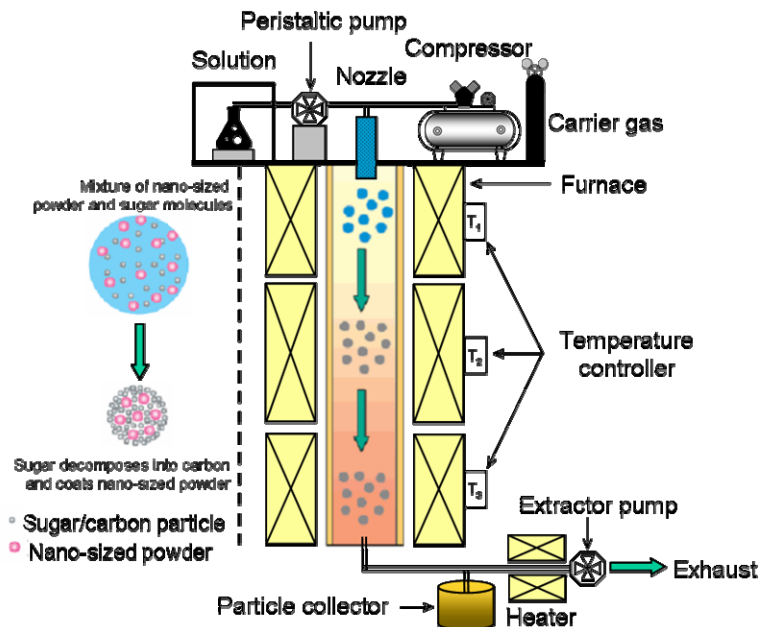


Figure 3.5: Schematic of spray pyrolysis apparatus. The model on the LHS details the mechanism of formation of $\text{Co}_3\text{O}_4\text{-C}$ powders.

3.3. Methods of Characterization

3.3.1. Structure and Morphology

The phase purity and crystal structure of all prepared powders were characterized by the XRD technique using a Philips PW-1730 diffractometer (40 kV, 25 mA) with monochromatized $\text{Cu K}\alpha$ radiation ($\lambda = 1.5418 \text{ \AA}$) at a scan rate of 1° min^{-1} . Crystallite sizes were estimated using the Scherrer^[256] equation:

$$D = \frac{0.9\lambda}{\beta \cos \theta} \quad (3.2)$$

where λ represents the x-ray wavelength, β is the observed full width at half maximum (FWHM), and θ is the Bragg angle. The goniometer was calibrated by performing a test scan on a silicon single crystal plate. All XRD patterns were initially analyzed using the Difftech Traces v6 software package and cross-matched for purity with the international centre for diffraction data (ICDD) database (2003). Many standard XRD patterns were also refined according to the Rietveld method

using the Rietica software package. The morphology of the powders was observed by a SEM (JEOL JSM-6460A) using either a LAB-6 or a tungsten filament, or field emission SEM (JEOL JEM-3000). A thin layer of gold was applied to samples with poor electrical conductivity using a Dynavac Mini Coater sputtering system. Surface element analysis and element mapping techniques were conducted using an EDXS apparatus attached to the above-mentioned SEM. Higher magnification visual observations and x-ray spectroscopy analyses were conducted using a JEOL 2010 TEM. The final stoichiometry of some powders was examined by the inductively coupled plasma (ICP) technique. Pre-test calibration of this equipment was performed using reliable chemical standard solutions.

Some powders were subjected to synchrotron XRD analyses that were conducted at the National Synchrotron Radiation Research Center (NSRRC), Taiwan. The energy storage ring was operated at 1.5 GeV and produced radiation with a wavelength of 0.516606 Å, which was passed through a silicon (111) monochromator. The integrated 1D patterns were processed by the FIT2D program.^[257] The diffraction angles were calibrated according to the NBS 640b silicon standard powder, and Rietveld refinements were carried out on the obtained diffraction data by using the General Structure Analysis System (GSAS) program.^[258]

3.3.2. Particle Surface Area Measurements

The multilayer adsorption theory, giving rise to what is known generally as the Brunauer-Emmett-Teller (BET) equation, has occupied a central position in gas adsorption studies and surface area measurement ever since it was derived in 1938.^[259] This theory assumes that the forces that produce condensation on a surface are chiefly responsible for the binding energy of multilayer adsorption and considers that the first of each layer of adsorbed molecules serves as a site for the adsorption of molecules into the second layer and so on. Using this theory and the BET method of calculation, surface area estimations were made using a Quantachrome NOVA 1000 nitrogen absorption apparatus. Powders were weighed, placed in a PyrexTM chamber and out gassed at 140 °C under inert gas flow for 1 h prior to measurement.

3.3.3. Electrical Conductivity

The measurement of electrical conductivity can give assistance in interpreting electrode behaviours that relate to charge-transfer and overall efficiency. Electrical resistivity was measured using the four probe technique on a Quantum 6000, Physical Properties Measurement System (PPMS). Powders were pelletized and sintered under the unique conditions required for phase formation of the specific material being investigated. The pellets were cut into rectangular shaped rods and polished with sandpaper to remove any surface contamination products. The final size of the prepared samples was approximately $5 \times 2 \times 0.5$ mm. The measurement process involved connecting four thin collinearly positioned copper wires to the sample. Electrical contact points between the wires and samples were made by using silver paste, which was then annealed at an elevated temperature to minimize contact resistance. Current was induced between the outer probes, while voltage was measured between the two inner probes. An electronic signal from the voltage wires was measured by a multimeter, and the sample resistance recorded by a computer *via* an IEEE488 bus interface.

The resistivity of the samples was calculated using Eqn. 3.3:

$$\rho = R \frac{A}{L} \quad (3.3)$$

where R (Ω) is the measured resistance value, A (cm^2) is the cross sectional area, and L (cm) is the distance between the inner voltage contacts. The conductivity of the samples was calculated using the relationship in Eqn. 3.4:

$$\sigma = \frac{1}{\rho} \quad (3.4)$$

3.3.4. Magnetic Measurements

Magnetic measurements are a fundamental tool for the characterization of many types of magnetic materials. The magnetic properties of EDAMM synthesized $\text{SrTi}_{0.5}\text{Co}_{0.5}\text{O}_3$ powders were assessed by plotting molar magnetic susceptibility (χ) versus temperature. Magnetic properties of the samples were measured using a Quantum XL Magnetic Properties Measurement System (MPMS). The dependence of the magnetization of the sample on the temperature under zero magnetic field cooling (ZFC) and applied magnetic field cooling (FC) were measured. The applied magnetic field during FC measurements was set to 1000 Oe. The Curie or Néel points and spin state of the magnetic ions were calculated from the inverse magnetic susceptibility curve ($1/\chi$). The curve was fitted in the 10–300 K temperature range by applying a modified Curie-Weiss law:

$$\chi = \frac{C}{T - \Theta_p} + \chi_0 \quad (3.5)$$

where χ_0 is the temperature independent susceptibility (sum of Pauli, Landau, and core susceptibilities), and Θ_p is the Pauli-Weiss temperature. The χ_0 term is introduced into the Curie-Weiss law to account for free electron susceptibility and diamagnetic susceptibility.

3.3.5. XAFS and XANES

An x-ray is a type of high energy light that can be absorbed by all matter through a process known as the photo-electric effect. This process is represented in Fig. 3.6, where an x-ray photon is absorbed by an electron in a tightly bound quantum core level of an atom. Any electronic core level can participate in the absorption, but only if the binding energy of this core level is less than the energy of the incident x-ray. Energy in excess of the binding energy is transferred to a photo-electron, which is ejected from the atom.

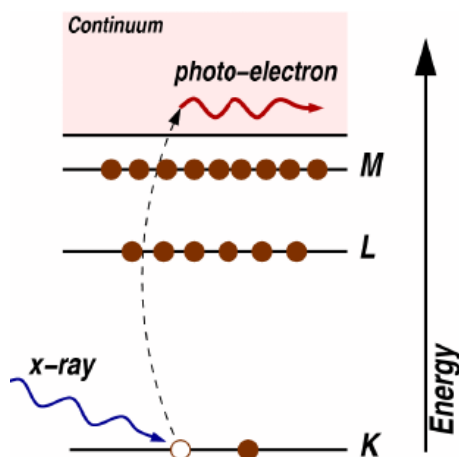


Figure 3.6: *The photoelectric effect.*

When an incident x-ray has energy equal to that of the binding energy of a core level electron, there is a sharp rise in absorption, and a so-called absorption edge can be identified. X-ray absorption techniques aim to determine the absorption coefficient (μ) which describes the probability that x-rays will be absorbed according to Beer's Law:

$$I = I_0 e^{-\mu t} \quad (3.6)$$

where I_0 is the x-ray intensity incident on a sample, t is the sample thickness, and I is the intensity transmitted through the sample. With another atom nearby, the ejected photo-electron can scatter from a neighboring atom and return back to the absorbing atom. The absorption coefficient shows an oscillatory nature and has similar amplitude to the total absorption, which extends over hundreds of electron volts beyond the x-ray absorption edge. This oscillation is known as the x-ray absorption fine structure (XAFS). The XAFS oscillations are an interference effect of the photo-electron with itself, due to the presence of neighboring atoms. Since every atom contains core-level electrons with well-defined binding energies, we can select an element to probe by tuning the x-ray energy to an appropriate absorption edge. The x-ray absorption spectrum can be divided into different regions, with the x-ray absorption near-edge spectroscopy (XANES) region identified within 50 eV of the absorption edge as shown in Fig. 3.7.

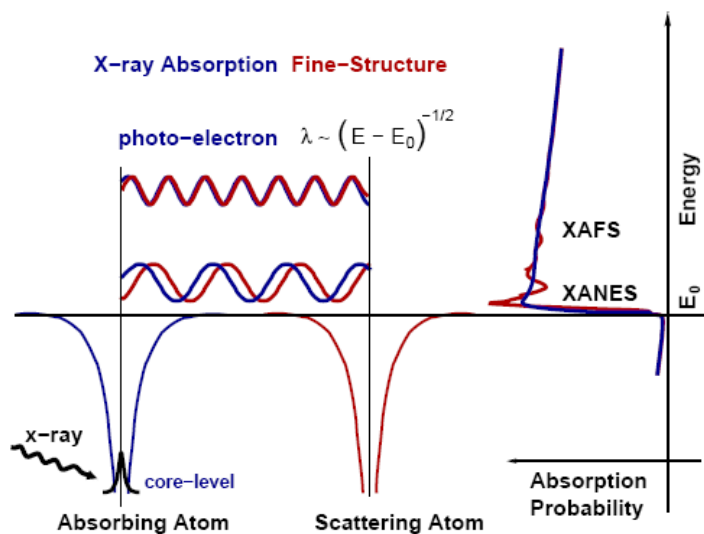


Figure 3.7: The process of photoelectron scattering and identification of the XANES region in the XAS spectrum.

In order for the incident beam to penetrate to the core levels in atomic shells of the atoms, high-intensity and tunable x-ray sources must be used. These are typically available only at synchrotron facilities and produce x-ray radiation on the order of 10^5 to 10^6 times as intense as that of conventional sources.

The oxygen *K*-edge, and vanadium and cobalt *L*-edge XANES measurements were conducted at the NSRRC, Taiwan, using a high-energy spherical grating monochromator (HSGM). XANES spectra were recorded in x-ray fluorescence-yield (FY) and total electron-yield (EY) modes for the oxygen *K*-edge and the transition metal *L*-edge, respectively. The x-ray FY was measured by utilizing a microchannel plate detector system. Photons were incident at an angle of 45° with respect to the sample normal. In the EY mode, the sample drain current was measured. The incident photon flux was monitored simultaneously with x-ray FY and EY by a nickel mesh located after the exit slit of the monochromator. The photon energies were calibrated with an accuracy of 0.1 eV using the known oxygen *K*-edge absorption peaks of a CuO compound. The x-ray FY absorption spectra were normalized to I_0 and subsequently corrected for self-absorption effects. The energy resolution of the monochromator was set to ~ 0.22 eV at the oxygen 1s absorption edge.

3.4. Electrochemical Assessment

3.4.1. Electrode Fabrication and Test Cell Assembly

Electrochemical measurements were conducted by assembly of standard R2032 coin-type test cells. Working electrodes were constructed by mixing 70-85 wt% active powder, 0-15 wt% carbon black, and 8-15 wt% polyvinylidene fluoride (pvdF) in a mortar and pestle. The dry powder mix was blended with N-methylpyrrolidinone (NMP) to make a slurry, which was then spread uniformly on a 1 cm² aluminum or copper substrate current collector. The choice of a material to be used as a current collector relates to its reactivity and surface chemistry. Copper is the preferred substrate to be coated in the preparation of anodes. Although copper does not dissolve electrochemically in non-aqueous lithium salt solutions in the operating potential range (0-3 V), it is reactive in the battery electrolyte solutions.^[260] Specifically, redox reactions between the copper and salt anions form a surface coating that is electrically conducting and can allow electron transfer to the active mass. In the case of cathode materials, aluminium is the substrate material of choice. Despite being thermodynamically unstable at operating voltages > 3 V, aluminium also derives a form of pseudo-stability due to passivation effects afforded by the formation of species such as aluminium fluoride.^[261]

The completed electrodes were dried in a vacuum oven for 12 h at 80 °C, then cold pressed at 300 kg cm⁻² in a uniaxial hydraulic press. All electrodes contained no more than 2 mg of active material and were assembled into a coin cell in a high purity argon-filled glove box where the concentration of H₂O < 5 ppm and O₂ < 10 ppm. Battery grade lithium foil was used as both the counter and reference electrodes. Celgard[®] 2400 (Celgard LLC, USA) was used as a separator membrane after soaking in a 1:1 by volume mixture of ethylene carbonate (EC) and diethyl carbonate (DEC) electrolyte solution. The lithium salt used for the purpose of this research was lithium hexafluorophosphate (LiPF₆) at a concentration of 1 M. Fig. 3.8 shows a schematic of a typical completed coin test cell.

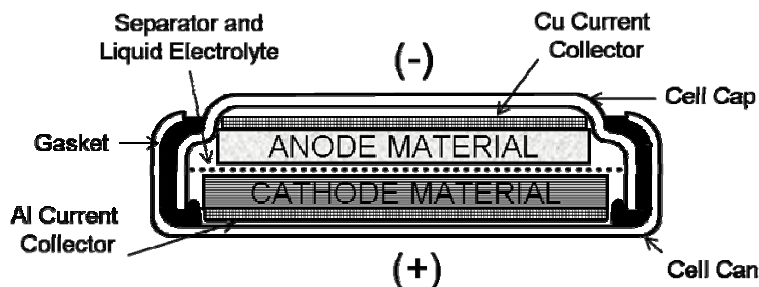


Figure 3.8: Schematic of an assembled R2032 coin-type test cell.

3.4.2. Galvanostatic Charge/Discharge Cycling

Charge/discharge cycles of the coin cells were measured using various voltage cut-offs on a Neware battery test system at a constant current of 0.01-0.2 mA. The rate of charge and discharge was selected depending upon the theoretical capacity of the material under investigation. The theoretical capacity was calculated using the relationship between the number of moles of lithium in the reaction product and the molar mass of the lithium host:

$$\text{Theoretical Capacity} = \frac{Fn}{3.6M} \quad (3.7)$$

where F is Faraday's constant, n is the number of moles of lithium in the reaction product, and M is the molar mass in grams of the lithium host. The C rate is a method of expressing the constant current applied to an electrode in relation to its theoretical capacity. For instance, the theoretical capacity of carbon is 372 mAh g^{-1} , and a discharge current of 74.4 mAh g^{-1} over 5 h is referred to as the C/5 rate ($5 \times 74.4 = 372$). A C/10 rate would be effected by using a discharge current of 37.2 mAh g^{-1} over 10 h. The specific capacity of all cells tested was calculated by considering only the active mass in the electrode, and all electrochemical testing was carried out at ambient temperature ($23 \text{ }^{\circ}\text{C} \pm 2 \text{ }^{\circ}\text{C}$).

3.4.3. Cyclic Voltammetry

Cyclic voltammetry provides a simple method for investigating the reversibility of an electrode reaction, as well as the nature of various electrochemical reactions. Cyclic voltammetry was first reported in 1938 and described theoretically in 1948 by Randles *et al.*^[262] The technique is performed by scanning the voltage between two chosen voltage limits at a known sweep rate (v), and measuring the current response arising from any electron transfer process. The process is repeated for a desired number of cycles. The voltage limits will define the electrode reactions that take place, therefore the starting voltage is preferentially chosen at a value where no electrode reaction will occur and swept towards positive or negative potentials to investigate oxidation or reduction processes, respectively. The resulting current-voltage (I-V) response curves for a simple reversible electrode reaction are characterized by asymmetrical peaks. The reversibility of a reaction closely depends upon the rate of electron transfer being sufficiently high to maintain the surface concentrations close to those demanded by the electrode potential through the Nernst equation. Therefore, when the scan rate is increased, a reversible reaction may be transformed into an irreversible one if the rate of electron transfer is slow in that particular material. Cyclic voltammograms (CV) were obtained in this work by measuring the I-V response at a scan rate of 0.01-0.1 mV s⁻¹ from 0-4.5 V using a CH Instruments model 660A electrochemical workstation. Parameters were optimized within these ranges depending upon the material under investigation.

3.4.4. Electrochemical Impedance Spectroscopy

Electrochemical impedance spectroscopy (EIS) is a powerful technique that can provide instantaneous information concerning polarization resistance, electrode kinetics, and mechanisms of charge transfer, such as oxide growth and metal dissolution. The method involves the analysis of the time taken (τ) for a steady-state system to re-establish equilibrium when it is perturbed by a small applied ac voltage. This relaxation process can be related to the resistance and capacitance of the system by the following equation:

$$\tau = RC \quad (3.8)$$

Within a wide frequency domain, fast processes have a low τ and occur at high frequencies, while slow processes have a high τ and occur at low frequencies. Thus, dipolar properties may be studied at high frequencies, bulk properties at intermediate frequencies and surface properties at low frequencies.^[263] Impedance measurements were performed using a CH Instruments model 660A electrochemical workstation. The obtained spectra were modeled with an equivalent circuit diagram and analyzed using ZviewTM computer software (Version 2.8, Scribner Associates, USA). The program dynamically fits the parameters of the equivalent circuit diagram using the complex nonlinear least squares method. Note that the electrodes used for comparative impedance analyses had a uniform film thickness of 60-70 μm to allow a valid comparison of results.

4. LiM_xCo_{1-x}O₂ Compounds Prepared *via* a Solid-State Method

4.1 Introduction

Lithium cobalt oxide (LiCoO₂) is a layered intercalation compound that has remained the cathode material of choice for rechargeable lithium batteries since it was first commercialized in 1991. The maximum practical capacity of LiCoO₂ is only 140 mAh g⁻¹, despite having a high theoretical capacity of 274 mAh g⁻¹. Attempts to gain additional capacity by increasing the upper cut-off voltage produces a large anisotropic structural change, resulting in unacceptably short cycle life.^[57] Structural change can sometimes be avoided by selective cation doping, which acts to maintain interlayer distance. For this method to be successful, doping must result in a solid solution of LiM_xCo_{1-x}O₂ that is isostructural with LiCoO₂. The most promising dopants are those that can exist as high valence cations, such as 4⁺, 5⁺, and 6⁺.

In this chapter, the solid state synthesis and electrochemical performance of LiM_{0.02}Co_{0.98}O₂, where M = Mg, V, and Mo, is presented. There is currently no literature on the synthesis and electrochemical performance of LiCoO₂ doped with V⁵⁺ and Mo⁶⁺ ions. The selective doping of LiCoO₂ powders produced by an easily scalable solid state process offers the most practical solution to increase the stability and capacity of LiCoO₂.

4.2 Experimental

LiM_{0.02}Co_{0.98}O₂ (M = Mg, V, Mo) powders were prepared in separate experiments using the solid-state method outlined in section 3.2.1. Synchrotron XRD analyses were carried out on the synthesized powders at the NSRRC, Taiwan. Rietveld refinements were carried out on the obtained diffraction data by using the GSAS program.^[258] The oxygen *K*-edge, and vanadium and cobalt *L*-edge XANES measurements were performed on beam line 20A at NSRRC. XANES spectra were recorded in x-ray FY and total EY modes for oxygen *K*-edge and cobalt *L*-edge spectra, respectively. Electrical resistivity was measured by the four probe technique using a PPMS.

Electrochemical measurements were conducted by assembly of standard R2032 coin-type test cells. Working electrodes were constructed by mixing 75 wt% active powder, 15 wt% carbon black, and 10 wt% pvdf in a mortar and pestle. The dry powder mix was blended with NMP to make a slurry, which was then spread uniformly on 1 cm² by 0.1 mm thick aluminum foil substrate to make the electrodes. Charge/discharge cycles of the coin cells were measured from 3.0 V to 4.2 V at 30 mA g⁻¹. Cyclic voltammograms were obtained by measuring the I-V response at a scan rate of 0.02 mV s⁻¹ from 3.0 V to 4.5 V.

4.3 Results and Discussion

4.3.1 Structural and Morphological Characterization

Crystal structures of LiM_{0.02}Co_{0.98}O₂ powders were refined according to the Rietveld method, starting with the atomic coordinates of a single crystal of LiCoO₂.^[264] A comparison between the observed and calculated XRD patterns, as well as the difference curves, are shown in Fig. 4.1a-c.

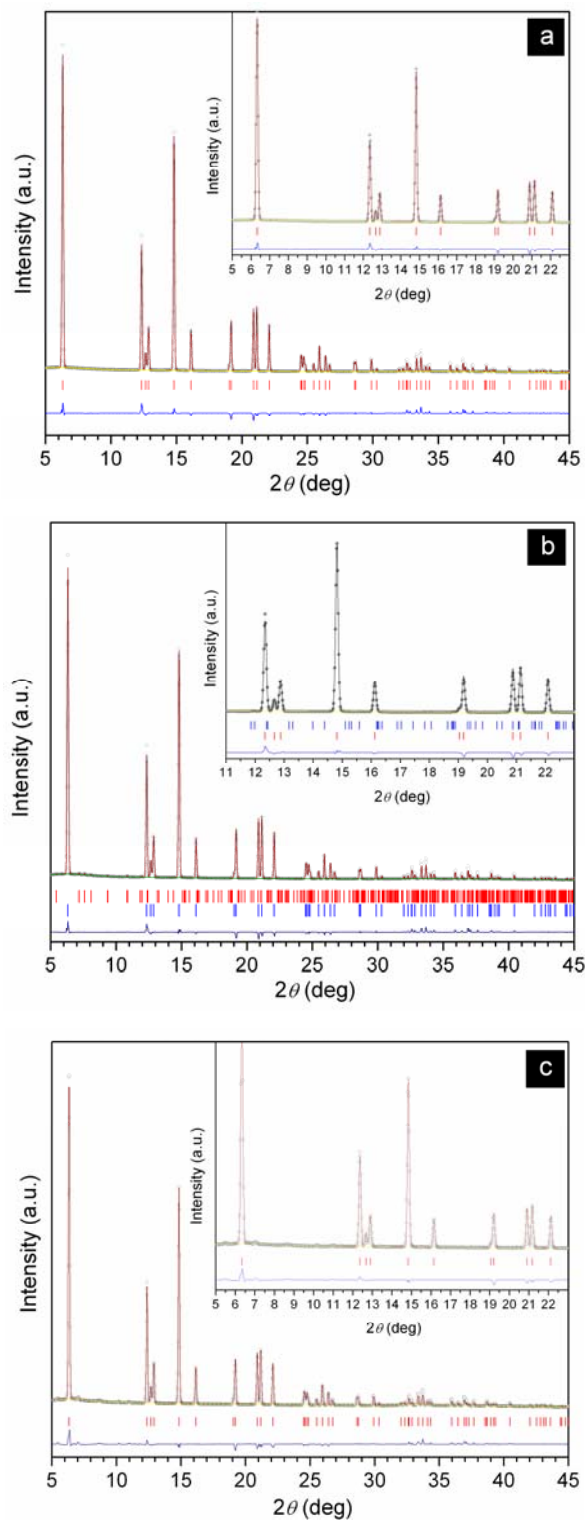


Figure 4.1: Rietveld refinement of synchrotron x-ray diffraction patterns obtained for LiM_{0.02}Co_{0.98}O₂ powders where M = Mg (a), V (b), and Mo (c). Insets show enlargements of specified angular ranges of spectra.

All major peaks are clearly identifiable with those of hex-LiCoO₂, which is isostructural to layered α -NaFeO₂ with a $R\bar{3}m$ space group. In this structure, the constituent cobalt, lithium, and oxygen atoms occupy the 3*a*, 3*b*, and 6*c* Wyckoff sites, respectively. Peak doublets located at $\sim 13^\circ$ [(006)-(102)] and $\sim 21^\circ$ [(108)-(110)] 2θ are well defined and separated in all diffraction patterns. This suggests a dimensionally stable structure with a highly ordered distribution of cations in the lattice.^[265]

Among the doped samples, only the LiMg_{0.02}Co_{0.98}O₂ (Fig. 4.1a) powder was found to be a single phase. Small fractions of lithium orthovanadate and molybdates were detected in the vanadium (Fig. 4.1b) and molybdenum (Fig. 4.1c) doped samples, respectively. The presence of impurity phases in these powders is in agreement with reports by Zou *et al.*^[75, 78, 266] and Tukamoto *et al.*,^[267] which showed that the attempted doping of LiCoO₂ powders with low levels of strontium, antimony, zirconium, indium and yttrium always resulted in samples with small, but detectable amounts of impurity phases when the diffraction data were properly refined.

Values of the refined parameters from the Rietveld analysis are given in Table 4.1 for all compositions. The Li₃VO₄ phase present in the V-doped powder was included in the Rietveld procedure, which involved refinement of the fraction factor, lattice, and profile parameters. The site occupation factors for oxygen atoms were also refined. The χ^2 , R_p (profile), and R_{wp} (weighted pattern) factors are included in Table 4.1, indicating the quality of the Rietveld refinements.

Table 4.1: Structural parameters of LiM_{0.02}Co_{0.98}O₂ (*M* = Mg, V, Mo) samples based on Rietveld refinement of synchrotron radiation ($\lambda = 0.516606 \text{ \AA}$) x-ray diffraction patterns measured at 300 K. Lithium, cobalt, and oxygen atoms occupy the (0, 0, 0), (0, 0, 0.5) and (0, 0, *z*) positions, respectively.

Parameter	Magnesium	Vanadium	Molybdenum
Composition	LiCoO ₂	LiCoO ₂ ; Li ₃ VO ₄	LiCoO ₂ ; lithium molybdates
<i>a</i> , Å	2.8159(3)	2.8159(3)	2.8136(3)
<i>c</i> , Å	14.0560(2)	14.0551(2)	14.0487(3)
<i>c/a</i> ratio	4.992	4.991	4.993
<i>V</i> , Å ³	96.525(2)	96.518(2)	96.315(2)
<i>z</i> (O)	0.2394(12)	0.2392(13)	0.2385(1)
Oxygen occupancy	0.965(6)	0.962(6)	0.975(6)
R _{wp} , %	7.48	7.58	6.68
R _p , %	4.65	4.75	4.52
χ^2	0.9532	1.011	0.9404

For the Mg-, V-, and Mo-doped powders, $R_p = 7.48, 7.58, 6.68$ and $R_{wp} = 4.65, 4.75, 4.52$, respectively. These low R factor values verify that there is good agreement between experimental and calculated XRD patterns. From Table 4.1, it should also be noted that another marker of the degree of cation order/disorder and the metal-metal layer distance can be discerned from the *c/a* ratio. The *c/a* ratio should generally be higher than 4.899 to avoid a face centered unit cell (*Fd3m*) that has a cation disordered spinel structure.^[42] For the Mg-, V-, and Mo-doped powders, the *c/a* ratio is 4.992, 4.991, and 4.993, respectively. These data support the visual observation of diffraction peak doublet separation and the presence of a well-ordered structure. However, it is recommended that the *c/a* ratio should not be used alone as a definitive measure of cation disorder, but rather as an indicator.

The crystal lattice parameters were $a = 2.8159(3), 2.8159(3), 2.8136(3)$ and $c = 14.0560(2), 14.0551(2), 14.0487(3)$ for the Mg-, V-, and Mo-doped LiCoO₂ powders, respectively. The calculated crystal lattice parameters of the hexagonal unit cell show only small differences between dopants and are in a good agreement with data published for pure LiCoO₂ powders.^[54] This may be explained by the low level of doping (2 mol%) and the presence of impurity phases, which further dilutes the

effect of doping on the lattice parameter, since less dopant ions replace Co³⁺ in 3a sites within the structure. The Mg-doped powder gives the largest *a* and *c* parameters due to the complete substitution of the larger ionic radii of Mg²⁺ (0.72 Å) for Co³⁺ (0.545 Å - low spin state) in the LiCoO₂ crystal structure. This effect provides a dominant force for the expansion of the unit cell parameters, despite the drive for a contraction of unit cell parameters caused by the shortening of Co-O bonds through oxidation of Co³⁺ to Co⁴⁺ and hole formation. Note that the latter effect represents a charge balance mechanism that results in a mixed 3⁺/4⁺ valence state of cobalt. Given that hole formation occurs by doping LiCoO₂ (*p*-type semiconductor) with magnesium ions, it follows that doping in this case should also increase the electronic conductivity of the material. However, this was not observed and will be discussed later.

In the case of the V-doped powder, confirmation of the oxidation state was achieved from the *L*-edge XAS spectrum of LiV_{0.02}Co_{0.98}O₂ and the vanadium oxide standards shown in Fig. 4.2. This spectrum corresponds to vanadium atoms in a pentavalent state and is in a good agreement with the XRD data, where lithium vanadate was detected as a vanadium containing phase.

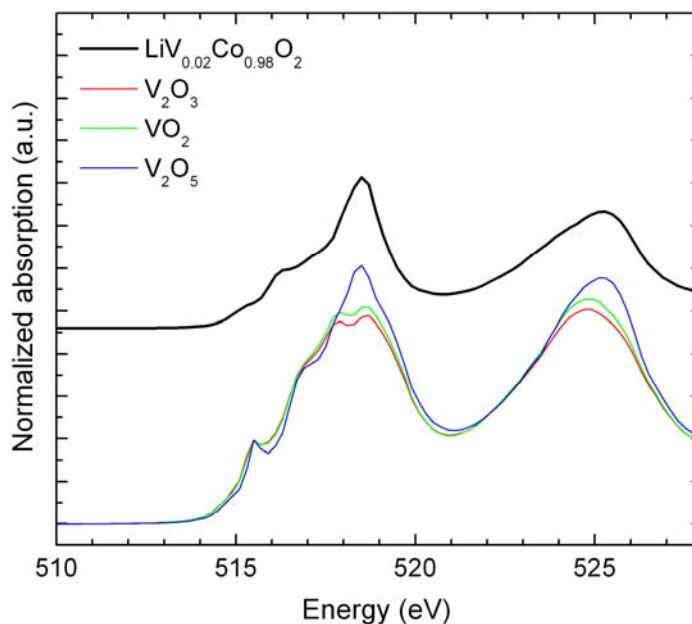
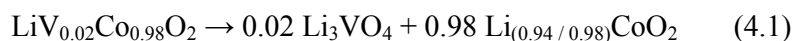


Figure 4.2: Vanadium *L*-edge XAS spectra of LiV_{0.02}Co_{0.98}O₂ and selected standards.

Jin *et al.*¹³ have linked the presence of vanadate secondary phases to improved electrochemical performance of LiCoO₂-based electrodes. In that report, commercial LiCoO₂ powders with the surface modified by Li₃VO₄ nanoparticles show enhanced electrochemical properties, particularly capacity retention, at the 1C rate. It is suggested that a Li₃VO₄ coating on the surface of the LiCoO₂ particles suppresses the reaction between the Co⁴⁺ and the electrolyte. In the present case, it is not expected that the secondary Li₃VO₄ phase would exist as a continuous coating on the surface of the LiCoO₂ particles, and therefore it would not provide any barrier effect. Regardless, the formation of Li₃VO₄ could proceed according to the reaction shown in Eqn. 4.1 and would lead to a lithium deficient LiCoO₂ structure:



The formation of lithium molybdates would occur in the same way and also result in a lithium deficient LiCoO₂. Powders with lithium-containing secondary phases should have smaller lithium concentrations and therefore a higher cobalt oxidation state when compared to the Mg-doped powder. Furthermore, it is possible that the smaller unit cell volume of Mo-doped (96.315 Å³) compared with those of the V- (96.518 Å³) and Mg- (96.525 Å³) doped powders is due to a slightly larger lithium non-stoichiometry caused by the precipitation of lithium molybdates.

Fig. 4.3 shows the cobalt *L*-edge XAS spectra of LiM_{0.02}Co_{0.98}O₂ compounds together with cobalt oxides and commercial LiCoO₂ (Aldrich) powder for comparison. Two peaks marked as L_{III} and L_{II} correspond to cobalt 2p_{3/2} and 2p_{1/2} core electron transitions to the unoccupied 3d level highly hybridized with oxygen 2p orbitals, respectively. Cobalt 2p-3d interaction and crystal field effects additionally split these peaks. In general, the spectra of LiM_{0.02}Co_{0.98}O₂ correspond to cobalt ions in a trivalent Co³⁺ low-spin state and are very similar to those of bulk^[268] and thin film^[269] LiCoO₂ reported by other groups.

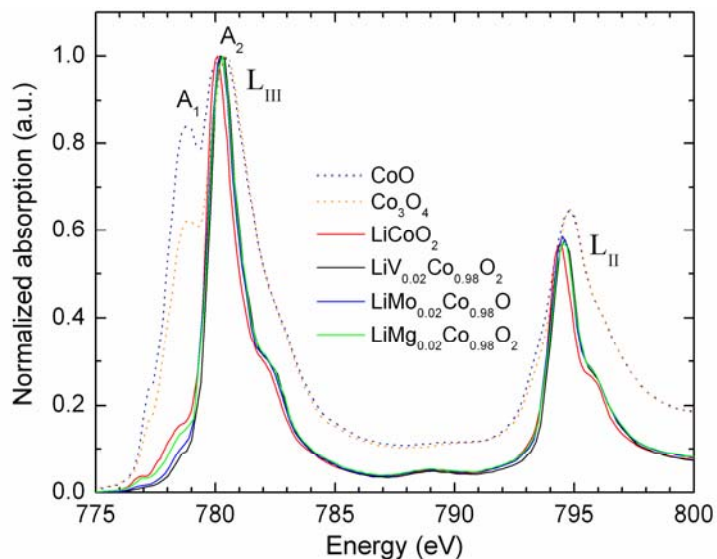


Figure 4.3: Cobalt *L*-edge XAS spectra of LiM_{0.02}Co_{0.98}O₂ and selected standards.

It was shown by Montoro *et al.*^[268] that cobalt atoms remain almost unaffected by the lithium deintercalation because of high stability of the Co³⁺ low-spin state. Instead of Co³⁺ oxidation during battery charging, charge compensation is achieved by rehybridization of Co-O orbitals (*i.e.*, oxygen oxidation). Thus, cobalt *L*-edge spectra demonstrate very little change with lithium ion deintercalation or other crystal defects which may alter the cobalt valence. However, it is noteworthy that as the cobalt oxidation state increases from 2⁺ in CoO to 3⁺ in LiCoO₂, the corresponding ratio between the A₁ and A₂ peaks decreases (Fig. 4.3). If one uses this ratio as a marker of cobalt valence, all the doped samples have cobalt atoms in a higher oxidation state in comparison with commercial LiCoO₂. Among them, cobalt is the most oxidized in LiV_{0.02}Co_{0.98}O₂ (*i.e.*, more Co⁴⁺ ions). The Co⁴⁺ ion is a well-known Jahn-Teller ion that causes spontaneous deformation in CoO₆ octahedra, which then disrupts the intercalation framework and reduces capacity. This interpretation suggests a destabilization of the layered structure in the LiV_{0.02}Co_{0.98}O₂ powder in particular and inferior electrochemical performance during cycling of the test cell.

Oxygen *K*-edge XANES spectra of LiM_{0.02}Co_{0.98}O₂ powders are shown in Figure 4.4. The two peaks at ~531 eV and 536-545 eV correspond to the oxygen 2p character mixed in the cobalt 3d and 4sp bands, respectively.^[270] The absorption intensity of the transition is proportional to the oxygen 2p hole concentration in the conduction band.^[79] The most remarkable feature of the LiM_{0.02}Co_{0.98}O₂ spectra is that the

oxygen 1s → oxygen 2p/cobalt 3d transition increases absorption intensity as we move from the commercial LiCoO₂ → Mg- → Mo- → V- doped powders. A higher absorption intensity indicates an increased oxygen 2p hole concentration, which correlates with the observed change in the cobalt oxidation state that was discussed earlier.

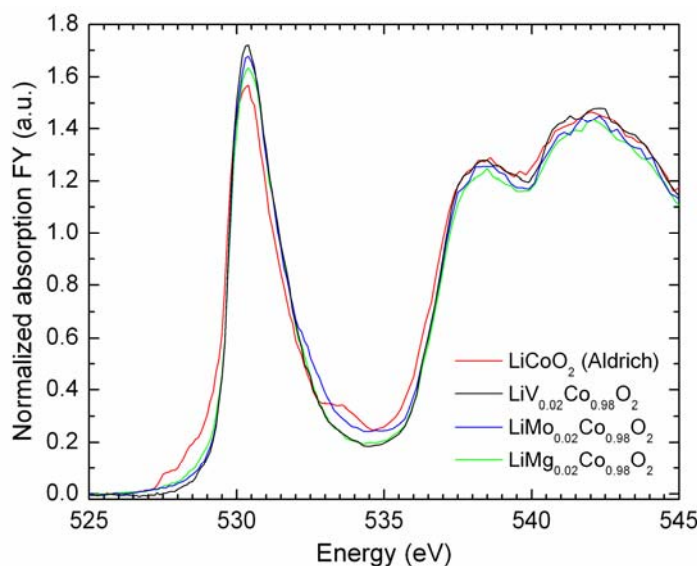


Figure 4.4: Oxygen *K*-edge XANES spectra of LiM_{0.02}Co_{0.98}O₂ and reference LiCoO₂ powders.

Fig. 4.5 shows the electrical conductivity of the powders measured from 290-300 K. The conductivity of the V-doped powder was essentially unchanged from the LiCoO₂ reference powder prepared under identical conditions. Conductivity was shown to decrease by an order of magnitude in Mg-doped powder and three orders of magnitude in the Mo-doped powder. The fact that the V-doped powder has the highest conductivity of all the dopants tested supports the high oxygen 2p hole concentration result determined by oxygen *K*-edge XANES measurements. It should be emphasized however, that although the hole concentration is higher in the V-doped powder, the conductivity does not improve above that of un-doped LiCoO₂.

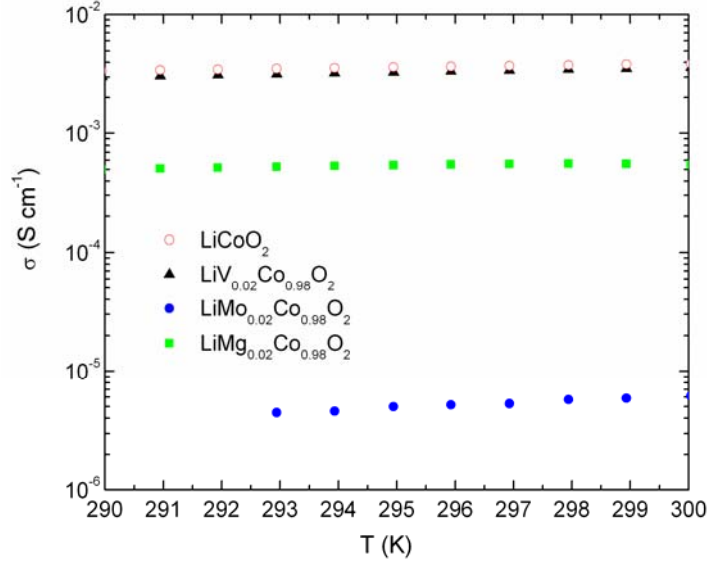


Figure 4.5: Electrical conductivity measurements of LiM_{0.02}Co_{0.98}O₂ pelletized powders.

In regard to the conductivity of the Mg-doped powder, work by Tukamoto *et al.*^[267] proposes that lower than expected conductivity could be related to the formation of a defective, lithium deficient structure during processing. It is well known that even nominally pure LiCoO₂ predominantly contains Co³⁺, with some Co⁴⁺ ions. A small quantity of lithium is usually volatilized during synthesis, so the most likely mechanism of charge compensation is by vacancy formation in the lithium sublattice, as shown in Eqn. 4.2. Low concentrations of Mg²⁺ added to the defective structure will result in a decrease in the concentration of Co⁴⁺ caused by Mg²⁺ substituting directly into lithium vacancies, as shown in Eqn. 4.3. On the other hand, dramatic improvements in conductivity have been shown by adding a higher concentration of Mg²⁺ ions, where simple charge balance demands the formation of more *p*-type current carrying holes.



To put these measurements into proper perspective, although the Mo-doped powder recorded the lowest conductivity of the dopant series (~10⁻⁵ S cm⁻¹), the value still easily exceeds that of the next generation olivine type LiFePO₄ (~10⁻¹⁰ S cm⁻¹) and is

of the same order of magnitude as LiMn₂O₄ cathode alternatives. Any loss in conductivity by doping was compensated by the addition of carbon black during electrode preparation procedure.

4.3.2 Electrochemical Properties

Cyclic voltammograms of the LiM_{0.02}Co_{0.98}O₂ cells in the second cycle are shown in Fig. 4.6. The primary oxidation (4.05-4.15 V) and reduction peaks (3.75-3.85 V) represent lithium deintercalation and intercalation into the active host respectively, and are characteristic of hexagonal phase in these layered compounds. An additional secondary peak situated roughly at 4.1 V can also be clearly seen during reduction in each curve, except for the curve for the Mg-doped sample. The presence of this peak has been previously reported,^[271] and corresponds to the well known hexagonal-monoclinic crystallographic phase transformation occurring at $x = 0.5$ in Li_xCoO₂. Overall, observed features are in good agreement with the I-V behavior reported in the literature^[272, 273] and indicate that the charge/discharge process occurs in a reversible manner from 3.0 V to 4.5 V.

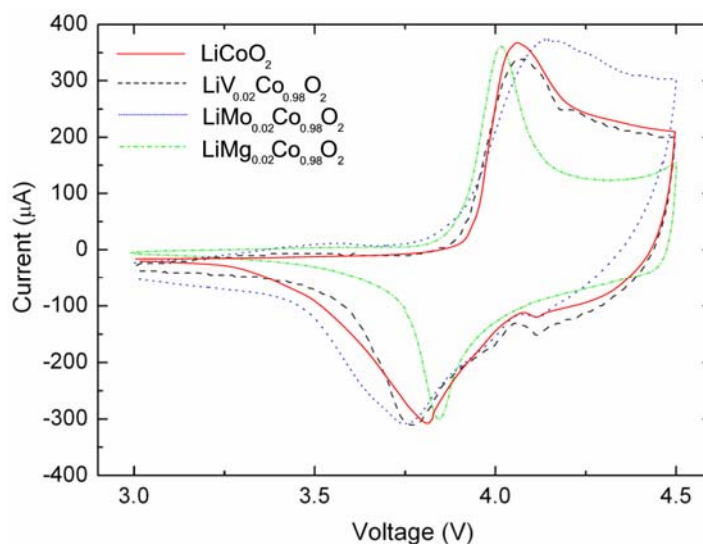


Figure 4.6: Cyclic voltammograms of LiM_{0.02}Co_{0.98}O₂ cells measured from 3.0 V to 4.5 V at a scan rate of 0.02 mV s⁻¹.

The electrochemical performance of coin cells was evaluated by galvanostatic cycling from 3 V to 4.2 V at 30 mA g⁻¹ over 30 cycles, as shown in Fig. 4.7. Cells exhibited an open circuit voltage (OCV) between 2.7 V and 3.2 V. All cells exhibit a high first charge in the range of 160 mAh g⁻¹, with the extent of the irreversible capacity loss between the first charge and first discharge highly dependent upon the type of metal ion dopant. The order of increasing irreversible capacity loss was Mg (20 mAh g⁻¹), Mo (22 mAh g⁻¹), and V (45 mAh g⁻¹). The rate of capacity fade over 30 cycles was also extremely varied between the metal dopants, but at the concentrations investigated, no dopant produced a superior electrochemical performance to that of the reference LiCoO₂. Cycling the V-doped cell led to rapid capacity fading and total failure in less than 15 cycles. The poor electrochemical performance of the V-doped electrode is due to the high concentration of Co⁴⁺ ions acting to disrupt the intercalation framework. The Mo-doped electrode produced the best electrochemical performance of all the doped samples due to a lower concentration of Co⁴⁺ ions and a possible structural stabilization effect produced by precipitation of lithium molybdates.

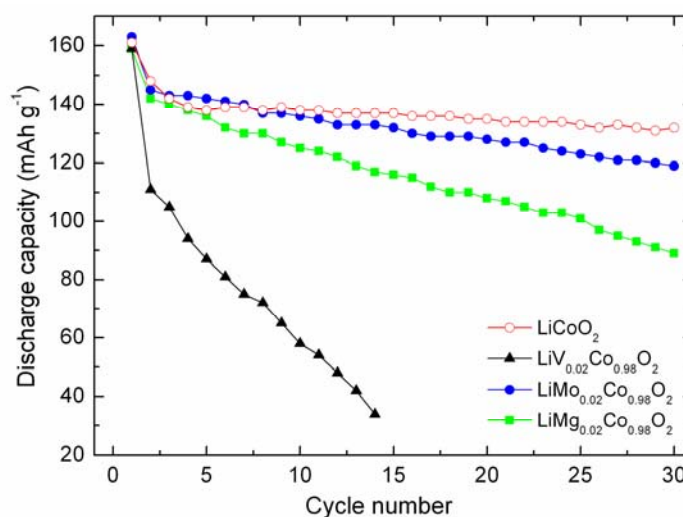


Figure 4.7: Discharge capacity of LiM_{0.02}Co_{0.98}O₂ electrodes cycled from 3.0 V to 4.2 V at 30 mA g⁻¹.

4.4 Summary

The structural and electrochemical properties of LiM_{0.02}Co_{0.98}O₂ (M = Mg, V, Mo) cathode materials synthesized by a solid-state process have been investigated. Rietveld refinement confirmed that a pure phase Mg-doped LiCoO₂ powder was formed, while small fractions of lithium orthovanadate and molybdates were detected in V- and Mo-doped powders, respectively. The electronic conductivity decreased by an order of magnitude and three orders of magnitude in the Mg- and Mo-doped powders, respectively, when compared to un-doped LiCoO₂. This was due to the formation of a lithium deficient structure (lost primarily *via* lithium volatilization, but also to secondary phases in the V- and Mo-doped materials) in which a proportion of dopant ions substituted directly into lithium vacancies, rather than contributing to the formation of charge carrying holes. A higher concentration of the Jahn-Teller Co⁴⁺ ion in the V-doped powder was detected by cobalt 2p XAS spectra and resulted in a disrupted intercalation framework and poor electrochemical performance. The Mo-doped powder recorded the best electrochemical performance among the doped powders (~120 mAh g⁻¹ after 30 cycles) due to a lower concentration of Co⁴⁺ and a possible structural stabilization effect produced by the precipitation of lithium molybdates.

5. The Effect of Titanium Doping on LiFePO₄ Prepared *via* a Sol-Gel Method

5.1 Introduction

LiFePO₄ has an olivine structure in which lithium, iron, and phosphorous atoms occupy octahedral 4a, octahedral 4c, and tetrahedral 4c sites, respectively. The oxygen atoms are in a slightly distorted, hexagonal close-packed arrangement. The FeO₆ octahedra share common corners in the *bc* plane and the LiO₆ octahedra form an edge sharing chain in the *b*-direction. The separation of the FeO₆ octahedra by PO₄ polyanions significantly reduces the electrical conductivity of materials, leading to poor rate capacity and low utilisation of lithium in the LiFePO₄ host structure.

Chung *et al.*^[113] first reported that the electronic conductivity of LiFePO₄ could be significantly increased by low-level aliovalent cation doping. Subsequent reports postulated that the source of the conductivity improvements was impurity phases located at grain boundaries.^[119, 122] Further evidence of the formation of impurity phases was presented by Islam *et al.*^[123] in a study on various dopants that had charges ranging from 2⁺ to 5⁺. In this study it was calculated that, on energetic grounds, the LiFePO₄ structure should be intolerant of high valence doping (*i.e.*, Al, Ga, Zr, Ti, Nb, and Ta) at either the lithium or iron octahedral sites. Several other authors^[125, 126] have reported that only divalent cations at low concentrations can be practically doped into the LiFePO₄ structure.

The aim of this work was to:

- a) determine whether cations with a valence higher than 2⁺ (*i.e.*, Ti³⁺) can be doped into the LiFePO₄ structure using the sol-gel method;
- b) assess any changes in the electronic conductivity of the powders using x-ray absorption spectroscopy techniques; and
- c) evaluate the electrochemical performance of the sol-gel synthesized LiFePO₄ and LiTi_{0.01}Fe_{0.99}PO₄ powders.

5.2 Experimental

LiFePO_4 and $\text{LiTi}_{0.01}\text{Fe}_{0.99}\text{PO}_4$ were synthesized *via* the sol-gel preparation route described in section 3.2.2. Synchrotron XRD was performed on the prepared compounds to determine phase purity. Rietveld refinements were carried out on the obtained diffraction data by using the GSAS program. The morphology of the LiFePO_4 powders was studied using a field emission TEM (JEOL JEM-3000F).

The synchrotron x-ray absorption experiments were carried out at the NSRRC in Taiwan. The iron *K*-edge XANES spectra were collected at the BL17C Wiggler beamline. A silicon (111) double-crystal monochromator was used for energy selection with a resolution ($\Delta E/E$) of about 2×10^{-4} . The XANES spectra at the iron *K*-edge were recorded at room temperature in transmission mode using gas-filled ionization chambers to measure the intensities of the incident (I_0), transmitted (I_t), and reference (I_{ref}) signals. A 7 μm thick iron foil was used as a reference. Both the iron foil and the I_{ref} detector were positioned downstream from the *in-situ* cell along the x-ray beam direction. The data from 3 scans were averaged, and the background was subtracted. The XANES spectra were normalized with respect to the edge jump step.

The oxygen 1s XANES measurements were performed on the high-energy spherical grating monochromator (HSGM) beamline. The oxygen *K*-edge XANES spectra were recorded in x-ray FY and EY mode. The x-ray FY was measured by utilizing a microchannel-plate (MCP) detector system. Photons were incident at an angle of 45° with respect to the sample normal. In the EY mode, the sample drain current is measured. Simultaneously with the x-ray FY and EY, the incident photon flux was monitored by a nickel mesh located after the exit slit of the monochromator. The photon energies were calibrated with an accuracy of 0.1 eV using the known oxygen *K*-edge absorption peaks of a CuO compound. The x-ray FY absorption spectra were normalized to I_0 and subsequently corrected for self-absorption effects. The energy resolution of the monochromator was set to ~ 0.22 eV at the oxygen 1s absorption edge.

Electrochemical characterization was performed by assembling standard R2032 coin-type test cells. The electrodes were made by dispersing 80 wt% active material, 10 wt% carbon black and 10 wt% pvdF in NMP to form a slurry that was coated onto aluminium foil. Cyclic voltammetry measurements were performed at a scanning rate of 0.1 mV s^{-1} . The cells were galvanostatically charged and discharged at the C/8 rate from 2.75 V to 4.3 V.

5.3 Results and Discussion

5.3.1 Structural and Morphological Characterization

General XRD patterns of LiFePO_4 and $\text{LiTi}_{0.01}\text{Fe}_{0.99}\text{PO}_4$ powders are shown in Fig. 5.1. All diffraction lines of LiFePO_4 are indexed to the orthorhombic crystal structure with the $Pnma$ space group. The titanium doped sample contains Li_3PO_4 and Fe_3P impurity phases, which are commonly reported as impurities in aliovalent doped LiFePO_4 powders.^[119]

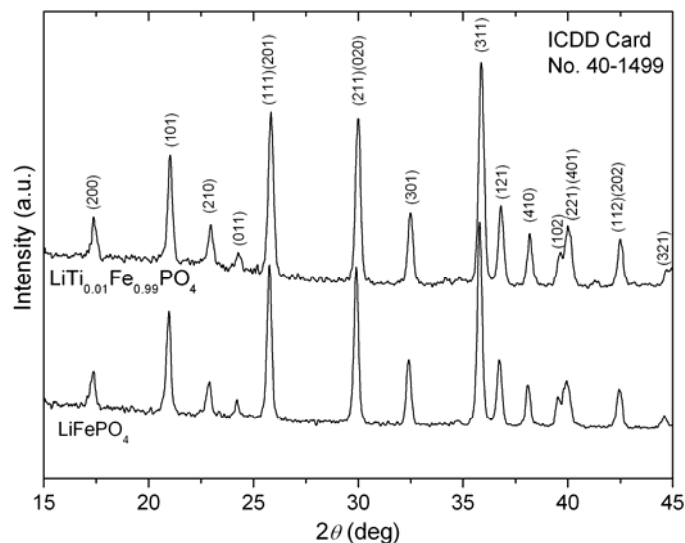


Figure 5.1: X-ray diffraction patterns of LiFePO_4 and $\text{LiTi}_{0.01}\text{Fe}_{0.99}\text{PO}_4$ powders.

Synchrotron XRD patterns for LiFePO_4 and $\text{LiTi}_{0.01}\text{Fe}_{0.99}\text{PO}_4$ powders were obtained and refined according to the Rietveld method to obtain detailed structural parameters. The XRD pattern for the titanium doped powder is shown in Fig. 5.2. The impurity phases, Li_3PO_4 and Fe_3P , were included in the refinement. A strong preferred

orientation of the [211] reflection was observed in the Fe₃P phase and was accounted for during the refinement.

The structural characteristics of LiFePO₄ and LiFe_{0.99}Ti_{0.01}PO₄ are summarized in Table 5.1 and Table 5.2, respectively. Titanium could not be included in the refinement process for LiFe_{0.99}Ti_{0.01}PO₄ due to the low levels present in the powder. LiFePO₄ had the following lattice parameters: $a = 10.3148(1) \text{ \AA}$, $b = 6.0009(7) \text{ \AA}$, $c = 4.6897(5) \text{ \AA}$, and $V = 290.28(5) \text{ \AA}^3$; while LiTi_{0.01}Fe_{0.99}PO₄ had the lattice parameters: $a = 10.3233(2) \text{ \AA}$, $b = 6.00313(8) \text{ \AA}$, $c = 4.69694(7) \text{ \AA}$, and $V = 291.077(7) \text{ \AA}^3$. These values indicate that the unit cell of LiTi_{0.01}Fe_{0.99}PO₄ was slightly expanded along all the directions, x, y, and z, and confirm that the titanium ions were accepted into the LiFePO₄ lattice. Further evidence of successful doping is given by the iron site occupancy of LiFe_{0.99}Ti_{0.01}PO₄ (0.984) which is close to the stoichiometric index of iron in the chemical formula.

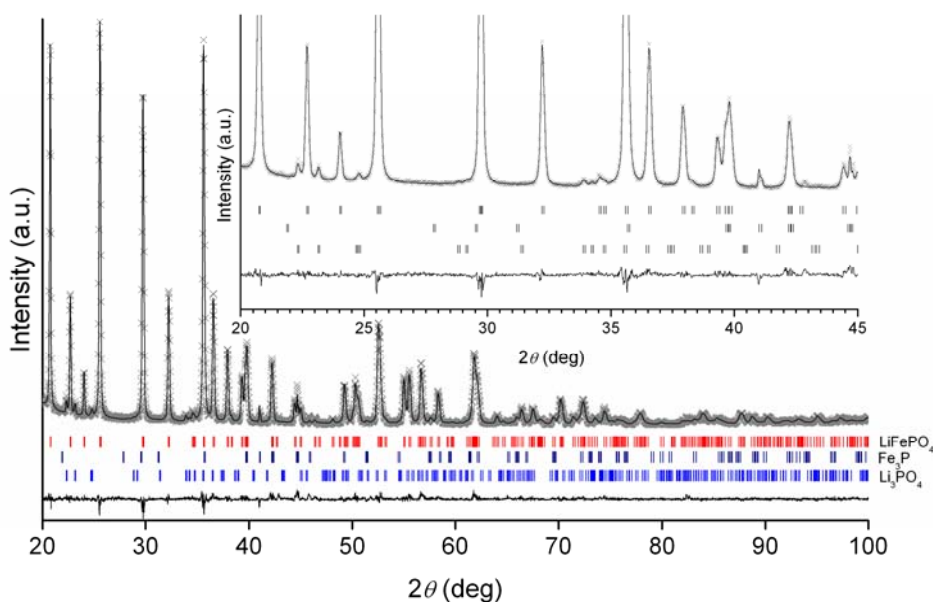


Figure 5.2: Synchrotron x-ray diffraction pattern and Rietveld refinement of LiTi_{0.01}Fe_{0.99}PO₄ powder. The inset shows an enlargement of the 20 - 45° range.

The calculated average Fe-O distances for LiFePO₄ and LiTi_{0.01}Fe_{0.99}PO₄ were 2.155 Å and 2.132 Å, respectively. Doping of low levels of titanium into the LiFePO₄ structure clearly has little effect on the Fe-O bond length and similarly would not be expected to significantly alter the OCV of the material. This is because the OCV of

the material is primarily determined by the PO₄³⁻ polyanion and can be understood by considering the interaction of the constituent atoms in the structure. In the olivine arrangement, the iron ions are located at the center of a distorted FeO₆ octahedron, and each octahedron is connected to four other FeO₆ octahedra and four PO₄ tetrahedra. The phosphorous ions share a common oxygen with iron along a Fe-O-P linkage. Therefore, the strength of the covalent Fe-O bond is weakened *via* the inductive effect of the Fe-O-P bond and the electrostatic repulsion between iron and phosphorus. This induces a higher OCV of the Fe²⁺/Fe³⁺ redox pair with respect to the Fermi level of lithium.

Table 5.1: Structural parameters of LiFePO₄ determined by XRD at 300 K.

Atom	<i>x</i>	<i>y</i>	<i>z</i>	Occupancy	Atomic Distances
Li	0	0	0	1	
Fe	0.2823(2)	0.25	0.9740(5)	1	Fe-O (ave.) 2.155 Å
P	0.0955(3)	0.25	0.4221(8)	1	P-O (ave.) 1.562 Å
O(1)	0.0924(1)	0.25	0.7445(2)	1	
O(2)	0.4542(2)	0.25	0.2170(2)	1	
O(3)	0.1677(9)	0.0467(1)	0.2836(1)	1	
Reliability factors: R _p = 4.88 %, R _{wp} = 6.55 %, χ ² = 0.63					
Cell volume: 290.28(5) Å ³					
Space group: <i>pnma</i> (orthorhombic)					
Unit cell: <i>a</i> = 10.3148(1) Å, <i>b</i> = 6.0009(7) Å, <i>c</i> = 4.4897(5) Å					

Table 5.2: Structural parameters of LiTi_{0.01}Fe_{0.99}PO₄ determined by XRD at 300 K.

Atom	<i>x</i>	<i>y</i>	<i>z</i>	Occupancy	Atomic Distances
Li	0	0	0	1	
Fe	0.2820(9)	0.25	0.9763(3)	0.984(1)	Fe-O (ave.) 2.1316 Å
P	0.0955(3)	0.25	0.4179(4)	1	P-O (ave.) 1.5663 Å
O(1)	0.1000(4)	0.25	0.7443(7)	1	
O(2)	0.4537(5)	0.25	0.2035(7)	1	
O(3)	0.1696(5)	0.0452(5)	0.2829(5)	1	
Reliability factors: R _p = 5.02 %, R _{wp} = 6.97 %, χ ² = 0.471					
Cell volume: 291.077(7) Å ³					
Space group: <i>pnma</i> (orthorhombic)					
Unit cell: <i>a</i> = 10.3233(2) Å, <i>b</i> = 6.00313(8) Å, <i>c</i> = 4.69694(7) Å					

Fig. 5.3a shows a typical TEM image of nanosized powder particles that were produced by the sol-gel method, and Fig. 5.3b shows the carbon coating (3–4 wt%) on the surface of these particles, formed due to the decomposition of organic precursors. The sol-gel method is often the technique of choice when atomic scale mixing of precursor ions is required. Therefore, the Ti^{4+} dopant ions and Li^+ , Fe^{2+} , and PO_4^{3-} ions should be distributed homogeneously in the LiFePO_4 crystal lattice.

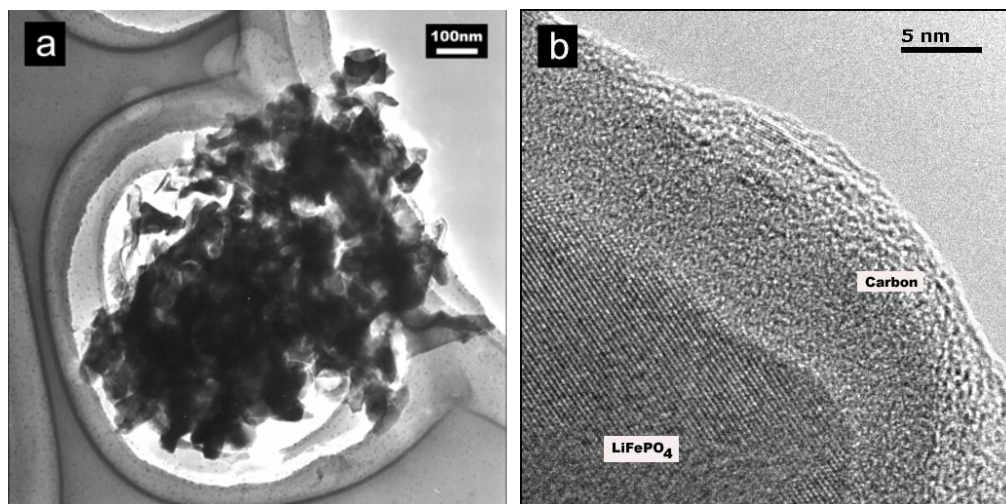


Figure 5.3: TEM image of LiFePO_4 powder (a) and a high resolution TEM image of carbon coated on the surface of individual nanocrystals (b).

Fig. 5.4 shows a comparison of the iron K -edge XANES spectra of LiFePO_4 and $\text{LiTi}_{0.01}\text{Fe}_{0.99}\text{PO}_4$ powders. The spectra feature the pre-edge and the main edge absorption peaks. The main absorption edge, also known as the white line, is the large peak located at 7127 eV for the LiFePO_4 and $\text{LiTi}_{0.01}\text{Fe}_{0.99}\text{PO}_4$ powders. As shown in the inset of Fig. 5.4, the white line of $\text{LiTi}_{0.01}\text{Fe}_{0.99}\text{PO}_4$ is more intense than that of un-doped LiFePO_4 . The increased white line intensity reflects a higher number of unoccupied d-states for iron ions in the surface layer of $\text{LiTi}_{0.01}\text{Fe}_{0.99}\text{PO}_4$ particles.^[274, 275] The 3d and 4s orbits are all empty in Ti^{4+} ions. There are four valence electrons in the t_{2g} orbital of Fe^{2+} ions with octahedral symmetry. Therefore, when Ti^{4+} is substituted for Fe^{2+} , Ti^{4+} ions would attract 3d electrons from Fe^{2+} , creating positive holes in the 3d states in Fe^{2+} ions. This overall effect would induce increased p -type conductivity. Chung et al.^[113] have previously reported that

aliovalent doping of LiFePO₄ results in extrinsic *p*-type semiconductivity, which supports the conclusion from the iron *K*-edge XANES measurement.

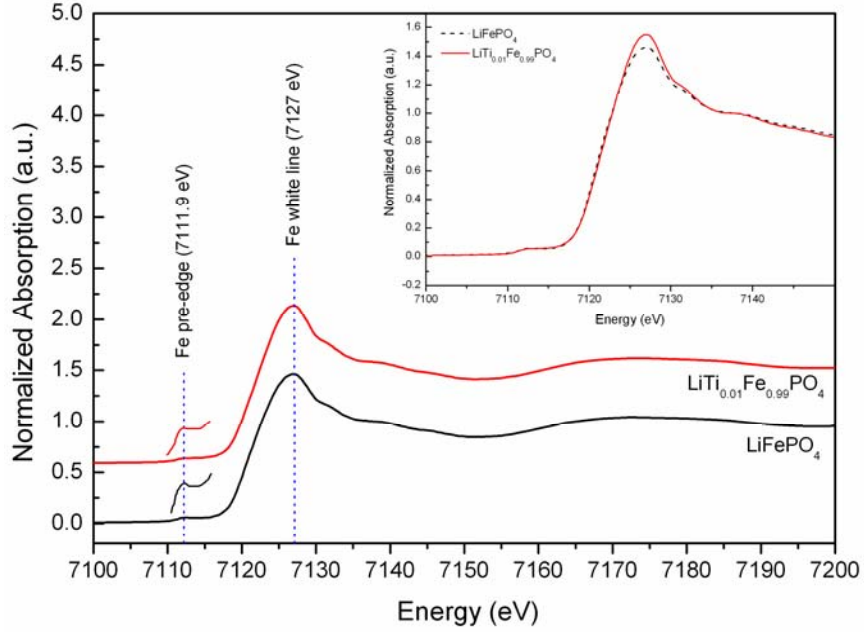


Figure 5.4: Individual iron *K*-edge XANES spectra of LiFePO₄ and LiTi_{0.01}Fe_{0.99}PO₄ powders showing the main absorption edge (known as the white line, although indicated in blue) at 7127 eV and the pre-edge peaks at ~7112 eV. The inset shows a comparison of the white line intensities of same two spectra.

By considering that titanium has been substituted into iron sites in the olivine structure, charge compensation can be achieved *via* vacancy formation in either the iron or lithium sublattices. Using Kroger-Vink defect notation this can be illustrated as follows:



Neither of these two mechanisms can give rise to enhanced charge carrier concentration or explain the increase in hole concentration on the surface of LiFePO₄ particles. However, it is thought that the second mechanism of charge compensation is the more likely, as it would lead to an increase in lithium ion mobility in the

structure, improving the electrochemical performance with only a small sacrifice in the overall capacity due to a decrease in the lithium ion content per formula unit.

The strong preferred orientation of the impurity Fe₃P phase present in LiTi_{0.01}Fe_{0.99}PO₄ can be explained if it forms a thin epitaxial layer on the surface of LiFePO₄ particles. In this case, the XAS behaviour of the surface and bulk of LiFePO₄ particles will be different. A thin layer of Fe₃P will cause charge transfer from the bulk of the material and an increase in intensity of the white line in the XAS spectrum of LiTi_{0.01}Fe_{0.99}PO₄.

The iron *K*-edge XANES pre-edge peak is located to the lower energy side of the white line in Fig. 5.4. In order to identify the features of the pre-edge, this part of the spectra was magnified 10 times. The pre-edge peak is the most useful characteristic for determining the iron oxidation state and coordination environment. The pre-edge peak of the iron 1s edge represents a 1s→3d quadrupolar electronic transition, which is a dipole forbidden process. However, it becomes possible due to the mixing of d-states of iron with the p-states of the surrounding oxygen atoms and the deviation of iron ion coordination geometry from an ideal octahedron.

The energy position of the pre-edge peak is sensitive to the iron oxidation state, while the intensity depends on site centrosymmetry, with the most centrosymmetric iron coordinations having the lowest intensity. Therefore, an octahedral coordination (O_h) will display the lowest pre-edge intensity, and a tetrahedral coordination (T_d) will display the highest. The pre-edge peak is positioned at 7111.9 eV for both LiFePO₄ and LiTi_{0.01}Fe_{0.99}PO₄ and is the same energy as previously reported for Fe²⁺, thus confirming that the iron valence in the bulk powders is 2⁺.^[276] There is no variation in the pre-edge peak position or intensity due to titanium doping, which indicates that the trace amount of dopant Ti⁴⁺ ions does not disturb the oxidation state of iron or the structural coordination in LiFePO₄ crystals. The pre-edge peak energy for Fe³⁺ in FePO₄ is reported to be located 2.3 eV higher than that of Fe²⁺ in LiFePO₄.^[277] This is due to the electrons in Fe³⁺ ions being strongly bound to the nucleus, which induces a shift of 1s→3d transitions to a higher energy level. There is no evidence of a pre-edge peak corresponding to Fe³⁺ in the LiFePO₄ or the LiTi_{0.01}Fe_{0.99}PO₄ powders.

The x-ray absorption oxygen K -edge spectra of LiFePO_4 and $\text{LiTi}_{0.01}\text{Fe}_{0.99}\text{PO}_4$ powders measured in EY and FY modes are shown in Fig. 5.5. It is well known that the EY measurement reflects only surface properties of the powder due to a probing depth of less than 50 Å, while the FY measurement has a probe depth of several thousand angstroms and reflects bulk material properties.

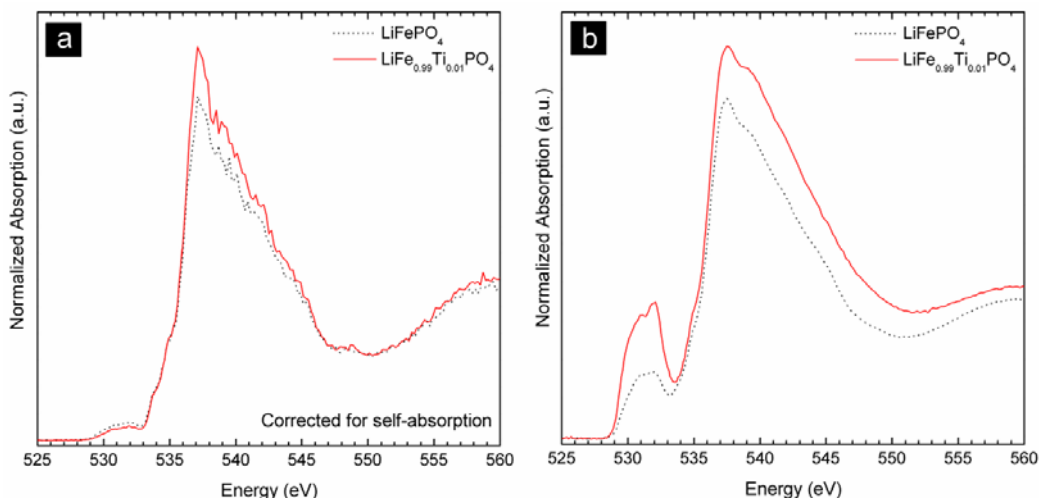


Figure 5.5: Oxygen K -edge x-ray absorption spectra of LiFePO_4 and $\text{LiFe}_{0.99}\text{Ti}_{0.01}\text{PO}_4$ powders measured in Fluorescence Yield (FY) mode (a) and Electron Yield (EY) mode (b).

Both the EY and the FY x-ray absorption spectra show a distinct absorption peak positioned just below the main oxygen 1s absorption edge. This feature has been previously reported by Abbate *et al.*^[278] in their study of Ti-, Al-, and Cu-doped LiFePO_4 compounds and corresponds to a transition to mixed oxygen 2p / iron 3d states. The absorption peak intensities in general are higher in the $\text{LiTi}_{0.01}\text{Fe}_{0.99}\text{PO}_4$ powders and are particularly evident in the EY spectra in measurements (Fig. 5.5b). Since EY x-ray absorption measurements reflect the surface layer properties, it is evident that the surface and bulk properties of $\text{LiTi}_{0.01}\text{Fe}_{0.99}\text{PO}_4$ differ more than those in LiFePO_4 . These observations agree well with the iron K -edge XANES data, where increased white line intensity in $\text{LiTi}_{0.01}\text{Fe}_{0.99}\text{PO}_4$ was explained by a higher hole concentration at the surface of the material compared to the bulk.

5.3.2 Electrochemical Properties

Cyclic voltammetry measurements were performed on LiFePO_4 and $\text{LiTi}_{0.01}\text{Fe}_{0.99}\text{PO}_4$ electrodes to identify the characteristics of the redox reactions. Fig. 5.6 shows the CV curves of LiFePO_4 and $\text{LiTi}_{0.01}\text{Fe}_{0.99}\text{PO}_4$ measured at a scan rate of 0.01 mV s^{-1} between 2.75 V and 4.25 V.

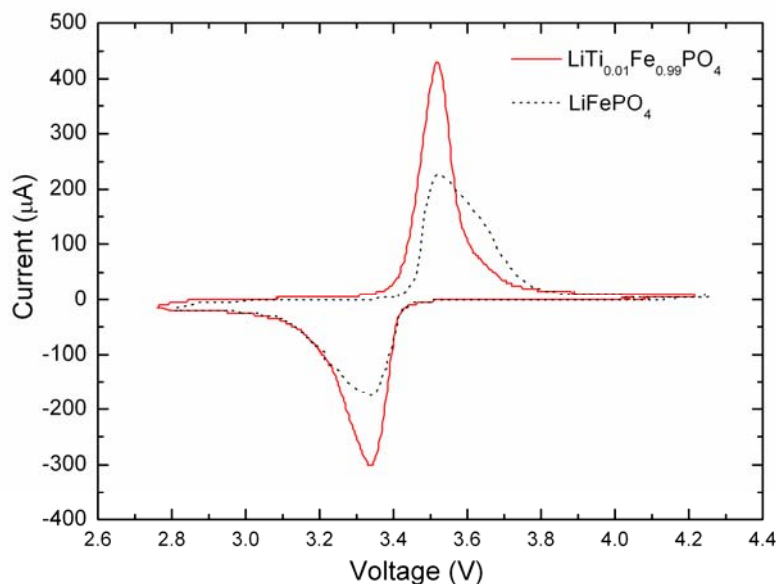


Figure 5.6: Cyclic voltammograms of LiFePO_4 and $\text{LiTi}_{0.01}\text{Fe}_{0.99}\text{PO}_4$ measured at a scan rate of 0.01 mV s^{-1} between 2.75 V and 4.25 V.

The reduction and oxidation peaks for LiFePO_4 and $\text{LiTi}_{0.01}\text{Fe}_{0.99}\text{PO}_4$ both occur at 3.34 V and 3.52 V, respectively, but the peak intensity is notably higher for the $\text{LiTi}_{0.01}\text{Fe}_{0.99}\text{PO}_4$ electrode. The position of these peaks confirms that the $\text{Fe}^{2+}/\text{Fe}^{3+}$ redox pair contributes to the gain and loss of electrons in both LiFePO_4 and $\text{LiTi}_{0.01}\text{Fe}_{0.99}\text{PO}_4$ crystal structures during the lithium insertion and extraction processes. Given that the experimental conditions were identical for both electrodes, the higher redox peak intensities for $\text{LiTi}_{0.01}\text{Fe}_{0.99}\text{PO}_4$ indicate an enhanced electrochemical reactivity of the Ti-doped compared to the un-doped LiFePO_4 .

The capacity and cyclability of LiFePO_4 and $\text{LiTi}_{0.01}\text{Fe}_{0.99}\text{PO}_4$ electrodes were determined by galvanostatic charge/discharge testing at a C/8 rate. Fig. 5.7 shows the voltage profiles of LiFePO_4 and $\text{LiTi}_{0.01}\text{Fe}_{0.99}\text{PO}_4$ electrodes in the first cycle. Both

electrodes exhibited flat charge and discharge plateaus that are characteristic of the electrochemical behaviour in the olivine structure.^[41, 108] The voltages of the charge and discharge plateaus correspond well the oxidation and reduction peaks in the CV curves. The first cycle discharge capacity of LiFePO_4 and $\text{LiTi}_{0.01}\text{Fe}_{0.99}\text{PO}_4$ was 157 mAh g^{-1} and 160 mAh g^{-1} , and are close to the theoretical capacity of 170 mAh g^{-1} . The discharge capacity over 50 cycles in the inset of Fig. 5.7 shows a marginally higher discharge capacity in the $\text{LiTi}_{0.01}\text{Fe}_{0.99}\text{PO}_4$ electrode. This improvement can be attributed to the enhanced electronic conductivity that was induced by increased *p*-type semiconductivity through the titanium doping effect. Overall, the LiFePO_4 and $\text{LiTi}_{0.01}\text{Fe}_{0.99}\text{PO}_4$ cathodes demonstrate excellent cycle life.

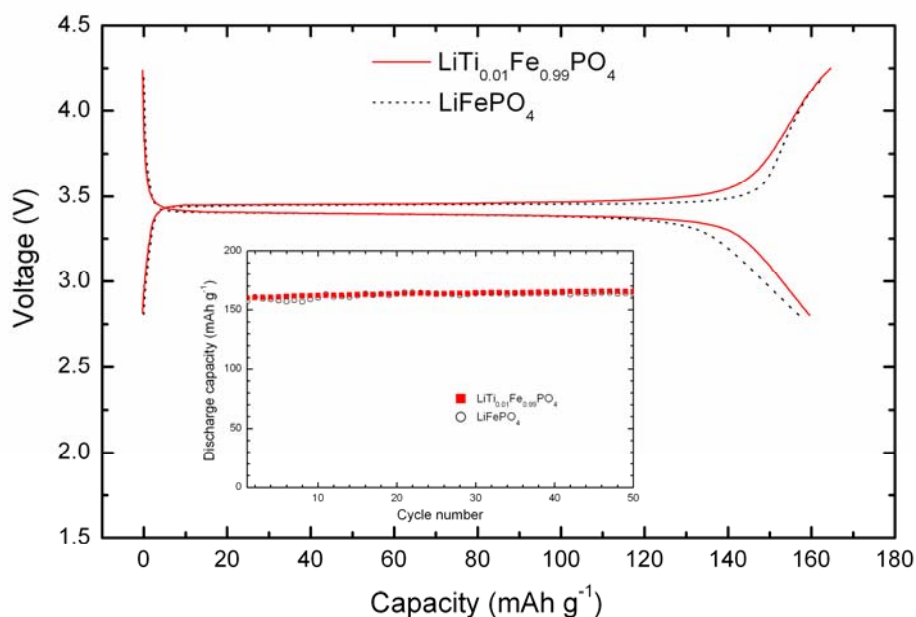


Figure 5.7: The charge/discharge profiles in the first cycle for LiFePO_4 and $\text{LiTi}_{0.01}\text{Fe}_{0.99}\text{PO}_4$ electrodes. The inset shows the discharge capacity vs. cycle number.

5.4 Summary

The structural and electrochemical properties of LiFePO_4 and $\text{LiTi}_{0.01}\text{Fe}_{0.99}\text{PO}_4$ cathode materials synthesized *via* a sol-gel process were systematically investigated. Synchrotron XRD patterns refined using the Rietveld technique confirmed that titanium atoms were properly substituted into the LiFePO_4 crystal lattice, despite the presence of trace amounts of Li_3PO_4 and Fe_3P secondary phases. Iron *K*-edge and oxygen *K*-edge x-ray absorption measurements indicated increased *p*-type semiconductivity for $\text{LiTi}_{0.01}\text{Fe}_{0.99}\text{PO}_4$ compared to the un-doped form. Electrodes made from the LiFePO_4 and $\text{LiTi}_{0.01}\text{Fe}_{0.99}\text{PO}_4$ powders demonstrated a high reversible capacity of 157 mAh g^{-1} and 160 mAh g^{-1} , respectively, and excellent cyclability. The higher discharge capacity from the $\text{LiTi}_{0.01}\text{Fe}_{0.99}\text{PO}_4$ electrode is due to the increased *p*-type semiconductivity, achieved through the successful doping of titanium into the LiFePO_4 crystal structure.

6. Functional oxides Prepared *via* a Novel Electric Discharge Assisted Mechanical Milling Method

“The synthesis of novel solids is as much an art as a science”

F. J. DiSalvo, *Science*, **1990**, 247: p. 649.

6.1 Introduction

An ongoing goal of synthetic solid-state chemistry is to enhance the reactivity of materials in order to speed up reaction kinetics. Fundamentally, the rate of a solid-state reaction is dependent on ionic conduction or diffusion within the solid. Diffusion within bulk oxides can only take place because of the presence of defects in the lattice such as vacancies and interstitial ions. The mole fraction (x) of any particular defect under equilibrium conditions can be related to temperature by the following equation based on Fick’s first and second laws:

$$x = \exp\left[-\frac{E_A}{RT}\right] \quad (6.1)$$

where E_A is the activation energy required for the formation of a particular defect, R is the gas constant, and T is the temperature. From this we find that the number of defects will increase with higher temperatures, which will allow more rapid diffusion and therefore a higher rate of reaction.

Fortunately, we do not need to rely upon high temperature alone to rapidly synthesize materials. Non-conventional synthesis methods such as mechanical milling can also accelerate reactions between species at lower temperatures by inducing defects and causing plastic deformation within a bulk material. Shearing and/or impact forces will create numerous atomically fresh and highly reactive surfaces. These introduced defects may be classified as line, plane, and surface types, which include grain boundaries, dislocations, and inner and outer surfaces. Diffusion at these sites occurs much faster than in the bulk, and therefore represents areas of high diffusivity or “easy diffusion paths”. Syntheses of materials by mechanical milling are far more complex than conventional solid-state “mix and heat” methods

because they involve multiple reaction mechanisms. Plasma processing represents another non-conventional technique that has been used to increase reaction kinetics. Specifically, the Spark-Plasma-Sintering (SPS) technique has proven to be an effective method for the rapid consolidation of fine-grained ceramic powders.^[279, 280]

EDAMM is a high-energy materials synthesis technique that utilizes mechanical milling and plasma processing simultaneously in one process. The most important feature of EDAMM is that nanoparticles can be synthesized by careful selection of electrical (voltage, current, total power) and mechanical (vibration frequency or amplitude) experimental parameters. The practical use of high surface area nanoparticles is of interest to many scientific communities. For example, in our field of rechargeable lithium batteries, a substantial improvement in the stored energy capacity can be achieved by the use of nanoparticles, which are more electrochemically active.^[281] General ceramic processing also utilizes nanoparticles to form potentially fully dense, ceramic products, while in the area of catalysis, nanoparticles offer substantially more active sites for a given weight of material.

6.2 Experimental

This chapter presents the EDAMM synthesis of LiCoO_2 and LiFePO_4 , which represent the current commercial standard and probable future of cathode materials used in rechargeable lithium batteries, respectively. The synthesis of SrTiO_3 and cobalt-substituted versions ($\text{SrTi}_{1-x}\text{Co}_x\text{O}_3$), where $x = 0, 0.1, 0.2$, and 0.5 , are also presented as functional oxides with potential magnetic applications. The functionality of as-synthesized powders is assessed by comparison to those prepared by conventional solid-state synthesis techniques. Details of the experimental procedures are given in section 3.2.3.

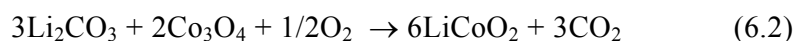
Analysis of the composition and crystal structure of the as-synthesized powders was conducted by XRD. The obtained patterns were refined according to the Rietveld method, and the crystallite size was estimated using the Scherrer equation. The morphology of the powders was observed by TEM and SEM. The final stoichiometry of some powders was examined by the ICP technique. Molar magnetic susceptibility (χ) versus temperature (T) for $\text{SrTi}_{0.5}\text{Co}_{0.5}\text{O}_3$ under a 1000 Oe applied magnetic field

was also measured. Electrochemical measurements of the cathode materials were conducted by assembly of standard R2032 coin-type test cells. Working electrodes were constructed by mixing 75 wt% active powder, 15 wt% carbon black, and 10 wt% pvdF in a mortar and pestle. The dry powder mix was blended with NMP to make a slurry, which was then spread uniformly on 1 cm² by 0.1 mm thick aluminum foil substrate to make the electrodes. Charge/discharge cycles of the LiCoO₂ cells were measured from 3.0 V to 4.2 V at 30 mA g⁻¹ and cyclic voltammograms were obtained at a scan rate of 0.02 mV s⁻¹ from 3.0 V to 4.5 V. For LiFePO₄, charge/discharge cycles were measured from 2.75 V to 4.3 V at 30 mA g⁻¹ and cyclic voltammograms were obtained at a scan rate of 0.1 mV s⁻¹ over the same voltage range.

6.3 Results and Discussion

6.3.1. Synthesis and Characterization of LiCoO₂

The formation of LiCoO₂ powders was achieved by reacting stoichiometric quantities of Li₂CO₃ and Co₃O₄ precursor powders (Eqn. 6.2). LiCoO₂ is traditionally formed by heating a mixture of carbonate, oxide, or hydroxide based precursors at 700–800 °C for up to 48 h.^[20]



The XRD pattern shown in Fig. 6.1 confirms that the structure of EDAMM synthesized LiCoO₂ is pure, with all major peaks corresponding to those of Hex-LiCoO₂ phase. This structure has a rhombohedral unit cell ($R\bar{3}m$) in a layered hexagonal setting, where the constituent cobalt, lithium, and oxygen atoms occupy the 3a, 3b, and 6c Wychoff sites, respectively. The refined unit cell parameters, including goodness factors, are shown in the inset of Fig. 6.1 and are in close agreement with parameters reported in the literature: $a = 2.815\text{--}2.816$ Å (intralayer metal–metal distance), $c = 14.05\text{--}14.08$ Å (interslab distance).^[49] A prime concern in the synthesis of LiCoO₂ was to ensure that cobalt was not misplaced into octahedral sites in the lithium layers. A high c/a ratio (4.998) and the clear splitting of the (006)-(102) and (108)-(110) diffraction peak doublets indicate the formation of a

dimensionally stable structure with a highly ordered distribution of cations in the lattice.^[265] Furthermore, the ratio of the (003) and (104) peak intensities (I_{003}/I_{104}) exceeded unity (1.37), which has been reported to be another important criterion in identifying minimal cation disorder in the structure.^[282] Well-defined lattice fringes observed by TEM can be seen in the inset in Fig. 6.1 and are formed by oxygen atoms in ABC stacking with alternating layers of lithium and cobalt ions in octahedral interstitial sites between the oxygen planes.^[54]

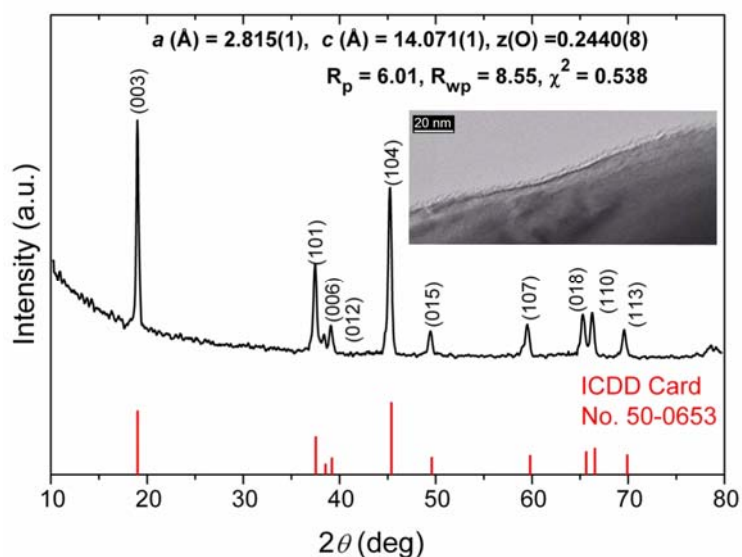


Figure 6.1: X-ray diffraction pattern of the LiCoO_2 powder produced by high power EDAMM (10 min). The refined lattice parameters are given, and the inset shows a TEM image of lattice fringes.

Fig. 6.2 shows the different types of LiCoO_2 powder morphology that can be produced by EDAMM at a vibration amplitude of 5 mm. In Fig. 6.2a, large spheres up to 100 μm in diameter were formed by using high power discharge for 10 min. In comparison, in Fig. 6.2b, nanocrystalline powders that agglomerate into particles measuring around 5 μm were formed by using low power discharge for 5 min.

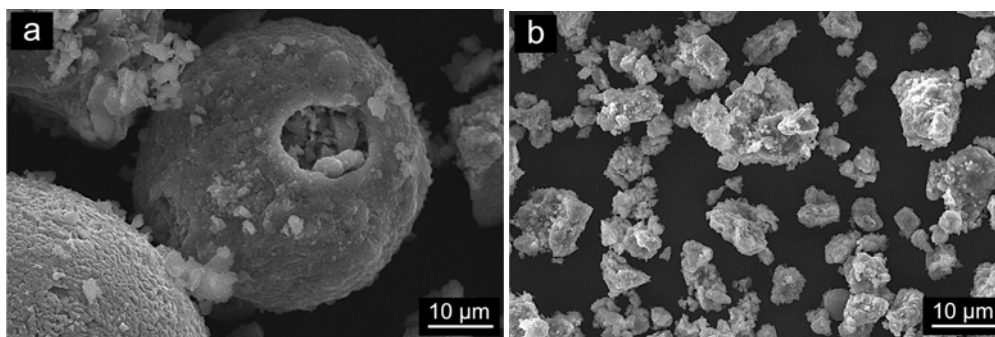


Figure 6.2: SEM images of LiCoO_2 particles produced at a vibration amplitude of 5 mm with high power for 10 min (a), and low power for 5 min (b).

The average crystallite sizes were calculated by (003) peak broadening using the Scherrer equation. Powders synthesized by high power EDAMM had an average crystallite size of 227 nm, whereas the powders produced by low power EDAMM had an average crystallite size of 43 nm. The formation of spherical particles with higher power levels was due to localized melting generated by the electric arc discharge and the subsequent partial fusing of neighbouring particles. Even though high temperatures generated *via* arc discharges would typically cause erosion of the electrodes, in this case, XRD and selected area EDXS techniques gave no evidence of significant contamination by Fe, Cr, Ni, etc. (< 0.7 at% total contamination for the powder produced by high power EDAMM). This is due to the small currents used and also because both the mill floor and the vibrating plunger become instantaneously coated with precursor powders. In this way, the arc discharge constituent of the plasma would be transferred between reacting powders covering the electrodes, thus avoiding erosion effects on the mill components. Another key concern with the use of EDAMM to synthesize LiCoO_2 was the possible volatilization of lithium. However, ICP results on the Li:Co (atomic ratio) for the high (0.982:1) and lower power (0.988:1) processed powders confirmed only a minimal loss of lithium, regardless of the power level selected for synthesis.

When the device was used as a vibrational mill only without activating any electric discharge, the powder remained a mixture of the two precursor materials, even after milling for more than 100 h. It is clear that the combination of a highly metastable plasma and the crushing/surface activation effect produced by mechanical milling dramatically facilitated solid-state reactions in this material.

6.3.2 Electrochemical Properties of LiCoO₂

The functionality of the LiCoO₂ cells was assessed by measuring the electrochemical reactivity using cyclic voltammetry and charge/discharge cycling. Fig. 6.3 shows cyclic voltammograms measured between 3.0 V and 4.2 V at a scan rate of 0.01 mV s⁻¹. The characteristic primary oxidation (~4.1 V) and reduction (~3.8 V) peaks are clearly visible and are in good agreement with the I-V behaviour reported in the literature.^[273, 283]

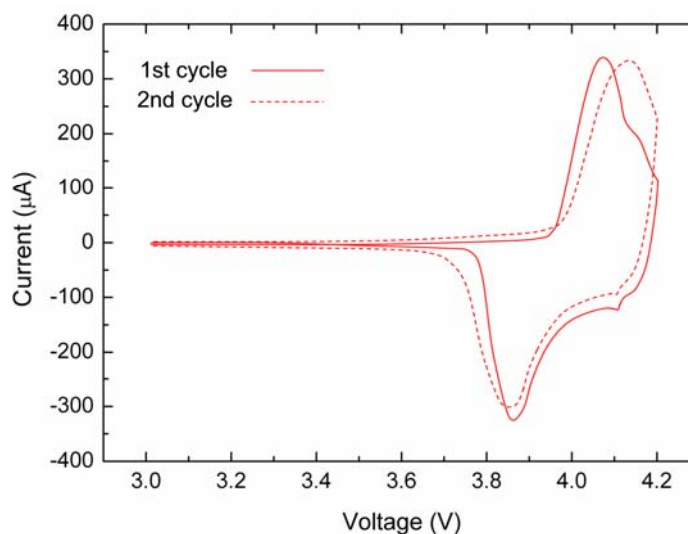


Figure 6.3: Cyclic voltammograms of Li/LiCoO₂ cell measured between 3.0 V and 4.2 V at a scan rate of 0.01 mV s⁻¹. Powder prepared by low power EDAMM with a vibration amplitude of 5 mm for 5 min.

The primary oxidation and reduction peaks also correspond well with the first cycle charge/discharge curves presented in Fig. 6.4. The cyclability of coin cells was assessed by charge/discharge cycling from 3.0 V to 4.2 V at the 30 mAh g⁻¹. The inset of Fig. 6.4 shows that the LiCoO₂ cells typically delivered 105 mAh g⁻¹ after 50 cycles, which is comparable to capacities reported in the literature for pure LiCoO₂ materials synthesized by traditional approaches.^[95]

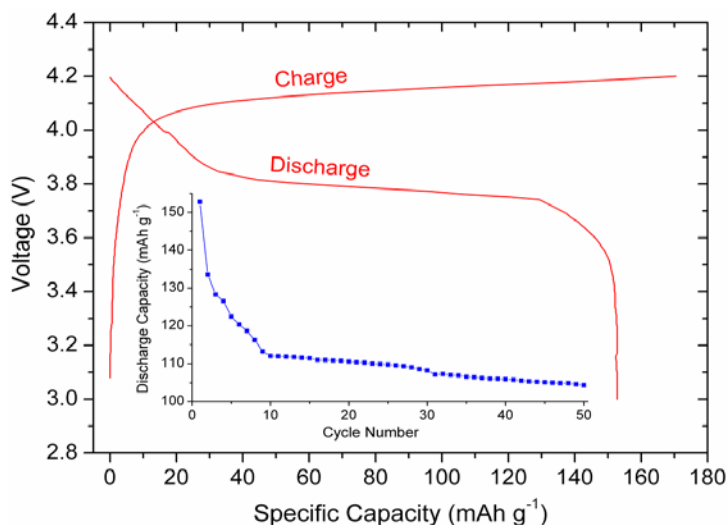
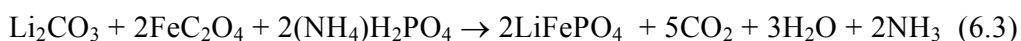


Figure 6.4: Charge/discharge curves for LiCoO_2 cycled at the $C/5$ rate from 3.0 V to 4.2 V. Powder prepared by low power EDAMM with a vibration amplitude of 5 mm for 5 min.

6.3.3 Synthesis and Characterization of LiFePO_4

LiFePO_4 powders were prepared by reacting a mixture of Li_2CO_3 , FeC_2O_4 , and $(\text{NH}_4)\text{H}_2\text{PO}_4$ precursors in a $\text{N}_2 + 3\% \text{H}_2$ atmosphere (Eqn. 6.3). A reducing environment was used in order to suppress the oxidation of Fe^{2+} . Synthesis of LiFePO_4 by direct solid-state reaction involves an initial decomposition reaction at 300–400 °C, regrinding, and final calcination at 700–800 °C for 12–24 h.^[117, 128] Recent attempts to reduce the synthesis time of LiFePO_4 have used an initial high energy milling of precursors, followed by a single calcination at 600 °C for 10 h.^[135]



The XRD patterns shown in Fig. 6.5 chart the phase development of LiFePO_4 precursor powders reacted for 0 min (mixed precursors), 1 min, 3 min, 5 min, and 10 min using EDAMM. After just 1 min, diffraction peaks that correspond to the ordered olivine structure of LiFePO_4 appeared along with diffraction peaks of unreacted precursors. As the reaction time is increased, the diffraction peaks of unreacted precursors gradually diminished. Complete transformation into LiFePO_4 occurred after only 10 min by using a vibration frequency of either 1 mm or 5 mm.

The inset of Fig. 6.5 also shows the refined lattice parameters: $a = 10.319(2) \text{ \AA}$, $b = 6.003(1) \text{ \AA}$, $c = 4.692(1) \text{ \AA}$, and $V = 290.648 \text{ \AA}^3$. All parameters are in good agreement with values found in the literature for the solid-state synthesis of LiFePO_4 .^[284]

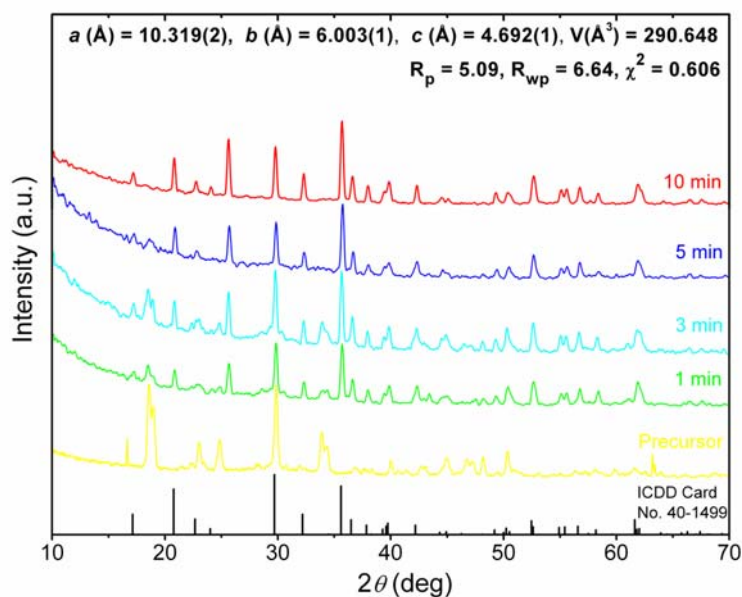


Figure 6.5: X-ray diffraction patterns of LiFePO_4 powders produced by high power EDAMM with a vibration amplitude of 1 mm for 0 min (precursors), 1 min, 3 min, 5 min, and 10 min. The inset shows the refined LiFePO_4 unit cell lattice parameters ($Pmnb$ space group) and goodness factors.

Fig. 6.6 shows the different types of powder morphologies able to be produced by varying the mill vibration amplitude and electrical parameters. High power discharge and a mill vibration amplitude of 1 mm enabled the synthesis of sub-micron LiFePO_4 particles, as seen in Fig. 6.6a. However, by using the same high power discharge and a larger vibration amplitude of 5 mm, melted LiFePO_4 particles that measured up to $100 \mu\text{m}$ were formed, as seen in Fig. 6.6b.

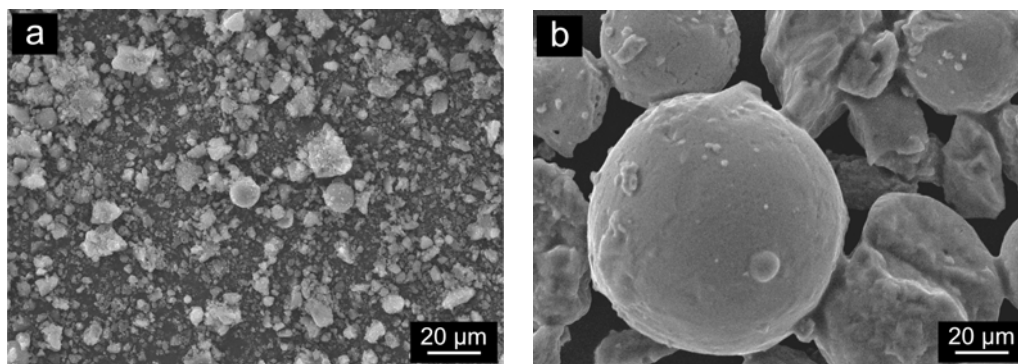


Figure 6.6: SEM images of LiFePO_4 particles produced by: a) high power EDAMM with a vibration amplitude of 1 mm for 10 min, and b) high power EDAMM with a vibration amplitude of 5 mm for 10 min.

6.3.4 Electrochemical Properties of LiFePO_4

The functionality of the LiFePO_4 cells was assessed by cyclic voltammetry and charge/discharge cycling. The cyclic voltammograms in Fig. 6.7 were measured from 2.6 V to 4.4 V at a scan rate of 0.2 mV s^{-1} . A pair of redox peaks can be clearly identified that corresponded to insertion/extraction of Li^+ into/from the LiFePO_4 crystal structure, respectively.

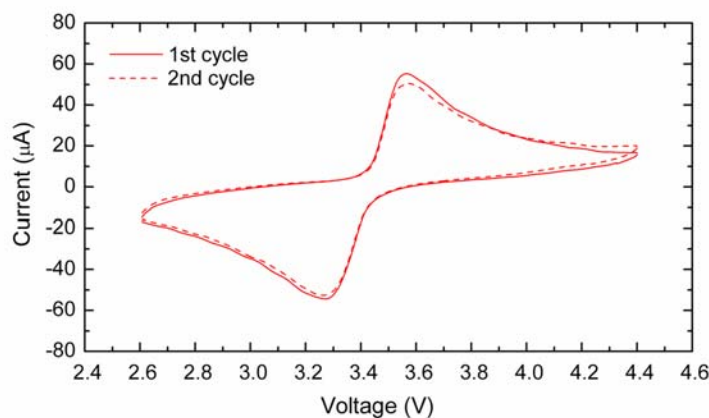


Figure 6.7: Cyclic voltammogram of Li/LiFePO_4 cell measured between 2.6 V and 4.4 V at a scan rate of 0.2 mV s^{-1} . Powder prepared by high power EDAMM with a vibration amplitude of 1 mm for 10 min.

This result was reflected in the charge/discharge curves for the 1st, 10th, and 100th cycles presented in Fig. 6.8. Capacity plateaus that are characteristic of LiFePO₄ occurred at ~3.5 V on charge and ~3.3 V on discharge, which confirmed that the Fe²⁺/Fe³⁺ redox couple contributed to the gain and loss of electrons in the crystal structure during the lithium insertion and extraction process. As shown in the inset of Fig. 6.8, the electrodes maintained a constant discharge capacity near 80 mAh g⁻¹ and demonstrated excellent cyclability over the 50 charge/discharge cycles measured. While discharge capacities in the 140-150 mAh g⁻¹ range have been reported for LiFePO₄ formed by different methods, the electrical conductivities of these materials were significantly enhanced by either carbon coating or doping.^[113, 285]

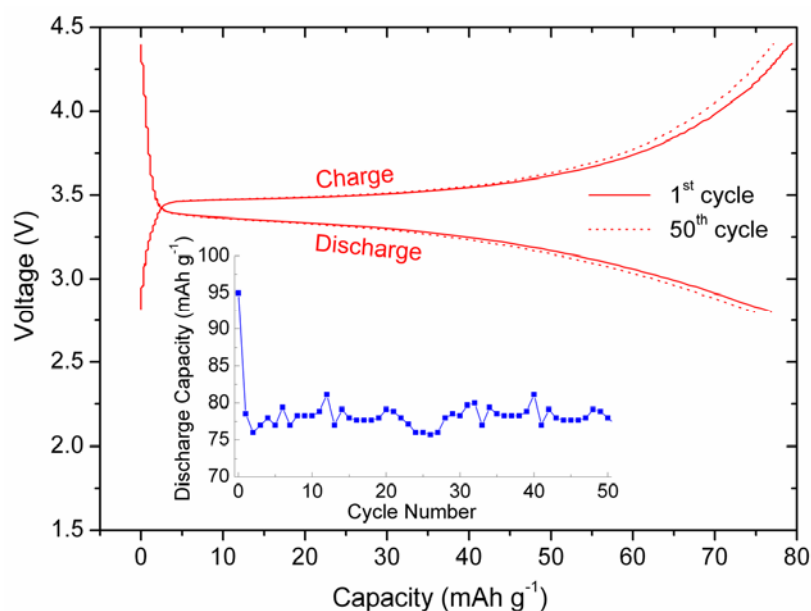


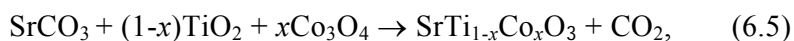
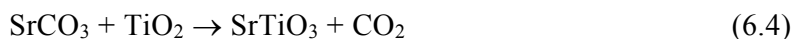
Figure 6.8: Charge/discharge curves for LiFePO₄ cycled at the C/5 rate from 2.8 V to 4.4 V. Inset shows discharge capacity vs. cycle number. Powder prepared by high power EDAMM with a vibration amplitude of 1 mm for 10 min.

6.3.5 Synthesis and Characterization of $\text{SrTi}_{1-x}\text{Co}_x\text{O}_3$ ($x = 0, 0.1, 0.2, \& 0.5$)

The final set of experiments sought to understand the scope of functional oxides that could be produced using EDAMM. To this end, we deviated from the central theme of this thesis and produced a material that was known not to be particularly suited for use in rechargeable lithium batteries. The key issues that needed to be addressed were:

- Could EDAMM be used to synthesize functional oxides that require high sintering temperatures ($> 1000\text{ }^\circ\text{C}$) when prepared by conventional solid-state methods?
- Could EDAMM be used to synthesize a solid solution over a wide composition range? The successful synthesis of doped or atomically substituted functional oxides would represent broader applicability of the EDAMM technique for the production of electronic materials.

The perovskite type compound SrTiO_3 (STO) was selected as a suitable candidate, as it required calcination at $1100\text{ }^\circ\text{C}$, and was reported to have a wide composition range.^[286, 287] The material is useful due to its large non-linear optical coefficient and large dielectric constant, but optimization of these properties requires careful control of particle morphology during synthesis.^[288, 289] The formation of pure STO powders was achieved by reacting stoichiometric quantities of SrCO_3 and TiO_2 according to Eqn. 6.4. A range of STO compounds with 10 %, 20 %, and 50 % cobalt substitution for titanium were also prepared according to Eqn. 6.5.



where $x = 0, 0.1, 0.2, \text{ and } 0.5$

Fig. 6.9 shows the XRD patterns of precursor powders with nominal compositions of $\text{SrTi}_{1-x}\text{Co}_x\text{O}_3$ subjected to high power EDAMM with a mill vibration amplitude of 1 mm. The results indicated that all powders were highly crystalline and of pure STO phase. Surface analysis performed by EDXS supported these findings and confirmed the approximately nominal stoichiometry of all phases.

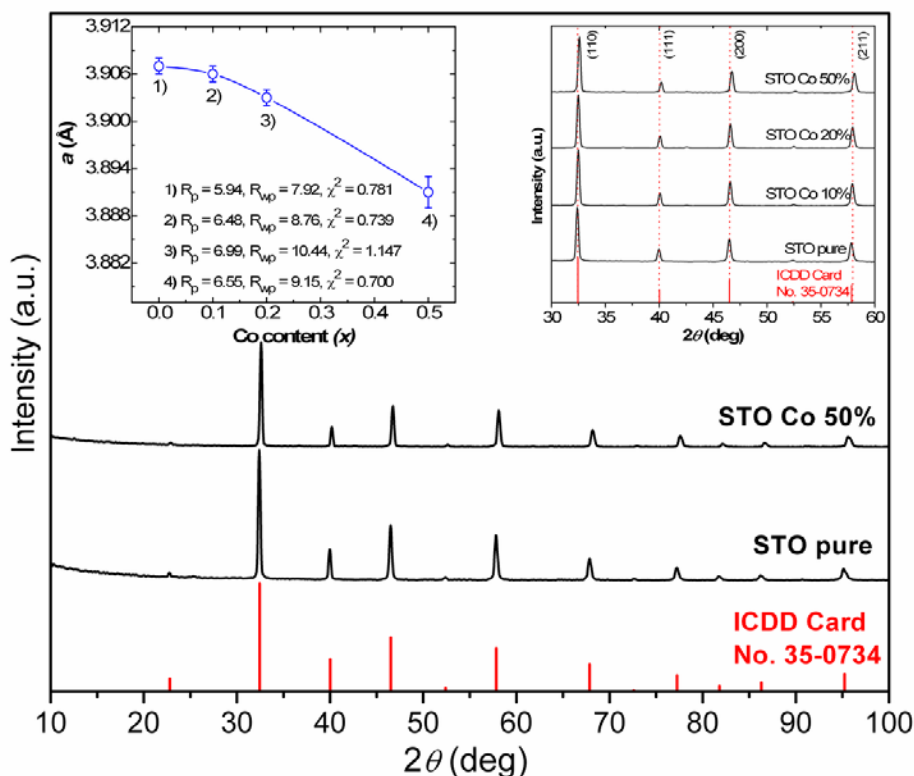


Figure 6.9: X-ray diffraction patterns of $\text{SrTi}_{1-x}\text{Co}_x\text{O}_3$ ($x = 0$ and 0.5) samples produced by high power discharge (30 min). Right inset shows magnified view of the patterns for all samples. Left inset shows the dependence of lattice parameter a on cobalt content (x) with corresponding goodness factors of Rietveld refinements.

The right inset in Fig. 6.9 shows a magnified view of the XRD patterns for all samples. With increasing cobalt content (x), the diffraction peak positions are shifted towards higher 2θ values, which is caused by the substitution of the smaller cobalt cation for the titanium cation. The substitution effect is also clearly illustrated by a systematic decrease in lattice parameter a (left inset in Fig. 6.9) calculated from Rietveld refinements of XRD patterns. The goodness factors of Rietveld refinements are given in the same inset. Typical TEM images of the nanosized particles produced are shown in Fig. 6.10.

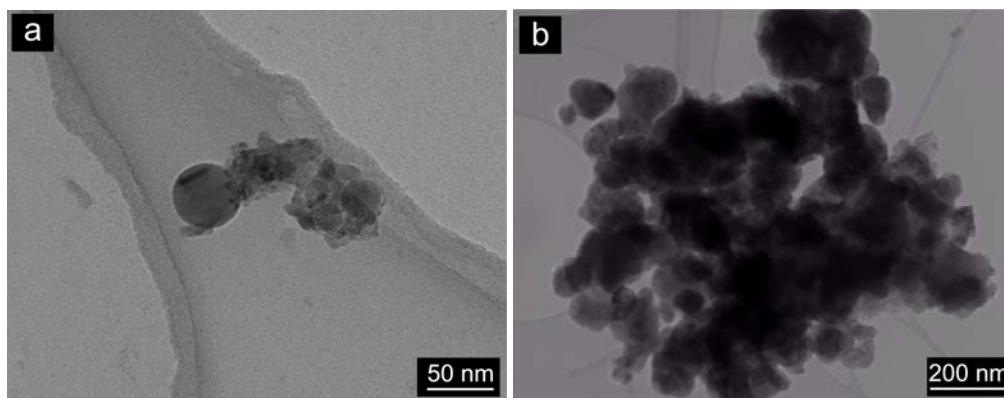


Figure 6.10: TEM images of $\text{SrTi}_{0.5}\text{Co}_{0.5}\text{O}_3$ particles produced by high power EDAMM with a mill vibration of 1 mm that show evidence of particle melting (a), and a general view of particle morphology (b).

6.3.6 Magnetic Properties of $\text{SrTi}_{0.5}\text{Co}_{0.5}\text{O}_3$

Fundamental magnetic properties of the as-synthesized $\text{SrTi}_{0.5}\text{Co}_{0.5}\text{O}_3$ powders were assessed by plotting molar magnetic susceptibility (χ) versus temperature (T) under a 1000 Oe applied magnetic field (Fig. 6.11). The χ - T curve shows typical paramagnetic behavior over the whole temperature range measured. This result is in contrast, however, with the data published by Malo *et al.*,^[290] where they showed a maximum in χ at around 50 K. The absence of this maximum suggests that the EDAMM prepared powders do not contain ferromagnetic clusters or secondary magnetic phases, which were obviously present in the work by Malo *et al.*

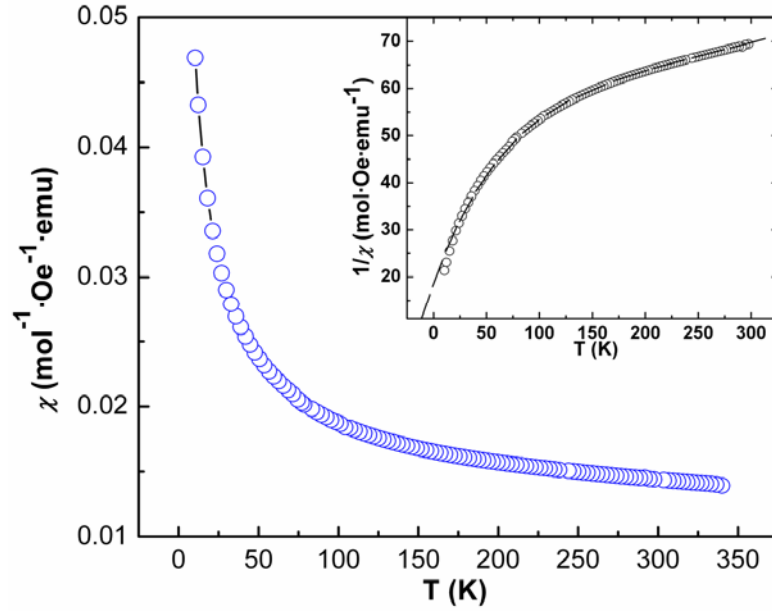


Figure 6.11: Molar magnetic susceptibility (χ) versus temperature (T) for $\text{SrTi}_{0.5}\text{Co}_{0.5}\text{O}_3$ under 1000 Oe applied magnetic field. The inset represents the inverse molar magnetic susceptibility ($1/\chi$) under the same conditions.

The spin state of cobalt ions was assessed from the inverse magnetic susceptibility curve ($1/\chi$) shown in the inset of Fig. 6.11. The curve was fitted in the 10–300 K temperature range by applying a modified Curie-Weiss law:

$$\chi = \frac{C}{T - \Theta_p} + \chi_0 \quad (6.6)$$

where χ_0 is the temperature independent susceptibility (sum of Pauli, Landau, and core susceptibilities) and Θ_p is the Pauli-Weiss temperature. The χ_0 term is introduced into Curie-Weiss law to account for free electron susceptibility and diamagnetic susceptibility. The calculated Θ_p and χ_0 values for our sample were 8.06 K and 0.0122, respectively. The negative Weiss temperature suggested that anti-ferromagnetic interactions slightly dominate the magnetic properties. The calculated effective magnetic moment, $\mu_{\text{eff}} = 2.19 \mu_B/\text{Co}$, is close to that of Co^{2+} in a low spin state ($\mu_{\text{eff}} = 1.73 \mu_B$). The calculated μ_{eff} is significantly smaller than that reported by Malo *et al.*²² It is speculated that the smaller effective magnetic moment of cobalt must be influenced by the presence of Co^{3+} ions in a low spin state. Rietveld

refinement results have provided us with an indirect evidence of such a possibility. The calculated oxygen occupancies decreased with increasing cobalt content (x), *i.e.* $O_{\text{occ}} = 0.9968$ for the sample with $x = 0$, and $O_{\text{occ}} = 0.9816$ when $x = 0.5$. Therefore, the oxygen content could have played a crucial role in the formation of a significant enough amount of Co^{3+} ions to have affected the effective magnetic moment of cobalt in the sample. More work is required to further elucidate the interesting magnetic properties demonstrated in EDAMM synthesized $\text{SrTi}_{1-x}\text{Co}_x\text{O}_3$ powders.

6.4 Scalability and Commercialization of EDAMM

The experimental apparatus used in this work was able to produce ~ 1 g of synthesized powder, but the concept has the potential to be scaled up to synthesize kilogram or tonne quantities. For industrial application, both the reaction chamber and the power supply would need to be scaled-up. The fabrication of a larger reaction chamber is relatively trivial. In the case of power supply, it is critical that the device is able to deliver power at the designated level. If the actual operating voltage was lower than anticipated, the power supply would be unable to deliver the required current. Highly resistive samples typically demand higher voltages to be able to deliver the required power output. In designing a power supply, the relevant variables in the electrical models for the operation of the mill are the total power, voltage, current, and discharge length. Specification of the current and discharge length (with all other physical properties such as powder resistivities known) allows the calculation of the total voltage across the reactor and hence the total power dissipated in the device. Indeed, a new larger power supply for a higher capacity mill has already been designed and manufactured by using existing electrical modeling methods and is currently being commissioned at the University of Wollongong, Australia.

6.5 Summary

The EDAMM technique offers an exciting new method for the rapid and controllable synthesis of functional oxides. The flexibility of EDAMM has been demonstrated by preparing powders from different crystallographic groups that are conventionally formed by labour intensive and time consuming processes (600-1100 °C, various atmospheres, various dopant levels, and multiple stages). The functionality of the oxides prepared, even at this early developmental stage of the technique, matches those of traditional approaches to preparation. The EDAMM technique provides significant commercial opportunities, as powder morphologies can be made to order, and the method has proven to be scalable. We are presently making efforts toward the synthesis of compounds that require calcination temperatures in excess of 2000 °C and identifying experimental conditions that will enable various nanostructures to be produced. Work is also ongoing to fully elucidate the nature of the mechanism(s) responsible for these results.

7. NiO Nanotubes Prepared *via* a Nanoscale Templating Method

7.1 Introduction

The interesting physical and chemical properties possessed by CNTs have initiated research into nanotubes of other materials that could be used as electrodes in rechargeable lithium batteries. Due to their one-dimensional topology, nanotubular structures are known to enhance the stored energy density of the material whilst allowing controlled Li^+ diffusion. There have been several reports in the literature on the synthesis of CuO, TiO_2 , and SnO_2 nanotubes and nanorods that demonstrate excellent electrochemical properties.^[217, 291-295] Nickel oxide (NiO) possesses almost double the theoretical capacity of carbon per unit mass (NiO, 718 mAh g^{-1} vs. C, 372 mAh g^{-1}) and almost triple the theoretical capacity per unit volume (NiO, 4789 mAh cm^{-3} vs. C, 841 mAh cm^{-3}). The work presented herein is the first report on the synthesis of NiO nanotubes and their application as anode materials in rechargeable lithium batteries.

7.2 Experimental

NiO nanotubes were formed according to the templating procedure outlined in section 3.2.4. A commercially available $\text{Ni}(\text{OH})_2$ powder was heated in air at 350°C for 1 h to convert to NiO for use as a reference powder. Analysis of the composition and structure of the precursor and synthesized powders was conducted by the XRD technique. The morphology of the powders was observed by SEM and TEM.

Composite electrodes were prepared by coating a thin layer of 82 wt% NiO nanotube powder, 8 wt% carbon black, and 12 wt% pvdF dissolved in several drops of NMP onto a 1 cm^2 copper disk substrate. Standard R2032 coin-type test cells were assembled in an argon filled glove box using the NiO nanotube and NiO reference powders as the working electrode and battery grade lithium foil as the counter and reference electrodes. The electrochemical performance of the half cells was assessed through cyclic voltammetry, charge/discharge cycling, and EIS.

7.3 Results and Discussion

7.3.1 Structural and Morphological Characterization

Fig. 7.1 shows the XRD patterns for the Ni(OH)_2 precursor nanotubes, the NiO nanotubes, and the NiO reference powder. All Bragg reflections for the Ni(OH)_2 nanotubes can be indexed to the $\alpha\text{-Ni(OH)}_2$ phase (ICDD 38-0715). The diffraction pattern features two major peaks at 11.3° and 23.5° ((003) and (006) reflections, respectively) and several minor peaks at higher angles. Ni(OH)_2 can exist as either α or β polymorphs that have the same hexagonal structure. The $\beta\text{-Ni(OH)}_2$ exhibits well ordered hydroxide layers with an interlayer separation of 0.46 nm, whereas the $\alpha\text{-Ni(OH)}_2$ has an interlayer separation of 0.8-0.9 nm and is also known as hydrated Ni(OH)_2 .^[296] The larger interlayer separation in the $\alpha\text{-Ni(OH)}_2$ is due to the intercalation of carbonate ions introduced by CO_2 in the atmosphere.^[297, 298] In addition, orientation of layers in this phase is completely random, or turbostratic, but the interlayer separation remains constant. It is this feature that is responsible for significant peak broadening in the XRD pattern.

Heat treatment of the $\alpha\text{-Ni(OH)}_2$ precursor nanotubes successfully converted them to NiO nanotubes. The diffraction pattern of NiO nanotubes corresponds well with standard crystallographic data (ICDD card 01-1237). The structure has a cubic unit cell with three major diffraction peaks at 37.4° , 43.5° , and 62.6° ((111), (200), and (220) reflections, respectively). Despite the conversion to the ordered cubic unit cell of NiO the diffraction peaks remain broad due to the fine tubular structure. The NiO reference powder was also in good agreement with standard crystallographic data. The NiO reference powder had a particle size of 1-5 μm and a crystallite size of 6-9 nm and will be referred to hereafter as nanocrystalline NiO.

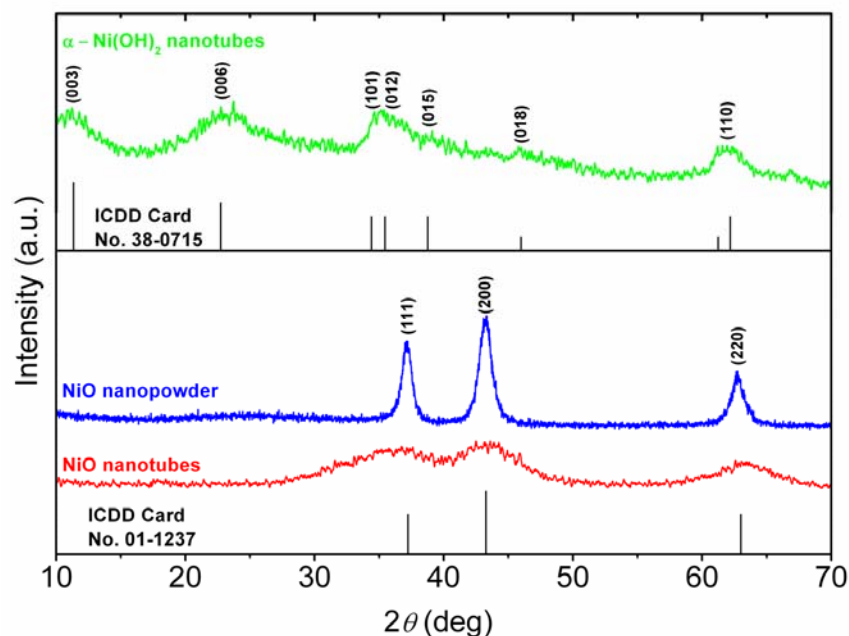


Figure 7.1: X-ray diffraction patterns of Ni(OH)₂ nanotubes, NiO nanotubes, and NiO nanocrystalline powder.

Fig. 7.2 shows representative images of NiO nanotubes at various magnifications. It can be seen in Fig. 7.2a-c that the nanotubes had a parallel arrangement and smooth surface alignment. The exterior dimensions of the nanotubes were diameter 200 nm and length up to 60 μ m, which corresponds to the dimensions of the pores in AAO template. The nanotubes existed in bundles that ranged from a micron to several tens of microns wide. This type of clustering in high aspect ratio nanomaterials has been reported previously in CuO nanorods^[293] and Ni(OH)₂ nanotubes,^[255] and is due to the electrostatic attraction or van der Waals forces between rods/wires/tubes. The bundles were able to be broken down into individual nanotubes through ultrasonication, but extended vibration resulted in destruction of their tubular structure. Higher magnification observations obtained through TEM (Fig. 7.2d) show that the central parts of the mesostructure are bright in comparison to the 10-20 nm thick tube walls. Overall, the nanotubes are well formed and are composed of an array of nanoparticles that resemble the scales on a fish.

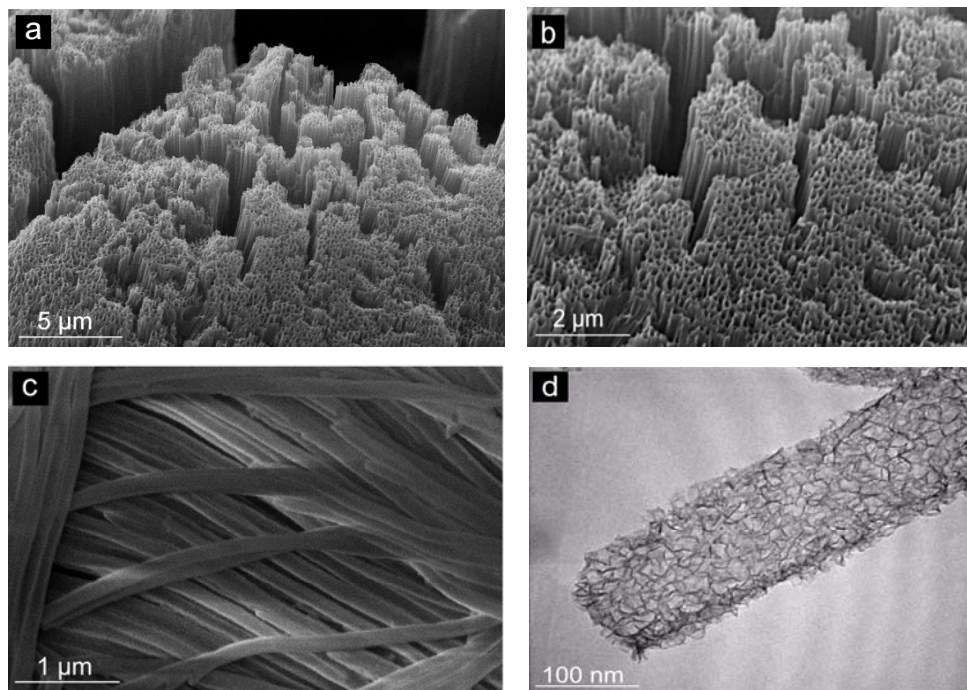


Figure 7.2: Images of NiO nanotubes at different magnifications captured by SEM (a)-(c) and TEM (d) techniques.

7.3.2 Electrochemical Properties

Electrochemical testing was conducted on electrodes made from NiO nanocrystalline and nanotube powders and assembled into a half cell using metallic lithium as the counter and reference electrode. The cyclic voltammograms presented in Fig. 7.3 were collected by measuring the current response at a sweep rate of 0.2 mV s^{-1} . For nanocrystalline NiO (Fig. 7.3a) the first cycle shows a major cathodic peak at 0.8 V and a minor cathodic peak at 0.4 V on discharge, followed by two major anodic peaks at 1.5 V and 2.25 V on charge. The minor cathodic peak is most likely to be associated with the decomposition of the electrolyte and partially reversible formation of the SEI or with temporary additional sites for lithium intercalation. The presence of this peak has been previously reported in work on NiO films to occur at 0.34 V.^[291] In the second cycle, the major cathodic peak shifts up to 0.95 V, and the minor cathodic peak is not detectable.

In comparison, the first cycle for NiO nanotubes (Fig. 7.3b) shows a major cathodic peak at 0.9 V on discharge and a broad anodic shelf that stretches from 1.5 V to 2.3

V on charge. In the second discharge the cathodic peak shifts up above 1 V and a new peak is detected at around 0.5 V in a similar position to the peak that represented the SEI formation in the first discharge of the nanocrystalline NiO powder. It is possible that this “new” peak existed in the first discharge but was masked by the major reaction peak that extended over a wide voltage range. Regardless, the presence of this peak indicates that the formation of the SEI in the case of the NiO nanotubes occurred over several cycles.

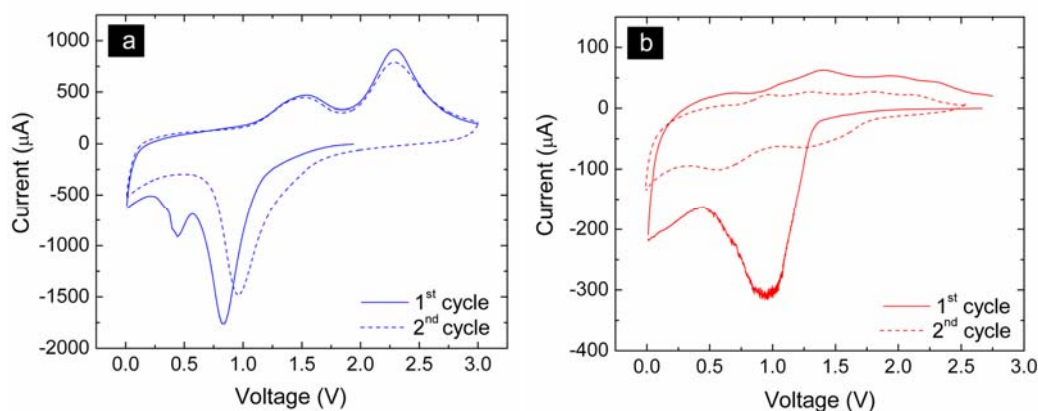


Figure 7.3: First and second cycle cyclic voltammograms performed at a sweep rate of 0.02 mV s^{-1} for NiO nanocrystalline powder (a) and NiO nanotubes (b).

Fig. 7.4 shows the charge/discharge curves of the NiO nanocrystalline and nanotube powders. It can be seen that nanocrystalline NiO (Fig. 7.4a) displays a large plateau at 0.8 V on the first discharge and two smaller plateaus at 1.5 V and 2.3 V on first charge that correspond well with the respective cathodic and anodic peaks observed in the CV curves. The irreversible minor cathodic peak observed on the first discharge at 0.4 V in Fig. 7.3a is not identified in the charge/discharge data. Second cycle plateaus at 1 V on discharge and 1.5 V and 2.2 V on charge correspond well with the observed shift in reaction potentials detected by CV measurement.

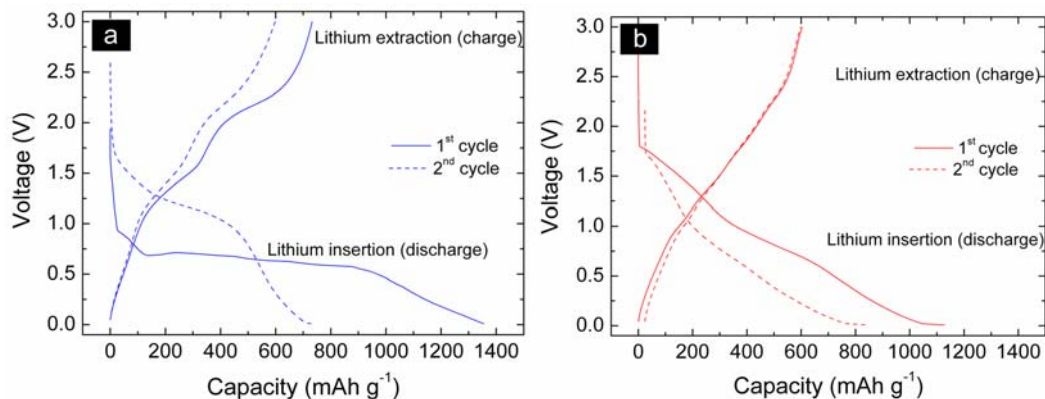


Figure 7.4: First and second cycle charge/discharge curves performed at a current of 0.025 mA for NiO nanocrystalline powder (a) and NiO nanotubes (b).

In contrast, the charge/discharge curves of NiO nanotubes (Fig. 7.4b) show a generally continuous slope that indicates that the insertion and extraction of lithium from the structure occurred over a wide potential range. This type of behaviour is similar to that demonstrated by NiO thin films.^[291, 292] NiO nanotubes exhibit a different electrochemical behavior from the irregular nanocrystalline particles due to their distinct morphological differences.

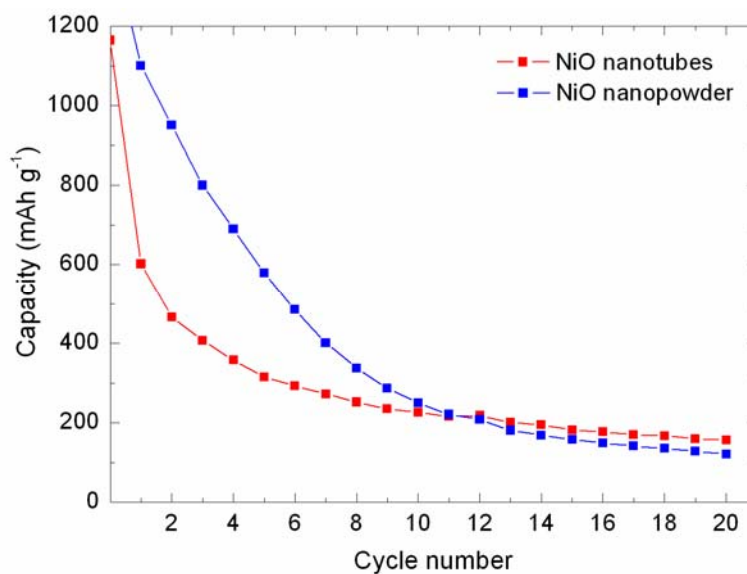
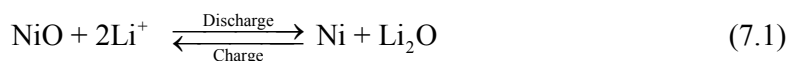


Figure 7.5: Discharge capacity of NiO nanocrystalline and nanotube powders performed at a current of 0.025 mA over 20 cycles.

Fig. 7.5 shows the discharge capacity for NiO nanocrystalline and nanotube powders performed at a current of 0.025 mA over 20 cycles. The capacities of both materials decrease sharply with initial cycling and stabilize after ten cycles. This can be explained by considering the electrochemical reaction described in Eqn. 7.1, where the first discharge of NiO yields fine metallic nickel dispersed in a Li₂O matrix:



The overall reaction is a surface based process that is affected by the reactivity of the participating species. The finely divided nickel produced in the first discharge is known to be highly reactive, and its reactivity is further enhanced upon repeated cycling. This process naturally intensifies the rate of electrolyte decomposition and the subsequent SEI formation. Powders that develop a thick SEI layer often display low ionic conduction, high irreversible capacity loss, and poor charge/discharge cyclability.

The nature of the SEI can be influenced by the selection of the TM oxide and the material texture. Work on CuO has shown that the SEI is a translucent film that surrounds particles and can gradually increase in thickness with cycling up to some limiting value.^[217] Alternatively, work on Co₃O₄ has shown that the SEI thickness can be reduced by careful texture control. This suggests that the observed high and sustained irreversible capacity loss up to about ten cycles is due to the SEI formation in both the NiO nanocrystalline and the nanotube powders. The thickness and rate of formation of the SEI will vary between powders due to their different texture.

The discharge capacity of the NiO nanotubes surpasses that of the nanocrystalline NiO after 10 cycles and is over 30 % higher after 20 cycles. This indicates that the NiO nanotubes possess a superior SEI layer (*i.e.*, thin and coherent) when compared to nanocrystalline NiO after 10 cycles, which allows more controlled and sustainable lithium diffusion.

7.3.3 Electrochemical Impedance Spectroscopy

Fig. 7.6 shows the impedance spectra for NiO nanocrystalline and nanotube powders measured at an OCV of 2 V after several cycles. A fundamental model of electrode component interactions is represented by the electrical equivalent circuit diagram shown in the inset with key variables being determined by curve fitting.

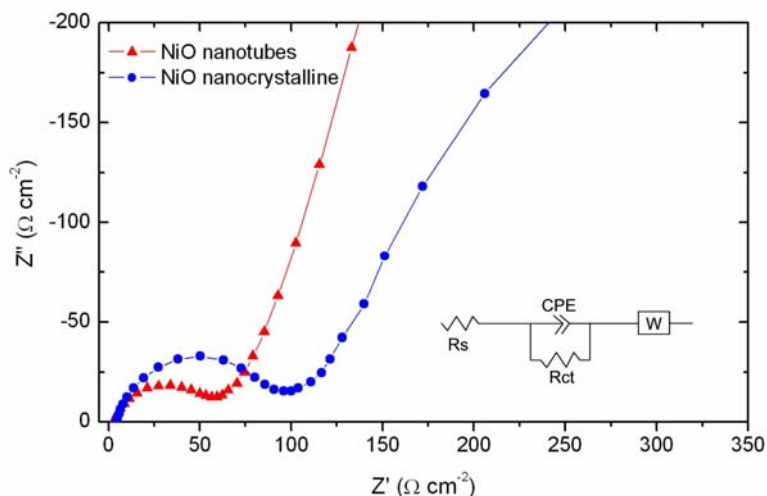


Figure 7.6: Impedance spectra for NiO nanocrystalline powder and NiO nanotubes. The inset shows an equivalent circuit where R_s = impedance due to the electrolyte and surface films, R_{ct} = charge-transfer resistance at the electrode/solution interface, CPE = constant phase element, and W = Warburg impedance and represents the diffusion of Li^+ within the bulk material.

The spectra exhibit a semi circle in the high-moderate frequency range. The frequency reaches its high limit (10 kHz) at the leftmost end of the semicircle, where it touches the x-axis. This semi circle is due to the impedance of lithium ion migration through the electrolyte and surface films (R_s). The values of R_s for the NiO nanocrystalline and nanotube powders were $4.2 \Omega \text{ cm}^{-2}$ and $2.4 \Omega \text{ cm}^{-2}$, respectively. This indicates that lithium ion migration through the NiO nanotubes under the test conditions was easier than in the nanocrystalline NiO powder. At moderate frequencies, we see the semicircle inverting to form the beginning of an extended tail. Around this point, impedance is dominated by the charge-transfer resistance at the electrode/solution interface (R_{ct}). Values of R_{ct} for the NiO nanocrystalline and nanotube powders were $95 \Omega \text{ cm}^{-2}$ and $50 \Omega \text{ cm}^{-2}$, respectively. The lower R_{ct} for the

NiO nanotubes confirms that its superior electrochemical performance when compared to the NiO nanocrystalline powder can be attributed to kinetic improvements.

7.4 Summary

The template synthesis technique is a novel approach for reliably preparing nanorod or nanotube structures. Regular NiO nanotube bundles were successfully synthesized by using the template method and subsequent heat treatment. The synthesized nanotubes are up to 60 μm long, have a 200 nm outer diameter, and are 20-30 nm thick. NiO nanotubes showed a 30 % improvement in the discharge capacity when compared to nanocrystalline NiO after 20 cycles, despite having a lower initial discharge capacity. The improved cyclability of NiO nanotube electrode has been explained in terms of differences in the kinetic behavior of the NiO nanocrystalline and nanotube powders. Further optimization of the structure of the NiO nanotubes can be made to further improve their discharge capacity and cyclic performance.

8. SnSb-Carbon Composites Prepared *via* a Reductive Precipitation Method

8.1 Introduction

Tin-based alloys have long been considered an attractive replacement for graphite anodes in rechargeable lithium battery systems due to their superior lithium storage capacity. In particular, SnSb alloys are a promising group of materials that offer two key design features: (1) both tin ($\text{Li}_{4.4}\text{Sn}$, 990 mAh g^{-1}) and antimony (Li_3Sb , 660 mAh g^{-1}) contribute to the capacity of the material, but at different stages in the electrochemical discharge process,^[194, 299, 300] and (2) the volume changes that occur during charge/discharge cycling can be partly buffered by a highly dispersed ductile tin phase.^[301] Using nanosized SnSb particles offers additional benefits, such as reducing the likelihood of electrode cracking by lowering the mechanical stresses within particles^[192, 203, 209, 302] and improving the kinetic variables of reactions.^[211, 303]

Despite these desirable features, the electrochemical performance of SnSb alloys remains limited by the agglomeration of nanoparticles during charge/discharge cycling. This effect reduces the alloy's ability to restrain volume changes and is considered to be the predominant barrier to the practical application of these materials.^[211, 304] The challenge for engineers is to restrict the agglomeration of nanoparticles in order to improve the electrode's cycle life, without sacrificing the high capacity that is achieved by the use of tin and antimony. Tin-rich SnSb (SnSb-Sn) materials have been reported to deliver extremely high initial capacities of over 800 mAh g^{-1} , but have been unable to demonstrate any improvement in the cyclability of the electrodes.^[206, 305]

Nanosized SnSb-C composite materials that use MCMB^[211] and amorphous carbon spherules^[212] as a stable framework structure have recently shown particular promise in extending the cycle life of the electrode. The beginning of this chapter reports on the synthesis and electrochemical performance of nanosized SnSb and SnSb-Sn powders physically mixed with various quantities of carbon black. Carbon black served as both a dispersant and conductive agent, and has been reported to be able to

restrict the agglomeration of fine particles when used in an approximately unitary ratio.^[191, 209, 306]

The later sections of this chapter present work on a nanocomposite material made by coating SnSb onto the surface of CNTs. CNTs are an exciting nanoscale framework material that possess extraordinary thermal and mechanical stability, and high electronic conductivity.^[307-309] As an alternative carbonaceous electrode material, CNTs react at a lower voltage and can accommodate more Li^+ ions due to their wider *d*-spacing (CNT, 0.34 nm *vs.* graphite, 0.33 nm) and larger surface to volume ratio.^[310]

8.2 Experimental

Nanosized SnSb and SnSb-Sn powders were synthesized by reductive precipitation of metal chlorides from an aqueous solution with NaBH_4 as described in section 3.2.5. The SnSn and SnSb-Sn powders were then physically mixed with 20 wt% and 50 wt% carbon black. To form the SnSb-CNT nanocomposite, 0.25 mg of multiwalled CNTs were added to the ionic solution during synthesis.

The structure and morphology of the materials were characterized by XRD, FE-SEM (JEOL JEM-3000), TEM (JEOL 2010), and Raman spectroscopy (Jobin Yvon HR800). Gas sorption experiments were conducted to determine the BET specific surface area of the powders. To measure electrochemical performance, electrodes were prepared by coating a thin layer of one of these mixtures dissolved in several drops of NMP and 10 wt% pvdF binder onto a 1cm^2 copper foil substrate. Standard R2032 coin-type test cells were assembled using the alloy powder composites as the working electrodes and battery grade lithium foil as the counter and reference electrodes. Electrodes were cycled between 0.025 V and 1.5 V at an average constant current density of 100 mA g^{-1} .

8.3 Results and Discussion

8.3.1 Structural and Morphological Characterization of SnSb Alloys

The XRD patterns of SnSb and SnSb-Sn are shown in Fig. 8.1. The primary peaks in both patterns have been indexed to rhombohedral β -SnSb (ICDD Card No. 33-0118), while SnSb-Sn also contained ductile tin (ICDD Card No. 04-0673). The average crystallite size estimated by applying the Scherrer equation to the primary (101) peak was in the 40-60 nm range for both powders. Nanosized powders containing tin and antimony can also be expected to have a thin surface oxide layer due to their high reactivity with atmospheric oxygen, even though there were no identifiable oxide peaks present in the diffraction patterns.^[306] From SAD measurements SnSb-Sn particles were estimated to contain 18-20 wt% additional tin.

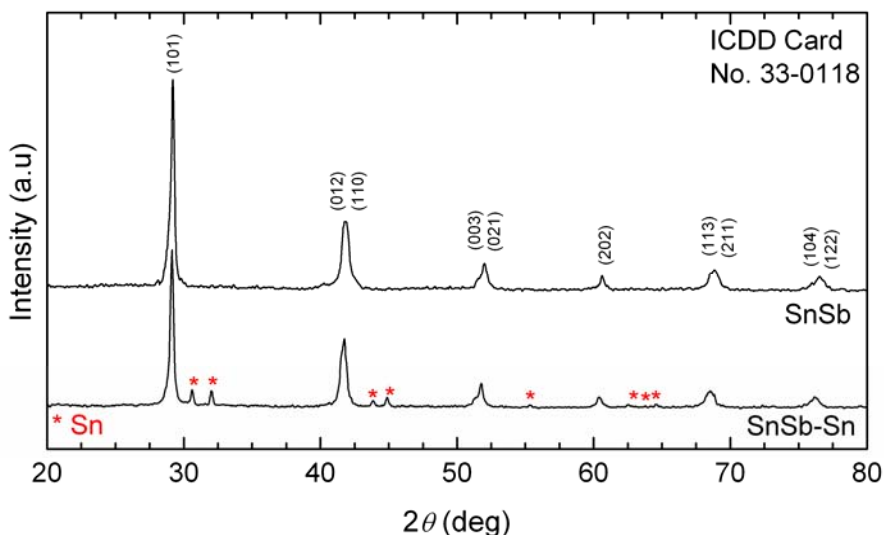


Figure 8.1: X-ray diffraction patterns of SnSb and SnSb-Sn powders.

A representative SEM image of SnSb and SnSb-Sn powders is shown in Fig. 8.2. There was no discernable visual difference between the powders, as both demonstrated a significant degree of agglomeration due to the enhanced electrostatic attraction that commonly occurs between the surfaces of the nanosized particles. The specific surface area of SnSb and SnSb-Sn powders calculated by the BET method was 5-20 m².

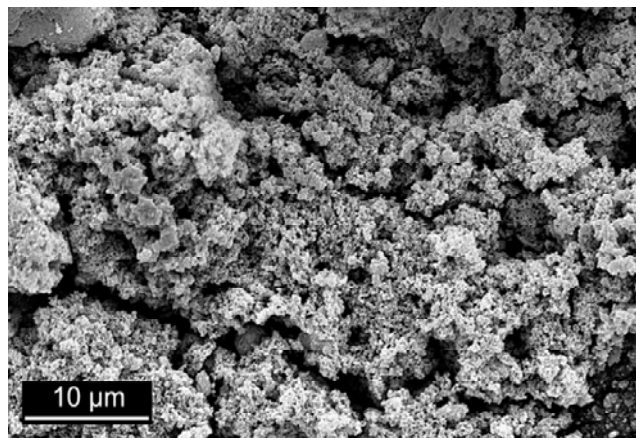


Figure 8.2: *Representative SEM image of the microstructure of SnSb and SnSb-Sn produced by reductive precipitation.*

8.3.2 Electrochemical Properties of SnSb-C

The SnSb and SnSb-Sn powders were physically mixed with 20 wt% and 50 wt% carbon black and used as the active electrode material in coin cells. A carbon-free SnSb reference electrode was used for comparative purposes. The discharge capacities for all electrodes cycled at 100 mA g⁻¹ for 50 cycles are presented in Fig. 8.3. The curves indicate that the cycle life of all carbon-containing electrodes is better than that of the SnSb reference electrode, since it failed after only 27 cycles. This highlights the requirement for some form of dispersant or conductive additive to render SnSb alloys usable.

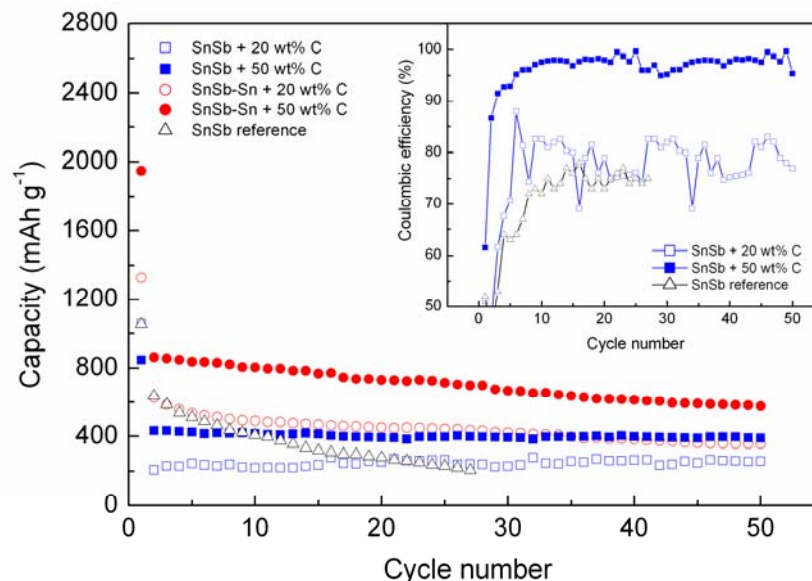


Figure 8.3: The discharge capacity of SnSb and SnSb-Sn electrodes with various quantities of carbon black. The inset shows the coulombic efficiency of the SnSb series.

A general comparison of the plots in Fig. 8.3 shows that the SnSb-Sn series clearly delivers a higher capacity than the SnSb series. This is due to the higher content of tin, which has a larger theoretical capacity than antimony and therefore contributes more to the overall cell capacity. However, it should be noted that the capacity gains produced by a higher tin content were tempered by a more significant capacity fade on repeated charge/discharge cycling. This is due to the larger volume expansion experienced by the full lithiation of tin ($\text{Li}_{22}\text{Sn}_4$, 676 %) compared to the full lithiation of antimony (Li_3Sb , 147 %).

The effects of adding different quantities of carbon black can be demonstrated by considering the coulombic efficiency of the cells, calculated by charge capacity/discharge capacity. The inset of Fig. 8.3 plots the coulombic efficiency of the SnSb series and shows that by increasing the carbon content, the coulombic efficiency also increased. We can see that the coulombic efficiency of the 20 wt% carbon electrode fluctuated between 70-85 % compared with a high stable coulombic efficiency in excess of 95 % for the 50 wt% carbon electrode. This effect can be explained by the higher carbon content providing improved electrical conduction, which enabled a better overall utilization of active particles.

Despite the improvement in cell efficiency by the addition of more carbon, it was clear that carbon was not able to effectively arrest cracking in the electrodes. Visual evidence of electrode cracking can be seen in the SEM images of the surface of an SnSb-Sn + 50 wt% C electrode taken after one cycle (Fig. 8.4a) and after 50 cycles (Fig. 8.4b). In Fig. 8.4a, the surface of the electrode after the first charge/discharge cycle is mapped for tin and antimony elements across the 125 μm scale bar, indicating the formation of micrometer-sized domains of tin and antimony dispersed throughout the amorphous carbon matrix. The surface of this electrode is relatively smooth and complete compared to an electrode from the same series after 50 charge/discharge cycles (Fig. 8.4b), which features extensive microcracking throughout the SnSb domains.

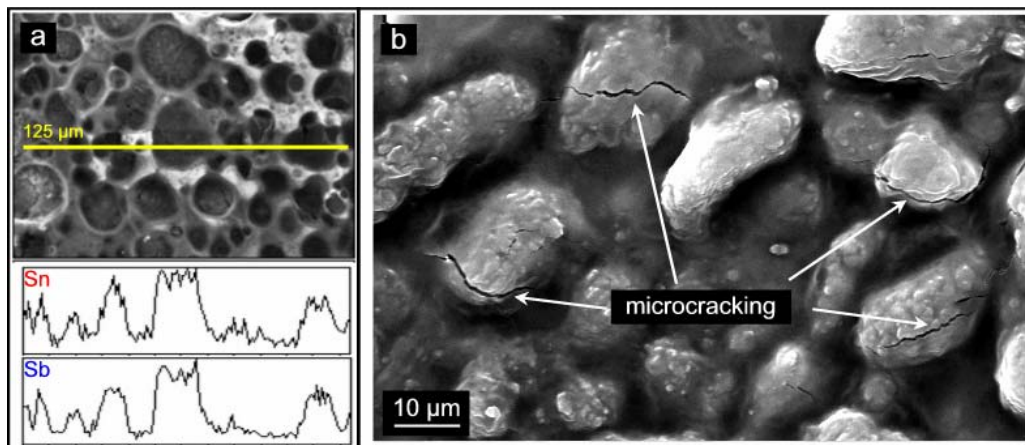


Figure 8.4: SEM images of a SnSb-Sn + 50 wt% carbon black electrode: (a) after one charge/discharge cycle, with inset showing line mapped across the scale bar for Sn and Sb elements, and (b) showing microcracking of the SnSb domains after 50 charge/discharge cycles.

The cycling characteristics of the SnSb and SnSb-Sn series can be further elucidated by considering the charge/discharge curves for the 1st, 5th, and 50th cycles presented in Fig. 8.5. The superior cyclability of the SnSb series is demonstrated by the proximity of the curves (Fig. 8.5a and b), compared to the dispersion of curves seen for the SnSb-Sn series (Fig. 8.5c and d).

It is also clear from these curves that a higher capacity was attained in both series by adding more carbon. In the SnSb series, 20 wt% and 50 wt% carbon additions gave a reversible discharge capacity of $\sim 300 \text{ mAh g}^{-1}$ and $\sim 430 \text{ mAh g}^{-1}$, respectively. The same trend can be seen in the SnSb-Sn series, where the 20 wt% and 50 wt% carbon additions gave a reversible discharge capacity of $\sim 550 \text{ mAh g}^{-1}$ and $\sim 862 \text{ mAh g}^{-1}$, respectively. These results are due to the additional carbon enabling an improved dispersion of the SnSb phases and a higher electrical conductivity. The carbon then allows a better utilization of these active particles, even if SnSb aggregates upon cycling.

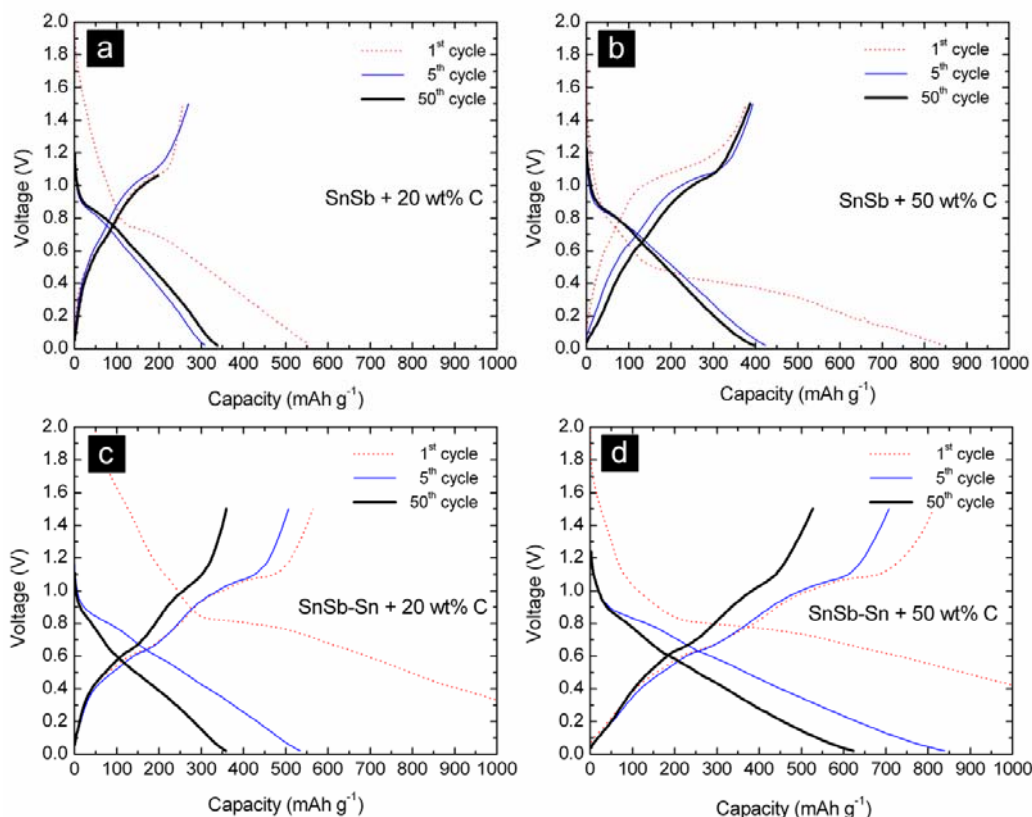


Figure 8.5: Charge/discharge curves for the 1st, 5th, and 50th cycles for SnSb + 20 wt% C (a), SnSb + 50 wt% C (b), SnSb-Sn + 20 wt% C (c), and SnSb-Sn + 50 wt% C (d).

8.3.3 Summary on SnSb-C

Nanosized SnSb and SnSb-Sn powders were synthesized by reductive precipitation. The original focus was to improve the life cycle of these systems by physically mixing increasing quantities of carbon black with pristine powders. It seems that adding carbon in this way does not noticeably improve the cycle life of the electrode, and agglomeration is not prevented. However, this approach does improve the realized capacity of the electrode by enhancing the electrical conduction of the material, allowing a better utilization of active particles that are available for lithium insertion.

8.3.4 Structural and Morphological Characterization of SnSb-CNT

The commercially available multiwall nanotubes used in this experiment show a random alignment, with individual tubes having an outer diameter of approximately 50-100 nm and a length of 200-300 μm (Fig. 8.6a and c). The SnSb-CNT nanocomposite synthesized by reductive precipitation features a high dispersion of SnSb nanoparticles on the outer walls of the CNTs (Fig. 8.6b and d).

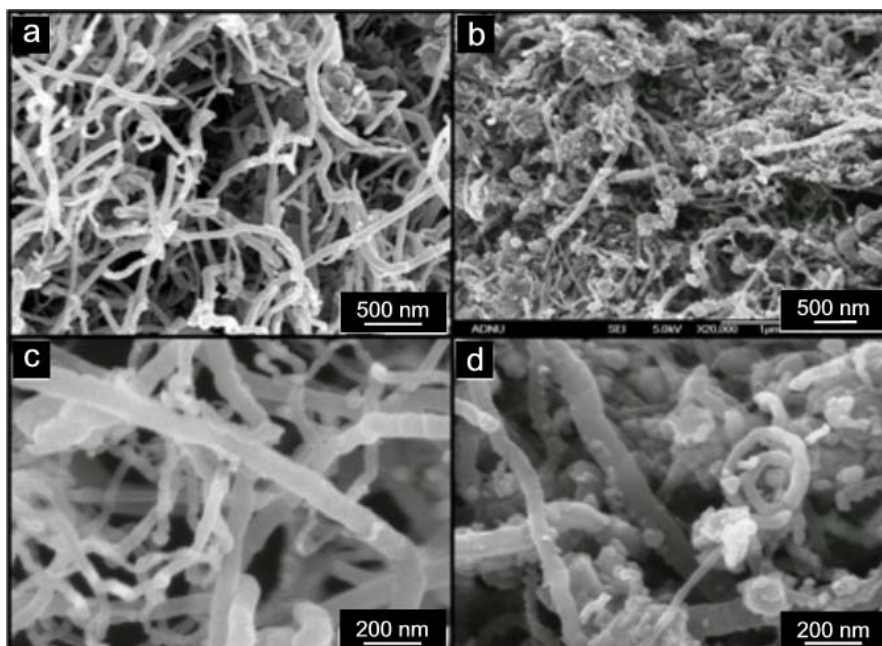


Figure 8.6: FE-SEM images at different magnifications of multiwall CNTs (a) and (c), and SnSb-CNT nanocomposite powder prepared by reductive precipitation of metal salts (b) and (d).

The average weight percent of tin, antimony, and CNTs was estimated by EDXS to be 24.91 %, 22.69 % and 52.40 %, respectively, and there was no evidence of Cl⁻ in the obtained SnSb-CNT powder. This result allows the estimation of the composition of SnSb nanoparticles in the composites to be Sn_{1.05}Sb_{0.95}, which is in good agreement with the XRD patterns in Fig. 8.7a. All reflections of β -SnSb phase are present in the SnSb-CNT powder. The primary (101) peak of CNTs is also clearly identified, and there is no evidence of any other tin- or antimony-containing secondary phases.

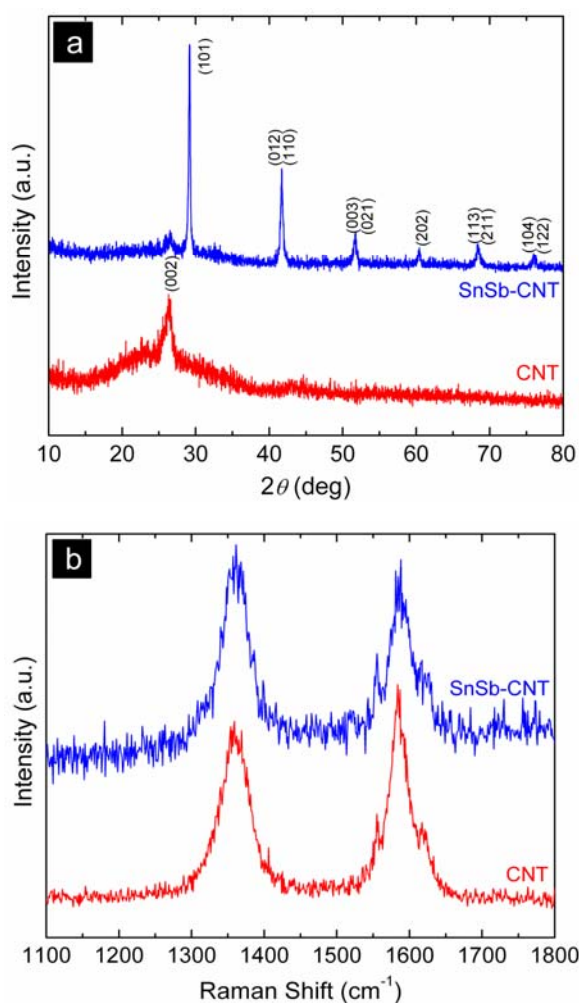


Figure 8.7: X-ray diffraction patterns (a) and room temperature Raman spectra (b) of SnSb-CNT nanocomposite powder and multiwall CNTs.

The room temperature Raman spectra in Fig. 8.7b show a difference in the crystallinity of CNTs before and after the reductive precipitation process. It is well known that CNTs possess two peaks located at 1354 cm^{-1} (*D* band) and at 1581 cm^{-1} (*G* band), with the intensity ratio (I_G/I_D) of these peaks indicating the degree of crystallinity of the CNTs. After reductive precipitation, the I_G/I_D ratio of the CNTs is reduced from 1.22 to 0.87, indicating that the atomic ordering or crystallinity of the CNTs was reduced. The lower I_G/I_D ratio also suggests that the precipitation of polycrystalline SnSb involved the formation of chemical bonds with the CNT surfaces, rather than only physical adsorption. The destructive nature of this chemical bonding would have changed the surface topography of the materials and produced additional highly reactive defect sites such as dangling bonds and pores. This is reflected in the BET surface area of the CNTs, which increased from $55.12\text{ m}^2\text{ g}^{-1}$ to $61.36\text{ m}^2\text{ g}^{-1}$ after reductive precipitation.

Fig. 8.8 shows typical TEM images of the SnSb-CNT nanocomposite at various magnification levels. In Fig. 8.8a and b, SnSb alloy particles with an average particle size of 30-50 nm are well coated onto the CNTs. The selected area diffraction (SAD) pattern in the inset of Fig. 8.8a confirms that the composite is composed of CNTs and polycrystalline SnSb nanoparticles. The higher resolution image in Fig. 8.8c shows that the average grain size of the deposited SnSb alloy was less than 10 nm and had a *d*-spacing of 0.53 nm.

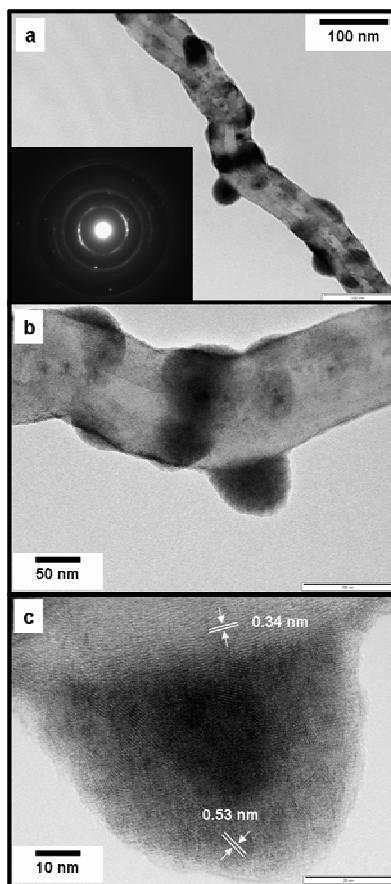


Figure 8.8: TEM image and selected area diffraction (SAD) pattern (inset) of an individual CNT coated with SnSb (a), a higher magnification TEM (b), and a HRTEM of the same area (c).

Particles with sizes less than about 100 nm commonly agglomerate due to the overwhelming driving force to reduce their surface energy.^[211, 304] This is particularly true of SnSb powders produced by the reductive precipitation technique, as was shown previously in Fig. 8.2. However, in the case of SnSb-CNT powders, the agglomeration of SnSb was prevented, since the particles were formed on the CNT framework surface. The mechanism for nucleation of the SnSb particles is thought to have involved existing surface defects and additional induced defects acting as nucleation sites onto which the alloy particles were precipitated. In this way, the Sn^{2+} and Sb^{3+} ions were substituted for carbon atoms at an atomic level, which then acted as seeds during the early stages of the precipitation. Reductive precipitation synthesis

therefore offers an effective method for the *in-situ* preparation of SnSb-CNT nanocomposite powders that feature SnSb nanoparticles pinned to the CNTs.

8.3.5 Electrochemical Properties of SnSb-CNT

The electrochemical performance of the CNT and SnSb-CNT powders was assessed by charge/discharge cycling from 0.025 V to 1.5 V at a constant current of 100 mA g⁻¹. In Fig. 8.9a, the SnSb-CNT had a first cycle discharge capacity of 1408 mAh g⁻¹ and a reversible capacity of ~700 mAh g⁻¹. The first cycle coulombic efficiency for the SnSb-CNT was 48.30 %, which was notably higher than that of the normal CNTs, 34.75 %. This improvement in the first cycle coulombic efficiency can be attributed to the SnSb phase, which reacted with lithium during the charge/discharge of the cell.

The charge/discharge reactions of SnSb-CNT were reversible over 50 cycles without any significant capacity fading induced by agglomeration of the SnSb nanoparticles.^[304] The CNT framework served to simultaneously pin the SnSb nanoparticles and also enhance the electronic conduction around the active phases, despite their enormous volume variation during lithium insertion and extraction. Furthermore, all components of the composite were reactive toward lithium, with the CNTs contributing to lithium storage.

In order to identify all of the electrochemical reactions, the differential charge/discharge capacity *vs.* voltage profiles of SnSb-CNT are presented in Fig. 8.9b. The first differential discharge profile shows a major reduction peak around 0.75 V derived from Li₃Sb formation when antimony reacts with lithium according to Eqn. 8.1 and numerous small peaks from 1.5 V to 0.75 V formed by electrolyte decomposition and SEI film formation.^[311, 312] The apparent peaks at 0.2 V and 0.55 V are most likely to be due to reactions between lithium and defects or buckled layers of CNTs. These reactions constituted an irreversible process since the peaks disappeared in subsequent cycles.

The complete alloying and de-alloying reaction of SnSb with lithium is described in Eqn. 8.2.^[313] Graphically, this process is clearly represented from the second cycle

by the reduction peak at 0.85 V and the oxidation peak at 1.1 V. The other pairs of reduction peaks between 0.25 V and 0.7 V during discharging and the oxidation peaks between 0.4 V and 0.8 V during charging, are related to the formation of various Li_xSn alloys as described by Eqn. 8.3.^[205, 314] Both reduction and oxidation peaks below 0.2 V are caused by the intercalation and de-intercalation of lithium into the CNTs.

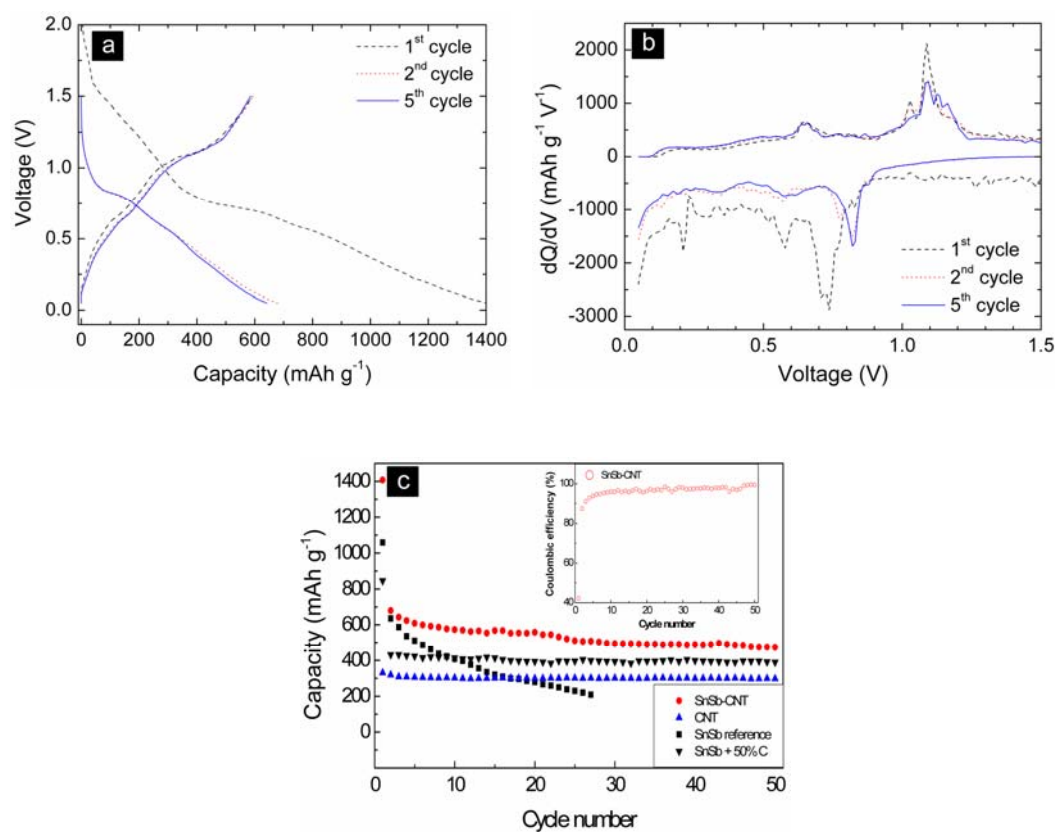


Figure 8.9: Galvanostatic voltage profiles for SnSb-CNT between 0.025 V and 1.5 V (a), differential charge/discharge vs. voltage plots at the 1st, 2nd, and 5th cycle for SnSb-CNT (b), and a comparison of the cyclic performance of SnSb, CNT, SnSb + 50 wt% C, and SnSb-CNT, with the inset showing the coulombic efficiency (c).

The discharge capacity of CNTs and SnSb-CNT, along with the data for the SnSb reference and SnSb + 50 wt% carbon powders presented previously, is given in Fig. 8.9c. The SnSb-CNT nanocomposite exhibited the highest reversible capacity ($\sim 700 \text{ mAh g}^{-1}$), good coulombic efficiency ($> 95 \%$ - see inset of Fig. 8.9c) and cycling performance over 50 cycles. Direct comparison of the SnSb-CNT and SnSb + 50 wt% carbon powders clearly demonstrates that the SnSb-CNT delivered a minimum of 100 mAh g^{-1} higher discharge capacity and improved cyclability.

It was clear from the analysis of the SnSb and the SnSb-Sn series physically mixed with carbon black that nanosized SnSb domains were responsible for the high capacity and that the carbon maintained the electronic conduction. This was also true of the SnSb-CNT nanocomposite, but the CNTs were also able to properly accommodate the significant volume variations occurring during charge/discharge cycles. Volume variations in the SnSb and SnSb-Sn series were unable to be accommodated by carbon additions at any level, which led to electrode cracking and poor cyclability. In the SnSb-CNT nanocomposite, the CNTs provided a random and open framework structure upon which particles could be chemically bonded. From the viewpoint of further enhancing the electrochemical performance of SnSb materials, CNTs offer more potential than other carbonaceous materials such as MCMB¹⁰ and amorphous carbon.^[212] This is particularly due to the ability of the CNT framework structure to retain excellent electrical contact between active components and its capability to accept high loading of active materials (*i.e.*, on outer and inter tube surfaces). Chemically bonding SnSb particles to the surfaces of CNTs is an effective approach to prevent the agglomeration of nanosized SnSb particles and therefore retain the enhanced electrical properties of SnSb alloys in a nanoscale form.

8.3.6 Summary on SnSb-CNT

SnSb-CNT nanocomposite powders were produced by the reductive precipitation of metal chloride salts. The CNTs were used as a framework upon which nanosized SnSb particles were pinned. The SnSb-CNT powder shows a high reversible capacity and stable cyclability. CNTs proved to be suitable hosts for pinning nanosized SnSb particles and preventing their agglomeration, as well as for maintaining the electrical connection around the SnSb particles. Careful attention to the design and fabrication of these types of complex nanocomposites may lead to their full potential being exploited in commercial rechargeable lithium batteries.

9. Transition Metal Oxide-Carbon Composites Prepared *via* the Spray Pyrolysis Method

9.1 Introduction

There have been a large amount of fundamental studies on TM oxides concerning the reaction mechanisms^[214, 217, 315] and the development of intermediate phases.^[221, 222] The commercial viability of these materials depends upon achieving practical improvements in terms of capacity retention or cycle life. For this study, NiO and Co₃O₄ were selected as promising TM oxide candidates that could be easily synthesized *via* the spray pyrolysis technique. The key advantages of this technique were that it could be easily scaled for mass production and the texture of the final powder product could be partially controlled (*i.e.*, crystallite and particle size and surface area). The texture of a TM oxide powder can influence the nature of the SEI film and therefore may be tailored in order to improve the cycle life of the electrode. The spray pyrolysis technique was also perfectly suited to synthesize TM oxide - carbon composite powders *in-situ*. Previous studies on TM oxide powders have indicated that the formation of a TM oxide - carbon composite can be an effective approach to contain the volume expansion experienced during charge/discharge cycling.^[209, 306]

9.2 Experimental

Nanostructured NiO, Co₃O₄, and Co₃O₄ - C powders were prepared in separate experiments using a vertical spray pyrolysis apparatus shown in section 3.2.6. The NiO and Co₃O₄ powders were obtained by spraying aqueous 0.2 M cobalt or nickel nitrate solutions at ambient temperature through an ultrasonic nozzle at 3 mL min⁻¹ into an open air 2 m quartz tube at 600 °C. For preparation of the Co₃O₄ - C powder, the precursor solution also contained 0.05 M sucrose. Sucrose was used as a carbon source because it is cheap, abundant, and has a high chemical purity. The experimental conditions for the pyrolysis of this solution were identical to those described for NiO and Co₃O₄ powders. All powders were dried overnight at 110 °C in a vacuum oven to evaporate excess moisture prior to electrochemical testing. The XRD technique was used to confirm the phase purity of the powders and the average

crystallite size was estimated using the Scherrer equation. The carbon content of the Co_3O_4 - C powder was analyzed by the TGA method performed in static air on a Setaram 92 apparatus at $10\text{ }^\circ\text{C min}^{-1}$. The morphology of the powders was observed using SEM and TEM. The results obtained from TGA experiment on Co_3O_4 - C powder were compared to the carbon content measured by EDXS. The specific surface area of the powders was calculated using the BET multipoint method, and particle size distributions were mapped using data obtained from a Malvern Instruments Mastersizer.

Electrochemical measurements were conducted by assembly of standard R2032 coin-type test cells. In the case of NiO and Co_3O_4 powders, working electrodes were constructed by mixing 80 wt% active powder, 8 wt% carbon black, and 12 wt% pvdF with a mortar and pestle. For the Co_3O_4 - C powder, 88 wt% of active material was used, with the remaining 12 wt% made up of pvdF binder. Charge/discharge cycles of the half cells were measured between 0.02 V and 3.0 V at a C/30 rate. EIS measurements were recorded potentiostatically by applying an ac voltage of 5 mV over a 100 kHz - 10 mHz range at various OCVs on the 10th discharge. A 2 h rest period was observed at each voltage to allow the system to establish equilibrium. The impedance spectra obtained were modeled with an equivalent circuit diagram and analyzed using the ZviewTM computer software.

9.3 Results and Discussion

9.3.1 Structural and Morphological Characterization

Fig. 9.1 shows the XRD patterns for the sprayed NiO, Co_3O_4 , and Co_3O_4 - C powders. The NiO powder (Fig. 9.1a) shows Bragg reflections that are indexed according to pure phase NiO Bunsenite compound with a cubic crystal structure and the $Fm-3m$ space group. The broadened nature of the three main diffraction peaks at 37.4° , 43.5° , and 62.6° ((111), (200), and (220) reflections, respectively) suggests that the powder has a nanocrystalline morphology, which is confirmed by the calculated crystallite size of 8.7 nm. The Co_3O_4 and Co_3O_4 - C powders (Fig. 9.1b) show Bragg reflections that are indexed to the cubic Co_3O_4 phase with the $Fd-3m$ space group. The crystallite sizes for Co_3O_4 and Co_3O_4 - C powders were calculated

to be 10.2 nm and 12 nm, respectively. The swollen nature of the $\text{Co}_3\text{O}_4 - \text{C}$ graph at low scattering angle ($2\theta < 30^\circ$) is indicative of disordered carbon.^[177, 178]

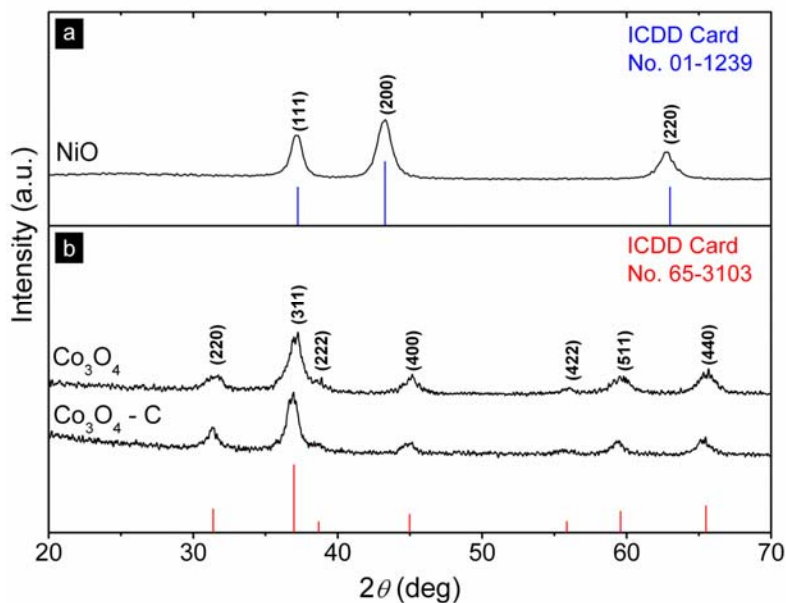


Figure 9.1: X-ray diffraction patterns of NiO (a), and Co_3O_4 and $\text{Co}_3\text{O}_4 - \text{C}$ (b).

The actual quantity of carbon in the $\text{Co}_3\text{O}_4 - \text{C}$ composite powder was calculated by TGA at 22 wt% and by EDXS area analysis at 27 wt%. The close agreement of these values confirms the carbon content of the composite to be in the 20-30 wt% range. It is expected that a large fraction of the carbon in the precursor solution was also lost to the atmosphere as CO_2 during pyrolysis.

Initial low magnification observations suggested that all three powders were composed of a mixture of partially and fully developed hollow spheres that were 1-5 μm in diameter and had an average wall thickness of 0.5-2 μm . An SEM image of this typical morphology is presented in Fig. 9.2a. It is expected that this general morphology forms as a result of the highly reactive particles coalescing within the reaction chamber moments after being sprayed. Higher magnification observations by TEM revealed that the morphology of the $\text{Co}_3\text{O}_4 - \text{C}$ powder shown in Fig. 9.2b and c was slightly different to those of the non-composite powders. Fig. 9.2b shows that each $\text{Co}_3\text{O}_4 - \text{C}$ sphere was actually an agglomeration of sub-micron particles coated with a thin carbon rich sheath as determined by SAD. The carbon sheath measured 2-5 nm (Fig. 9.2c) but was not thick enough to account for the entire

carbon content of 20-30 wt% that was determined by TGA. The remainder of the carbon can be identified as black spots (~ 1 nm) in Fig. 9.2c dispersed among larger domains of crystalline Co_3O_4 . EDXS analysis confirmed that the disordered carbon was evenly distributed across the surface of the $\text{Co}_3\text{O}_4 - \text{C}$ and also throughout the wall thickness of the particles.

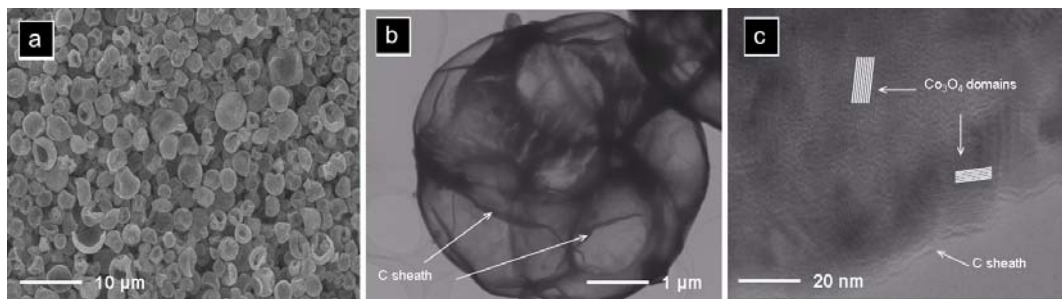


Figure 9.2: Images of $\text{Co}_3\text{O}_4 - \text{C}$ powder. A low magnification SEM view (a), a TEM image of the nanoporous carbon sheath coated on a $\text{Co}_3\text{O}_4 - \text{C}$ particle (b), and a higher magnification TEM image of finely distributed disordered C and crystalline Co_3O_4 domains within an individual particle (c).

Fig. 9.3 shows the particle size distribution and BET surface areas of NiO , Co_3O_4 , and $\text{Co}_3\text{O}_4 - \text{C}$ powders. All powders have a narrow Gaussian distribution from 3-6 µm, which supports SEM and TEM observations. The surface area of powders in decreasing order was $\text{Co}_3\text{O}_4 - \text{C}$, Co_3O_4 , and NiO . The larger surface area of $\text{Co}_3\text{O}_4 - \text{C}$ can be explained by the additional gases given off during the decomposition of the sugar solution, which would have produced a more aerated powder product.

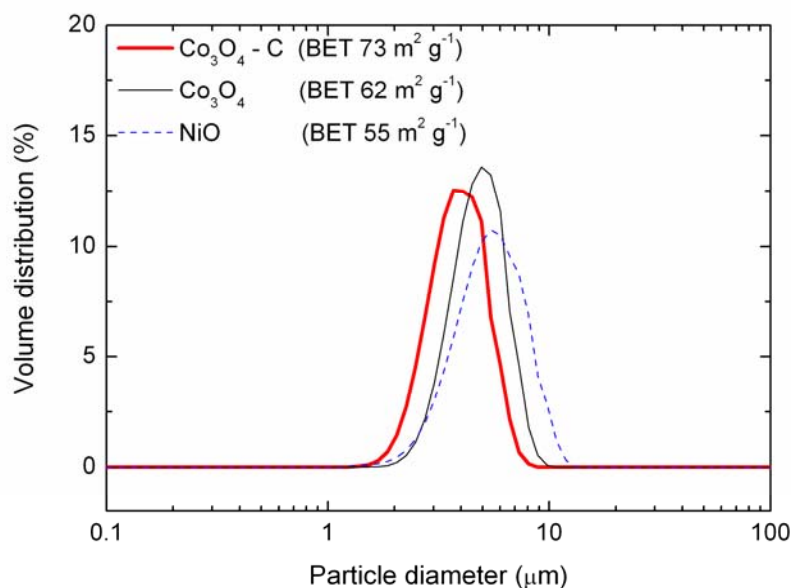


Figure 9.3: Particle size distribution and BET specific surface areas of NiO, Co_3O_4 , and $\text{Co}_3\text{O}_4 - \text{C}$ powders.

Based on small angle x-ray scattering experiments, it has been reported that pyrolyzed carbons contain a mix of open and closed nanopores and have an increased powder surface area by up to several hundred percent.^[316] It is well documented that using powders with an extremely large surface area ($> 100 \text{ m}^2 \text{ g}^{-1}$) can produce initial improvements in the cell capacity, but the cell will then suffer poor charge/discharge cyclability due to an enhanced electrolyte degradation and concomitant formation of a thick SEI layer.^[226, 317] The surface areas of all the TM oxide powders produced in this work ($55\text{--}73 \text{ m}^2 \text{ g}^{-1}$) are not considered to be excessively large.

9.3.2 Electrochemical Properties

The discharge capacity over 50 cycles and selected discharge curves are shown in Fig. 9.4. In Fig. 9.4a, $\text{Co}_3\text{O}_4 - \text{C}$ maintained a capacity of over 800 mAh g^{-1} for 50 cycles, whereas Co_3O_4 and NiO showed a steady decay to 300 mAh g^{-1} and 280 mAh g^{-1} , respectively. The capacity retention of $\text{Co}_3\text{O}_4 - \text{C}$ was also superior to that of Co_3O_4 powders that were prepared by thermal decomposition of a cobalt octacarbonyl compound as reported by the ISEM elsewhere.^[220, 223]

The 1st and 50th cycle discharge curves for NiO, Co₃O₄, and Co₃O₄ – C powders are shown in Fig. 9.4b. Here we see the voltage plateaus that were present for the non-composite Co₃O₄ (at 1.1 V) and NiO (at 0.6 V) during the 1st cycle, almost disappear in the 50th cycle. Conversely for Co₃O₄ – C, the voltage plateau that was responsible for the high capacity achieved in early cycling is preserved in the 50th cycle. The improved cyclability of Co₃O₄ – C can be partly attributed to the carbon coating on the surface of the Co₃O₄ crystals. The carbon coating simultaneously shields the electrolyte from advanced decomposition caused by exposure to cobalt nanoparticles and enhances the overall electronic conductivity of the electrode. Furthermore, the carbon coating and the fine distribution of disordered carbon present throughout the bulk powder would also help accommodate the volume expansion and contraction that occur during discharge/charge cycling by providing a cushion effect.

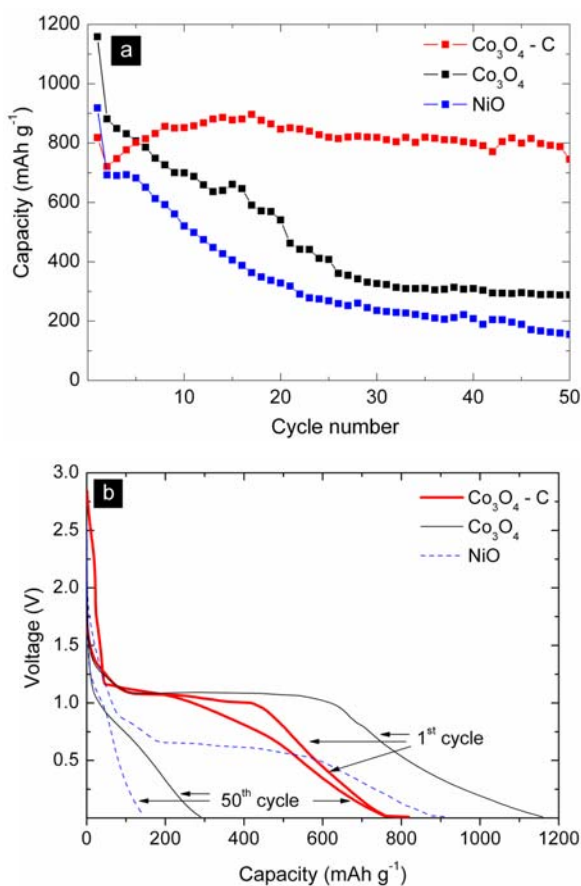


Figure 9.4: The electrochemical performance of Co₃O₄ – C, Co₃O₄, and NiO powders, showing discharge capacity over 50 cycles (a) and the 1st and 50th cycle discharge curves (b).

9.3.3 Electrochemical Impedance Spectroscopy

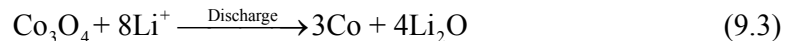
EIS was used to further elucidate the nature of the cyclability improvement demonstrated in $\text{Co}_3\text{O}_4 - \text{C}$ by collecting Nyquist plots at various predetermined voltages (2.0, 1.6, 1.2, 1.0, 0.8, 0.4, and 0.2 V) on the 10th discharge cycle. EIS is a powerful technique for electrode kinetic analysis due to the information that can be deduced for each reaction process, including those in the electrolyte, passivation layer(s), charge transfer, and Li^+ diffusion. The impedance spectra on the 10th discharge for $\text{Co}_3\text{O}_4 - \text{C}$ and Co_3O_4 at various OCV are presented in Fig. 9.5. For all measurements, the overall shape of the Nyquist plots show the characteristic depressed semicircle in the high and middle-frequency range and an extended tail at approximately 45° to the Z' axis. The semicircle is often considered to be the superposition of two individual semicircles, even though the exact separation of these is not well developed in our case. Usually a small high frequency semicircle is identified that corresponds to the formation of the SEI, which creates impedance at the surface of the active powder particles in contact with the organic electrolyte.^[318-320] The resistance (R) and capacitance (C) values associated with the migration of Li^+ through the SEI are described by the following:

$$R = \rho l / S \quad (9.1)$$

$$C = \epsilon S / l \quad (9.2)$$

where S is the electrode surface area and l is the thickness, ρ is the resistivity, and ϵ the permittivity of the SEI layer.^[321] However, since only one semicircle is distinguishable, the exact contribution of this component to the overall cell impedance is unable to be quantified. The existence of only one semicircle is common and has been reported previously.^[322]

The semicircle that dominates at intermediate frequency represents the charge transfer impedance (R_{ct}) through the electrode-electrolyte interface and is considered to account for a large proportion of the overall kinetic impedance of the cell. From Fig. 9.5a and b, the size of this semicircle in both powders is reduced considerably at voltages lower than 1.2 V, since the primary reaction plateau for the cell discharge described in Eqn. 9.3 occurs at just below this value.



The sloping line at $\sim 45^\circ$ to the Z' axis found at low frequency is known as the Warburg impedance and represents the diffusion of Li^+ within the bulk anode.^[323] The high frequency intercept at the Z' axis corresponds primarily to the electrolyte resistance (R_s) but small contributions may also exist from the wire resistance of the system and solid-solid contact.

To obtain quantitative results, an equivalent circuit (insets of Fig. 9.5a and b) was used to fit the Nyquist plots, where R_s = solution resistance, R_{ct} = charge transfer resistance, and W is the Li^+ diffusion resistance. A Constant Phase Element (CPE) was used to account for the complexity of the double layer effect associated with charge transfer resistance. The fit result parameters are summarized in Fig. 9.5c where the R_s values for $\text{Co}_3\text{O}_4 - \text{C}$ are lower than those of Co_3O_4 . The values of R_{ct} at various potentials also show the same trend, except at 0.8 V and 1.2 V, where the values are similar. The generally lower trend of values of R_s and R_{ct} for $\text{Co}_3\text{O}_4 - \text{C}$ can be attributed to the improvement of electronic conductivity due to the formation of a disordered carbon sheath. Moreover, the sheath that coats Co_3O_4 crystals in the $\text{Co}_3\text{O}_4 - \text{C}$ composite could also induce the formation of a coherent and stable SEI layer, thereby contributing to the excellent cycling performance.^[318]

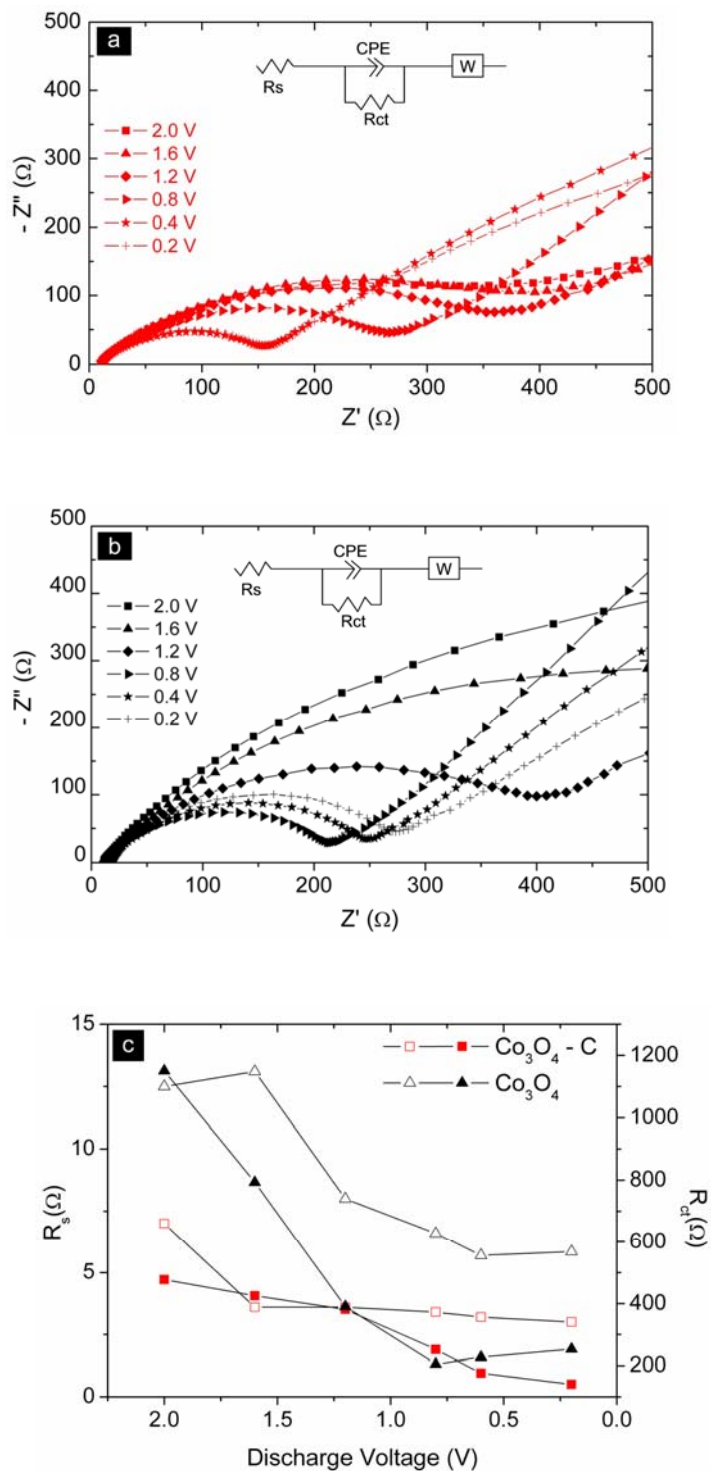


Figure 9.5: Nyquist plots of Co_3O_4 -C (a) and Co_3O_4 (b) electrodes, and the fitted equivalent circuit parameters vs. discharge voltage (c). R_s is represented by open symbols and R_{ct} by closed symbols.

9.4 Summary

Nanocrystalline TM oxide powders with a narrow Gaussian type particle size distribution (3-6 μm) were synthesized by the spray pyrolysis technique. Test cells made from $\text{Co}_3\text{O}_4 - \text{C}$ composite powder were characterized by a high reversible capacity of 800 mAh g^{-1} with negligible capacity fade, whereas the electrodes made from Co_3O_4 and NiO powders recorded steady capacity decay upon cycling to less than 40 % of their original capacity. The rapid capacity fade that is often associated with finely divided TM powders can be eliminated by the use of a carbon based composite. The improved electrochemical properties are related to the formation of a carbon sheath that surrounds the particles, shielding the catalytic action of the cobalt nanoparticles on electrolyte reduction and therefore retarding the development of a thick SEI that can impede charge transfer. Furthermore, a disordered carbon matrix is formed throughout the bulk powder, which assists in cushioning the volume expansion associated with the reversible electrochemical reaction.

10. Conclusions and Recommendations

This thesis has investigated various cathode and anode materials for use in rechargeable lithium batteries, as well as novel methods for their synthesis. Investigations into the effects of doping the current commercial cathode material, LiCoO_2 , and its likely replacement, LiFePO_4 , have been reported. Research into anode materials focused on the development of carbon-based composites formed *in-situ* during synthesis. These methods have proved to be a challenging, but rewarding path to improve the lithium storage capability and cyclability of some of the most promising anode materials.

Chapters 4 and 5 provided important structural data on the doping of LiCoO_2 and LiFePO_4 cathode materials, respectively. In the case of LiCoO_2 , doping with magnesium, vanadium, and molybdenum (2 at%) did not provide any improvement in electrochemical performance when compared to the un-doped product. For LiFePO_4 , doping with titanium (1 at%) provided a higher discharge capacity due to an increase in *p*-type semiconductivity. In both materials, the importance of conducting rigorous structural analysis was highlighted as a requirement to elucidate the causes of varied electrochemical performance.

Chapter 6 introduced the use of EDAMM as a new functional materials synthesis technique. The functionalities of the LiCoO_2 , LiFePO_4 , and $\text{SrTi}_{0.5}\text{Co}_{0.5}\text{O}_3$ compounds prepared matched those of powders prepared by traditional approaches. The most compelling feature of EDAMM is that nanoparticles of the desired material can be synthesized in several minutes by the careful selection of electrical and mechanical experimental parameters. It can be expected that the findings presented in this chapter will open innovative new directions for the preparation of a range of inorganic functional materials to be used in tomorrow's applications. More work is required to fully expose the nature of the mechanism(s) responsible for these results.

The benefits of synthesizing compounds in a nanotube form were clearly demonstrated in Chapter 7, which dealt with the formation and the electrochemical assessment of the first NiO nanotube powders. The NiO nanotubes produced a

discharge capacity over 30 % higher than that of NiO nanocrystalline powder and enhanced charge/discharge cyclability. The improved cyclability of NiO nanotube electrode was due to the kinetic advantages of the nanotube electrode. Further optimization of the structure of the NiO nanotubes can be made to further improve their discharge capacity and cyclic performance.

The primary aim in the work presented in Chapter 8 was to address the poor cyclability demonstrated in the high capacity SnSb intermetallic alloys. It was found that the realized capacity of nanosized SnSb and SnSb-Sn could be improved by around 50 % by forming a composite with carbon black (1:1 weight ratio), but not the cyclability. This was because the carbon network improved the electrical conduction, which allowed a better utilization of active particles. This carbon network was not capable of properly accommodating the large volume changes experienced upon cycling. A significant improvement in the cyclability of these alloys could, however, be achieved by forming a chemically bonded SnSb-CNT nanocomposite. In this case, the CNT network acted to simultaneously pin nanosized SnSb particles, preventing their agglomeration, and to absorb volume expansion and maintain excellent electrical connection around individual particles. Careful attention to the design and fabrication of these types of complex nanocomposites may lead to their full potential being exploited in commercial rechargeable lithium batteries.

Chapter 9 presented results from nanocrystalline TM oxide and TM oxide – carbon composite powders. The rapid capacity fade that is often associated with finely divided TM powders can be eliminated by synthesizing a carbon based composite. The Co_3O_4 – C composite powder produced a high reversible capacity with negligible capacity fade, whereas the electrodes made from Co_3O_4 and NiO powders recorded steady capacity decay upon cycling to less than 40 % of their original capacity. The improved cycling stability of the composite electrode was due to a carbon sheath that formed around the active particles, which prevented the catalytic action of the cobalt nanoparticles towards electrolyte reduction. Furthermore, a disordered carbon matrix was formed throughout the bulk powder, which assisted to cushion the volume expansion associated with the reversible electrochemical reaction. These results cannot be limited to the Co_3O_4 system, but also should apply to other promising TM oxide – C composite powders.

11. References

- [1]. J. Larminie and J. Lowry, *Electric Vehicle Technology Explained*, 1st ed, **2003**, England: John Wiley & Sons, 296 pages.
- [2]. W.H. Brock, *The Norton History of Chemistry*, in *Norton History of Science*, R. Porter (Ed), **1993**, New York: W.W. Norton & Company, pp. 480-512.
- [3]. R.M. Dell and D.A.J. Rand, *Understanding Batteries*, 1st ed. RSC Paperbacks, **2001**, Cambridge: Royal Society of Chemistry, 264 pages.
- [4]. I. Asimov, *Asimov's Biographical Encyclopedia of Science and Technology*, **1982**, Garden City: Doubleday & Company, 941 pages.
- [5]. I. Buchmann, *Batteries in a Portable World: A Handbook on Rechargeable Batteries for Non-Engineers*, 2nd ed, **2001**, New York: Cadex Electronics Inc., 292 pages.
- [6]. D. Cahan, *Hermann von Helmholtz and the Foundations of Nineteenth Century Science*, **1993**, California: University of California Press, 696 pages.
- [7]. T. Edison, *Research to Development at Menlo Park, January 1879 - March 1881*. The Papers of Thomas A. Edison, ed. P.B. Israel, L. Carlet, D. Hochfelder, and N. Nier, Vol. 5, **2004**, Chicago: The John Hopkins University Press, 1152 pages.
- [8]. M. Josephson, *Edison: A Biography*, Reprint ed, **1992**, Chicago: John Wiley & Sons, 528 pages.
- [9]. J.M. Tarascon and M. Armand, *Nature*, **2001**, 414(6861): p. 359.
- [10]. S. Coe, *World Rechargeable Battery Markets for Mobile IT and Communication Devices*, in *Environment & Energy series*, **2003**, New York: Frost and Sullivan Research Service, pp. 254-80.
- [11]. A. Robinson, *Science*, **1974**, 184: p. 554.
- [12]. K.M. Abraham, D.M. Pasquariello, and F.J. Martin, *J. Electrochem. Soc.*, **1986**, 133(4): p. 661.
- [13]. J.N. Carides and D.W. Murphy, *J. Electrochem. Soc.*, **1977**, 124(9): p. 1309.
- [14]. J.J. Auborn, Y.L. Barberio, K.J. Hanson, D.M. Schleich, and M.J. Martin, *J. Electrochem. Soc.*, **1987**, 134(3): p. 580.
- [15]. J.L. Tirado, *Mater. Sci. Eng. R*, **2003**, 40(3): p. 103.

- [16]. J.R. Dahn, A.K. Sleight, H. Shi, B.M. Way, W.J. Weydanz, J.N. Reimers, Q. Zhong, and U. von Sacken, *Lithium Batteries - New materials, developments and perspectives*, ed. G. Pistoia, **1994**, Amsterdam: Elsevier, 707 pages.
- [17]. J. Broadhead and A.D. Butherus, *Rechargeable non-aqueous battery*, Patent number US 3791867: filing date, 24 Jul. 1972; publication date, 12 Feb. 1974.
- [18]. J. Broadhead, F.J. DiSalvo, and F.A. Trumbore, *Non-aqueous battery using chalcogenide electrode*, Patent number US 3864167: filing date, 19 Apr. 1973; publication date, 4 Feb. 1975.
- [19]. K. Mizushima, P.C. Jones, P.J. Wiseman, and J.B. Goodenough, *Solid State Ionics*, **1980**, 3(4-5): p. 171.
- [20]. K. Mizushima, P.C. Jones, P.J. Wiseman, and J.B. Goodenough, *Mater. Res. Bull.*, **1980**, 15(6): p. 783.
- [21]. D.W. Murphy, F.J. Di Salvo, J.N. Carides, and J.V. Waszczak, *Mater. Res. Bull.*, **1978**, 13(12): p. 1395.
- [22]. M. Lazzari and B. Scrosati, *J. Electrochem. Soc.*, **1980**, 127: p. 773.
- [23]. B.D. Pietro, M. Patriaca, and B. Scrosati, *J. Power Sources*, **1982**, 8: p. 298.
- [24]. S. Basu, *Ambient temperature rechargeable battery*, Patent number US 4,423,125: filing date, 13 Sept. 1982; publication date, 27 Dec. 1983.
- [25]. M. Mohri, N. Yanagisawa, Y. Tajima, H. Tanaka, T. Mitate, S. Nakajima, M. Yoshida, Y. Yoshimoto, T. Suzuki, and H. Wada, *J. Power Sources*, **1989**, 26(3-4): p. 545.
- [26]. T. Nagaura and K. Tozawa, *Prog. Batteries Solar Cells*, **1990**, 9: p. 209.
- [27]. K. Sekai, H. Azuma, A. Omaru, S. Fujita, H. Imoto, T. Endo, I. Yamaura, I. Nishi, H. Mashiko, and M. Yokogawa, *J. Power Sources*, **1993**, 43-44: p. 241.
- [28]. Y. Kida, K. Yanagida, A. Funahashi, T. Nohma, and I. Yoneza, *J. Power Sources*, **2001**, 94: p. 74.
- [29]. H. Abe, T. Murai, and K. Zaghib, *J. Power Sources*, **1999**, 77: p. 110.
- [30]. H. Higuchi, K. Uenae, and A. Kawakami, *J. Power Sources*, **1997**, 68: p. 212.
- [31]. T. Iwahori, Y. Ozaki, A. Funahashi, H. Momose, I. Mitsuishi, S. Shiraga, S. Yoshitake, and H. Awata, *J. Power Sources*, **1999**, 81-82: p. 872.
- [32]. P. Arora, R.E. White, and M. Doyle, *J. Electrochem. Soc.*, **1998**, 145(10): p. 3647.

- [33]. G. Pistoia, A. Antonini, R. Rosati, and D. Zane, *Electrochim. Acta*, **1996**, 41(17): p. 2683.
- [34]. G.G. Amatucci, C.N. Schmutz, A. Blyr, C. Sigala, A.S. Gozdz, D. Larcher, and J.M. Tarascon, *J. Power Sources*, **1997**, 69(1-2): p. 11.
- [35]. R.A. Huggins, *Binary Electrodes under equilibrium or near-equilibrium conditions*, in *Materials for Lithium-Ion Batteries*, C. Julien and Z. Stoyanov (Eds), **2000**, New York: Kluwer Academic Publishers, pp. 74-104.
- [36]. M.S. Whittingham, *Prog. Solid State Chem.*, **1978**, 12(1): p. 41.
- [37]. C. Delmas, I. Saadoune, and A. Rougier, *J. Power Sources*, **1993**, 44(1-3): p. 595.
- [38]. M.H. Lee, Y.J. Kang, S.T. Myung, and Y.K. Sun, *Electrochim. Acta*, **2004**, 50(4): p. 939.
- [39]. J.R. Dahn, E.W. Fuller, M. Obrovac, and U. von Sacken, *Solid State Ionics*, **1994**, 69(3-4): p. 265.
- [40]. W.I.F. David, M.M. Thackeray, P.G. Bruce, and J.B. Goodenough, *Mater. Res. Bull.*, **1984**, 19(1): p. 99.
- [41]. A.K. Padhi, K.S. Nanjundaswamy, and J.B. Goodenough, *J. Electrochem. Soc.*, **1997**, 144(4): p. 1188.
- [42]. E. Rossen, J.N. Reimers, and J.R. Dahn, *Solid State Ionics*, **1993**, 62(1-2): p. 53.
- [43]. R.J. Gummow and M.M. Thackeray, *J. Electrochem. Soc.*, **1993**, 140(12): p. 3365.
- [44]. R.J. Gummow, M.M. Thackeray, W.I.F. David, and S. Hull, *Mater. Res. Bull.*, **1992**, 27(3): p. 327.
- [45]. M. Menetrier, I. Saadoune, S. Levasseur, and C. Delmas, *J. Mater. Chem.*, **1999**, 9(5): p. 1135.
- [46]. S.G. Kang, S.Y. Kang, K.S. Ryu, and S.H. Chang, *Solid State Ionics*, **1999**, 120(1): p. 155.
- [47]. K. Adhikary, M. Takahashi, and S. Kikkawa, *Mater. Res. Bull.*, **1998**, 33(12): p. 1845.
- [48]. B. Garcia, J. Farcy, J.P. Pereira-Ramos, and N. Baffier, *J. Electrochem. Soc.*, **1997**, 144(4): p. 1179.
- [49]. E. Antolini, *Solid State Ionics*, **2004**, 170(3-4): p. 159.

- [50]. M.G.S.R. Thomas, P.G. Bruce, and J.B. Goodenough, *J. Electrochem. Soc.*, **1985**, 132(7): p. 1521.
- [51]. M.G.S.R. Thomas, P.G. Bruce, and J.B. Goodenough, *Solid State Ionics*, **1985**, 17(1): p. 13.
- [52]. T. Ohzuku and A. Ueda, *Solid State Ionics*, **1994**, 69(3-4): p. 201.
- [53]. W.D. Johnston, R.R. Heikes, and D. Sestrich, *J. Phys. Chem. Solids*, **1958**, 7: p. 1.
- [54]. H.J. Orman and P.J. Wiseman, *Acta Cryst.*, **1984**, C40: p. 12.
- [55]. K. Kang, Y.S. Meng, J. Bréger, C.P. Grey, and G. Ceder, *Science*, **2006**, 311(5763): p. 977.
- [56]. A. Andersson, *Surface Phenomena in Li-ion Batteries*. Comprehensive Summaries of Uppsala Dissertations from the Faculty of Science and Technology, Vol. 656, **2001**: Acta Universitatis Upsaliensis, 54 pages.
- [57]. R. Alcantara, P. Lavela, J.L. Tirado, R. Stoyanova, and E. Zhecheva, *J. Solid State Chem.*, **1997**, 134(2): p. 265.
- [58]. G. Ceder, Y.M. Chiang, D.R. Sadoway, M.K. Aydinol, Y.I. Jang, and B. Huang, *Nature*, **1998**, 392(6677): p. 694.
- [59]. G.G. Amatucci, J.M. Tarascon, and L.C. Klein, *J. Electrochem. Soc.*, **1996**, 143(3): p. 1114.
- [60]. G.G. Amatucci, J.M. Tarascon, and L.C. Klein, *Solid State Ionics*, **1996**, 83(1-2): p. 167.
- [61]. N. Imanishi, M. Fujiyoshi, Y. Takeda, O. Yamamoto, and M. Tabuchi, *Solid State Ionics*, **1999**, 118(1-2): p. 121.
- [62]. A. Marini, V. Berbenni, V. Massarotti, D. Capsoni, and E. Antolini, *J. Solid State Chem.*, **1995**, 116(1): p. 15.
- [63]. J.M. Fernandez-Rodriguez, L. Hernan, J. Morales, and J.L. Tirado, *Mater. Res. Bull.*, **1988**, 23(6): p. 899.
- [64]. J.R. Dahn, U. von Sacken, and C.A. Michal, *Solid State Ionics*, **1990**, 44(1-2): p. 87.
- [65]. A. Honders, J.M. der Kinderen, A.H. van Heeren, J.H.W. de Wit, and G.H.J. Broers, *Solid State Ionics*, **1984**, 14(3): p. 205.
- [66]. C. Lagergren, A. Lundblad, and B. Bergman, *J. Electrochem. Soc.*, **1994**, 141(11): p. 2959.

- [67]. P. Barboux, J.M. Tarascon, and F.K. Shokoohi, *J. Solid State Chem.*, **1991**, 94(1): p. 185.
- [68]. M. Carewska, A. Di Bartolomeo, and S. Scaccia, *Thermochim. Acta*, **1995**, 269-270: p. 491.
- [69]. A. Lundblad and B. Bergman, *Solid State Ionics*, **1997**, 96(3-4): p. 183.
- [70]. K. Konstantinov, G.X. Wang, J. Yao, H.K. Liu, and S.X. Dou, *J. Power Sources*, **2003**, 119-121: p. 195.
- [71]. A. Ueda and T. Ohzuku, *J. Electrochem. Soc.*, **1994**, 141: p. 2010.
- [72]. W. Li and J.C. Currie, *J. Electrochem. Soc.*, **1997**, 144(8): p. 2773.
- [73]. S. Venkatraman, V. Subramanian, S. Gopukumar, N.G. Renganathan, and N. Muniyandi, *Electrochem. Comm.*, **2000**, 2(1): p. 18.
- [74]. Y.-I. Jang, B. Huang, H. Wang, D.R. Sadoway, G. Ceder, Y.-M. Chiang, H. Liu, and H. Tamura, *J. Electrochem. Soc.*, **1999**, 146(3): p. 862.
- [75]. M. Zou, M. Yoshio, S. Gopukumar, and J.I. Yamaki, *Chem. Mater.*, **2005**, 17(6): p. 1284.
- [76]. S. Levasseur, M. Menetrier, and C. Delmas, *J. Power Sources*, **2002**, 112(2): p. 419.
- [77]. Y. Jin, P. Lin, and C.H. Chen, *Solid State Ionics*, **2006**, 177(3-4): p. 317.
- [78]. M. Zou, M. Yoshio, S. Gopukumar, and J.I. Yamaki, *Electrochem. Solid-State Lett.*, **2004**, 7(7): p. A176.
- [79]. S.M. Lala, L.A. Montoro, V. Lemos, M. Abbate, and J.M. Rosolen, *Electrochim. Acta*, **2005**, 51(1): p. 7.
- [80]. S. Tao, Q. Wu, Z. Zhan, and G. Meng, *Solid State Ionics*, **1999**, 124(1): p. 53.
- [81]. W.S. Yoon and K.B. Kim, *J. Power Sources*, **1999**, 81-82: p. 517.
- [82]. I.H. Oh, S.A. Hong, and Y.K. Sun, *J. Mater. Sci.*, **1997**, 32(12): p. 3177.
- [83]. Y.K. Sun, I.H. Oh, and S.A. Hong, *J. Mater. Sci.*, **1996**, 31(14): p. 3617.
- [84]. A. Burukhin, O. Brylev, P. Hany, and B.R. Churagulov, *Solid State Ionics*, **2002**, 151(1-4): p. 259.
- [85]. K. Kanamura, A. Goto, R.Y. Ho, T. Umegaki, K. Toyoshima, K.I. Okada, Y. Hakuta, T. Adschiri, and K. Arai, *Electrochem. Solid-State Lett.*, **2000**, 3(6): p. 256.
- [86]. H. Yan, X. Huang, Z. Lu, H. Huang, R. Xue, and L. Chen, *J. Power Sources*, **1997**, 68(2): p. 530.

- [87]. C.H. Lu and P.Y. Yeh, *J. Mater. Chem.*, **2000**, 10(3): p. 599.
- [88]. T. Nakamura and A. Kajiyama, *Solid State Ionics*, **1999**, 123(1): p. 95.
- [89]. Y. Li, C. Wan, Y. Wu, C. Jiang, and Y. Zhu, *J. Power Sources*, **2000**, 85(2): p. 294.
- [90]. O.A. Brylev, O.A. Shlyakhtin, T.L. Kulova, A.M. Skundin, and Y.D. Tretyakov, *Solid State Ionics*, **2003**, 156(3-4): p. 291.
- [91]. C.H. Han, Y.S. Hong, C.M. Park, and K. Kim, *J. Power Sources*, **2001**, 92(1-2): p. 95.
- [92]. Z. Chen and J.R. Dahn, *Electrochem. Solid-State Lett.*, **2002**, 5(10): p. A213.
- [93]. Z. Wang, C. Wu, L. Liu, F. Wu, L. Chen, and X. Huang, *J. Electrochem. Soc.*, **2002**, 149(4): p. A466.
- [94]. G. Fey, H. Yang, T. Kumar, S. Naik, A. Chiang, D. Lee, and J. Lin, *J. Power Sources*, **2004**, 132: p. 172.
- [95]. J. Cho, Y.J. Kim, T.-J. Kim, and B. Park, *Angew. Chem. Int. Ed.*, **2001**, 40(18): p. 3367.
- [96]. J. Cho, Y.J. Kim, T.-J. Kim, and B. Park, *Chem. Mater.*, **2000**, 12: p. 3788.
- [97]. S.-M. Park, T.-H. Cho, Y.-M. Kim, and M. Yoshio, *Electrochem. Solid-State Lett.*, **2005**, 8(6): p. A299.
- [98]. J. Cho and G. Kim, *Electrochem. Solid-State Lett.*, **1999**, 2(6): p. 253.
- [99]. L. Liu, Z. Wang, H. Li, L. Chen, and X. Huang, *Solid State Ionics*, **2002**, 152-153: p. 341.
- [100]. C. Jaephil, K. Chan-Soo, and Y. Sang-Im, *Electrochem. Solid-State Lett.*, **2000**, 3(8): p. 362.
- [101]. M.S. Whittingham, *Chem. Rev.*, **2004**, 104(10): p. 4271.
- [102]. M.S. Whittingham, R.F. Savinell, and T. Zawodzinski, *Chem. Rev.*, **2004**, 104(10): p. 4243.
- [103]. Y. Takeda, K. Nakahara, M. Nishijima, N. Imanishi, O. Yamamoto, M. Takano, and R. Kanoo, *Mater. Res. Bull.*, **1994**, 29(6): p. 659.
- [104]. A. Le Mehaute, G. Ouvrard, R. Brec, and J. Rouxel, *Mater. Res. Bull.*, **1977**, 12(12): p. 1191.
- [105]. R. Brec, A. Dugast, and A. Le Mehaute, *Mater. Res. Bull.*, **1980**, 15(5): p. 619.

- [106]. A.K. Padhi, V. Manivannan, and J.B. Goodenough, *J. Electrochem. Soc.*, **1998**, 145(5): p. 1518.
- [107]. A.K. Padhi, K.S. Nanjundaswamy, C. Masquelier, and J.B. Goodenough, *J. Electrochem. Soc.*, **1997**, 144(8): p. 2581.
- [108]. A.K. Padhi, K.S. Nanjundaswamy, C. Masquelier, S. Okada, and J.B. Goodenough, *J. Electrochem. Soc.*, **1997**, 144(5): p. 1609.
- [109]. A. Manthiram and J.B. Goodenough, *J. Power Sources*, **1989**, 26(3-4): p. 403.
- [110]. C. Masquelier, C. Wurm, J. Rodriguez-Carvajal, J. Gaubicher, and L. Nazar, *Chem. Mater.*, **2000**, 12(2): p. 525.
- [111]. O. Garcia-Martin, M. Alvarez-Vega, F. Garcia-Alvarado, J. Garcia-Jaca, J.M. Gallardo-Amores, M.L. Sanjuán, and U. Amador, *Chem. Mater.*, **2001**, 13: p. 1570.
- [112]. S. Yang, Y. Song, P.Y. Zavalij, and M.S. Whittingham, *Electrochem. Comm.*, **2002**, 4: p. 239.
- [113]. S.Y. Chung, J.T. Bloking, and Y.M. Chiang, *Nature Mater.*, **2002**, 1(2): p. 123.
- [114]. S. Yang, Y. Song, K. Ngala, P.Y. Zavalij, and M.S. Whittingham, *J. Power Sources*, **2003**, 119-121: p. 239.
- [115]. A.S. Andersson, J.O. Thomas, B. Kalska, and L. Häggström, *Electrochem. Solid-State Lett.*, **2000**, 3(2): p. 66.
- [116]. N. Ravet, J.B. Goodenough, S. Besner, M. Simoneau, P. Hovington, and M. Armand, *Proceedings of the 196th ECS Meeting*, **1999**, Abstract 127.
- [117]. H. Huang, S.-C. Yin, and L.F. Nazar, *Electrochem. Solid-State Lett.*, **2001**, 4(10): p. A170.
- [118]. F. Croce, A. D'Epifanio, J. Hassoun, A. Deptula, T. Olczac, and B. Scrosati, *Electrochem. Solid-State Lett.*, **2002**, 5(3): p. A47.
- [119]. P.S. Herle, B. Ellis, N. Coombs, and L.F. Nazar, *Nature Mater.*, **2004**, 3(3): p. 147.
- [120]. C. Delacourt, P. Poizot, S. Levasseur, and C. Masquelier, *Electrochem. Solid-State Lett.*, **2006**, 9(7): p. A352.
- [121]. J. Molenda, A. Stoklosa, and T. Bak, *Solid State Ionics*, **1989**, 36: p. 53.
- [122]. N. Ravet, A. Abouimrane, M. Armand, S.-Y. Chung, J.T. Bloking, and Y.-M. Chiang, *Nature Mater.*, **2003**, 2(11): p. 702.

- [123]. M.S. Islam, D.J. Driscoll, C.A.J. Fisher, and P.R. Slater, *Chem. Mater.*, **2005**, 17(20): p. 5085.
- [124]. C. Delacourt, L. Laffont, R. Bouchet, C. Wurm, J.-B. Leriche, M. Morcrette, J.-M. Tarascon, and C. Masquelier, *J. Electrochem. Soc.*, **2005**, 152: p. A913.
- [125]. Y.L. Ruan and Z.Y. Tang, *Chinese Journal of Nonferrous Metals*, **2005**, 15(9): p. 1416.
- [126]. D. Wang, H. Li, S. Shi, X. Huang, and L. Chen, *Electrochim. Acta*, **2005**, 50(14): p. 2955.
- [127]. M. Takahashi, S. Tobishima, K. Takei, and Y. Sakurai, *J. Power Sources*, **2001**, 97-98: p. 508.
- [128]. A. Yamada, S.C. Chung, and K. Hinokuma, *J. Electrochem. Soc.*, **2001**, 148(3): p. A224.
- [129]. G. Meligrana, C. Gerbaldi, A. Tuel, S. Bodoardo, and N. Penazzi, *J. Power Sources*, **2006**, 160(1): p. 516.
- [130]. S. Yang, P.Y. Zavalij, and M.S. Whittingham, *Electrochem. Comm.*, **2001**, 3(9): p. 505.
- [131]. S. Franger, F. Le Cras, C. Bourbon, and H. Rouault, *Electrochem. Solid-State Lett.*, **2002**, 5(10): p. A231.
- [132]. F. Sauvage, E. Baudrin, M. Morcrette, and J.M. Tarascon, *Electrochem. Solid-State Lett.*, **2004**, 7(1): p. A15.
- [133]. J. Yang and J.J. Xu, *J. Electrochem. Soc.*, **2006**, 153(4): p. A716.
- [134]. Y. Hu, M.M. Doeff, R. Kostecki, and R. Finones, *J. Electrochem. Soc.*, **2004**, 151(8): p. A1279.
- [135]. S.J. Kwon, C.W. Kim, W.T. Jeong, and K.S. Lee, *J. Power Sources*, **2004**, 137(1): p. 93.
- [136]. D. Morgan, A. Van der Ven, and G. Ceder, *Electrochem. Solid-State Lett.*, **2004**, 7(2): p. A30.
- [137]. G. Nuspi, C. Vogler, M. Eisgruber, L. Wimmer, N. Schall, C. Fietzek, and W. Weydanz, *Proceedings of the 12th International Meeting on Lithium Batteries*, **2004**, Abstract 293.
- [138]. M.R. Yang, T.H. Teng, and S.H. Wu, *J. Power Sources*, **2006**, 159(1): p. 307.
- [139]. J. Lu, Z. Tang, Z. Zhang, and W. Shen, *Mater. Res. Bull.*, **2005**, 40(12): p. 2039.

- [140]. J.O. Besenhard, *Carbon*, **1976**, 14: p. 111.
- [141]. R. Yazami and P.H. Touzain, *J. Power Sources*, **1983**, 9: p. 365.
- [142]. Y. Akira, S. Kenichi, and N. Takayuki, *Secondary Battery*, Patent number US 4 668 595: filing date, 9 May 1986; publication date, 26 May 1987.
- [143]. S. Dresselhasu, G. Dresselhasu, K. Sugihare, I.L. Spain, and H.A. Goldberg, *Graphite Fibres and Filaments*, in *Cardona Manual*, **1988**, New York: Springer, 726 pages.
- [144]. K. Konishita, *Carbon - Electrochemical and Physicochemical Properties*, **1988**, New York: Wiley-Interscience, 560 pages.
- [145]. M. Noel and R. Santhanam, *J. Power Sources*, **1998**, 72: p. 53.
- [146]. M. Noel and V. Suryanarayanan, *J. Power Sources*, **2002**, 111(2): p. 193.
- [147]. K. Guerin, A.F. Bouvier, S. Flandrosis, M. Couzi, B. Simon, and P. Biensan, *J. Electrochem. Soc.*, **1999**, 146(10): p. 3660.
- [148]. J.R. Dahn, T. Zheng, Y. Liu, and J.S. Xue, *Science*, **1995**, 270(5236): p. 590.
- [149]. K. Ouchi and H. Honda, *Fuel*, **1959**, 38: p. 429.
- [150]. J.R. Dahn, W. Xing, and Y. Gao, *Carbon*, **1997**, 35(6): p. 825.
- [151]. T. Zheng, Y. Liu, E.W. Fuller, S. Tseng, U. von Sacken, and J.R. Dahn, *J. Electrochem. Soc.*, **1995**, 142(8): p. 2581.
- [152]. J.D. Bernal, *Proc Roy Soc (London)*, **1924**, A106: p. 749.
- [153]. H. Jagodzinski, *Acta Crystallogr.*, **1949**, 2: p. 298.
- [154]. H. Shi, J. Barker, M.Y. Saïdi, and R. Koksang, *J. Electrochem. Soc.*, **1996**, 143: p. 3466.
- [155]. B. Simon, S. Flandrois, A. Février-Bouvier, and P. Biensan, *Mol. Cryst. Liq. Cryst.*, **1998**, 310: p. 333.
- [156]. S. Flandrois and B. Simon, *Carbon* **1999**, 37: p. 165.
- [157]. R. Alcántara, J.M. Jiménez-Mateos, and J.L. Tirado, *J. Electrochem. Soc.*, **2002**, 149(2): p. A201.
- [158]. R. Alcántara, J.M. Jiménez-Mateos, P. Lavela, J. Morales, and J.L. Tirado, *Mat. Sci. Eng. B*, **1996**, 39(3): p. 216.
- [159]. R. Yazami, *Lithium Batteries - New Materials, Developments and Perspectives*, ed. G. Pistoia, **1994**, Amsterdam: Elsevier, 49 pages.
- [160]. D. Aurbach and O. Chusid, *J. Electrochem. Soc.*, **1993**, 140(11): p. 155.

- [161]. D. Aurbach, Y. Ein-Eli, B. Markovsky, A. Zaban, S. Luski, Y. Carmeli, and H. Yamin, *J. Electrochem. Soc.*, **1995**, 142(9): p. 2882.
- [162]. D. Aurbach, B. Markovsky, A. Shechter, Y. Ein-Eli, and H. Cohen, *J. Electrochem. Soc.*, **1996**, 143(12): p. 3809.
- [163]. D. Aurbach, B. Markovsky, I. Weissman, E. Levi, and Y. Ein-Eli, *Electrochim. Acta*, **1999**, 45(1): p. 67.
- [164]. D. Aurbach, Y. Talyosef, B. Markovsky, E. Markevich, E. Zinigrad, L. Asraf, J.S. Gnanaraj, and H.J. Kim, *Electrochim. Acta*, **2004**, 50(2-3): p. 247.
- [165]. D. Aurbach, A. Zaban, Y. Ein-Eli, I. Weissman, O. Chusid, B. Markovsky, M. Levi, E. Levi, A. Schechter, and E. Granot, *J. Power Sources*, **1997**, 68(1): p. 91.
- [166]. D. Aurbach, A. Zaban, A. Schechter, Y. Ein-Eli, E. Zinigrad, and B. Markovsky, *J. Electrochem. Soc.*, **1995**, 142(9): p. 2873.
- [167]. D. Aurbach, E. Zinigrad, Y. Cohen, and H. Teller, *Solid State Ionics*, **2002**, 148(3-4): p. 405.
- [168]. Y. Ein-Eli, B. Markovsky, D. Aurbach, Y. Carmeli, H. Yamin, and S. Luski, *Electrochim. Acta*, **1994**, 39(17): p. 2559.
- [169]. Y. Ein-Eli, S.F. McDevitt, D. Aurbach, B. Markovsky, and A. Schechter, *J. Electrochem. Soc.*, **1997**, 144(7): p. L180.
- [170]. Y. Ein-Eli, S.R. Thomas, V. Koch, D. Aurbach, B. Markovsky, and A. Schechter, *J. Electrochem. Soc.*, **1996**, 143(12): p. L273.
- [171]. R. McMillan, H. Sleg, Z.X. Shu, and W. Wang, *J. Power Sources*, **1999**, 81-82: p. 20.
- [172]. G.H. Wrodnigg, J.O. Besenhard, and M. Winter, *J. Electrochem. Soc.*, **1999**, 146: p. 470.
- [173]. V. Suryanarayanan and M. Noel, *J. Power Sources*, **2001**, 94: p. 137.
- [174]. D. Aurbach, A. Zaban, Y. Ein-Eli, L. Weissman, O. Chusid, O.A. Abramson, and B. Markovsky, *J. Power Sources*, **1995**, 54: p. 78.
- [175]. R. Owusu-Apenten, *Introduction to food chemistry*, **2004**, Boca Raton: CRC Press, 51 pages.
- [176]. P.M. Gaman and K.B. Sherrington, *The science of food: an introduction to food science, nutrition, and microbiology*, **1981**, New York: Pergamon Press, 252 pages.

- [177]. W. Xing, J.-S. Xue, and J.R. Dahn, *J. Electrochem. Soc.*, **1996**, 143: p. 3046.
- [178]. W. Xing, R.A. Dunlap, and J.R. Dahn, *J. Electrochem. Soc.*, **1998**, 145: p. 62.
- [179]. E. Buiel, A.E. George, and J.R. Dahn, *J. Electrochem. Soc.*, **1998**, 145: p. 2252.
- [180]. G.T.K. Fey and C.-L. Chen, *J. Power Sources*, **2001**, 97-98: p. 47.
- [181]. S.-I. Yamada, H. Imoto, K. Sekai, and M. Nagamine, in *Proceedings of the Electrochemical Society Spring Meeting*, **1997**, Montreal, Canada: The Electrochemical Society, Pennington, NJ: p. 85.
- [182]. V. Eskenaziand and E. Peled, in *Proceedings of the Electrochemical Society Fall Meeting*, **1996**, San Antonio, TX: The Electrochemical Society, Pennington, NJ: p. 1051.
- [183]. L. Yuan, K. Konstantinov, G.X. Wang, H.K. Liu, and S.X. Dou, *J. Power Sources*, **2005**, 146(1-2): p. 180.
- [184]. S.L. Bewlay, K. Konstantinov, G.X. Wang, S.X. Dou, and H.K. Liu, *Mater. Lett.*, **2004**, 58(11): p. 1788.
- [185]. J.O. Besenhard, M. Hess, and P. Komenda, *Solid State Ionics*, **1990**, 40-41(2): p. 525.
- [186]. J.O. Besenhard, J. Yang, and M. Winter, *J. Power Sources*, **1997**, 68(1): p. 87.
- [187]. B.A. Boukamp, G.C. Lesh, and R.A. Huggins, *J. Electrochem. Soc.*, **1981**, 128(4): p. 725.
- [188]. Y. Idota, T. Kubota, A. Matsufuji, Y. Maekawa, and T. Miyasaka, *Science*, **1997**, 276(5317): p. 1395.
- [189]. J. Yang, Y. Takeda, N. Imanishi, T. Ichikawa, and O. Yamamoto, *Solid State Ionics*, **2000**, 135(1-4): p. 175.
- [190]. J. Yang, Y. Takeda, N. Imanishi, J.Y. Xie, and O. Yamamoto, *Solid State Ionics*, **2000**, 133(3): p. 189.
- [191]. J. Yang, M. Wachtler, M. Winter, and J.O. Besenhard, *Electrochem. Solid-State Lett.*, **1999**, 2(2-4): p. 161.
- [192]. J. Yang, M. Winter, and J.O. Besenhard, *Solid State Ionics*, **1996**, 90(1-4): p. 281.
- [193]. M. Wachtler, J.O. Besenhard, and M. Winter, *J. Power Sources*, **2001**, 94(2): p. 189.

- [194]. M. Wachtler, M. Winter, and J.O. Besenhard, *J. Power Sources*, **2002**, 105(2): p. 151.
- [195]. A. Osawa, *Nature*, **1927**, 124: p. 14.
- [196]. W.M. Jones and E.G. Bowen, *Nature*, **1930**, 126: p. 846.
- [197]. C.A. MacKay, *J. Appl. Crystallogr.*, **1969**, 2: p. 295.
- [198]. V. Vassiliev, M. Lalaurain, and J. Hertz, *J. Alloys Compd.*, **1997**, 247: p. 223.
- [199]. E.P. Nikolaeva, V.A. Grigorenko, S.D. Gagarkina, and P.Y. Tsypkina, *Zap. Vseross. Mineral. Ova.*, **1970**, 99: p. 68.
- [200]. L. Noréna, R.L. Withersa, S. Schmid, F.J. Brinka, and V. Ting, *J. Solid State Chem.*, **2006**, 179: p. 404.
- [201]. G. Hägg and A.G. Hybinette, *Philos. Mag. Ser.*, **1935**, 7(20): p. 913.
- [202]. P.J.T.L. Oberndorff, A.A. Kodentsov, V. Vuorinen, J.K. Kivilahti, and F.J.J.v. Loo, *Ber. Bunsen-Ges. Phys. Chem.*, **1998**, 102: p. 1321.
- [203]. M. Winter and J.O. Besenhard, *Electrochim. Acta*, **1999**, 45(1): p. 31.
- [204]. J.T. Vaughey, J. O'Hara, and M.M. Thackeray, *Electrochem. Solid-State Lett.*, **2000**, 3(1): p. 13.
- [205]. I. Rom, M. Wachtler, I. Papst, M. Schmied, J.O. Besenhard, F. Hofer, and M. Winter, *Solid State Ionics*, **2001**, 143(3-4): p. 329.
- [206]. A. Trifonova, M. Wachtler, M.R. Wagner, H. Schroettner, C. Mitterbauer, F. Hofer, K.C. Möller, M. Winter, and J.O. Besenhard, *Solid State Ionics*, **2004**, 168(1-2): p. 51.
- [207]. H. Zhao, D.H.L. Ng, Z. Lu, and N. Ma, *J. Alloys Compd.*, **2005**, 395(1-2): p. 192.
- [208]. B. Predel and W. Schwermann, *J. Inst. Metals*, **1971**, 99: p. 169.
- [209]. H. Li, X.J. Huang, L.Q. Chen, Z.G. Wu, and Y. Liang, *Electrochem. Solid-State Lett.*, **1999**, 2: p. 547.
- [210]. H. Li, X. Huang, L. Chen, G. Zhou, Z. Zhang, D. Yu, Y. Jun Mo, and N. Pei, *Solid State Ionics*, **2000**, 135(1-4): p. 181.
- [211]. L. Shi, H. Li, Z. Wang, X. Huang, and L. Chen, *J. Mater. Chem.*, **2001**, 11(5): p. 1502.
- [212]. H. Li, Q. Wang, L. Shi, L. Chen, and X. Huang, *Chem. Mater.*, **2002**, 14(1): p. 103.
- [213]. H. Li, X. Huang, and L. Chen, *Solid State Ionics*, **1999**, 123(3-4): p. 189.

- [214]. P. Poizot, S. Laruelle, S. Grugéon, L. Dupont, and J.M. Tarascon, *Nature*, **2000**, 407(6803): p. 496.
- [215]. P. Buffat and J.P. Borel, *Phys. Rev. A*, **1976**, 13: p. 2287.
- [216]. R.I. Masel, *Principles of Adsorption and Reaction on Solid Surfaces*, **1996**, New York: John Wiley & Sons, 824 pages.
- [217]. S. Grugéon, S. Laruelle, R. Herrera-Urbina, L. Dupont, P. Poizot, and J.M. Tarascon, *J. Electrochem. Soc.*, **2001**, 148(4): p. A285.
- [218]. P. Poizot, S. Laruelle, S. Grugéon, and J.M. Tarascon, *J. Electrochem. Soc.*, **2002**, 149(9): p. A1212.
- [219]. M.M. Thackeray, W.I.F. David, and J.B. Goodenough, *J. Solid State Chem.*, **1984**, 55(3): p. 280.
- [220]. Y. Wang, Z.-W. Fu, and Q.-Z. Qin, *Thin Solid Films*, **2003**, 441: p. 19.
- [221]. D. Larcher, G. Sudant, J.-B. Leriche, Y. Chabre, and J.-M. Tarascon, *J. Electrochem. Soc.*, **2002**, 149(3): p. A234.
- [222]. M.M. Thackeray, S.D. Baker, K.T. Adendorff, and J.B. Goodenough, *Solid State Ionics*, **1985**, 17(2): p. 175.
- [223]. G.X. Wang, Y. Chen, K. Konstantinov, J. Yao, J.-H. Ahn, H.K. Liu, and S.X. Dou, *J. Alloys Compd.*, **2002**, 340: p. L5.
- [224]. Y. Chen, G.X. Wang, K. Kostantinov, J.H. Ahn, H.K. Liu, and S.X. Dou, *J. Metastable Nanocryst. Mat.*, **2003**, 15-16: p. 625.
- [225]. S. Laurelle, S. Grugéon, P. Poizot, M. Dolle, L. Dupont, and J.-M. Tarascon, *J. Electrochem. Soc.*, **2002**, 149(5): p. A627.
- [226]. Z. Yuan, F. Huang, C. Feng, J. Sun, and Y. Zhou, *Mat. Chem. Phys.*, **2003**, 79: p. 1.
- [227]. A.R. Armstrong, G. Armstrong, J. Canales, and P.G. Bruce, *J. Power Sources*, **2005**, 146(1-2): p. 501.
- [228]. A.R. Armstrong, G. Armstrong, J. Canales, and P.G. Bruce, *Angew. Chem.*, **2004**, 43(17): p. 2286.
- [229]. A.R. Armstrong, G. Armstrong, J. Canales, R. García, and P.G. Bruce, *Adv. Mater.*, **2005**, 17(7): p. 862.
- [230]. G. Armstrong, A.R. Armstrong, J. Canales, and P.G. Bruce, *Electrochem. Solid-State Lett.*, **2006**, 9(3): p. A139.

- [231]. G. Armstrong, A.R. Armstrong, J. Canales, and P.G. Bruce, *Chem. Comm.*, **2005**, 19: p. 2454.
- [232]. S. Iijima, *Nature*, **1991**, 354(6348): p. 56.
- [233]. P.M. Ajayan, *Chem. Rev.*, **1999**, 99(7): p. 1787.
- [234]. P.M. Ajayan and O.Z. Zhou, *Top. Appl. Phys.*, **2001**, 80: p. 391.
- [235]. G.E. Possin, *Rev. Sci. Instrum.*, **1970**, 41: p. 772.
- [236]. C.R. Martin, *Science*, **1994**, 266(5193): p. 1961.
- [237]. C.R. Martin, *Chem. Mater.*, **1996**, 8(8): p. 1739.
- [238]. C.R. Martin, *Acc. Chem. Res.*, **1995**, 28: p. 61.
- [239]. B.B. Lakshmi, P.K. Dorhout, and C.R. Martin, *Chem. Mater.*, **1997**, 9(3): p. 857.
- [240]. B.B. Lakshmi, C.J. Patrissi, and C.R. Martin, *Chem. Mater.*, **1997**, 9(11): p. 2544.
- [241]. Y. Wang, J.Y. Lee, and H.C. Zeng, *Chem. Mater.*, **2005**, 17(15): p. 3899.
- [242]. W.Y. Li, L.N. Xu, and J. Chen, *Adv. Funct. Mater.*, **2005**, 15(5): p. 851.
- [243]. J. Chen, L. Xu, W. Li, and X. Gou, *Adv. Mater.*, **2005**, 17(5): p. 582.
- [244]. X. Li, F. Cheng, B. Guo, and J. Chen, *J. Phys. Chem. B*, **2005**, 109(29): p. 14017.
- [245]. Y. Wang, K. Takahashi, K. Lee, and G. Cao, *Adv. Funct. Mater.*, **2006**, 16(9): p. 1133.
- [246]. S. Nordlinder, L. Nyholm, T. Gustafsson, and K. Edström, *Chem. Mater.*, **2006**, 18(2): p. 495.
- [247]. X. Shi, S. Han, R.J. Sanedrin, C. Galvez, D.G. Ho, B. Hernandez, F. Zhou, and M. Selke, *Nano Letters*, **2002**, 2(4): p. 289.
- [248]. J.Y. Eom, J.W. Park, H.S. Kwon, and S. Rajendran, *J. Electrochem. Soc.*, **2006**, 153(9): p. A1678.
- [249]. J. Yin, M. Wada, Y. Kitano, S. Tanase, O. Kajita, and T. Sakai, *J. Electrochem. Soc.*, **2005**, 152(7): p. A1341.
- [250]. Z.P. Guo, Z.W. Zhao, H.K. Liu, and S.X. Dou, *Carbon*, **2005**, 43(7): p. 1392.
- [251]. J.R. Owen, *Chem. Soc. Rev.*, **1997**, 26: p. 259.
- [252]. D. Aurbach, *Nonaqueous Electrochemistry*, **1999**, New York: Marcel Dekker, 608 pages.
- [253]. A. Calka and D. Wexler, *Nature*, **2002**, 419: p. 147.

- [254]. W.C. Davis and R.K. Marcus, *J. Anal. At. Spectrom.*, **2001**, 16: p. 931.
- [255]. F.-S. Cai, G.-Y. Zhang, J. Chen, X.-L. Gou, H.-K. Liu, and S.-X. Dou, *Angew. Chem.*, **2004**, 43(32): p. 4212.
- [256]. P. Scherrer, *Nachr. Ges. Wiss. Goettingen*, **1918**, 2: p. 98.
- [257]. A. Hammersley, *European Synchrotron Radiation Facility, (ESRF)*, e-mail hammersley@esrf.fr.
- [258]. A.C. Larson and R.B. Von Dreele, *Generalized Structure Analysis System (GSAS)*. **1994**, Los Alamos National Laboratory Report LAUR.
- [259]. S. Brunauer, P.H. Emmett, and E. Teller, *J. Am. Chem. Soc.*, **1938**, 60: p. 309.
- [260]. J. Kawakita and K. Kobayashi, *J. Power Sources*, **2001**, 101: p. 47.
- [261]. J.W. Braithwaite, A. Gonzales, G. Nagasubramanian, S.J. Lucero, D.E. Peebles, J.A. Ohlhausen, and W.R. Cieslak, *J. Electrochem. Soc.*, **1999**, 146: p. 448.
- [262]. D.H. Evans, *Review of voltammetric methods for the study of electrode reactions in microelectrodes: Theory and Applications in Nato ASI Series E*, M.I. Montenegro, M.A. Queirós, and J.L. Daschbach (Eds), **1991**, Dordrecht: Kluwer, pp. 17-32.
- [263]. M. Winter and R.J. Brodd, *Chem. Rev.*, **2004**, 104: p. 4245.
- [264]. J. Akimoto, Y. Gotoh, and Y. Oosawa, *J. Solid State Chem.*, **1998**, 141: p. 298.
- [265]. H. Wang, Y.I. Jang, B. Huang, D.R. Sadoway, and Y.M. Chiang, *J. Electrochem. Soc.*, **1999**, 146: p. 473.
- [266]. M. Zou, M. Yoshio, S. Gopukumar, and J.I. Yamaki, *Chem. Mater.*, **2003**, 15(25): p. 4699.
- [267]. H. Tukamoto and A.R. West, *J. Electrochem. Soc.*, **1997**, 144(9): p. 3164.
- [268]. L.A. Montoro, M. Abbate, and J.M. Rosolena, *Electrochem. Solid-State Lett.*, **2000**, 3(9): p. 410.
- [269]. W.S. Yoon, K.B. Kim, M.G. Kim, M.K. Lee, H.J. Shin, J.M. Lee, J.S. Lee, and C.H. Yo, *J. Phys. Chem. B*, **2002**, 106: p. 2526.
- [270]. C.D. Jones, E. Rossen, and J.R. Dahn, *Solid State Ionics*, **1994**, 68: p. 65.
- [271]. J.N. Reimers and J.R. Dahn, *J. Electrochem. Soc.*, **1992**, 139: p. 2091.
- [272]. Y.-M. Choi and S.-I. Pyun, *Solid State Ionics*, **1997**, 99.

- [273]. B. Huang, Y.-I. Jang, Y.-M. Chiang, and D.R. Sadoway, *J. Appl. Electrochem.*, **1998**, 28: p. 1365.
- [274]. A.N. Mansour, J.W. Cook, and D.E. Sayers, *J. Phys. Chem. B*, **1984**, 88: p. 2330.
- [275]. H. Yoshitake, T. Mochizuki, O. Yamazaki, and K. Ota, *J. Electroanal. Chem.*, **1993**, 361: p. 229.
- [276]. A. Deb, U. Bergmann, E.J. Cairns, and S.P. Cramer, *J. Phys. Chem. B.*, **2004**, 108: p. 7046.
- [277]. G. Berlier, G. Spoto, P. Fisicaro, S. Bordiga, A. Zecchina, E. Giamello, and C. Lamberti, *Microchem. J.*, **2002**, 71: p. 101.
- [278]. M. Abatte, S.M. Lala, L.A. Montoro, and J.M. Rosolen, *Electrochem. Solid-State Letters*, **2005**, 8(6): p. A288.
- [279]. U. Anselmi-Tamburini, S. Gennari, J.E. Garay, and Z.A. Munir, *Mater. Sci. Eng. A*, **2005**, 394: p. 139.
- [280]. W. Chen, U. Anselmi-Tamburini, J.E. Garay, J.R. Groza, and Z.A. Munir, *Mater. Sci. Eng. A*, **2005**, 394: p. 132.
- [281]. R. Dominko, D. Arcon, A. Mrzel, A. Zorko, P. Cevec, P. Venturini, M. Gaberscek, M. Remskar, and D. Mihailovic, *Adv. Mater.*, **2002**, 14(21): p. 1531.
- [282]. C.H. Lu and P.Y. Yeh, *J. Mater. Chem.*, **2000**, 10(3): p. 599.
- [283]. Y.-M. Choi and S.-I. Pyun, *Solid State Ionics*, **1997**, 99: p. 173.
- [284]. S.-T. Myung, S. Komaba, N. Hirosaki, H. Yashiro, and N. Kumakai, *Electrochim. Acta*, **2004**, 49: p. 4213.
- [285]. S. Franger, C. Bourbon, and F. Le Cras, *J. Electrochem. Soc.*, **2004**, 151(7): p. A1024.
- [286]. S. Stramare, V. Thangadurai, and W. Weppner, *Chem. Mater.*, **2003**, 15: p. 3974.
- [287]. A.J. Millis, *Nature*, **1998**, 392: p. 147.
- [288]. L.A. Wills, B.W. Wessels, D.S. Richeson, and T.J. Marks, *App. Phys. Lett.*, **1992**, 60(1): p. 41.
- [289]. X. Wang, Z. Zhang, and S. Zhou, *Mat. Sci. Eng. B*, **2001**, 86: p. 29.
- [290]. S. Malo and A. Maignan, *Inorg. Chem.*, **2004**, 43(25): p. 8169.
- [291]. Y.-N. Nuli, S.-L. Zhao, and Q.-Z. Qin, *J. Power Sources*, **2003**, 114: p. 113.

- [292]. Y. Wang and Q.-Z. Qin, *J. Electrochem. Soc.*, **2002**, 149: p. A873.
- [293]. X.P. Gao, Y. Lan, H.Y. Zhu, J.W. Liu, Y.P. Ge, F.Wu, and D.Y. Song, *Electrochem. Solid-State Lett.*, **2005**, 8(1): p. A26.
- [294]. T. Kasuga, M. Hiramatsu, A. Hoson, T.Sekino, and K. Niihara, *Langmuir*, **1998**, 14: p. 3160.
- [295]. S.M. Liu, L.M. Gan, L.H. Liu, W.D. Zhang, and H.C. Zeng, *Chem. Mater.*, **2002**, 14: p. 1391.
- [296]. A. Delahaye-Vidal and M. Figlarz, *J. Applied Electrochem.*, **1987**, 17: p. 589.
- [297]. C. Faure, C. Delmas, and P. Willman, *J. Power Sources*, **1991**, 35: p. 263.
- [298]. F. Portemer, A. Delahaye-Vidal, and M. Figlarz, *J. Electrochem. Soc.*, **1992**, 139(3): p. 671.
- [299]. R.A. Huggins, *J. Power Sources*, **1999**, 81-82: p. 13.
- [300]. M. Winter, J.O. Besenhard, M.E. Spahr, and P. Novak, *Adv. Mater.*, **1998**, 10(10): p. 725.
- [301]. S.A. Needham, G.X. Wang, and H.K. Liu, *J. Alloys Compd.*, **2005**, 400(1-2): p. 234.
- [302]. A.H. Whitehead, J.M. Elliott, and J.R. Owen, *J. Power Sources*, **1999**, 81: p. 33.
- [303]. J.O. Besenhard, M. Wachtler, M. Winter, R. Andreaus, I. Rom, and W. Sitte, *J. Power Sources*, **1999**, 81-82: p. 268.
- [304]. H. Li, L. Shi, Q. Wang, L. Chen, and X. Huang, *Solid State Ionics*, **2002**, 148(3-4): p. 247.
- [305]. H. Mukaibo, T. Osaka, P. Reale, S. Panero, B. Scrosati, and M. Wachtler, *J. Power Sources*, **2004**, 132(1-2): p. 225.
- [306]. H. Li, L. Shi, W. Lu, X. Huang, and L. Chen, *J. Electrochem. Soc.*, **2001**, 148(8): p. A915.
- [307]. E. Frackowiak, S. Gautier, H. Gaucher, S. Bonnamy, and F. Beguin, *Carbon*, **1999**, 37: p. 61.
- [308]. B. Gao, A. Kleinhammes, X.P. Tang, C. Bower, L. Fleming, Y. Wu, and O. Zhou, *Chem. Phys. Lett.*, **2000**, 307: p. 153.
- [309]. G.T. Wu, C.S. Wang, X.B. Zhang, F.S. Yang, Z.F. Qi, P.M. He, and W.Z. Li, *J. Electrochem. Soc.*, **1999**, 146: p. 1696.
- [310]. W.X. Chen, J.Y. Lee, and Z. Liu, *Electrochem. Commun.*, **2002**, 4: p. 260.

- [311]. G.M. Erlich, C. Durand, X. Chen, T.A. Hugener, F. Spiess, and S.L. Suib, *J. Electrochem. Soc.*, **2000**, 147: p. 278.
- [312]. M. Winter, J.O. Besenhard, J.H. Albering, J. Yang, and M. Wachtler, *Prog. Batt. Battery Mater.*, **1998**, 17: p. 208.
- [313]. E. Rönnebro, J. Yin, A. Kitano, M. Wada, S. Tanase, and T. Sakai, *J. Electrochem.Soc.*, **2005**, 152: p. A152.
- [314]. M.S. Park, G.X. Wang, Y.M. Kang, S.Y. Kim, H.K. Liu, and S.X. Dou, *Electrochem. Comm.*, **2007**, 9: p. 71.
- [315]. Z.-W. Fu, Y. Wang, Y. Zhang, and Q.-Z. Qin, *Solid State Ionics*, **2004**, 170: p. 105.
- [316]. A. Gibaud, J.S. Xue, and J.R. Dahn, *Carbon*, **1996**, 34(4): p. 499.
- [317]. P.A. Connor and J.T.S. Irvine, *Electrochim. Acta*, **2002**, 47: p. 2885.
- [318]. D. Aurbach, *J. Power Sources*, **2000**, 89(2): p. 206.
- [319]. D. Aurbach and A. Zaban, *J. Electrochem. Soc.*, **1994**, 141: p. 1808.
- [320]. M.D. Levi and D. Aurbach, *J. Phys. Chem. B*, **1997**, 101: p. 4630.
- [321]. M. Dolle, F. Orsini, A.S. Gozdz, and J.-M. Tarascon, *J. Electrochem. Soc.*, **2001**, 148(8): p. A851.
- [322]. W.-R. Liu, J.-H. Wang, H.-C. Wu, D.-T. Shieh, M.-H. Yang, and N.-L. Wu, *J. Electrochem. Soc.*, **2005**, 152(9): p. A1719.
- [323]. I.-S. Kim, G.E. Blomgren, and P.N. Kumta, *J. Electrochem. Soc.*, **2005**, 152(1): p. A248.

List of Symbols and Abbreviations

Symbol / Abbreviation	Name
\AA	Angstrom
atm	Atmospheric pressure
BET	Brunauer-Emmet-Teller specific surface area
C	Curie constant
C	Concentration of species at an electrode's surface
C_{dl}	Double layer capacitance
C_f	Passive film capacitance
cm	Centimetre
C_θ	Concentration of species in a bulk solution
CNT	Carbon nanotube
CPE	Constant phase element
C_T	Theoretical capacity
CV	Cyclic voltammetry
D	Diffusion coefficient
DC	Direct current
DEC	Diethyl carbonate
DTA	Differential Thermal Analysis
e	Electron
EC	Ethylene carbonate
EDXS	Energy dispersive x-ray spectroscopy
E_F	Fermi energy
<i>e.g.</i>	Exempli gratia, in Latin meaning “for example”
E_g	Energy gap at room temperature
EIS	Electrochemical impedance spectroscopy
emu	Electro-magnetic unit
Eqn	Equation
<i>et al.</i>	Et al ii, in Latin meaning “and others”
eV	Electronvolt
EV	Electric vehicle

Symbol / Abbreviation	Name
exp	Exponential
EY	Electron yield
F	Faradays constant, 95484.56 C mol ⁻¹
f	Degrees of freedom
FC	applied magnetic field cooling
Fig	Figure
FM	Ferromagnetism
FY	Fluorescence yield
g	Gram
GSAS	General structure analysis system
h	Hour
HEV	Hybrid electric vehicle
HSGM	high-energy spherical grating monochromator
I	Current
i_0	Exchange current density
I_0	X-ray intensity incident on a sample
I_t	X-ray intensity transmitted through a sample
ICP	Inductively coupled plasma
ICDD	International centre for diffraction data
<i>i.e.</i>	Id est, in Latin meaning “that is”
ISEM	Institute for superconducting & electronic materials
K	Kelvin
k, k_B	Boltzmann constant, J/K
m	Mass
M	Magnetization
mAh g ⁻¹	Milli ampere hour per gram
MCMB	Mesocarbon microbeads
min	Minute
mm	Millimetre
MPMS	Magnetic properties measurement system
MW	Molecular weight

Symbol / Abbreviation	Name
N_A	Avogadro's number
NMP	N-methyl pyrrolidinone
NSRRC	National synchrotron radiation research center
OCV	Open circuit voltage
Oe	Oersted
PLD	Pulsed laser deposition
R	Electrical resistance
R	Gas constant, 8.314472 J. K ⁻¹ mol ⁻¹
R_{ct}	Charge transfer resistance
R_f	Resistance of passive film
r_i	Ionic radius
R_p	Profile refinement factor, % (Rietveld)
R_s	Resistance of solution
R_{wp}	Weighted pattern refinement factor, % (Rietveld)
PPMS	Physical properties measurement system
pvdF	Polyvinylidenefluoride
S	Siemens
SAD	Selected area diffraction
sec	Second
SEI	Solid electrolyte interphase
SEM	Scanning electron microscopy
SHE	Standard hydrogen electrode
SPS	Spark plasma sintering
SRRC	Synchrotron radiation research centre
t	Time, sec, min, h
T	Temperature, K
T	Tesla
T_C	Curie temperature
TEM	Transmission electron microscopy
TGA	Thermo-gravimetric analysis
V	Volt

Symbol / Abbreviation	Name
V	Volume
W	Warburg diffusion in bulk solid (EIS)
w	Weight, mg, g, kg
wt%	Weight percent
XAFS	X-ray absorption fine structure
XANES	X-ray absorption near edge spectroscopy
XAS	X-ray absorption spectroscopy
XPS	X-ray photoemission spectroscopy
XRD	X-ray diffraction
ZFC	Zero magnetic field cooling
χ	Magnetic susceptibility
μ	Absorption co-efficient or micro
μ_{eff}	Effective magnetic moment
μ_{B}	Bohr magneton
μ_0	Magnetic permeability
2θ	Diffraction angle (XRD)
Ω	Ohm
$^{\circ}$	Degree
$^{\circ}\text{C}$	Degrees Celsius
$\chi^{-1}, (1/\chi)$	Reciprocal magnetic susceptibility
χ_0	Temperature independent magnetic susceptibility
ρ	Density
η	Overvoltage or polarization
β	Full width at half maximum (Scherrer Eqn)
λ	Wavelength
θ_{p}	Pauli-Weiss temperature
χ^2	Chi squared test (Statistical method)
ε	Permittivity of SEI layer

List of Materials and Chemicals

Chemical Name / Material	Reagent	Grade, %	Supplier
Acetone	C ₃ H ₆ O	99	Aldrich
Antimony chloride	SbCl ₃	99	Aldrich
Ammonium dihydrogenphosphate	NH ₄ H ₂ PO ₄	97	Aldrich
Ammonium hydroxide	NH ₄ OH	28-30, NH ₃	Aldrich
Carbon black	C	99.99	Lexel
Cobalt (II, III) oxide	Co ₃ O ₄	99.9	Aldrich
Cobalt nitrate hexahydrate	Co(NO ₃) ₂ .6H ₂ O	98 +	Aldrich
Iron (III) oxide	Fe ₂ O ₃	99.9	Aldrich
Tin (IV) oxide	SnO ₂	99.9	BCH
Ethylene carbonate	C ₃ H ₄ O ₃	99	Aldrich
Dithylcarbonate	(C ₂ H ₅ O) ₂ CO	99	Aldrich
Ethanol	C ₂ H ₅ OH	100	Aldrich
Hydrochloric acid	HCl	2 M	Aldrich
Indium (III) oxide	In ₂ O ₃	99.9	Aldrich
Iron oxalate	FeC ₂ O ₄ .2H ₂ O	99	Aldrich
Lithium carbonate	Li ₂ CO ₃	99.90	Aldrich
Lithium hexafluorophosphate	LiPF ₆	1 M	Aldrich
Lithium hydroxide	LiOH.H ₂ O	99.95	Aldrich
Magnesium (II) oxide	MgO	99.8	Aldrich
Molybdenum (III) oxide	Mo ₂ O ₃	99.5	Aldrich
N-methylpyrrolidinone, NMP	C ₅ H ₉ NO	99.5	Aldrich
Nickel chloride	NiCl ₂	99.9	Aldrich

Chemical Name / Material	Reagent	Grade, %	Supplier
Nickel hydroxide	Ni(OH) ₂	61, Ni	Alfa Aesar
Polyacrylic acid	C ₃ H ₄ O ₂	99.5	Aldrich
Polypropylene separator	(C ₃ H ₆) _n	100	Celgard
Polyvinylidene fluoride, pvdf	(C ₂ H ₂ F ₂) _n	99	Aldrich
Sodium borohydride	NaBH ₄	98	Aldrich
Sodium citrate dehydrate	Na ₃ C ₆ H ₅ O ₇ .2H ₂ O	99	BCH
Sodium hydroxide	NaOH	> 98	Aldrich
Sugar (white)	C ₁₂ H ₂₂ O ₁₁	99	CSR Brand
Tin (II) chloride dihydrate	SnCl ₂ .2H ₂ O	98	Aldrich
Titanium (IV) methoxide	Ti(OCH ₃) ₄	99	Aldrich
Vanadium (III) oxide	V ₂ O ₃	99	Aldrich

List of Figures

- Figure 2.1:** *Gravimetric and volumetric energy density comparison of different battery technologies.*
- Figure 2.2:** *(a) Temperature and (b) voltage binary phase diagrams of hypothetical alloy Li_xM . A voltage plateau corresponds to a phase coexistence region.*
- Figure 2.3:** *Schematic of the discharge process in a rechargeable lithium battery.*
- Figure 2.4:** *Voltage vs. capacity for cathode and anode electrode materials presently used or under serious consideration for the next generation of rechargeable lithium cells.*
- Figure 2.5:** *The first galvanostatic charge of Li/cubic- LiCoO_2 (dotted line) and Li/hex- LiCoO_2 (full line) electrochemical cells.*
- Figure 2.6:** *(a) The LiCoO_2 unit cell. (b) The structure of LiCoO_2 consists of layers of transition metal (TM) separated from lithium layers by oxygen. (c) Lithium moves from one octahedral site to another by passing through an intermediate tetrahedral site where it encounters strong repulsion from a nearby TM cation. The table shows the activation barrier for lithium motion for cobalt and nickel near the activated state.*
- Figure 2.7:** *The orthorhombic crystal structure of LiFePO_4 .*
- Figure 2.8:** *Charge/discharge cycling of LiFePO_4 conducted at 1 mA cm^{-2} .*
- Figure 2.9:** *Planar view of the level of organization in various carbons: (a) high energy defects present in hard carbons and some soft carbons heated below 1000°C ; (b) stacking faults and turbostratic arrangement particularly displayed in soft carbons heated in the $1000\text{-}1500^\circ\text{C}$ range; (c) hexagonal and rhombohedral graphite.*

- Figure 2.10:** *Electrochemical performance of various carbons: (a) first cycle capacity (thick line) and irreversible capacity (thin line) vs. heat treatment temperature for soft carbons; (b) typical second charge/discharge cycle for graphite and hard carbon.*
- Figure 2.11:** *SEI film formation in a graphite electrode for electrolytes based on EC (a), MF (b), and PC (c) solvents.*
- Figure 2.12:** *The theoretical capacity and volume expansion of various lithium alloys.*
- Figure 2.13:** *Different views of the rhombohedral crystal structure in β phase SnSb.*
- Figure 2.14:** *SEM of SnSb-Sn powders: (a) reduced by NaBH_4 ; (b) reduced by Zn in aqueous solution; (c) reduced by Zn in glycol.*
- Figure 2.15:** *Potential profiles in the first charge/discharge cycle of SnSb-Sn powders prepared by reductive precipitation.*
- Figure 2.16:** *Low resolution SEM images of a hard carbon spherule before (a) and after (b) coating with SnSb alloy.*
- Figure 2.17:** *Different views of the cubic crystal structure of Co_3O_4 .*
- Figure 2.18:** *Different views of the cubic crystal structure of NiO.*
- Figure 2.19:** *Schematic representation of two alternative routes for the electrochemical reaction of Co_3O_4 with lithium.*
- Figure 2.20:** *Variation of voltage with lithium content for $\text{TiO}_2(\text{B})$ materials cycled at a constant current of 10 mA g^{-1} between 1 V and 3 V.*
- Figure 2.21:** *Comparison of the electrochemical performance of SnO_2 thin films and nanostructured powders: (a) rate capability; (b) cyclability.*
- Figure 2.22:** *SEM images (a), (b), and a TEM image of the morphology of Co_3O_4 nanotubes (c). The discharge capacity of Co_3O_4 nanotubes, nanorods, and nanoparticles at a constant current of 50 mAh g^{-1} (d).*
- Figure 3.1:** *A flow chart detailing the experimental techniques and procedures.*

Figure 3.2: *Schematic of the EDAMM powder synthesis technique. The vibration of a stainless steel plunger connected to an ac voltage can cause the formation of various electric discharges for variable times; (a) athermal glow, and (b) thermal arc. (c) The interaction of an arc discharge with a powder particle produces a main plasma channel (trunk) and minor plasma channels (branches) of lower intensity.*

Figure 3.3: *Schematic showing the preparation of NiO nanotubes.*

Figure 3.4: *Various SnSb-based powders prepared by the reductive precipitation method.*

Figure 3.5: *Schematic of spray pyrolysis apparatus. The model on the LHS details the mechanism of formation of $\text{Co}_3\text{O}_4\text{-C}$ powders.*

Figure 3.6: *The photoelectric effect.*

Figure 3.7: *The process of photoelectron scattering and identification of the XANES region in the XAS spectrum.*

Figure 3.8: *Schematic of an assembled R2032 coin-type test cell.*

Figure 4.1: *Rietveld refinement of synchrotron x-ray diffraction patterns obtained for $\text{LiM}_{0.02}\text{Co}_{0.98}\text{O}_2$ powders where $M = \text{Mg}$ (a), V (b), and Mo (c). Insets show enlargements of specified angular ranges of spectra.*

Figure 4.2: *Vanadium L-edge XAS spectra of $\text{LiV}_{0.02}\text{Co}_{0.98}\text{O}_2$ and selected standards.*

Figure 4.3: *Cobalt L-edge XAS spectra of $\text{LiM}_{0.02}\text{Co}_{0.98}\text{O}_2$ and selected standards.*

Figure 4.4: *Oxygen K-edge XANES spectra of $\text{LiM}_{0.02}\text{Co}_{0.98}\text{O}_2$ and reference LiCoO_2 powders.*

Figure 4.5: *Electrical conductivity measurements of $\text{LiM}_{0.02}\text{Co}_{0.98}\text{O}_2$ pelletized powders.*

Figure 4.6: *Cyclic voltammograms of $\text{LiM}_{0.02}\text{Co}_{0.98}\text{O}_2$ cells measured from 3.0 V to 4.5 V at a scan rate of 0.02 mV s^{-1} .*

- Figure 4.7:** *Discharge capacity of $\text{LiM}_{0.02}\text{Co}_{0.98}\text{O}_2$ electrodes cycled from 3.0 V to 4.2 V at 30 mA g^{-1} .*
- Figure 5.1:** *X-ray diffraction patterns of LiFePO_4 and $\text{LiTi}_{0.01}\text{Fe}_{0.99}\text{PO}_4$ powders.*
- Figure 5.2:** *Synchrotron x-ray diffraction pattern and Rietveld refinement of $\text{LiTi}_{0.01}\text{Fe}_{0.99}\text{PO}_4$ powder. The inset shows an enlargement of the $20 - 45^\circ$ range.*
- Figure 5.3:** *TEM image of LiFePO_4 powder (a) and a high resolution TEM image of carbon coated on the surface of individual nanocrystals (b).*
- Figure 5.4:** *Individual iron K-edge XANES spectra of LiFePO_4 and $\text{LiTi}_{0.01}\text{Fe}_{0.99}\text{PO}_4$ powders showing the main absorption edge (known as the white line, although indicated in blue) at 7127 eV and the pre-edge peaks at $\sim 7112 \text{ eV}$. The inset shows a comparison of the white line intensities of same two spectra.*
- Figure 5.5:** *Oxygen K-edge x-ray absorption spectra of LiFePO_4 and $\text{LiFe}_{0.99}\text{Ti}_{0.01}\text{PO}_4$ powders measured in Fluorescence Yield (FY) mode (a) and Electron Yield (EY) mode (b).*
- Figure 5.6:** *Cyclic voltammograms of LiFePO_4 and $\text{LiTi}_{0.01}\text{Fe}_{0.99}\text{PO}_4$ measured at a scan rate of 0.01 mV s^{-1} between 2.75 V and 4.25 V.*
- Figure 5.7:** *The charge/discharge profiles in the first cycle for LiFePO_4 and $\text{LiTi}_{0.01}\text{Fe}_{0.99}\text{PO}_4$ electrodes. The inset shows the discharge capacity vs. cycle number.*
- Figure 6.1:** *X-ray diffraction pattern of the LiCoO_2 powder produced by high power EDAMM (10 min). The refined lattice parameters are given, and the inset shows a TEM image of lattice fringes.*
- Figure 6.2:** *SEM images of LiCoO_2 particles produced at a vibration amplitude of 5 mm with high power for 10 min (a), and low power for 5 min (b).*

- Figure 6.3:** *Cyclic voltammograms of Li/LiCoO₂ cell measured between 3.0 V and 4.2 V at a scan rate of 0.01 mV s⁻¹. Powder prepared by low power EDAMM with a vibration amplitude of 5 mm for 5 min.*
- Figure 6.4:** *Charge/discharge curves for LiCoO₂ cycled at the C/5 rate from 3.0 V to 4.2 V. Powder prepared by low power EDAMM with a vibration amplitude of 5 mm for 5 min.*
- Figure 6.5:** *X-ray diffraction patterns of LiFePO₄ powders produced by high power EDAMM with a vibration amplitude of 1 mm for 0 min (precursors), 1 min, 3 min, 5 min, and 10 min. The inset shows the refined LiFePO₄ unit cell lattice parameters (Pmnb space group) and goodness factors.*
- Figure 6.6:** *SEM images of LiFePO₄ particles produced by: a) high power EDAMM with a vibration amplitude of 1 mm for 10 min, and b) high power EDAMM with a vibration amplitude of 5 mm for 10 min.*
- Figure 6.7:** *Cyclic voltammogram of Li/LiFePO₄ cell measured between 2.6 V and 4.4 V at a scan rate of 0.2 mV s⁻¹. Powder prepared by high power EDAMM with a vibration amplitude of 1 mm for 10 min.*
- Figure 6.8:** *Charge/discharge curves for LiFePO₄ cycled at the C/5 rate from 2.8 V to 4.4 V. Inset shows discharge capacity vs. cycle number. Powder prepared by high power EDAMM with a vibration amplitude of 1 mm for 10 min.*
- Figure 6.9:** *X-ray diffraction patterns of SrTi_{1-x}Co_xO₃ (x = 0 and 0.5) samples produced by high power discharge (30 min). Right inset shows magnified view of the patterns for all samples. Left inset shows the dependence of lattice parameter a on cobalt content (x) with corresponding goodness factors of Rietveld refinements.*
- Figure 6.10:** *TEM images of SrTi_{0.5}Co_{0.5}O₃ particles produced by high power EDAMM with a mill vibration of 1mm that show evidence of particle melting (a), and a general view of particle morphology (b).*

- Figure 6.11:** *Molar magnetic susceptibility (χ) versus temperature (T) for $\text{SrTi}_{0.5}\text{Co}_{0.5}\text{O}_3$ under 1000 Oe applied magnetic field. The inset represents the inverse molar magnetic susceptibility ($1/\chi$) under the same conditions.*
- Figure 7.1:** *X-ray diffraction patterns of $\text{Ni}(\text{OH})_2$ nanotubes, NiO nanotubes, and NiO nanocrystalline powder.*
- Figure 7.2:** *Images of NiO nanotubes at different magnifications captured by SEM (a)-(c) and TEM (d) techniques.*
- Figure 7.3:** *First and second cycle cyclic voltammograms performed at a sweep rate of 0.02 mV s^{-1} for NiO nanocrystalline powder (a) and NiO nanotubes (b).*
- Figure 7.4:** *First and second cycle charge/discharge curves performed at a current of 0.025 mA for NiO nanocrystalline powder (a) and NiO nanotubes (b).*
- Figure 7.5:** *Discharge capacity of NiO nanocrystalline and nanotube powders performed at a current of 0.025 mA over 20 cycles.*
- Figure 7.6:** *Impedance spectra for NiO nanocrystalline powder and NiO nanotubes. The inset shows an equivalent circuit where R_s = impedance due to the electrolyte and surface films, R_{ct} = charge-transfer resistance at the electrode/solution interface, CPE = constant phase element, and W = Warburg impedance and represents the diffusion of Li^+ within the bulk material.*
- Figure 8.1:** *X-ray diffraction patterns of SnSb and SnSb-Sn powders.*
- Figure 8.2:** *Representative SEM image of the microstructure of SnSb and SnSb-Sn produced by reductive precipitation.*
- Figure 8.3:** *The discharge capacity of SnSb and SnSb-Sn electrodes with various quantities of carbon black. The inset shows the coulombic efficiency of the SnSb series.*

- Figure 8.4:** SEM images of a SnSb-Sn + 50 wt% carbon black electrode: (a) after one charge/discharge cycle, with inset showing line mapped across the scale bar for Sn and Sb elements, and (b) showing microcracking of the SnSb domains after 50 charge/discharge cycles.
- Figure 8.5:** Charge/discharge curves for the 1st, 5th, and 50th cycles for SnSb + 20 wt% C (a), SnSb + 50 wt% C (b), SnSb-Sn + 20 wt% C (c), and SnSb + 50 wt% C (d).
- Figure 8.6:** FE-SEM images at different magnifications of multiwall CNTs (a) and (c), and SnSb-CNT nanocomposite powder prepared by reductive precipitation of metal salts (b) and (d).
- Figure 8.7:** X-ray diffraction patterns (a) and room temperature Raman spectra (b) of SnSb-CNT nanocomposite powder and multiwall CNTs.
- Figure 8.8:** TEM image and selected area diffraction (SAD) pattern (inset) of an individual CNT coated with SnSb (a), a higher magnification TEM (b), and a HRTEM of the same area (c).
- Figure 8.9:** Galvanostatic voltage profiles for SnSb-CNT between 0.025 V and 1.5 V (a), differential charge/discharge vs. voltage plots at the 1st, 2nd, and 5th cycle for SnSb-CNT (b), and a comparison of the cyclic performance of SnSb, CNT, SnSb + 50 wt% C, and SnSb-CNT, with the inset showing the coulombic efficiency (c).
- Figure 9.1:** X-ray diffraction patterns of NiO (a), and Co₃O₄ and Co₃O₄ – C (b).
- Figure 9.2:** Images of Co₃O₄ – C powder. A low magnification SEM view (a), a TEM image of the nanoporous carbon sheath coated on a Co₃O₄ – C particle (b), and a higher magnification TEM image of finely distributed disordered C and crystalline Co₃O₄ domains within an individual particle (c).
- Figure 9.3:** Particle size distribution and BET specific surface areas of NiO, Co₃O₄, and Co₃O₄ – C powders.

Figure 9.4: *The electrochemical performance of Co_3O_4 - C, Co_3O_4 , and NiO powders, showing discharge capacity over 50 cycles (a) and the 1st and 50th cycle discharge curves (b).*

Figure 9.5: *Nyquist plots of Co_3O_4 - C (a) and Co_3O_4 (b) electrodes, and the fitted equivalent circuit parameters vs. discharge voltage (c). R_s is represented by open symbols and R_{ct} by closed symbols.*

List of Tables

Table 2.1: *A selection of cation doped LiCoO_2 compounds prepared by solid-state methods. Test cells constructed using 1 M LiPF_6 dissolved in 1:1 ethylene carbonate:diethylcarbonate (EC:DEC) electrolyte solution and subjected to galvanostatic charge/discharge cycling between 3.0 V and 4.2 V.*

Table 2.2: *Physical properties of important organic solvents.*

Table 4.1: *Structural parameters of $\text{LiM}_{0.02}\text{Co}_{0.98}\text{O}_2$ ($M = \text{Mg}, \text{V}, \text{Mo}$) samples based on Rietveld refinement of synchrotron radiation ($\lambda = 0.516606 \text{ \AA}$) x-ray diffraction patterns measured at 300 K. Lithium, cobalt, and oxygen atoms occupy the (0, 0, 0), (0, 0, 0.5) and (0, 0, z) positions, respectively.*

Table 5.1: *Structural parameters of LiFePO_4 determined by XRD at 300 K.*

Table 5.2: *Structural parameters of $\text{LiTi}_{0.01}\text{Fe}_{0.99}\text{PO}_4$ determined by XRD at 300 K.*

List of Author Publications

M.-S. Park, **S.A. Needham**, G.X. Wang, Y.-M. Kang, J.-S. Park, S.X. Dou, and H.K. Liu, “Nanostructured SnSb/Carbon Nanotube composites Synthesized by Reductive Precipitation for Lithium Batteries” *Chem. Mater.*, **2007**, 19: p. 2406.

S.A. Needham, A. Calka, G.X. Wang, G. Peleckis, H.K. Liu, “Synthesis of Functional Oxides by a Novel Mechanical Milling-Electric Discharge Method” *J. Mater. Chem.*, **2006**, 16: p. 4488.

S.A. Needham, A. Calka, G.X. Wang, A. Mosbah, H.K. Liu, “A New Rapid Synthesis Technique for Electrochemically Active Materials used in Energy Storage Applications” *Electrochem. Comm.*, **2006**, 8: p. 434.

S.A. Needham, G.X. Wang, K. Konstantinov, Y. Tournayre, Z. Lao, H.K. Liu, “Electrochemical Performance of Co_3O_4 -C Anode Materials” *Electrochem. Solid-State Lett.*, **2006**, 9(7): p. A315.

S.A. Needham, G.X. Wang, H.K. Liu, L. Yang “Nickel Oxide Nanotubes: Synthesis and Electrochemical Performance for use in Li-ion Batteries” *J. Nanosci. Nanotech.*, **2006**, 6(2): p. 1.

S.A. Needham, G.X. Wang, H.K. Liu, “Synthesis of NiO Nanotubes for Use as Negative Electrodes in Li-ion Batteries” *J. Power Sources*, **2006**, 159: p. 254.

S.A. Needham, G.X. Wang, H.K. Liu, “Electrochemical Performance of SnSb and Sn/SnSb Nanosized Powders as Anode Materials in Li-ion Cells” *J. Alloys Compd.*, **2005**, 400: p. 234.

S.A. Needham, G.X. Wang, H.K. Liu, “Synthesis and Electrochemical Performance of $\text{LiM}_{0.02}\text{Co}_{0.98}\text{O}_2$ Cathode Materials”, *J. Power Sources* (in print).

S.A. Needham, V. Drozd, G.X. Wang, H.K. Liu, R.S. Liu “On the Doping of LiCoO_2 with Mg^{2+} , V^{5+} , or Mo^{6+} ions”, *J. Mater. Chem.*, (under review).

G.X. Wang, **S.A. Needham**, J. Yao, J.Z. Wang, R.S. Liu, H.K. Liu, “A study on LiFePO_4 and its Doped Derivatives as Cathode Materials for Lithium-Ion Batteries”, *J. Power Sources*, **2006**, 159(1): p. 282.

G.X. Wang, S. Bewlay, **S.A. Needham**, H.K. Liu, R.S. Liu, V.A. Drozd, J.F. Lee, J.M. Chen “Synthesis and Characterization of LiFePO_4 and $\text{LiTi}_{0.01}\text{Fe}_{0.99}\text{PO}_4$ Cathode Materials” *J. Electrochem. Soc.*, **2006**, 153(1): p. A25.

D. Shanmukaraj, G.X. Wang, **S.A. Needham**, H.K. Liu, R. Murugan, “Synthesis and Characterization of $\text{SrBi}_4\text{Ti}_4\text{O}_{15}$ Ferroelectric Ceramic Filler Based Composite Polymer Electrolytes for Lithium Secondary Batteries”, *J. Power Sources* (in print).

G.X. Wang, Y. Chen, L. Yang, J. Yao, **S.A. Needham**, H.K. Liu, J.H. Ahn, “Synthesis of Nanocrystalline Transition Metal Oxides for Lithium Storage” *J. Power Sources*, **2005**, 146: p. 487.

Conference Publications, Presentations, and Reference Texts

S.A. Needham and H.K. Liu, “The Future of Rechargeable Lithium Batteries - Nanostructured Materials”, Invited chapter contribution for 2007 edition of the *Encyclopaedia of Nanoscience and Nanotechnology*, H. S. Nalwa (ed.), American Scientific Publishers.

S.A. Needham, Invited chapter contribution for the 2007 edition of *Advanced Materials and Methods for Lithium ion Batteries*, Research Signpost, Kerala, India.

S.A. Needham, G.X. Wang, K. Konstantinov, Y. Tournayre, G. Lao, and H.K. Liu, “Sprayed Transition Metal Oxide-Carbon Composites for Li-ion Batteries” MRS Fall Meeting, Nov 28-Dec 2, **2005**, Boston, MA, USA. (Abstract B7.6).

S.A. Needham, G.X. Wang, H.K. Liu, L. Yang “Nickel Oxide Nanotubes: Synthesis and Electrochemical Performance for use in Li-ion Batteries” 3rd International Conference on Materials for Advanced Technologies (ICMAT) and 9th International Conference on Advanced Materials (IUMRS-ICAM), July 3-8, **2005**, Singapore. (Abstract PA-6-PO27).

[Winner of Best Poster Award]

S.A. Needham, G.X. Wang, K. Konstantinov, Y. Tournayre, G. Lao, and H.K. Liu, “Investigation of Transition Metal Oxide - Carbon Composite Anode Materials Prepared by Spray Pyrolysis” 30th annual Condensed Matter and Materials Meeting, 7th -10th February, **2006**, Wagga Wagga, Australia. (Abstract WP-40).

N. Kalaiselvi, **S. A. Needham**, L. Yang, H.K. Liu, C.H Doh, S.I. Moon, M.S. Yun “An Investigation on the Synthesis of LiFePO₄ through Different Methods” 3rd International Conference on Materials for Advanced Technologies (ICMAT) and 9th International Conference on Advanced Materials (IUMRS-ICAM), July 3-8, **2005**, Singapore. (Oral Presentation PA2-OR6).

G.X Wang, S. Bewlay, **S.A. Needham**, J. Yao, “A Study on LiFePO₄ and its Doped Derivatives as Cathode Materials in Li-ion Batteries” 3rd International Conference on Materials for Advanced Technologies (ICMAT) and 9th International Conference on Advanced Materials (IUMRS-ICAM), July 3-8, **2005**, Singapore. (Invited Oral Presentation PA-5-IN6).

S.A. Needham, G.X. Wang, H.K. Liu, “Synthesis and Electrochemical Performance of LiM_{0.02}Co_{0.98}O₂ Cathode Materials” International Meeting on Lithium Batteries (IMLB), June 18-23, **2006**, Biarritz, France. (Abstract 90).

S.A. Needham, G.X. Wang, H.K. Liu, “Synthesis and Electrochemical Performance of Co₃O₄ and Co₃O₄ – C One Dimensional Nanostructures” International Meeting on Lithium Batteries (IMLB), June 18-23, **2006**, Biarritz, France. (Abstract 287).

G.X. Wang, M. Park, **S.A. Needham** “Nanostructured Anode Materials for Li-ion Batteries” International Meeting on Lithium Batteries (IMLB), June 18-23, **2006**, Biarritz, France. (Abstract 325).

D. Shanmukaraj, G.X. Wang, **S.A. Needham**, H.K. Liu, R. Murugan, “Synthesis and Characterization of $\text{SrBi}_4\text{Ti}_4\text{O}_{15}$ Ferroelectric Ceramic Filler Based Composite Polymer Electrolytes for Lithium Secondary Batteries” International Meeting on Lithium Batteries (IMLB), June 18-23, **2006**, Biarritz, France. (Abstract 420).